Laser-induced carbonization and graphitization of a transparent elastomer

July 2023

Shuichiro Hayashi

A Thesis for the Degree of Ph.D. in Engineering

Laser-induced carbonization and graphitization of a transparent elastomer

July 2023

Graduate School of Science and Technology
Keio University

Shuichiro Hayashi

Abstract

Carbonaceous materials such as graphite, diamond, and carbides each possesses unique material properties distinctive to their chemical structure, and have been applied to a wide range of applications. Laser-induced carbonization and graphitization, or LICG, offers the patterning of carbonaceous structures composed of various carbonaceous materials by simply scanning laser light on a polymer. This thesis discusses the chemical and physical processes that ensues as a result of light-matter interactions between the laser light and a transparent elastomer, polydimethylsiloxane (PDMS), and aims to clarify the mechanism in which carbonaceous structures form by LICG and the effects of the carbonaceous materials on the electrical properties of the carbonaceous structure, as well as to apply the carbonaceous structures towards novel devices. This thesis consists of seven chapters. Chapter 1 introduces the background and aim of this thesis. Chapter 2 outlines the chemical and physical processes that ensues as a result of laser irradiation, and provides the theoretical concepts required to discuss the subsequent experimental results. Chapters 3 and 4 will describe the experimental results regarding the basic characterizations of the carbonaceous structures patterned on the PDMS surface by LICG. Chapter 3 will examine the structural aspects of the carbonaceous structures. The mechanisms regarding the formation of carbonaceous structures, and the relationship between laser parameters and structure morphology will be discussed. Chapter 4 will address the electrical property of the carbonaceous structures. The patterning of carbonaceous structures exhibiting different electrical properties is demonstrated by LICG, and the effects of graphitic carbon and SiC-NCs on the electrical property of the overall structure will be discussed. Chapters 5 and 6 will describe the experimental results regarding the application of carbonaceous structures patterned on PDMS by LICG. Chapter 5 will focus on electrical applications using the carbonaceous structures. The piezoresistive properties of the structures are assessed by strain tests, and the fabrication of a micro-pressure sensor and an anisotropic strain sensor will be demonstrated. Chapter 6 will explore optical applications using the carbonaceous structures. It is revealed that fluorescent carbonaceous structures can be patterned by the LICG of PDMS, and the fabrication of an anti-counterfeiting security tag will be demonstrated. Moreover, by utilizing multiphoton interactions. the patterning of fluorescent carbonaceous structures inside PDMS will be demonstrated. Chapter 7 will provide the conclusion of this thesis, summarizing the key findings of each chapter and the thesis, then discuss future studies which have been triggered by this thesis.

Acknowledgments

First and foremost, I would like to express my sincerest gratitude to my advisor, Professor Mitsuhiro Terakawa. As an advisor, you have given the perfect balance between providing guidance and encouraging independence. Since I have joined the Terakawa Group you have challenged me to tackle difficult tasks, and this has over time led me to develop the confidence, mindset, and skills to overcome them. I appreciate the many opportunities you have provided me, and I hope to apply such experiences for my future endeavors in a positive manner. Professor Terakawa, I could not have completed this journey without your continued encouragement and support, thank you.

Also, I sincerely thank my committee members, Professor Jiwang Yan, Professor Yasuhiro Kakinuma, and Professor Kei Noda, for the valuable feedback and advice regarding my thesis. Thank you all for your precious time and cooperation.

I am incredibly fortunate to have had Dr. Yasutaka Nakajima and Dr. Manan Machida as my mentors, collaborators, and friends, who have offered countless advice and guidance throughout my graduate studies at the Terakawa Group. Dr. Nakajima, you were a crucial person who had triggered me to pursue research, and I am glad to have met you during my first year in the Terakawa Group. Dr. Machida, you were a person I could always count on, and provided a nurturing atmosphere for the Terakawa group. I will forever cherish all of the conversations I have had with you two, along with the wonderful memories shared at various conferences and private events.

I am also thankful to all of the past and current members of the Terakawa Group for making my days at Keio University memorable. I appreciate, Akito Katayama, Kosuke Mizuguchi, and Hiroki Sugiyama, for being wonderful companions during my graduate studies and for the countless laughable memories. Thanks to you all, I always had someone to invite for dinner and drinks. I also appreciate, Naonari Kondo, Toshihiko Uemura, Ryo Sano, Izumi Takayama, Fumiya Morosawa, Yo Nagano, Kaneto Tsunemitsu, Rikuto Miyakoshi, Keiki Muranaka, Rei Funayama, Masato Kai, Yuma Hattori, Ken Kashikawa, Yosuke Kondo, and Kosuke Tsukada, for being great colleagues. Thanks to you all, I did not feel lonely during my graduate studies.

Although it was a short period of time, I am also extremely grateful to have met amazing colleagues at Princeton University. Thank you, Professor Craig B. Arnold, for allowing me to join your group and research under your guidance for a semester. It was an unforgettable experience and I am grateful for all that you have done for me. I appreciate, Dr. Amanda Du, Macro Rupp, and Shukai Wang, for being amazing friends

and making my time studying abroad the best. Meals at the dining hall are an unforgettable memory, and I hope we can do it again. I also appreciate the other members of the Arnold Group, Dr. Kai Filsinger, Dr. Jason Liu, Dr. Yang Du, Satya Butler, Yannick Eatmon, Joseph Stiles, and Shaharyar Wani, for the fruitful research discussions and countless precious memories. I regard Princeton University as my second home, and hope to cross paths again with my tiger friends in the future.

I am thankful for the financial support from the Japan Society for the Promotion of Science. My graduate studies would not have been possible without the support from the "Research Fellowship for Young Scientists (DC1)" and "Overseas Challenge Program for Young Researchers" grants.

Last, but not least, I would like to give my deepest gratitude and love to my family. None of this could have been possible without the endless and warm support from them. Kate, thank you for walking every step of the way throughout my graduate studies. I understand that I may have been a handful but I am thankful that you stood firmly beside me and supported me in every way imaginable. I do not think either of us thought this would happen, but I am glad to have had you beside me and would not have it any other way even if I had a chance to redo my graduate studies. Dad, thank you for financially supporting me, but also being my role model as a researcher. When I needed someone to talk to about research, I knew I could always depend on and ask for advice. I hope that I can also become a well-known researcher like you some day. Mom, thank you for your endless love and emotional support all of these years. I am sure I will forever be a baby in your eyes, and a potential source of stress; but I hope, especially through my graduate studies, that I have grown into a son that you can be very proud of. My younger brothers, Kenji and Takahide, your existence is one of the driving forces I strive to be a greater person every day. Thanks to the fact that you two are excellent students, and highly promising future medical doctors, I need to work extra hard so that I am not ashamed to call myself your older brother. Note the sarcasm, but in all honesty, I am very proud of you boys. And, of course, Tadashi and Mariko, thank you two for your heart-warming love and support. You two are the best grandparents anyone could ask for.

Without the support from all of the people involved in my graduate studies, it would have been impossible for me to keep moving forward. These encounters are the reason I am the person I am today, and one last time, thank you everyone for everything.

Sincerely,

Shuichiro Hayashi

Table of contents

1. Background

1.1. Introduction

Carbon is the sixth most abundant element in the universe, and exists in most of the things around us, even in our bodies.[1] In fact, the Earth's crust contains more than 3×10^{16} tons of carbon which exists in various forms, whether it be an allotype or a composite, each with a uniquely different material property.[1] Humans have long held a fascination for this material, and the utilization of carbonaceous materials date back to 3750 BC in Egypt, where Egyptians used coal to disinfect wounds.[1] Since then, the development of new carbonaceous materials, such as graphene, has contributed to the advancement of science and technology. Moreover, in recent years, with the constantly depleting reserve of rare earth minerals carbonaceous materials have been discussed to be a realistic replacement, as the material properties can be vastly tuned.[2] In Section 1.2., different types of carbonaceous materials will be briefly reviewed. From Section 1.3. to Section 1.5., various techniques to synthesize and/or pattern carbonaceous materials will be introduced, and the characteristics of each technique will be discussed. In Section 1.6., the objective of this thesis will be given.

1.2. Different types of carbonaceous materials

Carbon is considered to be one of the most chemically versatile elements, capable of bonding with a wide range of different atoms in various combinations.[3] For example, carbon can have an oxidation value of +4 to form compounds such as carbon dioxide (CO_2), or have an oxidation value of -4 to form methane (CH_4). Carbon can also have intermediate oxidation values such as +2 or -2 to form compounds such as carbon monoxide (CO) or methanol (CH_3OH), respectively. In addition, carbon can form single, double, or triple bonds with other carbon atoms or other heteroatoms. This versatile chemistry of carbon leads to different allotropes with unique physical and chemical properties, which reflects their differences in atomic orientation (Figure 1.1).[3] Solid carbonaceous materials can be largely divided by their atomic orientation being ordered (i.e., crystalline) or disordered (i.e., amorphous). Below different types of carbonaceous materials will be introduced.

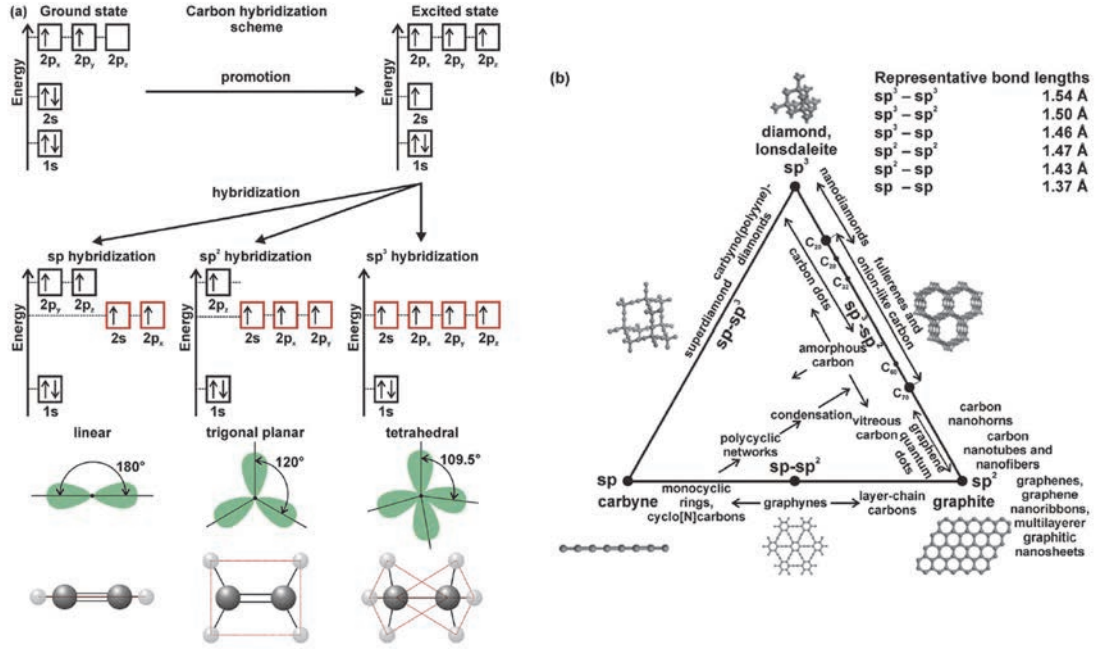

Figure 1.1 (a) Schematic description of sp, sp^2, and sp^3 hybridization in carbon with an illustration of the bonding structure. (b) Ternary phase diagram of carbon (nano)allotropes/nanostructures depending on the hybridization state they show. The positions/intervals of the most common carbon (nano)allotropes/nanostructures are indicated. Carbon forms with a single hybridization state are found at the vertices of the triangle, carbon species with mixed hybridization states lie along the sides of the triangle, and carbon compounds with all the three hybridization states are placed inside the triangle. The representative bond lengths between carbon atoms with specific hybridizations are also listed. Reprinted and reformatted with permission from the Royal Society of Chemistry, Copyright ©2018.[4]

1.2.1. Crystalline material

1.2.1.1. Graphitic carbon

Graphitic carbon, is a crystalline material ideally consisting purely of carbon atoms. The carbon atoms in graphitic carbon are each covalently bonded to three neighboring carbon atoms via three σ and one π bond. This trigonal bonding results from a hybridized orientation of three carbon orbitals; appropriately referred to as sp^2-hybridization, as one 2s orbital mixes, or hybridizes, with two 2p orbitals (Figure 1.1 (a)). The repeating of this trigonal bonding forms a hexagonal honeycomb layer, which is further stacked to form a three-dimensional (3D) crystal lattice. Depending on the number of layers, overall size, and shape of the crystal, the resulting graphitic carbon possesses vastly different material properties. For example, graphene (i.e., two-dimensional (2D) single layer of graphite),

carbon nanotubes (CNTs) (i.e., one-dimensional rolled tube of graphene), and graphene quantum dots (GQDs) (i.e., zero-dimensional particle of graphene), each uniquely exhibits high optical transparency, mechanical tensile strength, and fluorescence, respectively.[4,5] One of the most common natural graphitic carbon is graphite, which has been used as lead in pencils since the 1600's.[6] As graphite is a crystalline material, the formation of graphite requires high temperatures and pressures and thus naturally forms at deeper regions of the Earth's crust near the mantle.[1,3,7]

1.2.1.2. Diamond

Diamond, is another crystalline material ideally consisting purely of carbon in which each carbon atom is covalently bonded to four neighboring carbon atoms via four σ bonds. This tetrahedral bonding results from a hybridized orientation of four carbon orbitals; referred to as sp^3-hybridization, as one 2s orbital hybridizes with three 2p orbitals (Figure 1.1 (a)). The repeating of this tetrahedral bonding forms a cubic 3D lattice. Owing to this uniquely stable lattice and strong chemical bonds, diamond exhibits exceptionally high strength, and chemical inertness; therefore, has been utilized in various industrial cutting and drilling tools. Moreover, due to the strong bonds, the material interacts minimally with light and thus is visibly transparent. Recently, as nanosized diamonds, or nanodiamonds (NDs), also possesses these unique material properties, in addition to its small size, NDs have become a promising candidate to use for nanotechnologies in harsh environments (i.e., drug delivery).[8] As sp^3-hybridized bonds require more energy for formation compared to sp^2-hybridized bonds, significantly higher temperatures and pressures are required for the formation of diamond compared to graphite. Therefore, diamond is naturally formed deep in the Earth's mantle.[1,3,7] Such diamonds are brought near the Earth's surface through volcanic eruptions, where they can then be mined.[1,3,7]

1.2.1.3. Carbide

Carbides are crystalline alloys of carbon, in which a carbon atom is bonded to a different metal atom. The material property of the carbide is strongly related to the electronegativity of the non-carbon metal atom. For example, depending on if the non-carbon metal atom is an alkali metal or a transitional metal, the resulting carbide can be utilized as a reactive chemical catalyst or an inert drilling tool.[3] Currently there are ten different types of carbides known to exist naturally, for example cohenite (iron carbide, (Fe,Ni,Co)3C), qusongite (tungsten carbide, WC), and moissanite (silicon carbide, SiC), to name a few.[3] Particularly SiC has become a top candidate to use for next-generation

semiconductor applications, owing to its wide bandgap, high electric field strength, high thermal conductivity, and chemical inertness.[9,10] Carbides are an extremely rare natural material, as the formation requires specific conditions, including precise atomic concentrations and the presence of reducing agents, in addition to extremely high temperatures and pressures. For example, on the Earth's surface, SiC may naturally form only at the boundaries between silicate-based magmas and carbon-rich coal beds, with appropriate pressures and cooling rates.[3]

1.2.2. Non-crystalline material

1.2.2.1. Amorphous carbon

Amorphous carbon is a non-crystalline material with a mix of sp^2 and sp^3-hybridized bonds (Figure 1.1 (b)). Amorphous carbon typically contains traces of various heteroatoms, for example hydrogen, sulfur, oxygen, and nitrogen, in addition to carbon.[1,3,7] As amorphous carbon in part contains ordered sp^2 and sp^3-hybridized nano-domains, the clear transition between amorphous carbon and graphitic carbon or diamond is ambiguous. A typical example of this is graphite oxide (GO), which is a highly oxidized form of graphite.[11] Graphite is considered to be an electrically conductive material owing to the ordered sp^2-hybridized crystal lattice (mechanism of electrical conductivity is discussed in Section 2.4.1.), whereas GO is considered to be an insulating material due to the high content of sp^3-hybridized bonds. Due to the abundant oxygen-containing functional groups, the crystal lattice is highly defective to the point where the material loses its electrical conductivity. Regardless, GO has been commonly referred to be a crystalline material, making the transition between amorphous carbon and graphitic carbon unclear. On a side note, it can be understood from this that depending on the content of heteroatoms, and the ratio between disordered sp^2 and sp^3-hybridized bonds the properties of the resulting material will be completely different. For example, depending on if the heteroatom content is more than 40wt% (i.e., soot) or less than 3wt% (i.e., carbon black) the chemical inertness of the material changes,[12] and if the sp^3-hybridized bonds are significantly greater in ratio than sp^2-hybridized bonds (i.e., glassy carbon) the density and hardness of the material increases.[3] One of the most important naturally forming amorphous carbon is coal, as it is used as fuel to generate electricity for our daily lives. Coal forms from biomass wastes, namely plant debris, which are compacted, hardened, chemically altered, and metamorphosed over time in the Earth's crust by heat and pressure.[1,3,7] Notably, the formation of coal takes thousands of years,

and requires more than ten times the volume of debris to the volume of formed coal.[1,3,7]

1.3. Synthesis of carbonaceous materials

Owing to the growing interest of carbonaceous materials, the value and potential of such materials for various devices became evident. The types of applications can be generalized as either homogeneous or heterogeneous, depending on if the application requires one or multiple materials to perform its minimal functions, respectively. Homogeneous applications are the simplest type of application, as the carbonaceous material is the only functioning component for the application. Examples of homogeneous applications are air filters using porous amorphous carbon, or activated carbon, and biomarkers using fluorescent GQDs. Heterogenous applications, such as electronic devices, are more complex in that these applications require multiple materials (i.e., different material for the substrate, conductive wire, and semiconductive unit), and also require that these materials be combined in desired orientations. The realization of heterogenous applications require advanced patterning techniques, and will be discussed in more detail later (Section 1.4.).

With the development of a wide range of applications, the demand of carbonaceous materials also escalated rapidly. The most basic approach to supply carbonaceous materials is from mining; however, the natural formation of such materials requires thousands of years and therefore cannot keep up with the demands simply from mining. To answer these demands, humans have over time developed new techniques which allow for the synthesis of carbonaceous materials. Currently there are a multitude of available techniques, each with its own unique advantages and disadvantages. The material synthesis techniques can be divided into either a top-down or a bottom-up technique (Figure 1.2). Although top-down techniques are also highly effective, such techniques generally require high-value precursors, such as those mentioned in Section 1.2., and therefore require extensive mining. Here, bottom-up techniques will be focused on, as these techniques offer the synthesis of high-value carbonaceous materials from relatively lower-value precursors (i.e., hydrocarbons, biomasses, and synthetic polymers).

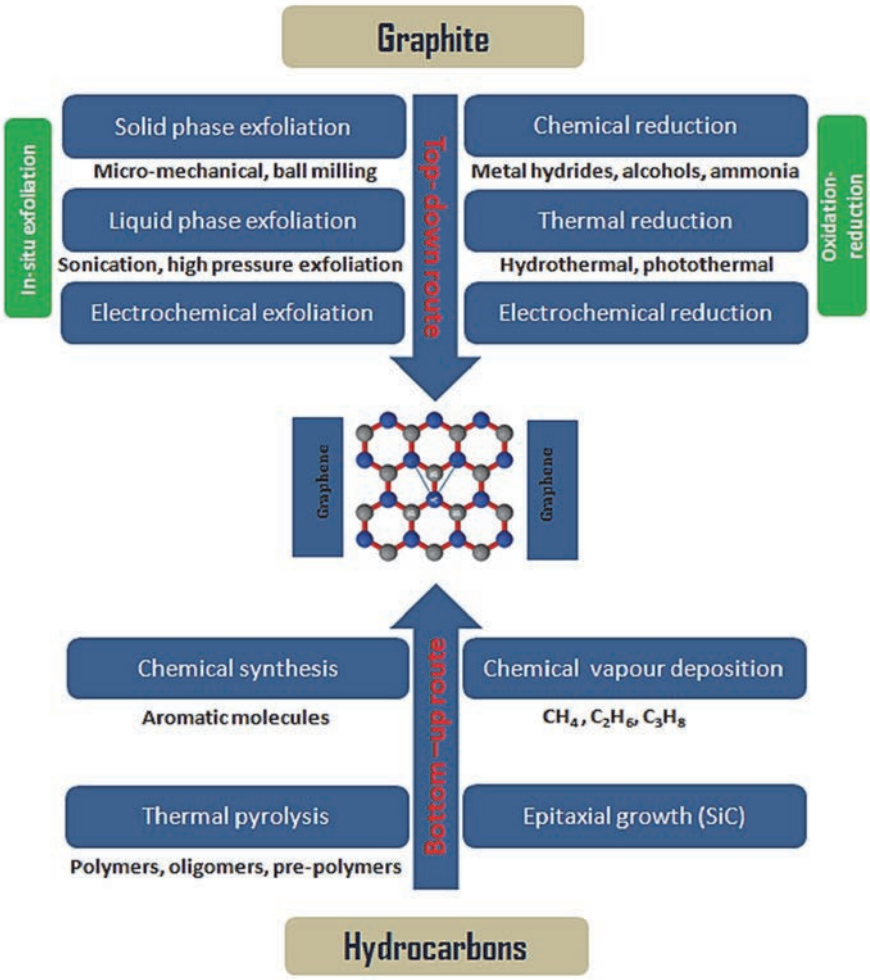

Figure 1.2 Synthesis techniques of graphene. Synthesis techniques can be generalized into two types: Top-down or bottom-up. Reprinted and reformatted with permission from MDPI, Copyright ©2022.[13] Open Access Creative Commons Attribution license.

1.3.1. Thermal carbonization

Generally speaking, carbonization is a process in which an organic material is converted into a carbonaceous material by thermal treatment. By thermally treating a carbon-containing precursor, non-carbon atoms (i.e., oxygen and hydrogen) are desorbed, forming a carbon-rich product. During the stone ages, more than twenty thousand years ago, cave artists lighted wood on fire and used the resulting carbon black as color pigments to draw cave paintings.[1,7] Considering this, the oldest form of artificial synthesis of carbonaceous materials can be denoted as the carbonization of wood using “fire” as the heat source for thermal treatment. With time, more complex systems, including furnaces and microwaves,[14] have been implemented to allow for better control of

processing parameters (i.e., temperature, reaction time, and pressure) and the processing environments (i.e., Ar, N_2, and O_2 atmospheres). Depending on these variables, a wide range of carbonaceous materials can be synthesized by the thermal carbonization (TC) technique, including gaseous carbon (i.e., hydrocarbons), liquid carbon (i.e., tar and oil), carbon black, carbon fibers, carbon aerogels, graphite, and carbides.[3,6,14]

Hydrothermal carbonization (HTC) is a widely used variant of TC in which precursors, typically biomasses, are thermally treated in water.[15] As biomasses are 40–60% oxygen, thermal treatment typically leads to combustion before converting into carbonaceous materials, such as graphite. It has been discussed that water assists the carbonization process by serving as both a reactant and a medium, allowing for the efficient carbonization of biomasses.[16] However, as water is used as a medium, the resulting carbonaceous material is typically low in crystallinity, as diffusion kinetics are limited due to viscosity and the existence of heteroatoms derived from water.[17]

1.3.2. Chemical vapor deposition

Chemical vapor deposition (CVD) is a widely known technique to synthesize 2D crystalline carbonaceous films. In this technique, gaseous precursors are flown into a heated tube furnace, and deposited onto a metal-catalyzed substrate to “grow” crystalline films (Figure 1.3). By changing the composition of the gaseous precursors, films of various material compositions can be synthesized.[18] For example, whether the gaseous precursors contain only hydrocarbon gases (i.e., methane, ethylene), a mixture of silane and hydrocarbon gases,[19] or a mixture of tungsten hexafluoride and hydrocarbon gases,[20] the resulting material can be films of graphene, SiC, or WC, respectively. The most notable advantage of CVD is that it allows for the precise control of crystal growth, realizing the synthesis of high-quality thin films with specific thicknesses and material compositions with atomic precision.[18] However, as a tradeoff, the CVD technique has a relatively slow processing speed. Moreover, as extremely thin films are grown onto a catalytic surface, subsequent removal and transferring of the grown film onto a desired substrate without damaging the film is a constant challenge.[21]

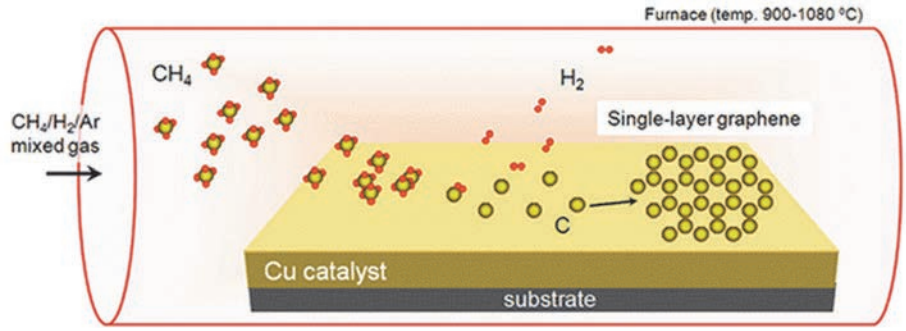

Figure 1.3 Schematic of the CVD setup. Reprinted and reformatted with permission from Springer, Copyright ©2015.[22]

1.3.3. Detonation

Detonation (DET) is a technique to synthesize carbonaceous particles, by chemical reactions induced by explosions. In this technique, a closed chamber is filled with precursors, charge mixture (i.e., trinitrotoluene and hexogen), and stabilizers (i.e., inert gas, water, or ice), then subsequently ignited by an electric spark to initiate a blast explosion.[23] The high temperature and pressure conditions induced in the closed chamber creates a supersaturated environment, leading to the nucleation and growth of particles. With regards to carbonaceous-material synthesis, the charge mixture, in addition to the precursor, can also serve as a source of carbon atoms; however, can also become a source of contamination reducing the purity of the resulting material.[24] As DET is based on the nucleation of blast products in high temperature and pressure conditions, it offers the fast, efficient, and low-cost synthesis of nano and sub-micrometer sized crystalline carbonaceous materials, for example, nanocrystals (NCs) of SiC and Fe_3C, or NDs, to name a few.[25–27]

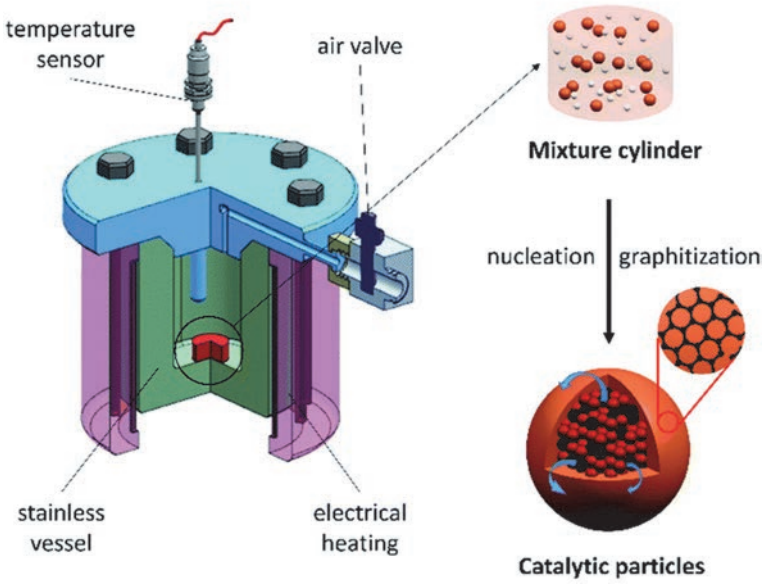

Figure 1.4 Schematic of the DET setup. Reprinted and reformatted with permission from the Royal Society of Chemistry, Copyright ©2017.[28]

1.3.4. Electric arc discharge

Electric arc discharge (EAD) is a technique to synthesize carbonaceous materials by plasma-assisted sublimation of precursors.[29] The EAD technique generally consists of a pair of electrodes and a closed chamber filled with some kind of gaseous medium, typically H_2, He, or Ar (Figure 1.5). The anode electrode is a compacted rod composed of powdered precursor material and a metal catalyst (i.e., Ni, Fe, Co, etc.), whereas the cathode electrode is a conductive bulk material.[30] By applying a voltage between the electrodes, and bringing the two electrodes sufficiently close, an electric arc is generated between. The high temperature plasma of the arc sublimes the precursor material into a gas. Subsequently, the gas condenses onto the cathode and/or walls of the chamber, forming clusters of carbonaceous material. In the case of EAD, since the direction of growth after nucleation can be driven preferentially in one direction via the arc, it is an effective synthesis technique of fibrous carbonaceous materials, such as CNTs and SiC nanowires.[31,32]

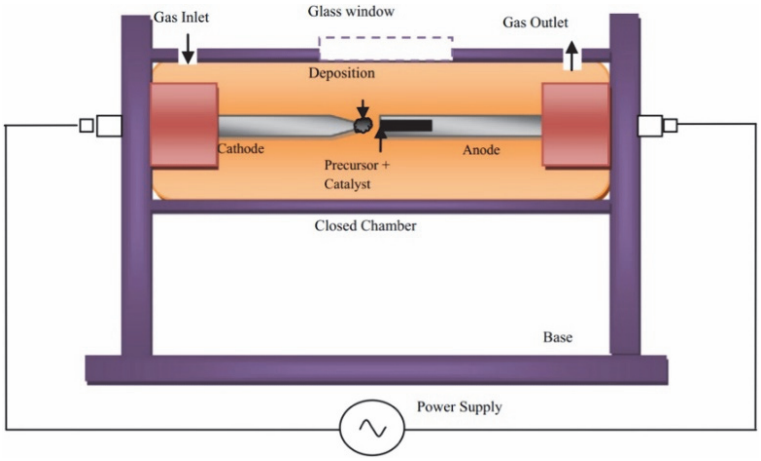

Figure 1.5 Schematic of the EAD setup. Reprinted and reformatted with permission from Elsevier, Copyright ©2014.[29]

1.3.5. Flash joule heating

Flash joule heating (FJH), or more commercially recognized as field-assisted sintering, is a technique in which precursors are thermally treated by joule heating.[30] Typically, powder mixtures containing carbon or metallic precursors are tightly compacted, and a current is passed through to internally generate heat and convert the material. FJH is similar to EAD in many aspects, for example, it is desirable that the precursor is in powder form, the powder mixture should be lightly conductive, and an electrical source is used for synthesis. While FJH is not as effective in synthesizing fibrous materials as EAD, it offers significantly larger synthesis volumes per process (gram-scale) of large carbonaceous crystals, such as graphene, graphite, and carbides.[33,34] Also, as heat rates as high as 1000 K/min can be reached in FJH, it has been regarded to be more efficient than other techniques in synthesizing amorphous glassy carbon, as the kinetics for crystallization can be limited.[23] In recent years, the advantageous of FJH for the recycling of valuable metals from discarded old electronic devices has been indicated.[35,36]

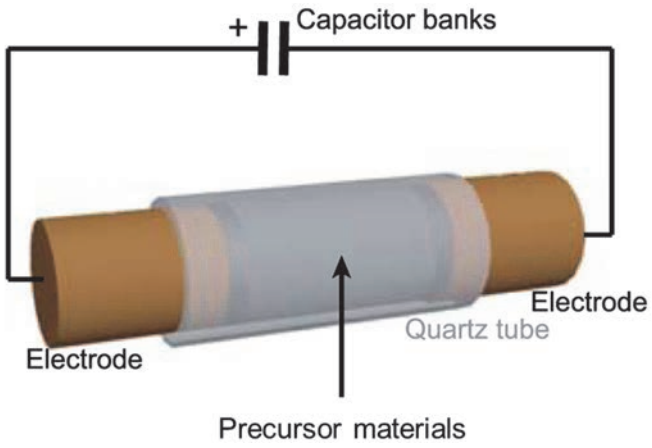

Figure 1.6 Schematic of the FJH setup. Reprinted and reformatted with permission from Springer Nature, Copyright ©2022.[34] Open Access Creative Commons Attribution license.

1.3.6. Self-propagating high-temperature synthesis

Self-propagating high-temperature synthesis (SHS) is a chemical technique to synthesize carbonaceous materials by oxidation-reduction, or redox, reactions (Figure 1.7).[37] A mixture of precursor and a reducing agent is prepared, and a redox reaction is initiated typically through thermal stimulation.[38] The initiation induces exothermic redox reactions, which generate large amounts of heat and self-propagate the conversion process of the precursor into a carbonaceous material, hence the name. The processing times of SHS can vary greatly (i.e., seconds to hours) depending on the volume and surface area of the precursor, as well as the reactivity of the precursor with the reducing agent. Initiation temperatures as low as 90 °C can be used for the synthesis of graphitic carbon in the case of SHS,[39] which is significantly lower than that typically used for TC (1000–3000 °C). Moreover, as materials such as CO_2 and biomasses can be used as precursors, SHS has been regarded as an environmentally friendly and sustainable synthesis technique of carbonaceous materials.[39,40] Due to the nature of the technique, the resulting material is typically low in crystallinity, and inevitably contains many impurities and defects.

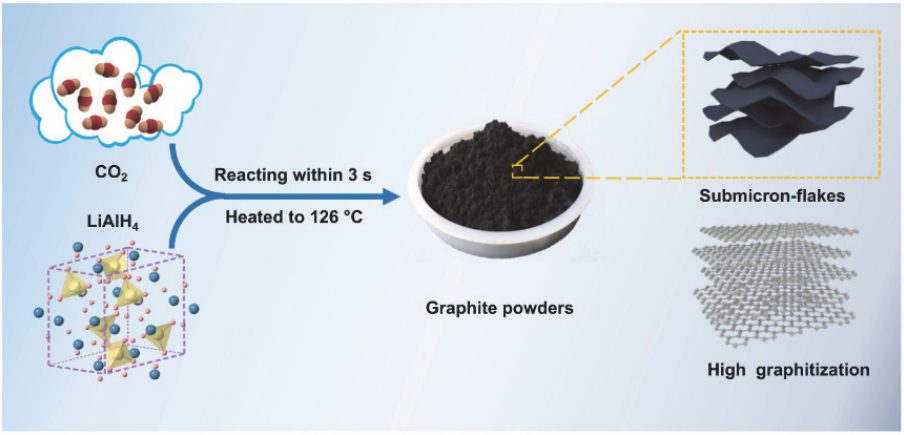

Figure 1.7 Schematic diagram of the synthesis process by the SHS technique. Reprinted and reformatted with permission from Springer Nature, Copyright ©2021.[37] Open Access Creative Commons Attribution license.

1.4. Patterning for device fabrication

As new synthesis techniques as well as new types of carbonaceous materials were established, different ways of using the carbonaceous materials were also explored. Although the carbonaceous materials synthesized by the techniques mentioned in Section 1.3. can also be directly used in bulk (i.e., homogenous applications), the integration and structuring, hereon collectively referred to as patterning, of such materials onto different substrates can further expand the possibilities for application (i.e., heterogeneous applications). The possibilities are endless as the resulting application can be changed with a multitude of variables, such as the type of patterned carbonaceous material, the type of substrate, and the pattern of the carbonaceous material. For example, by patterning either bilayer or monolayer graphene films onto silicon substrates, electronic or optoelectronic devices can be fabricated, such as field-effect transistors[41] or solar cells[42]. Moreover, by substituting the rigid silicon substrate with a soft substrate, such as polymers, flexible and skin-conformable electronic and optoelectronic devices can be fabricated.[43] The carbonaceous materials can also be structured into arbitrary architectures, such as a serpentine architecture, to endow additional functions or improve existing functions, such as bendability and stretchability.[44] Depending on the desired device, the appropriate patterning technique should be chosen, as each technique has its unique advantages (i.e., patternable material, usable substrate, patterning resolution, etc.) according to the patterning mechanism. For example, traditional semiconductor-based patterning techniques are generally not suitable for the fabrication of flexible electronic

devices, as the essential chemical and thermal treatments involved may lead to the severe damaging of the polymer substrate. Below, notable patterning techniques of carbonaceous materials for the fabrication of devices will be introduced.

1.4.1. Selective etching

Selective etching (SE) is a subtractive technique in which a film of carbonaceous material that was either transferred or grown on a substrate is selectively removed by etching.[45] The etching process can be conducted by different approaches, such as photon or electron beam activation followed by dry or wet etching,[46–48] or simply by ion or laser ablation.[49,50] The first approach is based on the localized alternation of the chemical reactivity of the target film by the irradiation of photons or electrons, typically assisted with the use of a resist mask. Then the film is treated with an etching agent (i.e., gas, plasma, or solvent), which selectively removes the irradiated (positive etching) or non-irradiated (negative etching) areas, depending on the change in chemical reactivity. The second approach is based on the localized removal of the film by the irradiation of ions or photons. As the second approach does not require any etching agents, unintended alternations (i.e., defect formation) in the resulting material properties are significantly less.[51] However, since the removal process is performed typically point-by-point, the throughput of the second approach tends to be lower than the first approach. Nonetheless, as various approaches are available for etching, SE offers the precise patterning of almost any type of carbonaceous material, even if the material is extremely delicate. For example, a single-atom thick graphene film was precisely patterned into a mesh architecture to significantly improve the mechanical flexibility, realizing a highly transparent and flexible electrode for foldable devices (Figure 1.8).[52]

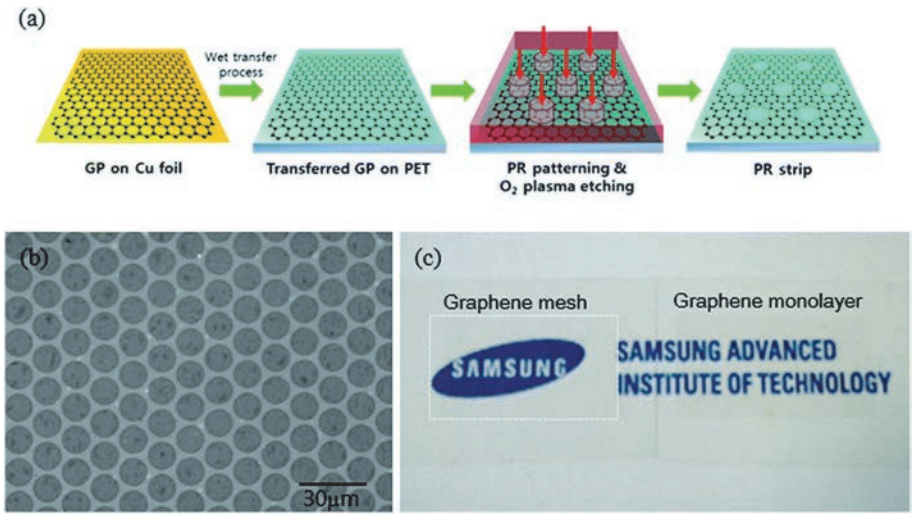

Figure 1.8 Schematic diagram of the patterning process by the SE technique. (a) Schematic illustration of the fabrication process of a graphene mesh (GP) using conventional wet transfer and photoresist (PR) lithography processes. (b) A hexagonally arranged circular hole array. (c) Photographs of the GP (left) and the graphene monolayer (right) on the polyethylene terephthalate (PET) film. Reprinted and reformatted with permission from the Royal Society of Chemistry, Copyright ©2018.[52]

1.4.2. Transfer printing

Transfer printing (TP), or microcontact printing, is an additive technique in which carbonaceous materials are transferred onto a target substrate using an elastic stamp (Figure 1.9). Successful transfer depends on the relationship between the adhesion energies of the transferred material, the stamp, and the target substrate. If the adhesion between the transferred material and the stamp is equal or greater than that with the target substrate, partial or no transferring will occur. Therefore, the fine tuning of adhesion energies via the control of the stamp material and/or surface treatment of the target substrate is important for successful printing.[53] In other words, as long as the adhesion energies are considered, almost any material can be transferred. Once the adhesion considerations are complete, TP is an extremely simple and straight forward technique as the dimensions and patterns of the transferred material depend on the shape of the contact surface of the stamp.[54] Moreover, as transferring only occurs at the contacted areas, multiple materials can be easily transferred onto a single substrate. For example, a multi-material microarray sensor was fabricated using TP, realizing the sensing of chemical and electrical signals with one device.[55] However, as the transferring process requires direct contact between the stamp and the transferred material, undesired mechanical damaging of the transferred material and the deterioration in the material properties due to patterning

may occur.

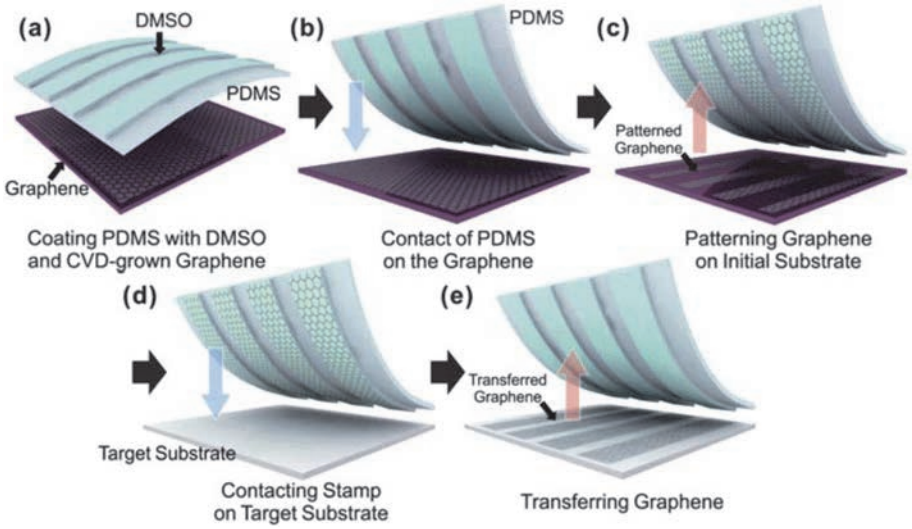

Figure 1.9 Schematic diagram of the patterning process by the TP technique. (a) Polydimethylsiloxane (PDMS) surface coating with dimethyl sulfoxide (DMSO) for increasing the surface energy of PDMS and CVD-grown graphene on the initial substrate. (b) Contact of the PDMS coated with DMSO on the graphene. (c) Patterning of the graphene layer on the initial substrate. (d) Contact of the PDMS stamp on a target substrate. (e) Transferring graphene on the PMDS stamp to the target substrate. Reprinted and reformatted with permission from the Royal Society of Chemistry, Copyright ©2013.[56]

1.4.3. Inkjet printing

Inkjet printing (IP), is an additive technique in which carbonaceous materials are deposited onto a target substrate in the form of a liquid solution.[57] In IP, a nozzle deposits a liquid solution containing carbonaceous material, or an “ink”, onto the target substrate. After deposition, the ink dries up, precipitating the carbonaceous material onto the surface (Figure 1.10). As IP does not require any masks or stamps for patterning, and the nozzle can be digitally controlled, complex patterns, such as fingerprints,[58] can be easily patterned on the fly. However, in order to achieve accurate patterning, the careful formulation of the ink is crucial. For example, as the viscosity of the ink determines the radial spread of the ink after deposition, higher viscosity inks result in significantly higher patterning resolutions. At the same time, higher viscosity inks may also lead to the clogging of the nozzle, causing unstable patterning or chaotic behavior during patterning. Moreover, the type of carbonaceous material patternable is generally limited to hydrophilic materials, as a liquid ink is required for patterning.

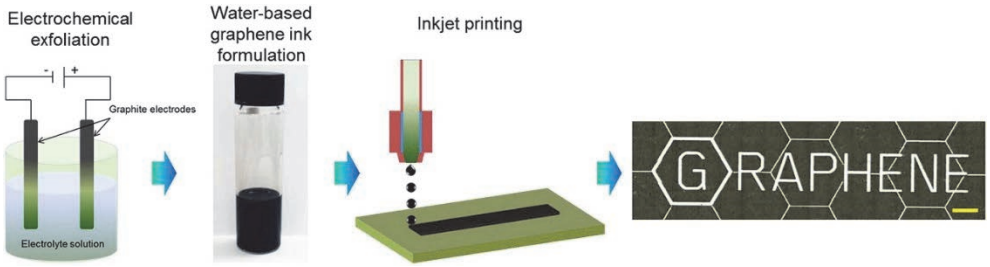

Figure 1.10 Schematic diagram showing the general process flow the IP technique. Right image is a printed 'Graphene' logo on a paper substrate. Scale bar is 2 mm. Reprinted and reformatted with permission from Elsevier, Copyright ©2019.[59]

1.4.4. Laser-induced forward transfer

Laser-induced forward transfer (LIFT) is a laser-based additive technique in which carbonaceous materials are transferred from a donor substrate to a receiver substrate in small amounts by the irradiation of a laser pulse.[60] The LIFT technique consists of four components as shown in Figure 1.11: a pulsed laser, a transparent donor substrate, a thin film of a desired material being transferred, and a receiver substrate. When laser pulses are absorbed at the interface between the transparent donor substrate and the thin film, blistering occurs at the interface, "ejecting" the film material onto a receiver substrate. As long as the desired material can be prepared in film-form, LIFT offers the transferring of almost any material, whether it be a solid or liquid, with relatively minimal alteration of the material properties. Moreover, materials can be transferred layer-by-layer, offering the patterning of stacked multi-layered structures. Owing to this, LIFT has been regarded as a promising technique for the fabrication of multi-layered components of electronic devices, for instance thin-film transistors, light-emitting diodes, and micro-electromechanical systems (MEMS).[60]

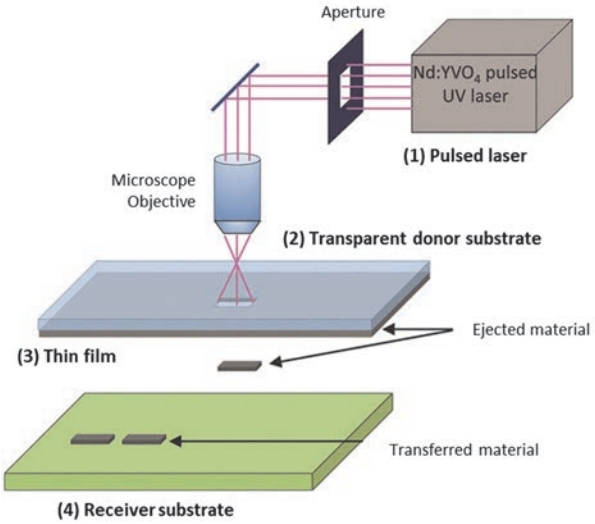

Figure 1.11 Schematic of the LIFT setup. The setup consists of four important components: a pulsed laser, a transparent donor substrate, a thin film of a desired material being transferred, and a receiver substrate. Reprinted and reformatted with permission from John Wiley & Sons, Copyright ©2019.[61]

1.5. Simultaneous synthesis and patterning

As discussed thus far, the patterning of carbonaceous materials realizes the fabrication of novel devices possessing various attractive properties. However, the patterning techniques mentioned thus far are all based on two separate synthesis and patterning processes; where materials are first synthesized and finely tuned, then subsequently patterned. In this regard, the two-stepped process tends to have two major drawbacks. One, by the simple fact that multiple techniques are required, the overall processing speed is low. Two, as some sort of mechanical or chemical treatment is required for patterning, the finely tuned material can be altered in some degree due to the patterning procedure. To overcome these issues, the development of techniques capable of the simultaneous synthesis and patterning of carbonaceous materials have been explored. In other words, techniques in which the material properties are decided concurrently with its position. Below, introduces notable techniques capable of the simultaneous synthesis and patterning of carbonaceous materials.

1.5.1. Substrate-assisted growth

Substrate-assisted growth (SAG) is an CVD-based additive technique in which crystalline carbonaceous materials are selectively grown at specific areas of the target

substrate. As SAG is a variation of the CVD technique, the advantages and disadvantages of CVD also applies for this technique. By locally catalyzing the target substrate with metallic templates to spatially promote precursor adhesion, or using a mask to spatially prevent precursor adhesion, the simultaneous synthesis and patterning can be realized.[62] In addition to patterned growth, the use of metallic templates offers the fine control of crystal orientation and growth direction, as the growth of the resulting material will be influenced by the crystal structure of the metal template.[45] However, it is generally required that the metal template be etched away afterwards, which may lead to damaging of the grown material. On the contrary, the mask-based approach is an etching-free option, offering the growth of high-quality patterned structures. However, regardless of the approach used, SAG requires a pre-prepared template or mask, therefore the patterns cannot be changed on the fly limiting its patterning versatility.

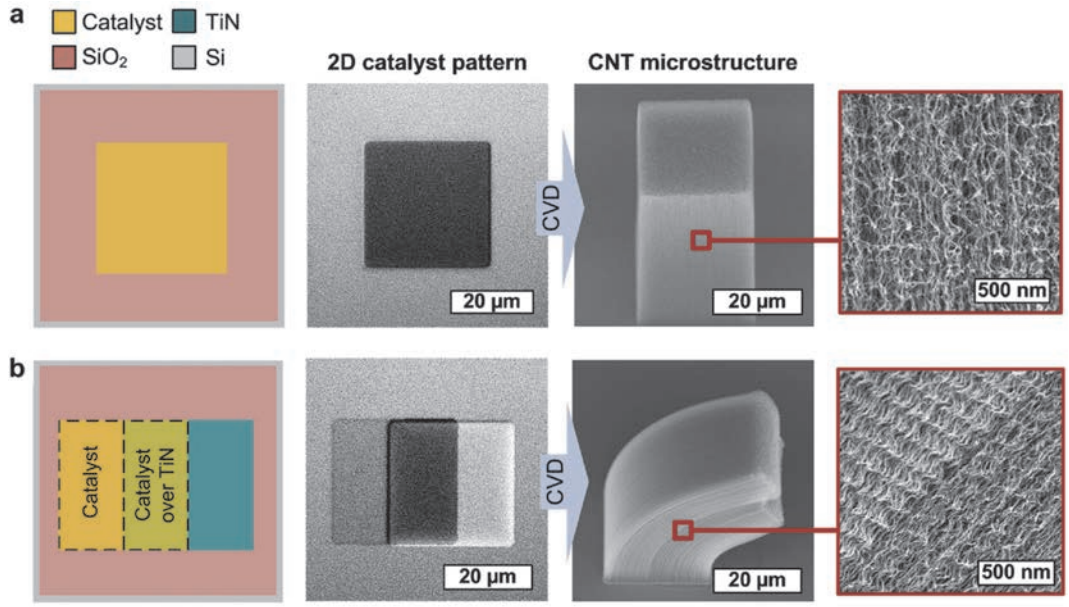

Figure 1.12 Schematic diagram of the SAG technique. (a) From left to right: standard catalyst microfeature design, optical microscope image of catalyst (Fe/Al_2O_3) on SiO_2/Si substrate, scanning electron microscopy (SEM) image of resulting CNT microstructures vertically grown from the substrate by chemical vapor deposition, and high magnification SEM image of CNTs within the microstructure. (b) From left to right: multi-layer offset pattern of catalyst and TiN underlayer, optical microscope image of offset pattern, SEM image of curved CNT micropillar grown from this pattern, and high magnification SEM image of CNTs near the SiO_2/TiN interface. Reprinted and reformatted with permission from John Wiley & Sons, Copyright ©2016.[63]

1.5.2. Laser-induced photoreduction of graphene oxide

Laser-induced photoreduction of GO (LIPR) is a modificative laser direct writing (LDW) technique in which GO is locally converted into reduced GO (rGO) by the laser irradiation.[64] Laser irradiation of electrically insulating GO (>20 Mohm/sq) induces localized desorption of oxygen-containing functional groups and the rearrangement of carbon atoms, reducing the material into ordered graphitic carbon, which exhibits metal-like electrical properties (80–500 ohm/sq).[64] By simply scanning a laser pulses over a film of GO (Figure 1.13), conductive rGO can be simultaneously synthesized and patterned. Moreover, as LIPR is a LDW technique where the laser path can be digitally controlled, patterns can be changed on the fly, offering high patterning versatility. As GO films can be prepared on different substrates, notably flexible polymers (i.e., PET[65] and polyimide (PI)[66]), LIPR offers the rapid fabrication of flexible electronic devices, such as flexible sensors and photovoltaic cells.[67,68]

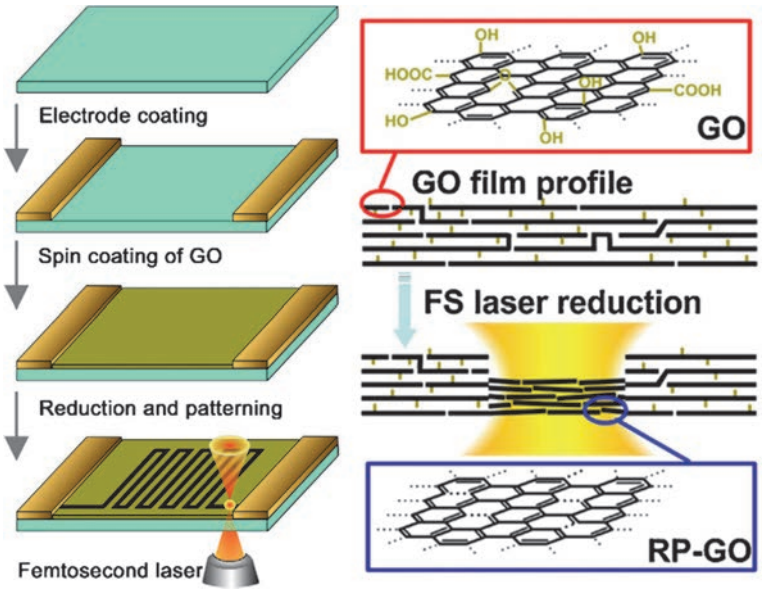

Figure 1.13 Schematic diagram of (left) the patterning process by the LIPR technique and (right) the conversion of GO film to reduced and patterned GO (RP-GO) induced by the irradiation of femtosecond (fs) laser pulses. Reprinted and reformatted with permission from Elsevier, Copyright ©2010.[65]

1.5.3. Laser-induced carbonization and graphitization

Laser-induced carbonization and graphitization (LICG) is another modificative LDW

technique in which a polymer precursor is locally converted into carbonaceous materials by laser irradiation (Figure 1.14).[69] Contrary to the other techniques, in the case of LICG, a variety of carbonaceous materials are "synthesized" simultaneously, resulting in the formation of a composite structure, hereon referred to as a carbonaceous structure. The carbonaceous structure is typically composed of electrically conductive graphitic carbon, or turbostratic graphite, which has been generally termed as laser-induced graphene (LIG). LICG can be understood as a variant of TC (Section 1.3.1.), in which laser light is used as the heat source for thermal treatment. However, contrary to conventional TC techniques, as a laser light is used as the heat source, carbonaceous structures can be locally patterned with minimal alternation to the bulk. The most notable advantage of LICG over the two other patterning techniques introduced in Section 1.5. is that the material preparation is extremely simple. For example, in the case of SAG, a template/mask and a gaseous precursor, and in the case of LIPR, GO in film form, needs to be prepared in addition to the substrate. In the case of LICG, only a polymer film is required, as the polymer serves as both the precursor and the substrate.

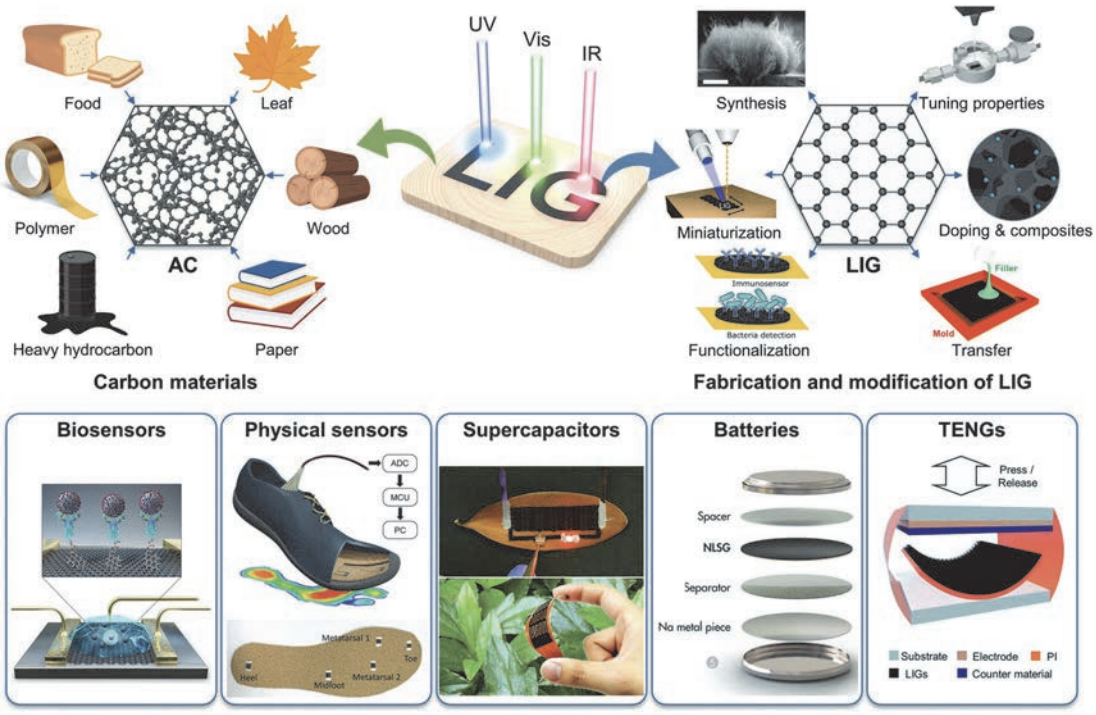

Figure 1.14 Schematic diagram of the LICG technique. Under laser irradiation, the carbon precursors are rapidly converted to amorphous carbon (AC) and LIG. The structural and material properties of LIG can be easily tuned offering a wide range of potential applications, such as biosensors, physical sensors, supercapacitors, batteries, and triboelectric nanogenerators (TENGs). Reprinted and reformatted with permission from John Wiley & Sons, Copyright ©2022.[70]

1.5.3.1. Progress of LICG

A progress timeline of LICG technique is presented in Figure 1.15.[69,71–80] The initial reports of the LICG technique date back as early as 1983, where PI was converted into conductive carbonaceous structures by laser irradiation.[71] Moreover, in 1986 the synthesis of carbides, such as SiC, by the LICG of organosilane polymers has been reported.[72] However, most of these reports were proof-of-concept demonstrations aimed at developing new synthesis methods of carbonaceous materials; therefore, detailed analyses of the synthesized materials, but more importantly demonstrations of device fabrication utilizing the patterning capabilities of LICG were lacking.

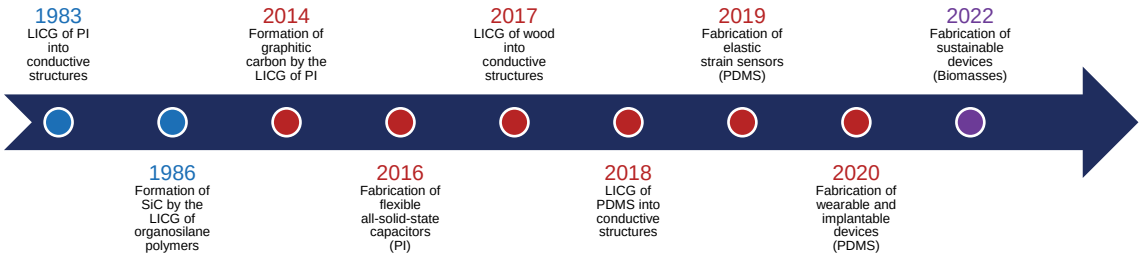

Figure 1.15 Progress timeline of the LICG technique. [69,71–80]

Although there have been a few reports of the LICG technique over the years, the number of reports increased drastically in the 2010s, revitalized by the study in 2014.[69] In this report, the macro (i.e., structural morphology and electrical properties) and micro (i.e., material composition) details of the carbonaceous structures resulting from the LICG of PI were investigated (Figure 1.16). Since then, a multitude of studies exploring the possible applications of the carbonaceous structures have been reported in the context of flexible electronics.[73,81] To further expand the possibilities for application, polymer precursors other than PI were also heavily investigated.[74,75,82]

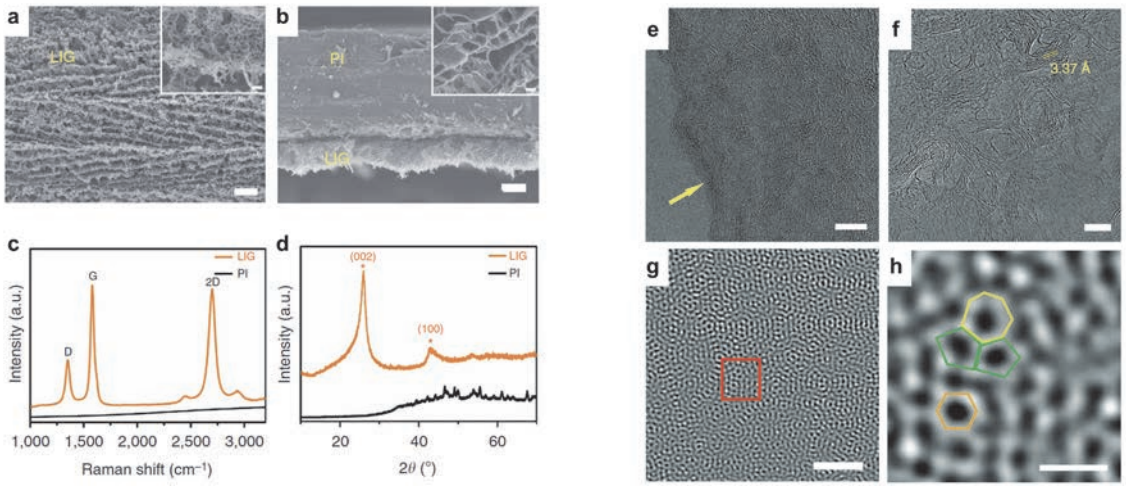

Figure 1.16 (a) SEM image of LIG formed on the surface of the PI substrate; scale bar, 10 mm. (b) Cross-sectional SEM image of LIG; scale bar, 20 mm. Both insets are higher magnification SEM images; scale bar, 1 mm. (c) Raman spectrum of PI and LIG. (d) X-ray diffraction (XRD) spectra of PI and LIG. (e) Transmission electron microscopy (TEM) image of LIG; scale bar, 10 nm. (f) TEM image of LIG showing lattice spacings which corresponds to the (002) planes of graphitic materials; scale bar, 5 nm. (g) Corrector-spherical aberration scanning TEM (Cs-STEM) image taken at the edge of LIG; scale bar, 2 nm. (h) TEM image of the selected area indicated as a rectangle in (g); scale bar, 5 Å. Reprinted and reformatted with permission from Springer Nature, Copyright ©2014.[69] Open Access Creative Commons Attribution license.

Elastomers, such as PDMS, are a group of polymers widely used in medical, food, and other industries owing to its high flexibility and stretchability, chemical and thermal stability, optical transparency, and biocompatibility. The LICG of elastomers realizes the one-stepped fabrication of strain sensors with significantly higher sensitivities, since such materials undergoes larger deformations when the same degree of strain is applied.[76,83] Moreover, for the development of wearable and implantable electronics, elastomers are better suited, as they can better conform with the skin.[77] The LICG of PDMS into carbonaceous structures have been reported since 2009;[84] however, the first study of electrically conducting carbonaceous structures was reported in 2018.[75] Since this report in 2018, the number of studies regarding the LICG of PDMS has been steadily increasing every year. Furthermore, as PDMS is an organosilane polymer, in addition to graphitic carbon, crystalline SiC forms. Combined with the inherent high elasticity of PDMS, the formation of SiC nanocrystals (SiC-NCs) may be one of the unique reasons the LICG of PDMS has been actively investigated in recent years. As SiC is an attractive semiconducting material, the selective LDW of highly conductive and semiconductive

structures on PDMS may realize the rapid fabrication of complex electronic devices simply by irradiating PDMS. A literature review on the LICG of silicon-based elastomers is presented in Table 1.1.

Table 1.1 Literature review on the LICG of silicon-based elastomers. For the substrate column, silicone refers to silicone rubber. For the environment column, blank cell indicates ambient air conditions. For the graphitic carbon (GC) and SiC columns, X indicates that the formation of graphitic carbon and/or SiC was experimentally evidenced in the study. RR, CW, and TEG are abbreviations for repetition rate, continuous wave, and triethylene glycol, respectively.

Year	Substrate	Additive/filler	Laser type	Wavelength	RR	Environment	Aim	GC	SiC	Ref.
2009	PDMS		Pulse (ns)	266 nm	10 Hz		Texturing	X	X	84
2013	PDMS	Carbon NPs	CW	785 nm			Texturing	X		85
2015	PDMS		Pulse (fs)	800 nm	1 kHz		Optical			86
2016	PDMS		Pulse (ns)	1064 - 266 nm	1-10 Hz		Fundamental			87
2016	PDMS		Pulse (fs)	1055 - 263 nm	33 Hz		Fundamental			88
2017	PDMS		CW	10.6 μm			Texturing			89
2018	PDMS		Pulse (fs)	522 nm	63 MHz		Electrical		X	75
2019	Silicone		CW	532 nm			Electrical	X	X	76
2019	PDMS		CW	405 nm			Electrical	X		83
2019	PDMS		Pulse (fs)	522 nm	63 MHz		Electrical			90
2019	PDMS	PI	CW	10.6 μm			Electrical	X		91
2020	PDMS	Gold NPs	Pulse (ns)	1064 nm	10 Hz	Vacuum	Fundamental			92
2020	PDMS	Ge-derivatives	Pulse (fs)	1030, 515 nm	101, 606 kHz		Optical			93
2020	PDMS		Pulse (fs)	522 nm	63 MHz		Fundamental	X	X	94
2020	PDMS		CW	10.6 μm		Nitrogen	Electrical	X	X	77
2021	PDMS	Lignin	CW	410 nm			Electrical	X		95
2021	PDMS	PI	Pulse (ns)	355 nm	1 Hz - 300 kHz		Electrical	X		96
2021	PDMS		Pulse (fs)	522 nm	63 MHz		Electrical	X		97
2021	PDMS		CW	532 nm			Texturing		X	98
2021	PDMS	TEG	CW	10.6 μm			Electrical	X		99
2022	PDMS		Pulse (fs)	522 nm	63 MHz		Optical	X	X	100
2022	PDMS	Lignin	Pulse (ns)	355 nm	1 Hz - 300 kHz		Electrical	X		101
2022	PDMS	$CuAc_2$ or $NiAc_2$	Pulse (fs)	515 nm	50 kHz		Electrical	X	X	102
2022	Silicone		CW	10.6 μm			Texturing			103
2022	PDMS	PI	CW	10.6 μm			Electrical	X		104
2022	PDMS	Cloth	CW	10.6 μm			Electrical	X	X	105
2023	PDMS	Cloth	CW	10.6 μm			Fundamental	X	X	106
2023	PDMS		Pulse (fs)	522 nm	4.2 - 21 MHz		Fundamental	X	X	107

It had been generally understood that the LICG of biomasses, such as wood,[74] results in carbonaceous structures with significantly lower electrical conductivities than those formed by the LICG of synthetic polymers, such as PI. However, accompanied by the deeper understanding of the LICG technique, the formation of highly conductive

carbonaceous structures by the LICG of biomasses have been recently achieved.[78,108,109] As a result, the LICG of biomasses for "sustainable" applications have been a growing interest in the past years.[78–80,109]

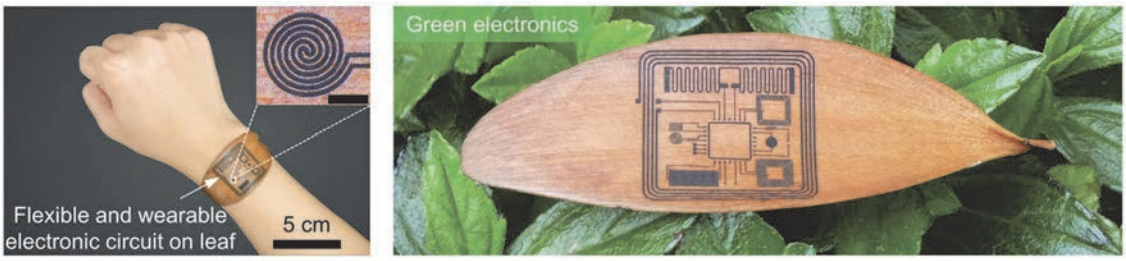

Figure 1.17 Photograph of (left) an LIG electronic circuit on a thin leaf for flexible and wearable devices, and (right) a LIG electronic device on a leaf for green electronics. The inset on the left shows an enlarged optical image of the temperature sensor (scale bar: 1 mm). Reprinted and reformatted with permission from John Wiley & Sons, Copyright ©2019.[109]

As shown so far, the formation of spatially patterned carbonaceous structures on polymer substrates by LICG offers the potential for the rapid roll-to-roll manufacturing of a variety of key applications, including large area sensors, flexible electronics, energy storage/conversion, and other consumer applications. In this technique, laser irradiation induces permanent photothermal changes to a polymer substrate, endowing it with attractive properties such as high optical absorption, surface area, electrical conductivity, and thermal stability [69,89,110]. While the application aspects of LICG have been heavily investigated (i.e., possible applications, optimum laser parameters, etc.), the basic aspects of LICG have been largely ignored (i.e., formation mechanism, effect of carbonaceous material on structural properties, etc.). Despite the versatility and scalability of this technique, a deeper understanding of the underlying mechanisms is required to exquisitely control the resulting morphology and properties of the carbonaceous structures to allow for the successful implementation of LICG into commercial settings. Especially towards future automated manufacturing schemes, the accurate prediction of the resulting structure simply from the combination of laser parameters is ideal. The specific formation mechanism of the carbonaceous structures has been an issue of debate for many years with the prevailing notion of a simple photothermal conversion reaction that mainly depends on the total laser energy. [110–112] However, this view has been shown to be inconsistent with experimental observations of nonlinear changes in the resulting structures when multiple processing parameters are simultaneously changed, and an improved model is required. The theoretical mechanisms and the nonlinearity of LICG will be discussed in more detail later (Sections 2.6. and 2.7.).

1.6. Aim of this thesis

Carbon and humans have had a close relationship throughout history; correspondingly, various techniques have been developed to synthesize and/or pattern a wide range of carbonaceous materials and/or structures. Out of the many techniques, laser-induced carbonization and graphitization, or LICG, offers the simultaneous synthesis and patterning of carbonaceous structures composed of various carbonaceous materials by the direct conversion of the polymer substrate. As the polymer serves as both the precursor and the substrate, material preparation is extremely simple in the case of LICG. Moreover, as electrically conductive carbonaceous structures can be seamlessly integrated onto flexible and stretchable polymers simply by laser irradiation, LICG has been regarded as a facile technique to rapidly fabricate polymer-based devices, such as flexible electronics. However, as mentioned in Section 1.5.3.1., the underlying mechanisms of LICG is still not well understood. The aim of this thesis is to discuss the chemical and physical processes that ensue when a transparent elastomer, PDMS, is irradiated by laser light to reveal the mechanism in which carbonaceous structures form by LICG, to clarify the effect of the carbonaceous materials on the electrical properties of the overall structure, and to indicate the applicability of the carbonaceous structures towards electrical and optical applications.

The organization of this thesis is provided in Figure 1.18. Chapter 2 lays down the fundamentals required to discuss the experimental results provided in the subsequent chapters. The chemical and physical processes that ensues as a result of laser irradiation are outlined, and the principles of LICG is established. Chapter 3 and 4 describe the experimental results regarding the basic characterizations of the carbonaceous structures patterned on the PDMS surface by LICG. Chapter 3 examines the structural aspects of the carbonaceous structures. The mechanisms regarding the formation of carbonaceous structures, and the relationship between laser parameters and structure morphology is discussed. Chapter 4 addresses the electrical property of the carbonaceous structures. The patterning of carbonaceous structures exhibiting different electrical properties is demonstrated by LICG, and the effects of graphitic carbon and SiC-NCs on the electrical property of the overall structure are discussed. Chapters 5 and 6 describes the experimental results regarding the application of carbonaceous structures patterned on PDMS by LICG. Chapter 5 focuses on electrical applications using the carbonaceous structures. The piezoresistive properties of the structures are assessed by strain tests, and the fabrication a micro-pressure sensor and an anisotropic strain sensor, which apply the

piezoresistive properties of the structures, is demonstrated. Chapter 6 explores optical applications using the carbonaceous structures. It is revealed that fluorescent carbonaceous structures can be patterned by the LICG of PDMS, and the fabrication of an anti-counterfeiting security tag, which apply the fluorescent property, is demonstrated. Moreover, by utilizing multiphoton interactions. the patterning of fluorescent carbonaceous structures inside PDMS is demonstrated. Chapter 7 provides the conclusions, summarizing the key findings of each chapter and the entire thesis, then discusses future studies which have been triggered by the findings in this thesis.

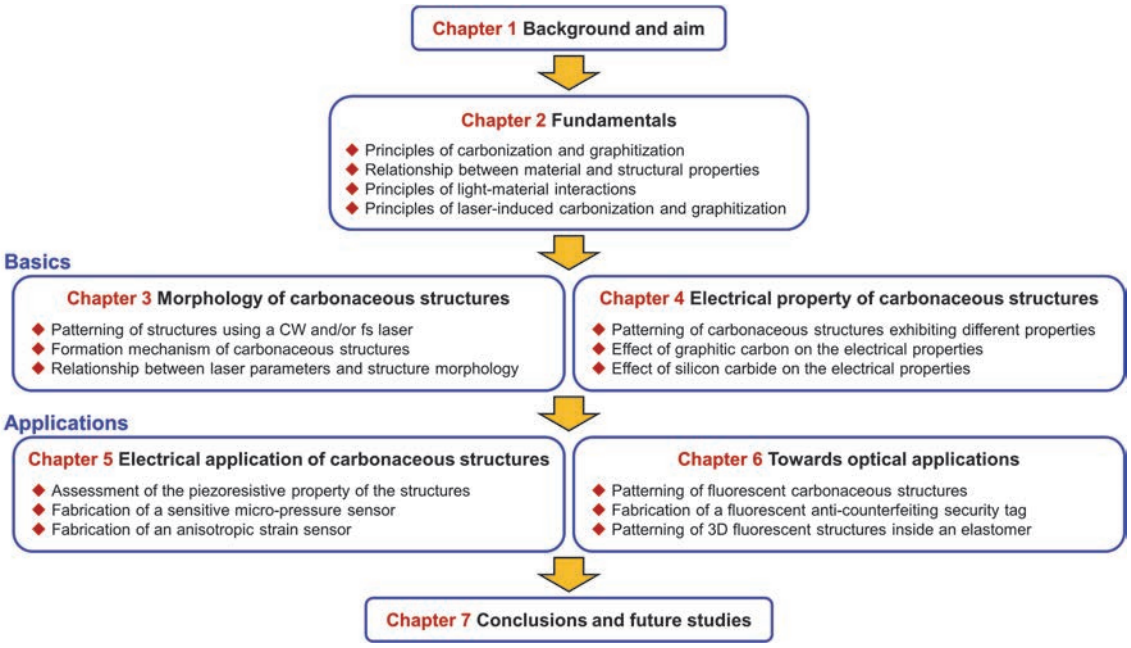

Figure 1.18 Flow chart summarizing the organization of this thesis.

2. Fundamentals

2.1. Introduction

The laser irradiation of a material induces various chemical and physical processes that can lead to permanent changes to the material that depend greatly on the target material and the laser parameters. By irradiating an organic material, such as a polymer, the material can be converted into a carbonaceous structure composed of graphitic carbon through the combination of various processes. The aim of Chapter 2 is to provide the fundamental theories necessary to understand and discuss the experimental results described in Chapters 3 to 6. In Section 2.2., the general process in which organic material is converted into graphitic carbon via thermal treatment will be described. Building on this, in Section 2.3., the effect of various variables on the carbonization and graphitization processes will be discussed. Furthermore, the relationship between the material and the structural property will be explained in Section 2.4. In Section 2.5., a sequence of processes involved in light-material interactions will be introduced. Then, based on the theories discussed in Sections 2.2. and 2.5., the principles of LICG will be established in Section 2.6.; and in Section 2.7., the nonlinearity in LICG will be briefly discussed according to the established principles of LICG. Lastly, in Section 2.8., a summary of this chapter will be given.

2.2. Principles of carbonization and graphitization

Carbonization is an exothermal process in which an organic precursor is converted into a carbon-rich product. Graphitization is, in a sense, a later stage of carbonization in which crystalline graphitic product is obtained.[6] There are three phases regarding the carbonization of an organic precursor into graphitic products (Figure 2.1).[113,114] The transition between phases is not a gradual shift, but more of a step-wise shift with an activation energy barrier E_a. The E_a for each phase mentioned below are estimated values for aromatic organic sediments, such as coals and kerogens, and thus may not apply for every material.[113]

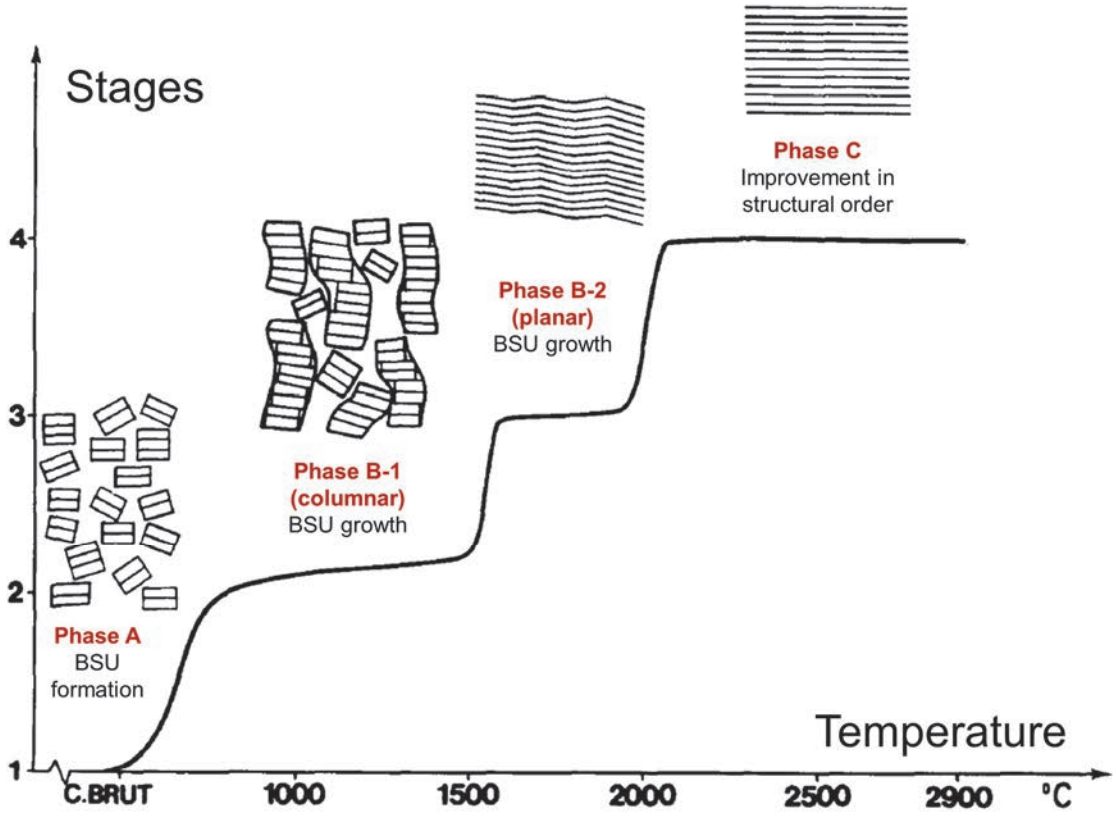

Figure 2.1 Phases of the carbonization and graphitization process. Reprinted and reformatted with permission from Elsevier, Copyright ©1984.[114]

2.2.1. Phase A: Nucleation of BSUs

During Phase A (E_a: 70–80 kcal/mol), the fragmentation of mainly aliphatic groups occurs.[113] This leads to the release of condensable hydrocarbon gases and the formation of radicals. The recombination of the radicals results in the nucleation of a basic structural unit (BSU) (Figure 2.1, Phase A). BSU is a conceptual basic unit of the final product. However, BSU is difficult to define as the concept of "basic unit" is subjective, and can also differ greatly depending on the precursor type and final product.[114] Nonetheless, the BSUs of graphitic products are considered to be polyaromatic compounds with diameters less than 1 nm, consisting of two to four stacked layers of carbon atoms in a sp^2 hybridized orientation.[113]

2.2.2. Phase B: Growth of BSUs into crystallites

During Phase B (E_a: 120–150 kcal/mol), the fragmentation of aromatic groups

occurs.[113] Aromatic groups include those native to the precursor as well as those of the BSUs. Contrary to Phase A, smaller and lighter non-condensable gases (i.e., H_2 and CH_4) are released during this phase. The fragmentation of aromatic groups forms heavier radicals, which rapidly recombine with neighboring radicals to form larger aromatic compounds. Phase B consists of two stages, which depend on the temperature. In the first stage (relatively lower temperatures), mainly columnar coherence ensues (Figure 2.1, Phase B-1). The vertical reordering within individual BSUs, as well as the stacking of neighboring BSUs, results in the ordered vertical growth of BSUs. The reordering of BSUs typically results in the slight decrease in inter-plane distance. In the second stage (relatively higher temperatures), lateral coherence ensues, along with the progression of columnar coherence (Figure 2.1, Phase B-2). Adjacent BSUs coalesce to form continuous, but distorted (either by twisting or gliding), layers. Moreover, the number of layers significantly increase in this stage, and turbostratic graphite forms (Figure 2.2). After the second stage of Phase B, theoretically, heteroatoms are completely removed and pure-carbon products are obtained.[6,113] Furthermore, it is generally understood that the concept of BSU disappears as such basic units mostly coalesced to form significantly larger crystalline structures.

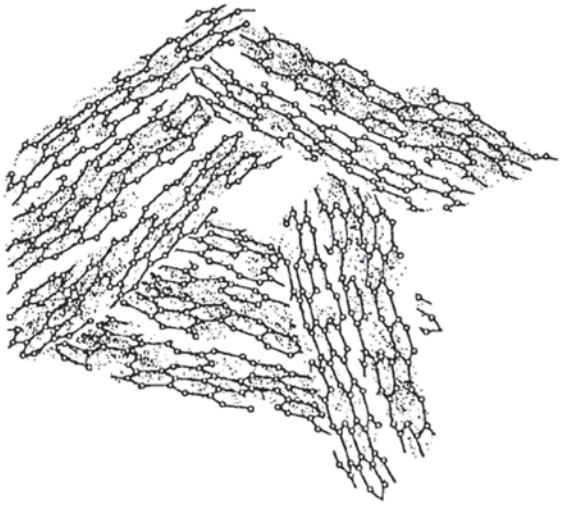

Figure 2.2 Structure of turbostratic graphite. Reprinted and reformatted with permission from Elsevier, Copyright ©1994.[6]

2.2.3. Phase C: Improvement in structural order

During Phase C (E_a: 250–280 kcal/mol), the sudden increase in carbon mobility occurs.[113] This leads to single-carbon-atom and vacancy displacements, and the subsequent decrease in in-plane defects (Figure 2.1, Phase C). As a result, the structural

morphology of the product typically shifts from porous to smooth during this phase. Moreover, inter-plane stacking is rearranged into ABAB stacking (Figure 2.3), and the inter-plane distance significantly decreases. The probability P_l of finding a pair of ordered graphitic layers in ABAB stacking is often mentioned to discuss the degree of graphitization, where a higher P_l indicates a greater degree of graphitization. P_l depends greatly on the reaction time in Phase C as well as other variables, such as the precursor and environment. Note that the exact moment at which the process shifts from simple "carbonization" to "graphitization" is difficult to specify, as the definition of a "crystalline graphitic product" is ambiguous. Nonetheless, for simplicity, in this thesis graphitization will be defined as when turbostratic graphite forms.

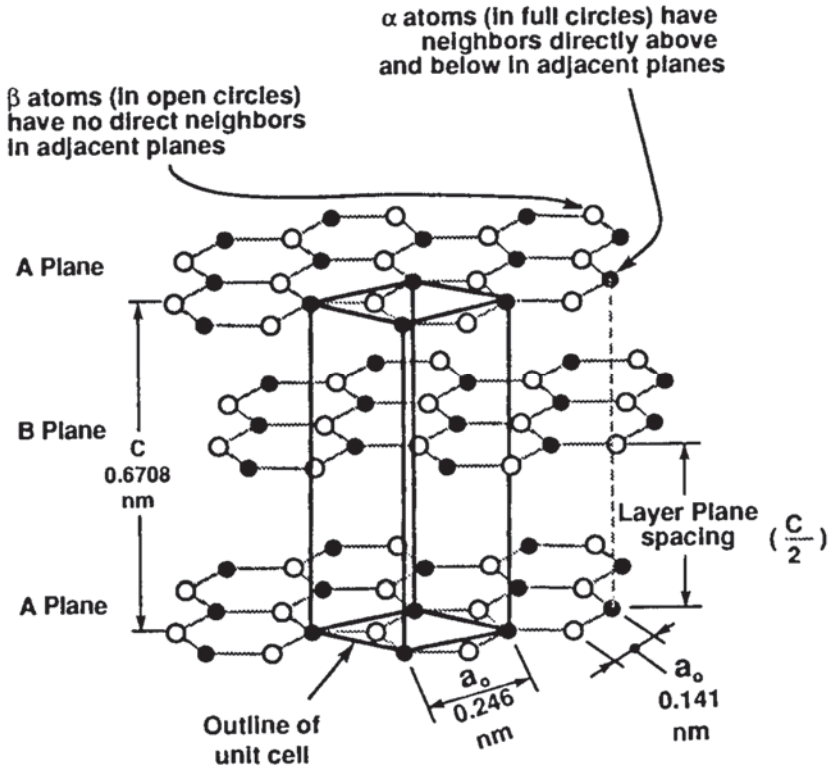

Figure 2.3 Crystal structure of graphite showing ABAB stacking sequence and unit cell. Reprinted and reformatted with permission from Elsevier, Copyright ©1994.[6]

2.3. Variables of carbonization and graphitization

2.3.1. Temperature

The main role of heat is to overcome the activation barriers for compound

fragmentation and atom rearrangement, and has been regarded to be the key condition for the carbonization and graphitization processes. Since the peak temperature determines which phase of carbonization the process can progress to, the resulting material depends highly on the temperature. Depending on the progressed phase, the products can vary from liquid tar and solid amorphous carbon (typical products of Phase A) to solid graphite (typical product of Phase B and C).[6]

2.3.2. Heating rate

As kinetic reactions are involved, changing the reaction times will result in different products. The reaction time can be mainly changed by adjusting the heating rates during processing. For example, if sufficient time is not provided for the removal of heavier condensable gases (Phase A) prior to the formation of graphitic layers (Phase B), the released gases can adhere or penetrate the layers, resulting in chemical (i.e., functional groups) and mechanical (i.e., pores) defects, respectively.[6,113] Moreover, as longer reaction times will allow for sufficient rearrangement times (Phase C), this will result in highly ordered and uniform products (i.e., higher P_l).[6,113]

2.3.3. Pressure

Pressure can assist the formation and growth of crystals according to nucleation theory.[115] However, in the case of carbonization and graphitization, the effect of pressure requires different considerations depending on the phase of the process. In Phase A, the effect of gas pressure is considerable as pressure assists the removal of condensable gases and increases non-released radical density, facilitating BSU nucleation.[6] In Phase B and C, it has been regarded that pressure may assist in the stacking and rearrangement of carbon atoms, improving anisotropy.[116] However, improvement in structural order is achieved only when a unidirectional pressure is applied perpendicularly to the layer plane. For example, if pressure is applied perpendicularly to the layer plane, the reordering of the distorted planes can be accelerated, transitioning the graphitic carbon from turbostratic graphite to “ideal” graphite.[117] Therefore, in the case of Phase B and C, consideration of the direction of pressure is important, where as in the case of Phase A, the direction of pressure is not important. In the case of the formation of carbonaceous materials that are less anisotropic, such as SiC, the direction of pressure is not as important, as the crystal can grow in any direction. Therefore, higher pressures, regardless of the direction, will generally progress formation and growth for such crystals.[115]

2.3.4. Environment

The radicals formed during Phase A and B can react with the environment forming unintended products. Accordingly, with the aim of forming crystalline graphitic products, the carbonization and graphitization processes are typically conducted in inert media, such as Ar or N_2 gases.[113,114] Conducting the process in non-inert media, such as O_2 gas or H_2O liquid, can result in oxidized products (i.e., lower P_l). However, the use of such non-inert media is not necessarily a disadvantage. For example, as mentioned in Section 1.3.1, water can serve as both a medium and a reactant, and therefore under optimum conditions can assist the carbonization process. High temperature thermal treatment using water can assist with the removal of heteroatoms by hydrolysis and subsequent dehydration and decarboxylation.[17,118] Moreover, the presence of the liquid medium causes an increase in localized pressures, facilitating BSU nucleation.[17,118]

2.3.5. Precursor

Possible organic precursors for carbonization and graphitization can be divided into simple hydrocarbons and complex polymers. Hydrocarbons are organic compounds which consists of only hydrogen and carbon (Figure 2.4). Aliphatic hydrocarbons are difficult to graphitize, as the aliphatic carbon backbone is easily fragmented into lighter compounds during Phase A.[6] Such compounds are readily released as gases, leaving no carbon residue for BSU nucleation. On the contrary, aromatic hydrocarbons will start to fragment during Phase B.[6] The heavier radicals are difficult to be released as gases, and thus condense into larger aromatic compounds, leading to efficient BSU nucleation. As gas release is minimal and the residual mass of the resulting product is high, aromatic hydrocarbons are considered to be an efficient precursor to obtain carbon-rich products.

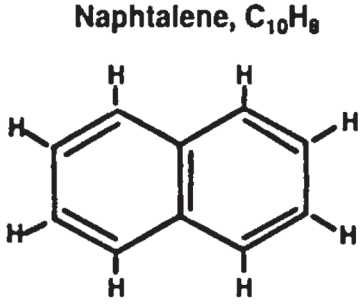

Figure 2.4 Chemical structure of a hydrocarbon precursor commonly used. Reprinted and reformatted with permission from Elsevier, Copyright ©1994.[6]

Polymers are organic materials which consists of large compounds composed of multiple repeating subunits. The viability of a particular polymer as a precursor for carbonization and graphitization can be roughly estimated by the chemical structure as in the case of hydrocarbons.[6] For example, low molecular weight polymers containing mostly aliphatic groups are generally not suitable as a precursor, for the same reasons as an aliphatic hydrocarbon. On the contrary, high molecular weight polymers containing mostly aromatic groups can generally graphitize more efficiently, for the same reasons as an aromatic hydrocarbon (Figure 2.5). Among polymers which can undergo graphitization, the resulting material composition and structural morphology can vary greatly depending on various factors, such as polymer cross-linking, type of heteroatoms, and aromatic-to-aliphatic group ratio.[6,113]

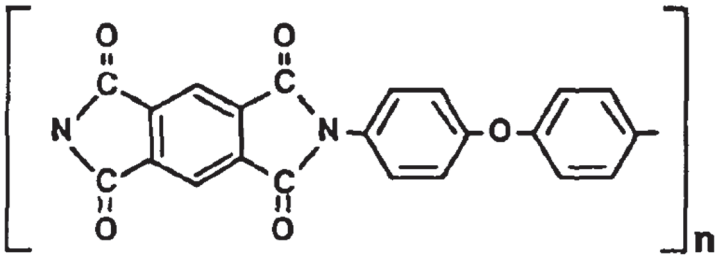

Figure 2.5 Chemical structure of a polymer precursor commonly used. Reprinted and reformatted with permission from Elsevier, Copyright ©1994.[6]

However, as the chemical structure of polymers is considerably more intricate than hydrocarbons, the conversion process is significantly more complex. Therefore, considerations of intermediate products are also required to better assess the viability of a particular polymer as a precursor. For example, considering that PDMS possesses a linear backbone, the carbonization of PDMS should yield minimal residue, similar to the case of polymers containing mostly aliphatic groups. However, as PDMS is carbonized, stable cyclic oligomers (i.e., hexamethylcyclotrisiloxane, HCS) are formed as an intermediate product (Figure 2.6).[119] Since HCS cannot be readily removed due to its large size, gas release is minimal and the residual mass stays high. The formation of HCS can occur at any point of the polymer chain, and will continuously occur until the chain is too short to cyclize.[119,120]

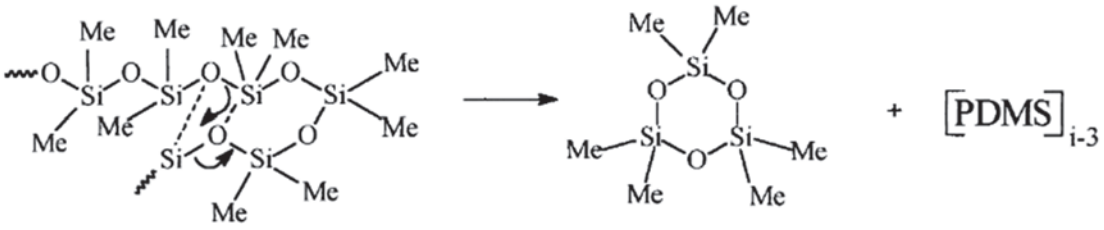

Figure 2.6 Mechanism for the formation of HCS from PDMS. Reprinted and reformatted with permission from Elsevier S.A., Copyright ©2001.[119]

With the increase in temperature, the dehydration of HCS and subsequent recombination of neighboring HCS radicals (similar in concept to Phase B) will form an SiCO matrix, consisting of nanodomains of silica and sp^2-hybridized carbon, and an interdomain boundary of SiC_xO_{4-x} interconnecting the nanodomains (Figure 2.7).[121,122] In the case of PDMS, the nanodomains of sp^2-hybridized carbon will become the BSU for the formation of graphitic carbon. As the temperature is further increased, the dimensions of sp^2-hybridized carbon will increase, forming a network of graphitic carbon. However, above a temperature threshold the carbon content will start to decrease as the graphitic carbon reacts with the nanodomains of silica to form crystalline SiC and gaseous CO via chemical reduction (Eq. 2.1 and Eq. 2.2).[123]

$$SiO_2(s) + C(s) \rightarrow SiO(s) + CO(g) \qquad \text{Eq. 2.1}$$

$$SiO(s) + 2C(s) \rightarrow SiC(s) + CO(g) \qquad \text{Eq. 2.2}$$

This threshold temperature has been mentioned to be approximately 1500 °C, but could differ depending on the form of the material (i.e., bulk or powdered) or environment (i.e., atmosphere and pressure).[123]

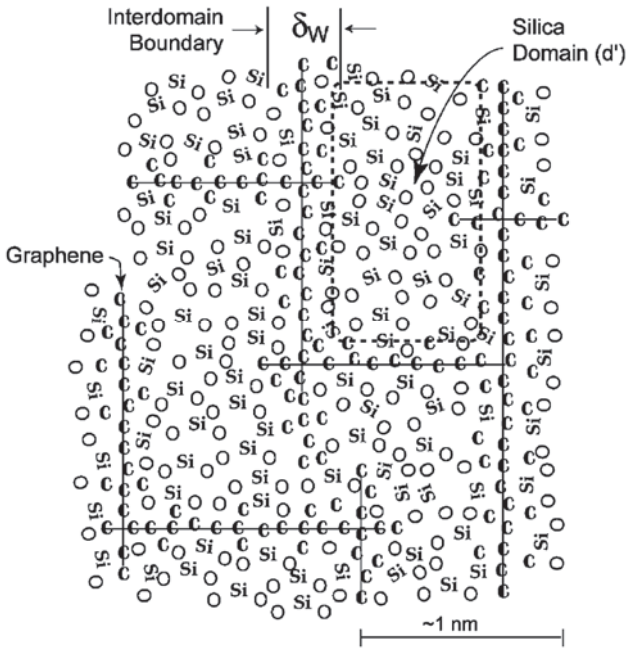

Figure 2.7 A concept of the molecular make-up of the nanodomains. Note that the interdomain boundary consists of graphene layers with mixed Si-C-O bonds forming the interface with the silica domains. Reprinted and reformatted with permission from John Wiley & Sons, Copyright ©2006.[122]

2.4. Relationship between material and property

2.4.1. Electrical properties

In general, the conduction of "electricity" can be carried out either by electrons or by ions. As ionic compounds are out of the scope of this thesis, only electron conduction will be discussed. How "easy" electrons can travel through a material, or the electrical conductivity, depends on the mobility of the electron. For materials such as semiconductors and dielectrics, since the valence electrons are strongly bounded by the nucleus (i.e., low mobility), the electrical conductivity is low. On the contrary, for materials such as metals, since the valence electrons are loosely bounded by the nucleus (i.e., high mobility), the electrical conductivity is high. In the case of ideal graphite, three valence electrons of the carbon atoms are covalently bonded to three adjacent atoms to form a hexagonal honeycomb layer. The fourth valance electron is delocalized and projected out of plane, forming a toroidal "cloud" of mobile electrons along the plane (Figure 2.8). Owing to this, graphite has a high electrical conductivity (metal-like) within

its planes (i.e., *ab* direction). However, between the planes (i.e., *c* direction), as the atomic distances are comparatively larger than the *ab* direction, graphite has a low electrical conductivity (dielectric-like) in the *c* direction.

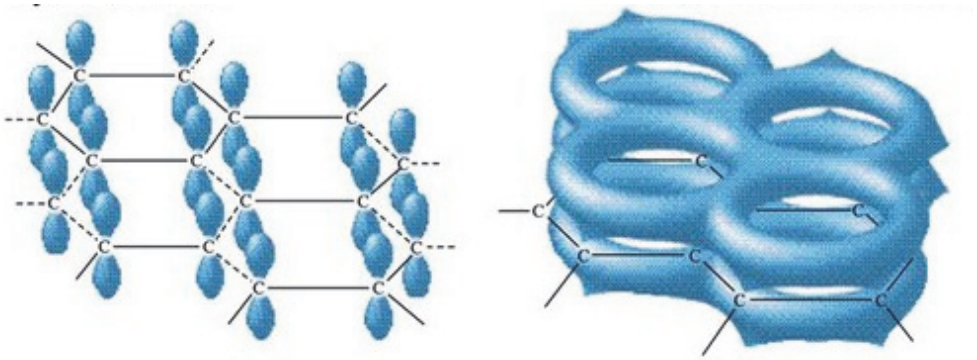

Figure 2.8 Schematic of the carbon atoms in graphite. Reprinted and reformatted with permission from Cengage Learning, Copyright ©2002.[124]

The existence of defects, such as vacancies, impurities, and distortions, within the layers can significantly affect the electrical conductivity of graphitic materials.[125] Such defects can lead to an increase in atomic distances, localized curvature of the planes, and electron scattering, causing a decrease in electron mean free path distance. This indicates a decrease in electron mobility, or electrical conductivity. As the size of defects significantly increase, the defects will appear as potential barriers (i.e., emergence of a bandgap), as electrons will need to be transported through a combination of tunneling, hopping, and percolation conduction pathways.[125,126]

In the case of composites structures which are composed of various materials with different material properties, the considerations of the material features are required. For example, as the carbonaceous structures formed by the carbonization and graphitization of PDMS is a composite structure composed of ribbons of graphitic carbon (conducting) and NCs of SiC (semiconducting), the structure can exhibit two different conducting regimes (Figure 2.9). The transition between the two regimes can be discussed by the required concentration of material to form a continuous network, or percolation threshold.[123,127] For example, if the concentration of graphitic carbon is greater than the percolation threshold, the structure will exhibit a metal-like electrical property, distinctive of the graphitic carbon (Figure 2.9 (a)).[128] On the other hand, if the concentration of graphitic carbon is less than the percolation threshold, the structure will exhibit a semiconductor-like, or insulator-like, electrical property, distinctive of the SiC-NCs or the amorphous material (Figure 2.9 (b)).

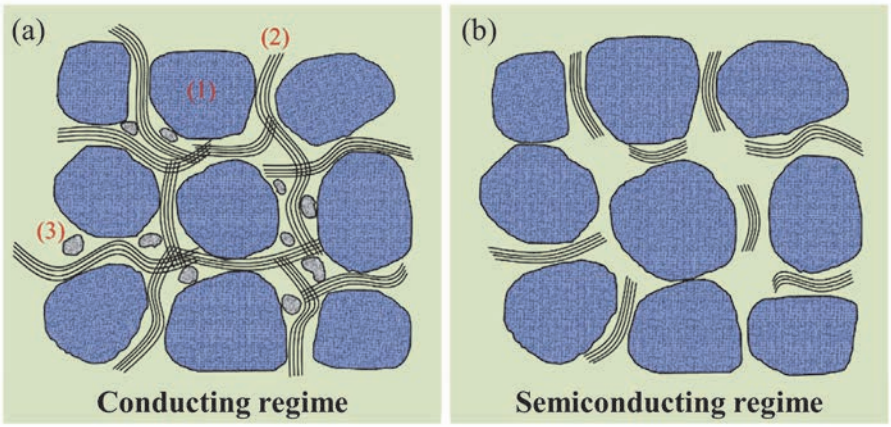

Figure 2.9 Models for composite structures with different conducting regimes. (1), (2) and (3) are SiC-based nanodomains, graphitic carbon nanodomains, and other nanodomains (SiC polytypes or amorphous carbonaceous material), respectively. Reprinted and reformatted with permission from Elsevier, Copyright ©2020.[123]

The percolation threshold is highly dependent on the mean size and shape of the material. For example, in the case of wider and longer ribbons of graphitic carbon, the concentration required for percolation will decrease. Moreover, the concentration, size, and shape of the other materials consisting the composite structure can also affect the percolation threshold.[128–130] For example, if the composite structure consists of extremely large SiC-NCs at a relatively high concentration, the percolation threshold for the graphitic carbon will increase as it will become more difficult to form a network.

2.4.2. Optical properties

Photoluminescence, including fluorescence and phosphorescence, is a process in which a material absorbs light and then re-emits light.[131,132] The initial illumination of light excites an electron from the valence band to the conduction band, and as the electron relaxes from the conduction band to the valence band, light with energy equal to that of radiative relaxation energy is emitted. As the electron relaxes, it may undergo multiple decay processes, including internal and external conversion, vibrational relaxation, and intersystem crossing;[131] therefore, the emitted light typically possesses less energy (i.e., longer wavelength) than the excitation light. This shift in the wavelength between excitation and emission light is referred to as the Stoke's shift. As the wavelength of emission light depends on the radiative relaxation energy, different materials emit light of different wavelengths. Moreover, by altering the band structure of the material, the

wavelength can be vastly tuned.[132] In the case of metals and metal-like materials, such as graphite, as there is no bandgap, photoluminescence is generally not observed. However, such materials can exhibit fluorescence, by introducing a bandgap. For example, in the case of graphite, a bandgap can be introduced by forming structural defects or by reducing the structural size, such as in the case of GQDs.

As energy bands are simply a collection of individual energy levels of the atoms in a material, by reducing the dimensions of materials from 100 nm or less towards the de-Broglie wavelength of the atom, discrete energy levels emerge (Figure 2.10).[132] This emergence of levels due to the reduction in dimensions is referred to as the quantum confinement effect, and results in narrow emission bands.[132] Such materials which exhibit fluorescence owing to its small size are referred collectively as quantum dots (QDs). Moreover, as the dimensions of the material is reduced, the surface states can also affect the fluorescent properties as the surface-area-to-volume ratio increases.[133,134] For QDs composed of semiconductors, as the probability density of the excited electrons is largely distributed inside the material and very small at the edges (i.e., surface), the fluorescent properties are closely related to the bulk properties (i.e., size, crystallinity, and shape), rather than the surface states.[135] On the other hand, for QDs composed of metals, as the probability density of the excited electrons at the edges are significant, the fluorescent properties are closely related to the surface states, rather than the bulk properties.[135] Therefore, in the case of GQDs, the fluorescent properties have been largely tuned by doping or edge functionalization. Thus far the correlation between the size of the GQDs and the fluorescent properties have been inconclusive. [135] Moreover, due to the chemical versatility of carbon atoms (as mentioned in Section 1.2.), the edge groups as well as edge crystal structure (i.e., zig-zag or armchair) can vary greatly, leading to a significantly broader fluorescence spectra compared to conventional semiconductor QDs.[135]

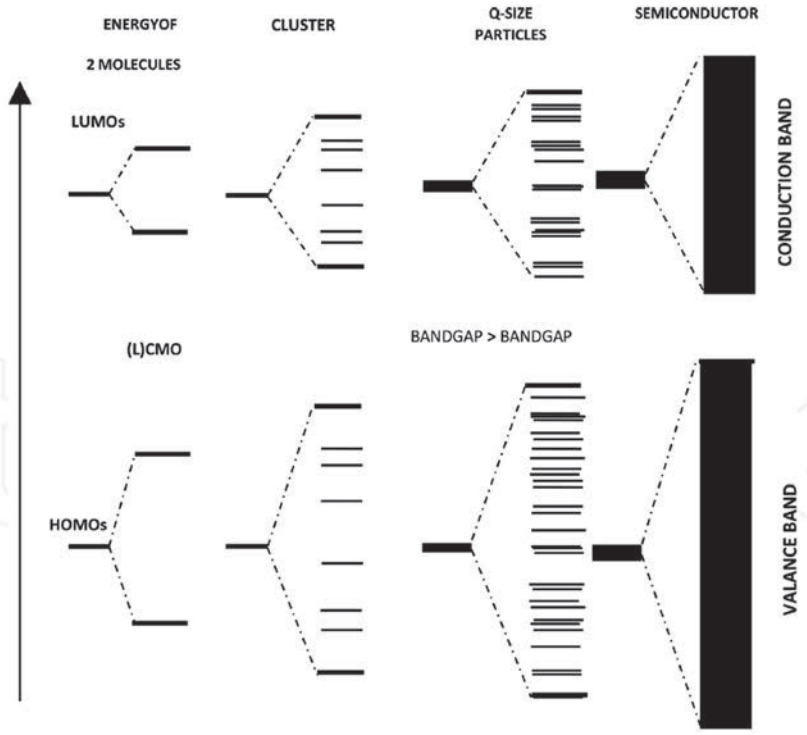

Figure 2.10 A schematic diagram of the molecular orbital model for band structure. Reprinted and reformatted with permission from IntechOpen, Copyright ©2020.[132] Open Access Creative Commons Attribution license.

2.5. Principles of light-material interactions

When light comes into contact with a material interface, the electrons or the lattice of the surface material may resonate with the incident light. Lattice resonance generally occurs in the case of light with far infrared wavelengths, and are not of particular importance regarding the discussions for this thesis (to discuss the results described in Chapters 3 to 6). Therefore, Section 2.5. will focus on the light-material interactions for visible and ultraviolet wavelengths, unless otherwise mentioned. When the electrons cannot resonate with the incident light, the incident light is transmitted though the material without any interaction. On the other hand, when the electrons can resonate with the incident light, an electric dipole is formed (Figure 2.11). As the electric dipole oscillates, it can emit light, referred to as electric dipole radiation, in the opposite and same direction as the incident light.[136] The electric dipole radiation traveling in the opposite direction of the incident light is called reflected light, whereas electric dipole radiation traveling in the same direction of the incident light is called propagating light.[136]

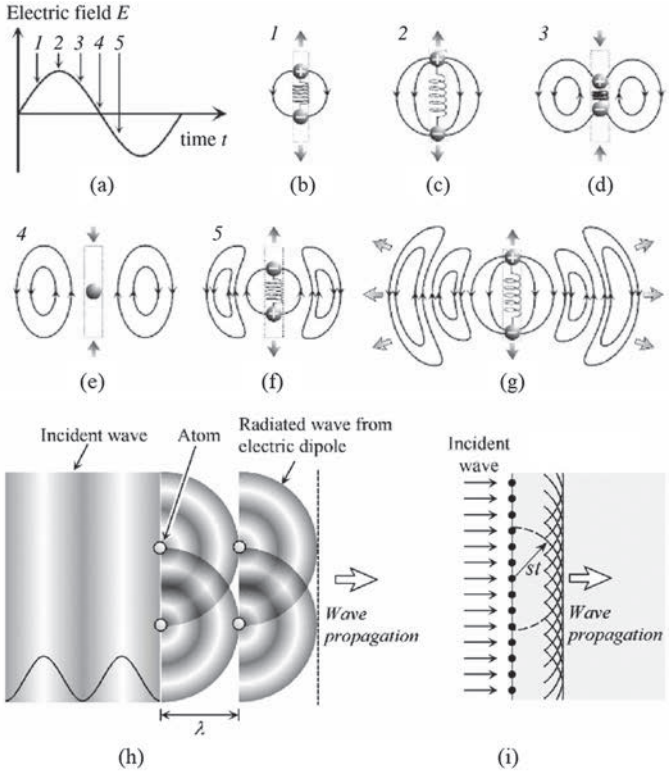

Figure 2.11 Schematic process of electric dipole radiation: (a) an external electric field applied to a material and (b–f) the behavior of an electric dipole when the external field of 1–5 in (a) is applied, respectively. (h) Propagation process of light and (i) propagation of light according to Huygen's principle. In (h), atoms are shown with the interval of the light wavelength λ. In (i), *st* shows a distance to which light travels with a speed *s* during a time *t*. Reprinted and reformatted with permission from John Wiley & Sons, Copyright ©2007.[136]

As the propagating light travels through the material, the light can be absorbed by the material gradually attenuating the propagating light. Light absorption can induce a sequence of processes which can lead to structural changes to the material. Figure 2.12 shows the different processes that could occur when laser light is irradiated and its respective timescales. Note that these timescales are for semiconductors (i.e., GaAs and GeSb),[137] and therefore may be slightly different for different materials, such as metals and polymers. As the charge-to-mass ratio of electrons are comparably higher than that of the protons in the nucleus of an atom, the electronic state of a material is closely related to the optical response of a material. As previously mentioned, the electronic states of a material can be understood by energy levels describing the energy distribution of electrons in an individual atom, or by energy bands indicating the energy distribution of a collection of atoms in a material (Figure 2.10).[138] The processes in Figure 2.12 will be

discussed using such energy levels in more detail below.

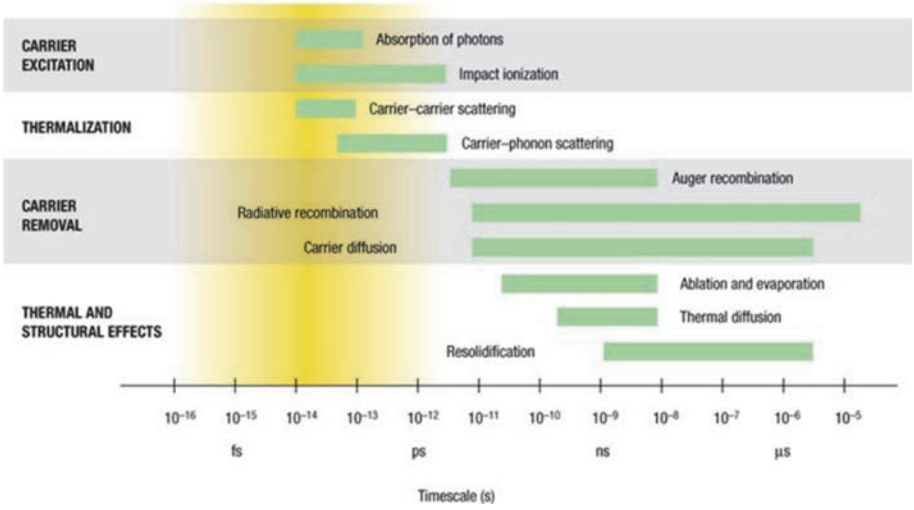

Figure 2.12 Timescales of various electron and lattice processes in laser-excited solids. Each green bar represents an approximate range of characteristic times over a range of carrier densities from 10^{17} cm^{-3} to 10^{22} cm^{-3}. Reprinted and reformatted with permission from Springer Nature, Copyright ©2002.[137]

2.5.1. Electron excitation

When light is irradiated to a material, whether or not electron resonance occurs mainly depends on the relationship between the energy of a photon of light and the energy required for electronic transitions of electrons between levels or bands. If the energy of the photon is sufficient for electronic transitions, the bounded electrons gain energy and are transitioned to a higher level or band (i.e., absorption). This increase in energy increases the mobility of electrons, allowing for inter-atom movements (i.e., excitation). As the transition energies of inner orbital electrons are much greater than the photon energies of light, the valence or outer orbital electrons generally contribute to absorption.[138] On the other hand, if the photon energy is less than the energy required for electronic transitions, no interaction occurs and the light is transmitted. In the case of metals (Figure 2.13), as the electrons are loosely bounded to the nucleus, these electrons can move relatively freely. Therefore, photons of light of various wavelengths can be easily absorbed by the material surface, forming a layer of electric dipoles mentioned previously (Figure 2.11). The formation of this dipole layer results in a collection of reflecting and propagating light. However, as it is difficult for light to propagate through metals, reflected light is considerable for metals. On the contrary, in the case of semiconductors and dielectrics (Figure 2.13), as the electrons are tightly bounded to the

nucleus (in the valence band), a certain photon energy is required to loosen the binding of electrons for inter-atom movements (in the conduction band). The energy required for the loosening of this binding is referred to as the energy bandgap ΔE_{band}, and can be considered as an indicator of the degree of bounding between the valence electron and the nucleus. The wider the bandgap is, the tighter the binding of electrons is, and therefore, more photon energy is required to induce the excitation of electrons. Especially in the case of dielectrics such as glass, since a single photon of a visible-wavelength light generally does not have sufficient energy to induce excitation and therefore mostly transmitted, such materials appear transparent.

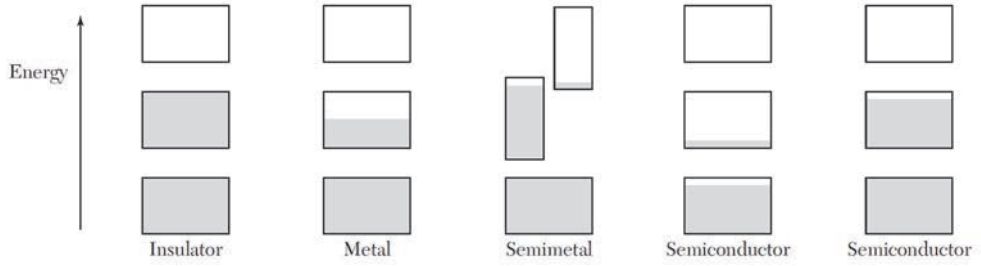

Figure 2.13 Schematic electron occupancy of allowed energy bands for an insulator, metal, semimetal, and semiconductor. The vertical extent of the boxes indicates the allowed energy regions; the shaded areas indicate the regions filled with electrons. The left of the two semiconductors shown is at a finite temperature, with carriers excited thermally. The other semiconductor is electron-deficient because of impurities. Reprinted and reformatted with permission from John Wiley & Sons, Copyright ©2005.[139]

Nonetheless even in the case of a wide bandgap materials, excitation can be induced by a visible-wavelength light with sufficiently high intensities, such as in the case of ultrashort laser pulses. In the case of high intensities, or high photon densities, multiple photons can interact simultaneously with a single electron to induce excitation. The energy requirement for excitation induced by multiple photons, or multiphoton excitation, is expressed by Eq. 2.3 as,

$$\Delta E_{band} \leq n \times \hbar\omega \qquad \text{Eq. 2.3}$$

where n is the number of photons, $\hbar$ is the reduced Planck's constant, and ω is the angular frequency of the photon (i.e., laser frequency). $\hbar\omega$ is the energy per unit photon.

Once the electrons of semiconductors and dielectrics are excited, they can behave similarly to valence electrons of metals. If the excited electron e_1 gains more than twice the energy for electronic transitions, e_1 can subsequently collide and excite a non-excited electron e_2, by impact excitation. As a result, both e_1 and e_2 will be excited. These electrons can then absorb additional photons and gain energy to further excite additional

non-excited electrons by impact excitation (i.e., e_3 and e_4). As long as the laser light is being irradiated, the density of excited electrons will increase exponentially, and accordingly this process is referred to as avalanche effect.

2.5.2. Energy transfer

The excitation of electrons through the absorption of photons leads to the transfer of energy throughout the electronic system and the lattice (Figure 2.14).[137,138] Initially, absorption will result in an electronic system of excited electrons with a narrow distribution of momentum. The electrons will quickly go out of phase with one another by electrostatic interactions and the distribution of momentum will widen (i.e., electron-electron scattering).[138] This scattering is merely a "redistribution" of energy between excited electrons and thus the number of excited electrons nor the total energy of the electronic system does not change. The timescale for electron-electron scattering depends on the initial density of excited electrons, but it has been regarded to occur in less than 20 fs.[140] Through multiple electron-electron scatterings the momentum distribution of the excited electrons will approach a Fermi-Dirac distribution within a few hundred fs (Figure 2.14, Phase 1).[138]

While electron-electron scattering pursues, electrons can lose or gain energy and momentum by the emission or absorption of phonons (i.e., electron-phonon scattering). Since electron-phonon coupling is weaker than electron-electron coupling, the timescale for electron-phonon scattering is longer than electron-electron scattering, and is on the order of a few hundred fs.[138] Moreover, as electron-phonon scattering can only transfer small amounts of energy per scatter, multiple electron-phonon scatterings is required to transfer the excess energy of the electronic system to the lattice and bring the material to equilibrium. Therefore, the timescale for the material to reach equilibrium is generally in the order of ps.[137,138] Electron-phonon scattering can occur within the initial band, referred to as intravalley scattering (Figure 2.14, Phase 2), or into a different band, referred to as intervalley scattering (Figure 2.14, Phase 3). In the case of intervalley scattering, the energy of the electron after the emission or absorption of phonons must be greater than the energy required for excitation in that band.

As the energy of electrons decrease due to scattering, the excited electrons can become rebounded and return to the valence band (i.e., relaxation). Two of the most important relaxation processes are radiative relaxation and Auger relaxation.[137,138] In radiative relaxation, as an excited electron returns to the valence band, the spontaneous emission of a photon occurs (i.e., photoluminescence). Therefore, in the case of radiative relaxation,

both the number of excited electrons and the total energy of the electronic system decrease. In Auger relaxation, as an excited electron returns to the valence band, the excess energy is transferred to another excited electron (Figure 2.14, Phase 4). In Auger relaxation, the number of excited electrons decreases; however, the total energy of the electronic system remains unchanged. The excited electron can then undergo additional energy transferring and relaxation processes to further decrease the total energy of the electronic system.

Although not a "relaxation" process, electron diffusion is another important process that can locally reduce the density of excited electrons. The diffusion rate of excited electrons R_d can be expressed by Eq. 2.4 as,

$$R_d = (k_B T_e \mu_a / e) \times \nabla^2 N \qquad \text{Eq. 2.4}$$

where k_B is the Boltzmann constant, T_e is the electronic system temperature, μ_a is the electron mobility in the excited state, e is the electrical charge, and N is the electron density. Determining R_d is extremely complicated as T_e dynamically changes during laser irradiation, as well as the implicit dependency of μ_a to T_e combined with the difficulty of determining μ_a. In general, higher T_e will result in higher R_d. However, in the case of high densities of excited electrons, diffusion can be hindered by electron confinement, decreasing R_d.[141]

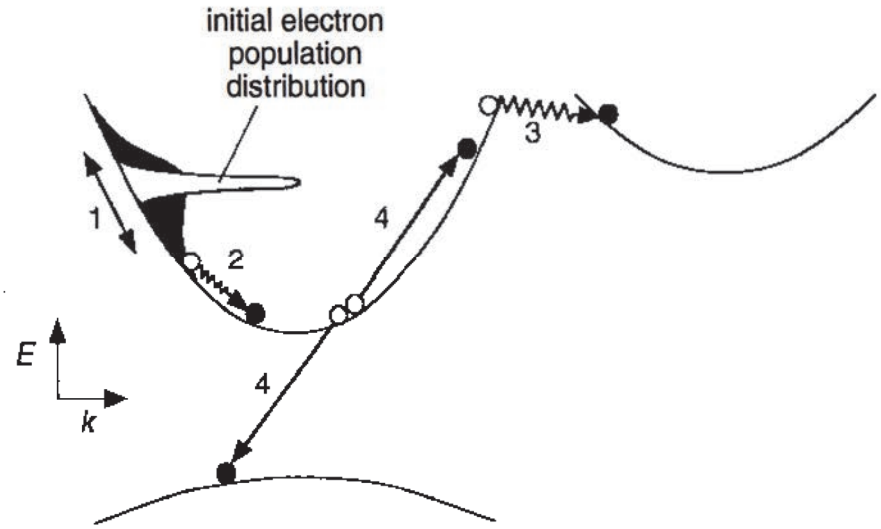

Figure 2.14 Representation of scattering processes following laser excitation. Process 1 indicates the spreading out of the initial carrier distribution in *k*-space through carrier-carrier scattering. Processes 2 and 3 show intravalley and intervalley carrier-phonon scattering, respectively. The interaction of carriers and phonons leads to electron-lattice equilibration. Carrier-density relaxation occurs through recombination processes such as Auger recombination, shown by process 4. Reprinted and reformatted with permission from Annual Reviews, Inc., Copyright ©1995.[138]

2.5.3. Thermalization

As the energy of the electronic system is transferred to the lattice by electron-phonon scattering, the temperature of the material T increases (i.e., thermalization).[142] The spatial and temporal distribution of T when laser light is irradiated can be expressed by Eq. 2.5 as a function of x, y, z, and t,

$$\rho C_p \frac{\partial T(x,y,z,t)}{\partial t} = \nabla \cdot \big(\kappa \nabla T(x,y,z,t)\big) + Q(x,y,z) \qquad \text{Eq. 2.5}$$

where ρ, C_p, and κ are the density, specific heat capacity, and thermal conductivity of the material, respectively, and Q is the heat input distribution due to laser irradiation. Considering a stationary laser light centered at xy-coordinates (0,0) being irradiated from the top surface of a material ($z = 0$), Q can be estimated by Eq. 2.6 as a function of x, y, z,

$$Q(x,y,z) = P(1-R)\frac{A}{\pi \sigma_x \sigma_y} e^{-\left[\frac{x^2}{2{\sigma_x}^2}+\frac{y^2}{2{\sigma_y}^2}\right]} \times e^{-Az} \qquad \text{Eq. 2.6}$$

where, P is the max laser power of the laser light, σ_x and σ_y are the focal beam radius in the x and y dimensions, respectively, and R and A are the reflection and absorption coefficients of the material, respectively. As the peak temperatures reach the melting and boiling temperatures of the material by thermalization, structural changes to the material, such as melting and vaporization, respectively, can occur.[137]

Assuming material properties do not change dynamically, it is relatively straightforward when discussing attained peak temperatures in the case of CW lasers, as there is a continuous heat input.[142] However, in the case of ultrashort pulsed lasers, as thermalization occurs in intervals, the repetition rate (RR), or the frequency of pulses f_{RR}, becomes important when determining peak temperatures. If the time between pulses $1/f_{RR}$ is less than the time for the complete dissipation of heat energy inputted by a single pulse out of the laser spot diameter t_d, expressed by Eq. 2.7 as,

$$\frac{1}{f_{RR}} < t_d \qquad \text{Eq. 2.7}$$

accumulation of heat within the irradiated area will occur. As the RR increases, the time allowed for heat dissipation between pulses decreases, leading to more heat accumulation (i.e., higher peak temperatures).

When thermalization occurs due to laser irradiation, thermomechanical effects can occur simultaneously. The instantaneous temperature increase and subsequent material expansion due to laser irradiation generates a radial thermoelastic stress (i.e., laser-

induced shockwave), and a localized increase in pressure.[143,144] The instantaneous pressure p induced by thermalization can be generalized by Eq. 2.8 as,

$$p = \frac{c^2\beta}{C_p}Q = \Gamma Q \qquad \text{Eq. 2.8}$$

where c is the speed of light and β is the thermal expansion coefficient of the material. Γ is the Grüneisen coefficient, which is a dimensionless value that indicates the efficiency of the material in converting heat into pressure. It can be seen from Eq. 2.8 that the magnitude of pressure depends linearly on Q, or the amount of energy absorbed per unit volume and unit time. As high intensities can be readily realized using ultrashort pulsed lasers, the irradiation of ultrashort laser pulses, such as fs laser pulses, can induce localized pressures in the magnitude of MPa and GPa.[145,146] Generally, rigid materials, such as metals, have a higher Γ than soft materials, such as polymers; therefore, with the same Q, higher instantaneous pressures will be induced for such materials. Note that Eq. 2.8 is just a generalization and is overly simplified. For example, the current equation considers that the confined region is uniformly surrounded in all direction by a single material. Therefore, depending on if the thermalized region is exactly at the material surface, slightly below the material surface, or deep within the bulk material, the instantaneous pressures, as well as the temporal decay in localized pressures will be vastly different.

2.5.4. Ionization

In the case of extremely high intensities, electrons can become completely unbounded from the nucleus and removed from the material (i.e., ionization). Two of the most prominent ionization processes are multiphoton ionization and tunnel ionization.[147,148] The transition between these ionization processes have been discussed using the Keldysh parameter γ which can be expressed by Eq. 2.9 as,

$$\gamma = \frac{\omega\sqrt{2I_0}}{F} \qquad \text{Eq. 2.9}$$

where I_0 is the ionization potential and F is the laser electrical field strength. The relationship between laser intensity I and F can be expressed by Eq. 2.10 as,

$$I = \varepsilon_0 cn|E|^2 \qquad \text{Eq. 2.10}$$

where ε_0 is the vacuum permeability and n is the refractive index.

Multiphoton ionization is a similar concept to multiphoton excitation discussed in

Section 2.5.1, where ΔE_{band} is simply substituted for I_0. In tunnel ionization, the electrons are unbounded from the nucleus by the electrical field of the laser light. The Keldysh parameter can be interpreted as a ratio between the intrinsic atomic momentum $(2I_0)^{1/2}$ and the laser induced momentum F/ω. Therefore, when $(2I_0)^{1/2}$ is sufficiently greater than F/ω, or $\gamma >> 1$, multiphoton ionization is dominant; whereas, when $(2I_0)^{1/2}$ is sufficiently smaller than F/ω, or $\gamma << 1$, tunnel ionization is dominant. Note that although the Keldysh parameter assists in providing a general boundary between multiphoton and tunnel ionization, it cannot provide an accurate characterization of the details regarding the ionization process for every material.[148]

As the unbounded electrons, commonly referred to as "free" electrons, escape from the material, such electrons can collide with bounded electrons and unbind them by impact ionization. This concept is similar to impact excitation, and the free electron must have sufficient energy to ionize a bounded electron without relaxing. This sequential ionization leads to avalanche ionization, and the total density of free electrons n_e exponentially grows. The rate at which n_e increases due to laser irradiation can be expressed by Eq. 2.11 as,

$$\frac{\partial n_e}{\partial t} = n_{mpi+ti} + \delta_{imp} n_e \qquad \text{Eq. 2.11}$$

where n_{mpi+ti} is the combined ionization rate of multiphoton and tunnel ionization, and δ_{imp} is the probability of impact ionization. As n_e goes above a certain critical density, irreversible changes to the material are induced without thermalization, such as ablation due to coulomb explosion.[137,147]

2.6. Principles of LICG

The specific formation mechanism of carbonaceous structures composed of graphitic carbon by LICG has been an issue of debate for many years with the prevailing notion of a simple photothermal conversion reaction that mainly depends on the amount of energy input, or laser fluence.[70] However, this view has been shown to be inconsistent with experimental observations of nonlinear changes in the resulting structures when multiple processing parameters are simultaneously changed.[149–152] This may be due to the lack of consideration regarding two points. Firstly, the laser light is oversimplified as a simple source of heat energy, and most of the light-material interaction processes are not considered. Secondly, from the carbonization and graphitization processes discussed in Section 2.2., it can be easily understood that the consideration of peak temperature alone is insufficient, and temporal considerations are also crucial. Here, the principle of LICG

is discussed by combining the principles of carbonization and graphitization (Section 2.2. and 2.3.) with the principles of light-material interactions (Section 2.5.).

2.6.1. Light absorption

As the laser light is irradiated onto a polymer, the incident light can either be transmitted through the material, reflected at the surface, or propagated into the material (as discussed in Section 2.5.). Absorption will occur when the incident light propagates into the material, where the efficiency of light absorption is highly dependent on the relationship between the irradiated polymer and the wavelength of the incident light. This relationship is quantitatively expressed by the absorption coefficient, which defines how far the incident light propagates into the material before being completely absorbed. The wavelengths of commonly used lasers for LICG can be grouped into ultraviolet (≤ 405 nm), visible (405–750 nm), and infrared (0.75–25 μm).[70] In the case of ultraviolet and visible wavelengths, the irradiated light will be absorbed by the electrons and subsequently transferred to the lattice via electron-phonon scattering. For the LICG of transparent polymers, such as PDMS, as a single photon of visible-wavelength light typically does not have sufficient energy to induce electron excitation, multiphoton excitation using ultrashort pulsed lasers is preferred for such wavelengths (i.e., nonlinear absorption). On the other hand, for infrared wavelengths, the irradiated light can be absorbed directly by the lattice, as the frequency of the incident light resonates with the vibration modes of the lattice bonds.[153] For example, infrared wavelengths in the range of 9 to 11 μm, resonate with the vibration modes of C-C bonds of polymers; therefore, the use of a CO_2 laser can realize the heating of polymers without electron excitation.[154]

2.6.2. Bond fragmentation

Due to the absorption of photons, localized heating of the material will occur. Since the photons will be absorbed while propagating into the material, a thin near-surface layer will be heated, in which the thickness depends on the inverse of the absorption coefficient (i.e., penetration depth). However, due to the environment-polymer surface boundary effects, such as light scattering and/or thermal conduction, the peak temperature will be reached, not at the surface, but rather few μm below the surface (hot spot in Figure 2.15).[112,155,156]

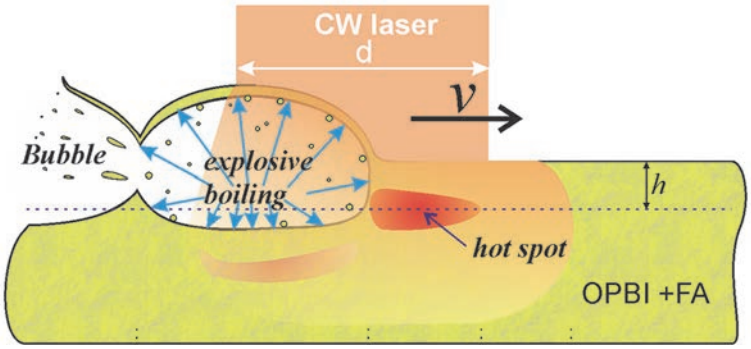

Figure 2.15 Schematic illustrating the formation mechanism of a porous structure by the laser irradiation of a poly-2,2'-p-oxydiphenylene-5,5'-bis-benzimidazole (OPBI) and formic acid (FA) composite polymer. Scanning of a CW laser beam with a diameter of *d* at a speed of *v*, will induce a hot spot at a depth of *h* from the surface. Reprinted and reformatted with permission from MDPI, Copyright ©2021.[155] Open Access Creative Commons Attribution license.

The high temperatures induced by laser irradiation will be sufficient for the bond fragmentation (Phase A and B-1 in Section 2.2.), initiating BSU formation. In addition to this, the irradiated light can also induce the fragmentation of bonds non-thermally by ionization. As ionization is prominent for extremely high laser intensities, considerations of non-thermal fragmentation may only become important in the case of LICG using ultrashort pulsed lasers. The non-thermal fragmentation of bonds by ionization has been commonly referred to as photolysis or photochemical degradation, and consists of three steps: initiation, propagation, and termination.[157] Most radicals formed non-thermally cannot diffuse easily through the polymer and rapidly recombine with neighboring radicals, due to their low mobility. Hydrogen radicals can diffuse easily through the polymer matrix, owing to their small size, and recombine with other hydrogen radicals to be released as H_2 gas.[157] Therefore, non-thermal fragmentation typically results in slight alterations in the chemical structure of the polymer, and release of heteroatoms by non-thermal fragmentation alone is difficult. As heteroatoms cannot be removed to increase the carbon content by non-thermal fragmentation, the formation of graphitic carbon by laser irradiation is assumed to be a thermally-dominated phenomenon rather than an optically-dominated phenomenon. Nonetheless, this slight alteration in the chemical structure could be significant in the case of LICG, as the absorption coefficient of the irradiated material could increase. Moreover, by combining thermal and non-thermal fragmentation, BSU formation may be accelerated. However, excessive fragmentation will result in the formation of light compounds that are easily removed as gases (as in the case of aliphatic hydrocarbons in Section 2.3.5.), leaving no carbon residue for BSU

nucleation (i.e., laser ablation).

2.6.3. Structural formation

As the polymer is heated, it will undergo the graphitization process to form carbonaceous structures composed of graphitic carbon. The heating rates due to laser irradiation can easily reach values up to 1000 °C/s,[70] leading to the rapid release of condensable gases (Phase A in Section 2.2.). As the hotspot is slightly below the surface, the release of gases will form multiple highly-compressed microbubbles below the surface (explosive boiling in Figure 2.15).[155,156] As condensable gases are further released, the microbubbles will expand into macrobubbles. The expansion of the macrobubbles will be directed towards the polymer surface, and eventually explode through the surface. This commonly results in the formation of a protruding carbonaceous structure containing large amounts of macro-pores. The concentration and sizes of the macro-pores will depend highly on the degree in which the released gases condense. For example, in the case of higher heating rates, although more gases may be released leading to a higher concentration of macro-pores, the sizes of the macro-pores may be low as time for condensation of gases is insufficient. Moreover, as the macrobubble explodes, the gases rapidly cool and condense into solid debris, which can further precipitate onto the surface.[155]

Due to the high heating rate, nucleation and growth of BSUs can start while the gases are still being released. The previously mentioned explosive bubbling, in addition to the generation of laser-induced shockwaves owing to the high heating rate, can result in highly pressurized regions which can assist BSU nucleation. As the BSUs grow, the released non-condensable gases (Phase B in Section 2.2.) can puncture the graphitic layers, forming a graphitic carbon crystal with nano-pores throughout its layers. By changing the heating rate, the degree and timing of gas release can be adjusted to tune the macro- and nano-morphology of the resulting structure and material (Figure 2.16).[158]

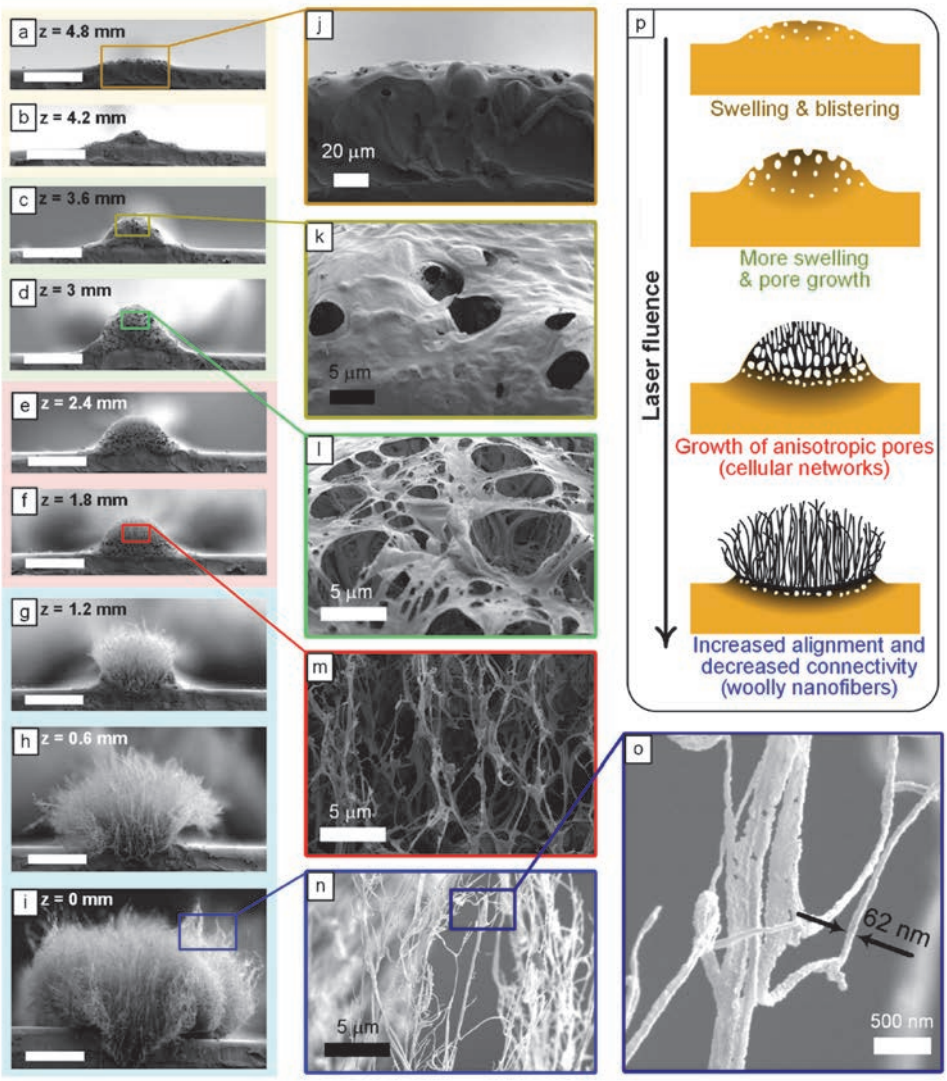

Figure 2.16 (a–i) SEM images of side views of the structures formed with different laser defocus distances *z* (Scale bar: 100 µm). (j–o) Higher resolution SEM images. (j) SEM showing the swelling of polyimide. (k) SEM showing pore formation and growth. (i) SEM showing increase in pore shape anisotropy. (m) SEM showing the formation of anisotropic cellular networks. (n) SEM showing the formation of carbon nanofibers. (o) High resolution image showing 60-nm thick nanofibers. (p) Schematic illustrating the structural evolution with increasing fluence, showing the transitions between different morphologies. Reprinted and reformatted with permission from the American Chemical Society, Copyright ©2021.[158]

In addition to the importance of rapid gas release on structuring, this rapid gas release may also minimize the effect of the processing environment on the resulting structure. Typically for conventional carbonization and graphitization, inert atmospheres are necessary to prevent oxidation (as mentioned in Section 2.3.4.). On the other hand, the

carbonization and graphitization processes using a laser can be performed in air without consequential oxidation.[70] The fast-heating rates, in combination to the rapid release of gases, hinders atmospheric gases from reacting with the radicals formed by laser irradiation. Note that the graphitic carbon formed by LICG is by no means defect-free, and is typically distorted (i.e., turbostratic), as the reaction times for the reordering of the graphitic lattice is insufficient (Phase C in Section 2.2.). Moreover, if the heating rate is significantly slowed down, the considerable oxidation of the resulting graphitic carbon can occur even in the case of LICG, as gas release weakens and there is sufficient time for atmospheric gases to diffuse.

2.7. Discussions on the nonlinearity in LICG

Conditions that critically affect the material and/or structure resulting from LICG, such as the peak temperature and heating rate, can be easily changed by altering the laser parameters. For example, the attained peak temperature and heating rate can be adjusted by changing the amount of laser energy absorbed by the material via combination of laser parameters, including the laser wavelength, pulse duration, focal beam diameter, laser power, pulse energy, repetition rate, and scanning speed. As the peak temperature determines which phase of carbonization and graphitization the LICG process can progress to (Section 2.3.1.), the resulting material is expected to be correlated linearly to the energy input. However, considering that the LICG process is governed by light-material interactions and the irradiated material is dynamically changing, the resulting material is expected to be correlated nonlinearly to the energy input.

As the polymer initially absorbs light, the thermal and non-thermal fragmentation leads to localized changes in the absorption coefficient of the irradiated area. Typically, this leads to a slight increase in light absorption, which further continuously increases to a certain value as laser irradiation proceeds. However, this increases in absorption during irradiation and resultant high peak temperature can also induce unexpected damaging of the material and/or structure. While this ensues, the thermal stability of the material can also change significantly during laser irradiation. Compared to polymers, intermediate products of LICG, notably amorphous carbon, have significantly higher thermal stability. Therefore, if a substantial amount of amorphous carbon forms during laser irradiation, it can suppress the unexpected damaging even if there is an increase in light absorption. Moreover, as this increase in thermal stability will also allow for more energy input, graphitic products with higher crystallinity can be obtained. Nonetheless, if the energy input is excessive, damaging of the material and/or structure via oxidation and/or laser

ablation can occur regardless of the formation of thermally stable intermediates. The effects of these two aspects have been previously indicated by Chyan et al. when a CW laser beam was scanned multiple times.[82] Typically in the case of biomass-based polymers, such as bread, cardboard, and wood, the irradiation with laser fluences necessary for graphitization leads to laser ablation. On the other hand, by intentionally scanning the CW laser beam with a lower laser fluence first, a layer of non-graphitic amorphous carbon can be formed. By subsequently scanning the CW laser beam, the amorphous carbon can be further converted into graphitic carbon without laser ablation.[82] Considering that graphitization requires a certain activation energy, it can be understood that the amount of absorbed energy increased during the subsequent scan. Chyan et al. further discussed that the multiple scanning concept can be easily achieved by defocusing the CW laser beam. Chyan et al. claimed that by defocusing the CW laser beam, the laser fluence can be decreased, while increasing the beam overlap leading to the same effect as multiple scanning. Although Chyan et al. indicated the importance of laser fluence and graduation conversion of the polymer, the critical temporal aspects of LICG was not clearly indicated.

Recently, Murray, et al. conducted an orthogonal parameter study and assessed the applicability of machine learning in predicting the morphologies and properties of the structures formed by LICG.[150] Their results clearly indicated that even in the case of two parameters (i.e., laser power and scanning speed), the relationship between the laser parameter and resulting structure was highly nonlinear and required polynomial terms in the fifth order to predict with sufficient accuracy. The fact that scanning speed was involved in the nonlinearity suggests that there is a critical temporal aspect of LICG, in addition to the laser fluence; however, this aspect was not discussed, and this study was purely focused on the engineering aspect rather than the mechanisms. Just from the brief discussions above regarding the dynamic change in light absorption and thermal stability, it can be easily understood that LICG is a highly complex, multivariable process which cannot be explained solely by the energy input, or laser fluence.

2.8. Summary

In Chapter 2, the fundamentals required to discuss the experimental results in Chapters 3 to 6 were provided. This included the fundamentals regarding carbonization and graphitization, relationship between material and structural properties, light-material interactions, and laser-induced carbonization and graphitization, or LICG. The principles of LICG were discussed to consists of three steps: light absorption, bond fragmentation, and structural formation. As the LICG of polymers is governed by light-material

interactions, the absorption of light determines the total amount of energy inputted into the polymer. Therefore, the wavelength of light and the absorption coefficient of the irradiated material becomes crucial variables when discussing the results of LICG. After the photons of light are absorbed by the polymer, the fragmentation of bonds and subsequent formation of structures ensues. The fragmentation of bonds can be induced thermally and/or nonthermally, and this fragmentation results in the release of gases. Especially in the case of thermal fragmentation, as a hotspot is induced slightly below the surface, this release of gases will result in the formation of a microbubble. With the continuous release of gases, the microbubble will grow into a macrobubble and eventually explode through the surface resulting in a protruding structure. Moreover, owing to the high heating rate of LICG, structural formation occurs concurrently with gas release. This typically results in the formation of highly porous carbonaceous structures with many macro- and nano-pores. By changing the laser parameters, the rate of gas release, and resultantly, the porosity of the resulting carbonaceous structure can be tuned making LICG a highly versatile technique. However, as the light-material interactions dynamically change during the process, LICG is a highly complex and multivariable process which cannot be explained solely by the energy input, or laser fluence, and require temporal considerations.

3. Morphology of carbonaceous structures

3.1. Introduction

The specific mechanism in which carbonaceous structures form by the laser irradiation of polymers has been an issue of debate for many years with the prevailing notion of a simple photothermal conversion reaction that mainly depends on the laser fluence. However, this view has been shown to be inconsistent and Chapter 3 aims to provide a deeper understanding of the mechanisms for structural formation regarding LICG. In Section 3.2, the LICG of PDMS will be demonstrated by irradiating a CW laser beam. By examining structures formed with various combinations of laser parameters, the effect of laser parameters on structural formation will be discussed. Through this, a formation mechanism based on laser-induced defects will be proposed. As the irradiation of fs laser pulses realizes the efficient nucleation of laser-induced defects owing to the high laser intensity, in Section 3.3, a fs laser will be used for the LICG of PDMS. However, as the irradiation of a single fs laser pulse cannot induce sufficient thermalization for the conversion of cavities into carbonaceous structures, a CW laser will be used in addition to a fs laser in this section. As the implications of establishing a two-laser setup that combines both defect nucleation and thermal conversion, in Section 3.4, a high RR fs laser will be used for the LICG of PDMS. The differences in the morphologies of carbonaceous structures formed using the different lasers will be discussed, and the necessary considerations when using a high RR fs laser for LICG will be indicated.

3.2. Using a continuous wave laser

3.2.1. Materials and methods

3.2.1.1. Material preparation

A 10:1 mixture of polymer to curing agent of thermally-cured SYLGARD 184 PDMS (Dow Corning, USA) was prepared. The mixture was drop casted onto a glass slab and degassed in vacuum to remove any air bubbles trapped during the mixing procedure. Furthermore, the mixture was cured in an oven at 80℃ for 60 min to prepare PDMS sheets. The PDMS sheets prepared in this study were approximately 1 mm in thickness.

Before irradiation experiments, the surfaces of PDMS were washed with ethanol to remove any debris.

3.2.1.2. Laser irradiation

Laser irradiation experiments were conducted using a YLR-100 CW laser (IPG Photonics, USA) which generated a CW laser beam with a central wavelength of 1060 nm. The CW laser beam was focused and scanned across the top surface of the PDMS sheet using a Focus Shifter digital galvo laser scanner (Raylase GmbH, Germany).

All irradiation experiments were conducted in ambient conditions.

3.2.1.3. Characterization

Optical microscopy (OM) and confocal laser scanning microscopy (CLSM) intensity images were obtained using an LEXT confocal laser scanning microscope (Olympus, Japan). Raman spectra were obtained using a LabRAM Aramis laser-excited Raman spectrometer (Horiba, Japan). The excitation wavelength and laser power for Raman analyses were set to 532 nm and approximately 36 mW, respectively. SEM images were obtained using an Inspect F50 scanning electron microscope (FEI, USA). Prior to SEM observations, iridium coatings with a thickness of approximately 10 nm were applied by ion sputtering.

3.2.1.4. Temperature simulation

The increase in surface temperature of a PDMS sheet when irradiated by a stationary CW laser beam with a constant laser power was simulated using a 2D axisymmetric finite element model in COMSOL Multiphysics software™ (version 5.5). The default Heat Transfer in Solids module was used for the simulations, and the initial temperature was set at 293 K. Q was expressed by Eq. 3.1 as a function of r and z.

$$Q(r,z) = P\frac{A}{\pi\sigma^2}e^{-\left(\frac{r}{\sigma}\right)^2} \times e^{-Az} \qquad \text{Eq. 3.1}$$

R was assumed to be 0 for the simulations. The top surface of the PDMS sheet was set to be z = 0. The CW laser beam was irradiated at coordinates of (0,0). The simulated temperatures at (0,0) were recorded for different resident times. The material properties were assumed to be constant throughout the simulations, as the simulations at this time were focused on understanding the initial growth mechanics of defects (before considerable material conversion). To calculate the induced temperatures with more

accuracy, the dynamic change in material properties should be considered; however, are out of the scope of the current study and are a subject for future studies. Table 3.1 lists the properties, variables, and values used for the simulations.

Table 3.1 Parameters for COMSOL simulations.

Parameter	Variable	Value
Laser power	P	20, 40, 60, 80 (J/s)
Focal beam radius	σ	25 (μm)
Absorption coefficient	A	2.86 (1/cm)
Heat capacity	C_p	1460 (J/kg K)
Density	ρ	970 (kg/m^3)
Thermal conductivity	k	0.16 (J/s m K)

3.2.2. Results and discussions

3.2.2.1. Effect of laser parameters on structural formation

A CW laser beam was focused and scanned across the surface of a PDMS sheet once to pattern a line structure, or track (Figure 3.1 (a)). From the SEM images of the track patterned with 5 W, 75 mm/s, it can be observed that the track surface is highly porous and possess a flake-like morphology (Figure 3.1 (a,b)). In the case of LICG, it has been commonly discussed that the violent gas release during structural formation results in a porous morphology. The formation mechanism of the flakes will be further discussed later (Section 3.3.2.1.). To assess which parameter combinations allow for the continuous formation of tracks, CW laser beams were scanned once with different parameter combinations of laser powers and scanning speeds. The parameter combination was defined to be “continuous”, if there is a visibly continuous track 2 mm or longer in at least three out of five experiments. Parameter combinations resulting in anything else, including no visible modification of the PDMS surface, was deemed “discontinuous”. Note that material compositions and properties of the resulting structures were disregarded from defining the continuity. Figure 3.1 (c–h) shows OM and CLSM intensity images of representative discontinuous and continuous structures patterned with a constant laser power of 80 W. From the OM images (Figure 3.1 (a–c)), it can be observed that the surface of the transparent PDMS sheet was modified into a visibly black-colored material after laser scanning, suggesting carbonization. For a scanning speed of 720 mm/s (Figure 3.1 (c)), 480 mm/s (Figure 3.1 (d)), and 240 mm/s (Figure 3.1 (e)), the formation

of a defect, island, and a track is observed, respectively. From the CLSM intensity images (Figure 3.1 (d–f)), especially for those of defects (Figure 3.1 (d)), it is clearly shown that the structures are 3D and slightly protruding from the surface. As discussed in Section 2.6., hot spots are induced a few μm below the surface due to the environment-polymer surface boundary effects.[112,155,156] As the polymer is fragmentated, a microbubble filled with gaseous products will form below the surface. With continued laser irradiation, the microbubble will expand into a macrobubble, and eventually explode through the polymer surface, resulting in a protruding defect.[155] As the surrounding polymer is stretched due to the formation of the protruding defect, a mechanical stress will be oriented circularly around the structure.[159] Since wrinkling will be induced perpendicularly to the direction of mechanical stress, the wrinkles will be oriented radially from the structures as observed in Figure 3.1 (c–h).

The type of structure formed for each laser power and scanning speed parameter combination is summarized in Figure 3.1 (i). It is observed that the scanning speed required for the continuous formation of tracks tends to increase as the laser power is increased. However, it can be observed that the parameter combinations which yield continuous formation cannot be determined solely from the laser fluence *F*, which can be calculated using Eq. 3.2.

$$F = \frac{P}{v \cdot 2\sigma} \qquad \text{Eq. 3.2}$$

where *v* is the scanning speed. Note that the focal beam radius was fixed at 50 μm in this study. With the same laser fluence, continuous tracks were able to be formed with low laser power and slow scanning speed parameter combinations, whereas tracks could not be formed with high laser power and fast scanning speed parameter combinations. The results of Figure 3.1 (i) clearly indicates that the resulting structure does not strictly depend on the combined parameter of laser fluence, consistent with the discussions in Section 2.7., but rather on the scanning speed, or the resident time of the CW laser beam.

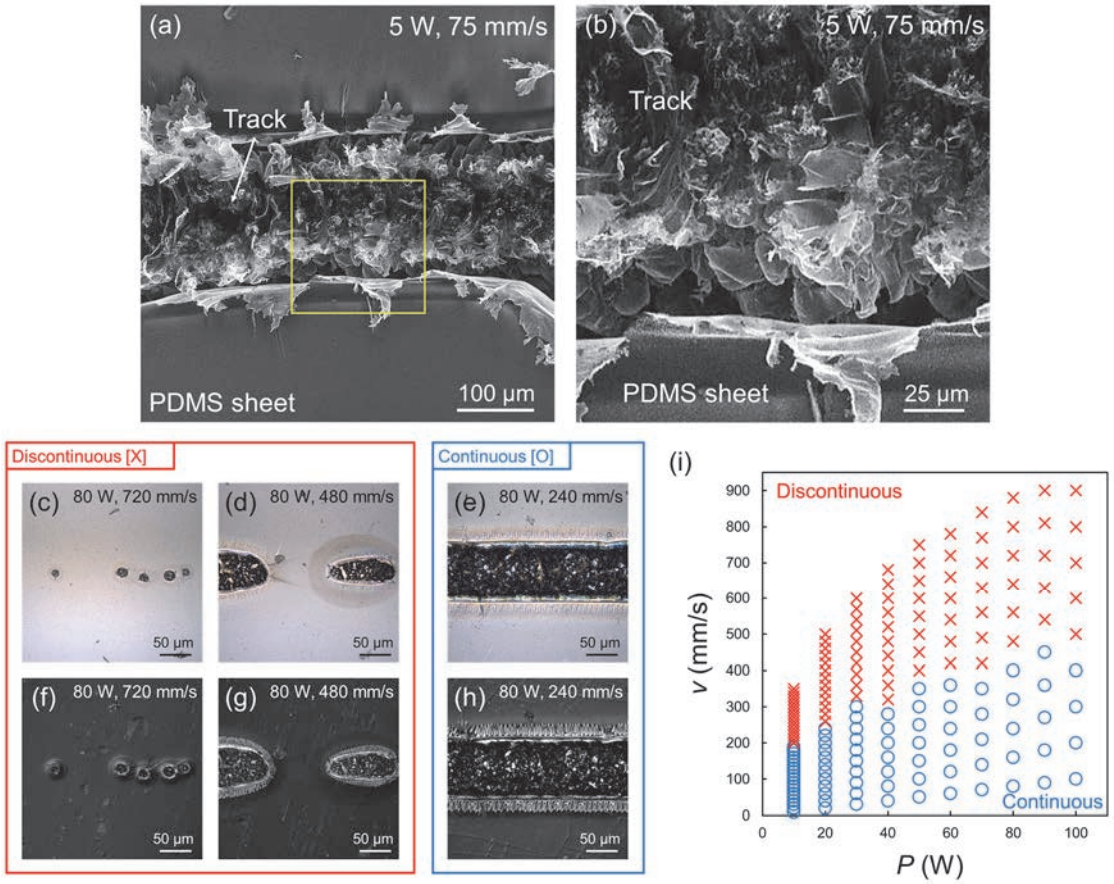

Figure 3.1 (a) SEM image of a continuous track patterned with a laser power and scanning speed of 5 W and 75 mm/s, respectively. (b) Enlarged SEM image of the area indicated by the yellow square in (a). Respective OM and CLSM intensity images of structures formed with ((a) and (d)) 720 mm/s, ((b) and (e)) 480 mm/s, and ((c) and (f)) 240 mm/s, with a constant laser power of 80 W. (g) Structural formation for different combinations of laser power and scanning speed. Discontinuous and continuous combinations are indicated by red crosses and blue circle markers, respectively.

3.2.2.2. Temporal evolution of carbonaceous structures

To shed some light on the effect of resident time on structure formation, a stationary CW laser beam was irradiated onto the surface of a PDMS sheet and the resident time was changed. Figure 3.2 (a–e) shows OM images of structures formed with different resident times with a constant laser power of 40 W. At 90 µs, the formation of a defect smaller than the focal beam diameter ($2\sigma \approx 50$ µm), with a polymeric flap (indicated by A), is observed on the surface (Figure 3.2 (b)). As the resident time is increased, the defect grows in diameter (Figure 3.2 (c)), and the emergence of evident bubble-like bumps are observed on the defect surface (indicated by B) (Figure 3.2 (d,e)). Moreover, the surfaces

neighboring the defects (Figure 3.2 (b–e)) are considerably contaminated compared to before laser irradiation (Figure 3.2 (a)), possibly due to the ejection of debris during explosive formation (indicated by C). These observations are consistent with the theoretical mechanism discussed in Section 2.6. regarding structural formation. The filled circles in Figure 3.2 (f) shows the experimentally measured diameters of the defects formed at different resident times with various laser powers. For all laser powers, the defects significantly grew in diameters at a critical resident time, $t_{critical}$ (indicated by the black asterisks in Figure 3.2 (f)). Moreover, the increase in diameter after $t_{critical}$ was linearly related to $t^{1/2}$ (inset Figure 3.2 (f)). This linear increase in diameter after $t_{critical}$ is expected, as defect growth beyond the focal beam diameter is driven by radial diffusion of thermal energy, and should correspond to the thermal diffusion length l_d, which is approximated with Eq. 3.3 as.

$$l_d = \frac{d}{2} = \sqrt{4\alpha t} \qquad \text{Eq. 3.3}$$

where α is the thermal diffusivity of the material. From the results shown in the inset of Figure 3.2 (f), α can be calculated to be approximately 0.9 cm^2/s, which agrees with the thermal diffusivity of pristine PDMS which is approximately 1.1 cm^2/s.

Since the growth mechanics of the defects are closely related with thermal effects,[160] the time-dependent temperature change in the PDMS surface resulting from the irradiation of a stationary CW laser beam with a constant laser power was simulated using COMSOL. The properties of the target material, in this case PDMS, were set to be constant throughout the simulation. The increase in peak temperature with respect to resident time for each laser power is plotted in Figure 3.2 (f) as dashed lines. PDMS starts carbonizing at a temperature of approximately 600 K, and starts graphitizing into crystallites of graphitic carbon within a temperature range of 1100 K to 1300 K.[123] Accordingly, $t_{critical}$ coincides with the critical translation time in which the temperature shifts from the carbonization temperature (indicated as the orange region) to the graphitization temperature (indicated as the blue region). In other words, the defects significantly grow in size when the temperature induced by laser irradiation reaches the temperature threshold for graphitization. As graphitic carbon forms, the properties of the irradiated material, specifically the absorption coefficient, increases substantially from approximately 3 cm^{-1} for pristine PDMS[87] to 40000 cm^{-1} for graphite[161]. This will result in a drastic increase in the absorbed laser energy, and a sudden increase in defect size.

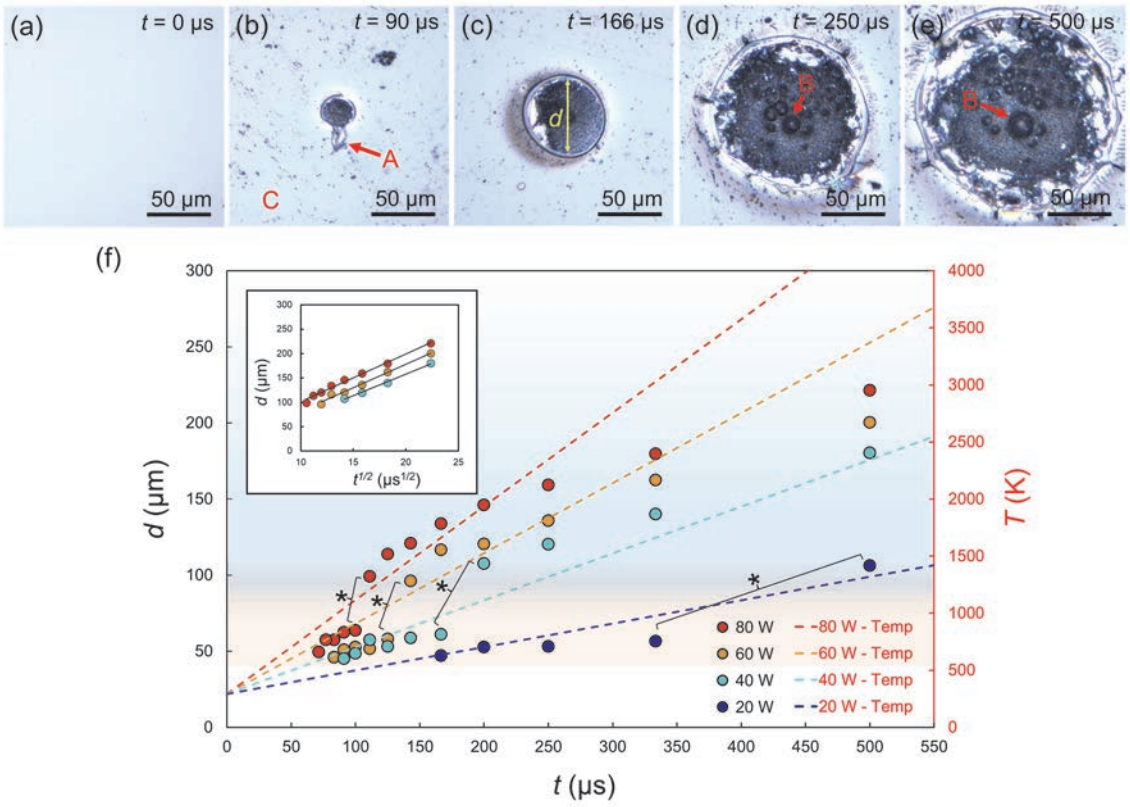

Figure 3.2 OM images of defects formed with resident times of t = (a) 0 µs, (b) 90 µs, (c) 166 µs, (d) 250 µs, and (e) 500 µs, with a constant laser power of 40 W. Black asterisks indicate the $t_{critical}$ for each laser power. (f) Experimentally measured diameters of defects formed with different laser powers and resident times. Dashed lines indicate the peak temperatures with respect to resident time simulated with COMSOL for different laser powers. Inset shows the measured diameters of defects for resident times greater than $t_{critical}$ with respect to $t^{1/2}$.

To investigate if the COMSOL temperature simulations align with the actual resulting material due to laser irradiation, material analyses were conducted on the defects. Figure 3.3 (a) shows Raman spectra obtained from the defects formed at different resident times with a constant laser power of 40 W. The Raman peaks and their originating bonds for pristine PDMS are listed in Table 3.2. Note that each spectrum was normalized with respect to its individual raw maximum intensity measured for the peak originating from the methyl groups at 2800 cm^{-1} to 3000 cm^{-1}, hereon referred to as the m band. For resident times shorter than 166 µs, only PDMS-related peaks are confirmed, indicating no significant graphitization of the material. At a resident time of 200 µs, the emergence extremely weak peaks are observed at 1350 cm^{-1} and 1580 cm^{-1}. Such peaks are commonly referred to as the D and G bands and originate from out-plane vibrational modes of defects and edge functional groups of sp^2-hybridized carbon domains, and in-

plane vibrational modes of sp^2-hybridized carbon domains, respectively.[162] For resident times of 200 μs and 250 μs, a significant increase in the relative intensities of the D and G bands, as well as the emergence of broad peaks at 860 cm^{-1} and 2700 cm^{-1} are observed. The 860 cm^{-1} peak originates from vibration modes of SiC, and is consistent with previous results indicating the formation of SiC-NCs due to the thermal treatment of PDMS.[163] The fact that sharp transverse optical and longitudinal optical vibration modes of SiC cannot be distinguished indicates that the formed SiC-NCs are extremely small or highly defective.[163] The 2700 cm^{-1} peak is commonly referred to as the 2D band, and originates from the second-order resonance modes of sp^2-hybridized carbon domains.[164] The emergence of the broad symmetrical 2D band suggests that the graphitic carbon is multilayered and turbostratic in orientation, consistent with previous results regarding the LICG of polymers.[165,166] The emergence of the strong D and G bands, in addition to the 2D band, after resident times of 200 μs and longer, is consistent with the COMSOL results suggesting the transition into the graphitization temperature.

Table 3.2 Typical Raman peaks of pristine PDMS.

Wavenumber (cm^{-1})	Originating bond
488	Si-O-Si symmetric stretching
687	Si-C symmetric rocking
708	Si-C symmetric stretching
787	Si-C asymmetric stretching
1262	Si-C symmetric bending
1412	Si-C asymmetric bending
2907	C-H symmetric stretching
2965	C-H asymmetric stretching

Figure 3.3 (b) shows the relative intensities of the m band I_m and the G band I_G for each resident time. The I_m and I_G values for each resident time were normalized with respect to the raw I_m and I_G values for a resident time of 90 μs. Although significant differences in the shape of the spectra could not be distinguished for resident times shorter than 166 μs, a gradual decrease in I_m is observed with an increase in resident time, suggesting progressive fragmentation of methyl bonds by laser irradiation and the carbonization of PDMS. As the resident time is further increased to 250 μs, I_m continues to decrease to less than 1% of the initial intensity at 90 μs. Contrarily, an increase in the I_G is observed with the increase in resident time. For resident times of 143 μs and 166 μs, slight increases in relative I_G are observed. Considering the extremely weak intensity, this is indicative of the formation of amorphous carbon domains within a polymeric matrix rather than

formation of distinct crystalline graphitic domains.[123,167] For resident times of 200 μs and 250 μs, a comparably higher I_G is observed, indicating the formation of larger distinguished graphitic domains. The critical time in which significant transformation in material composition to graphitic carbon occurs, suggested by the large change in I_G, matches well with $t_{critical}$ for the significant growth of defects (Figure 3.2 (f) and Figure 3.3 (b)).

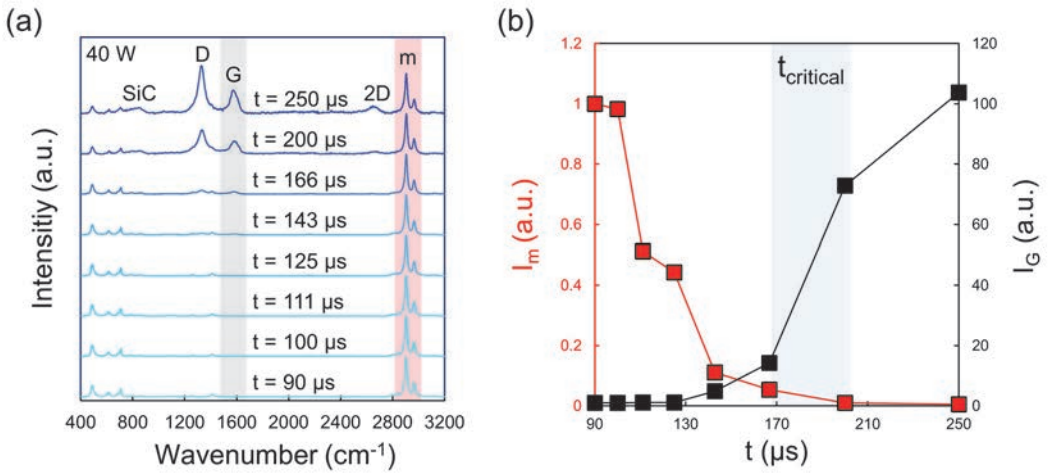

Figure 3.3 (a) Raman spectrum of defects formed with different resident times. Each spectrum was normalized with respect to its individual raw I_m value. (b) Relative I_m and I_G for each resident time. I_m and I_G values for each resident time were normalized with respect to the raw I_m and I_G value for a resident time of 90 μs.

Table 3.3 summarizes the times where growths of defects $t_{critical}$ were observed in Figure 3.2 (f), scanning speeds where shifts from discontinuous to continuous structures $v_{continuity}$ were observed in Figure 3.1 (b), and assumed resident times $t_{continuity}$ calculated from $v_{continuity}$ for each laser power.

Table 3.3 Summary of resident times.

P (W)	$t_{critical}$ (μs)	$v_{continuity}$ (mm/s)	$t_{continuity}$ (μs)
80	100–111	480–400	104–125
60	125–142	420–360	119–139
40	166–200	320–280	156–179
20	250–333	260–240	192–208

In the case of laser powers of 80 W, 60 W, and 40 W, $t_{critical}$ matches well with $t_{continuity}$, and suggests that continuous track formation occurs when the temperature reaches that for the initiation of graphitization. However, in the case of a laser power of 20 W, $t_{critical}$

is significantly longer than $t_{continuity}$, suggesting temperature lower than the graphitization temperature are sufficient for the formation of continuous tracks.

3.2.2.3. Proposal of a mechanism based on laser-induced defects

A formation mechanism which explains the difference in resident times required for continuous track formation is proposed in Figure 3.4.

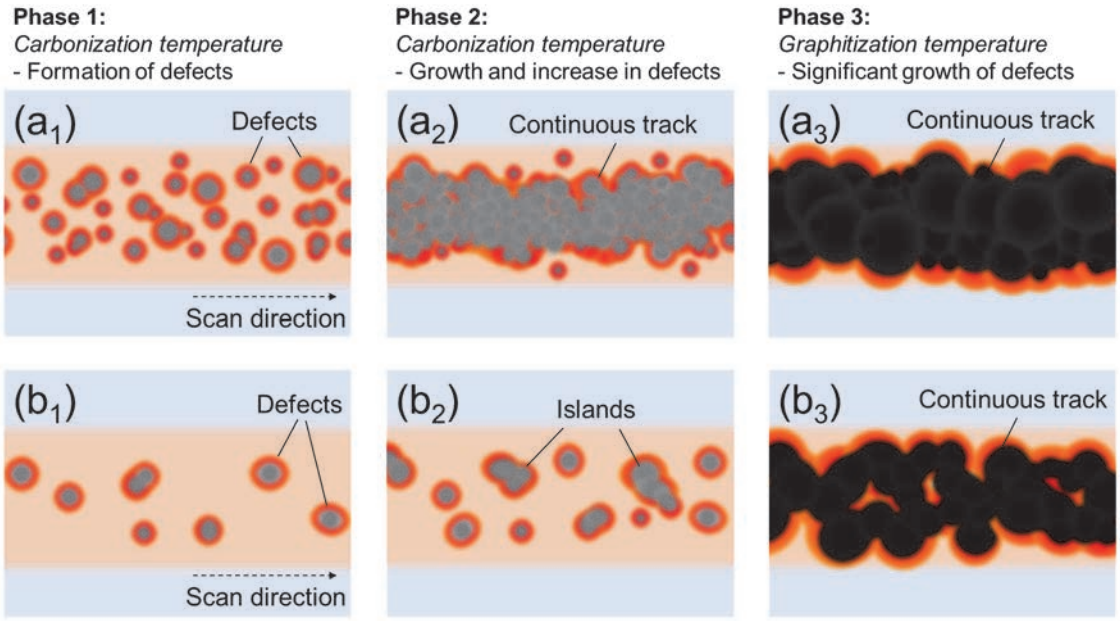

Figure 3.4 Schematic of the proposed formation mechanism of continuous tracks in the case of (a) slow and (b) fast heating by laser irradiation. Subscripts correspond to the respective phases.

Scanning of the PDMS surface by a CW laser beam will induce an increase in temperature, in which the total increase in temperature should depend on the laser fluence. Considering the same laser fluence, low laser powers and slow scanning speed parameter combinations will induce slower heating of the PDMS sheet surface compared to high laser power and fast scanning speeds parameter combinations. As the PDMS sheet is heated to the carbonization temperature, the material will undergo thermal fragmentation and the formation of bubbles below the surface will initiate the nucleation of a protruding defect (Phase 1). Such defects will be initially scattered as nucleation is inhomogeneous.[168] In the case of slow heating (Figure 3.4 (a_1)), as there is sufficient time for the nucleation of laser-induced defects, the overall number of defects will be greater than in the case of fast heating (Figure 3.4 (b_1)). As the PDMS sheet is further heated, the preexisting defects will act as initiation sites and slightly grow in size. Moreover, the

number of defects will steadily increase due to additional nucleation. As the defects come into contact with neighboring defects, they will merge to form larger structures (Phase 2). In the case of slow heating, since the density of defect formation is high, the merging of neighboring defects will result in a continuous track (Figure 3.4 (a_2)). On the contrary, in the case of fast heating, since the density of defect formation is low, the merging of neighboring defects will only result in a discontinuous island (Figure 3.4 (b_2)), as observed in Figure 3.1 (b). Once the temperature reaches the graphitization threshold, the defects will significantly grow in size, further bridging neighboring unmerged structures (Phase 3). Unlike the case of slow heating, in the case of fast heating, the exponential growth in defect size owing to graphitization is required to compensate for the low defect density in order to achieve a continuous track (Figure 3.4 (b_3)). Due to the differences in defect densities, the resulting graphitic track in Phase 3 is expected to be more uniform and denser in the case of slow heating (Figure 3.4 (a_3)) compared to fast heating (Figure 3.4 (b_3)).

3.2.2.4. Validation of proposed formation mechanism

To validate the proposed formation mechanism, structures formed by relatively slow heating and fast heating were compared. Material analyses preformed on structures formed with assumed temperatures in the carbonization temperature (low laser fluence), are shown in Figure 3.5 (a–c). For 20 W, 200 mm/s (slow heating), the formation of a continuous track can be observed (Figure 3.5 (a)). On the other hand, for 80 W, 800 mm/s (fast heating), the formation of discontinuous defects can be observed (Figure 3.5 (b)). However, comparing the Raman spectra obtained from the structures, it is revealed that the material compositions of the track and defects are comparable (Figure 3.5 (c)). Moreover, the relatively low I_G and high I_m supports the assumption that the induced temperatures are in the carbonization temperature. These results clearly support the differences in Phase 2 between slow and fast heating illustrated in Figure 3.4 (a_2) and Figure 3.4 (b_2), respectively.

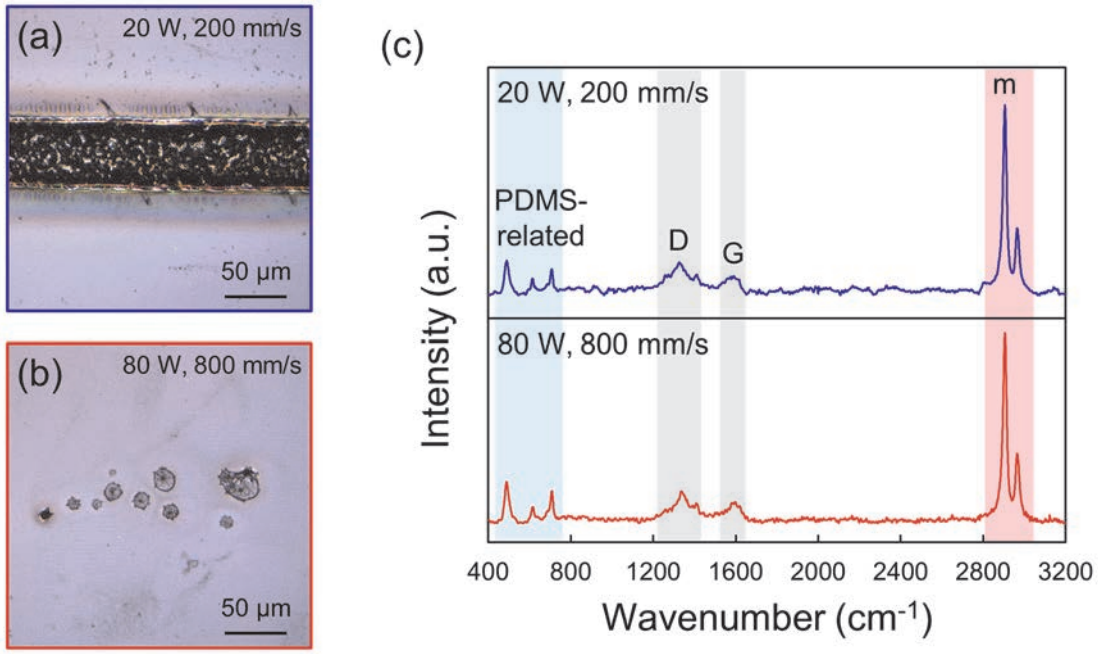

Figure 3.5 OM images of the structure formed with (a) 20 W, 200 mm/s and (b) 80 W, 800 mm/s. (c) Raman spectrum of structures shown in (a) and (b).

Next, material analyses preformed on structures formed with assumed temperatures in the graphitization temperature (high laser fluence), are shown in Figure 3.6. Compared to the structures in Figure 3.5 (a), all structures are visibly continuous regardless of parameter combinations (Figure 3.6 (a–d)). For 20 W, 80 mm/s (slow heating), the entirety of the track appears black colored (Figure 3.6 (a)). However, as the laser power and scanning speed increase (shift towards faster heating), non-black-colored regions start to emerge (Figure 3.6 (b–d)). Moreover, for 80 W, 320 mm/s (Figure 3.6 (d)), the black-colored regions are distributed in patches (red circles). Figure 3.6 (e–h) shows 2D Raman intensity maps with regards to I_m for a 72 μm × 72 μm area. The bright regions represent a high I_m, indicating a low degree of graphitization, whereas dark regions represent a low I_m, suggesting a high degree of graphitization. For the Raman intensity map of 20 W, 80 mm/s (Figure 3.6 (e)), the whole field-of-view is dark, suggesting high degree of graphitization of the entire area. As the laser power and scanning speed increase (Figure 3.6 (f–h)), bright regions start to emerge. The bright regions observed in the Raman intensity maps corresponded to the non-black-colored boundaries observed in the OM images. For the Raman intensity map of 80 W, 320 mm/s (Figure 3.6 (h)), dark regions, or graphitic structures, are observed as dark patches (yellow arrows), consistent with OM observations (Figure 3.6 (d)). These results clearly support this difference in Phase 3 between slow and fast heating mentioned in Figure 3.4 (a_3) and Figure 3.4 (b_3),

respectively.

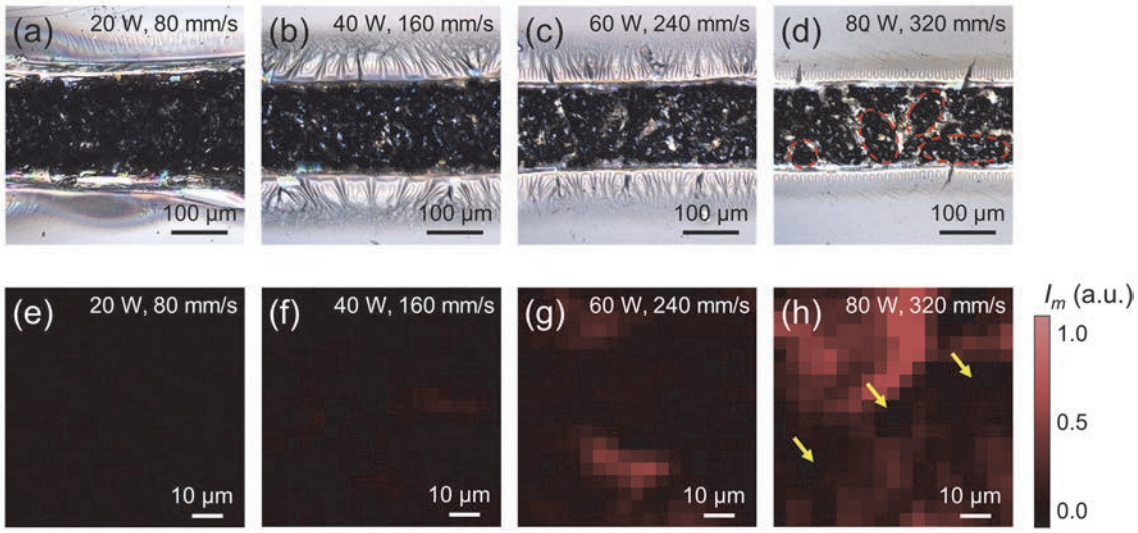

Figure 3.6 Respective OM images and Raman intensity maps of structures formed with ((a) and (e)) 20 W, 80 mm/s, ((b) and (f)) 40 W, 160 mm/s, ((c) and (g)) 60 W, 240 mm/s, and ((d) and (h)) 80 W, 320 mm/s. Mapping intensity is normalized with respect to the highest I_m recorded for 80 W, 320 mm/s. Each pixel of the map is 4 µm, and the total area of each map is 72 µm × 72 µm.

Comparing the Raman spectra of the graphitized black-colored regions of 80 W, 320 mm/s and 20 W, 80 mm/s (Figure 3.7), evident differences in the spectra can be observed. Firstly, the m band peak, as well as other PDMS-related peaks, are virtually absent in the case of 20 W, 80 mm/s, suggesting minimal residual PDMS. Secondly, the 2D band peak is slightly sharper and stronger in the case of 20 W, 80 mm/s. Generally, in the case of turbostratic graphite, thinner 2D band peaks and higher intensity ratios between the 2D and G band I_{2D}/I_G suggest a greater vertical dimension (i.e., more layers) of the graphitic carbon.[169,170] Comparing the full width at half-maximum (FWHM) of the 2D band and the I_{2D}/I_G, it can be inferred that the vertical dimensions of the graphitic carbon are greater in the case of 20 W, 80 mm/s, indicating the formation of thicker graphitic carbon crystals. Therefore, it can be inferred that graphitization of PDMS progressed with 20 W, 80 mm/s compared to 80 W, 320 mm/s, although the laser fluence was constant. For slow heating (i.e., 20 W, 80 mm/s), continuous tracks form at an earlier time than for fast heating (i.e., 80 W, 320 mm/s) as illustrated in Figure 3.4. As the material converts into carbonaceous material, the absorption coefficient of the material increases dynamically and thus the attained peak temperatures in the case of slow heating will become relatively higher than fast heating even if the energy input is constant. This is consistent with the nonlinearity of LICG previously discussed (Section 2.7.). Moreover, the intensity ratio between the D

and G band (I_D/I_G) can be used to approximate the lateral dimensions L_a of the graphitic carbon by Eq. 3.4 as,

$$L_a = (2.4 \times 10^{-10}) \times \lambda^4 \times (I_D/I_G)^{-1} \quad \text{Eq. 3.4}$$

where, λ is the excitation wavelength during Raman analyses.[162] According to this, when comparing the I_D/I_G of the two spectra, it is indicated that the lateral dimensions (i.e., *ab* direction) of the graphitic carbon formed are similar, although the vertical dimensions (i.e., *c* direction) are different. This preferential growth of the graphitic carbon in the *c* direction over the *ab* direction is consistent with the principles of carbonization and graphitization discussed in Section 2.2. and suggests the LICG process is in Phase B-1 of Figure 2.1.

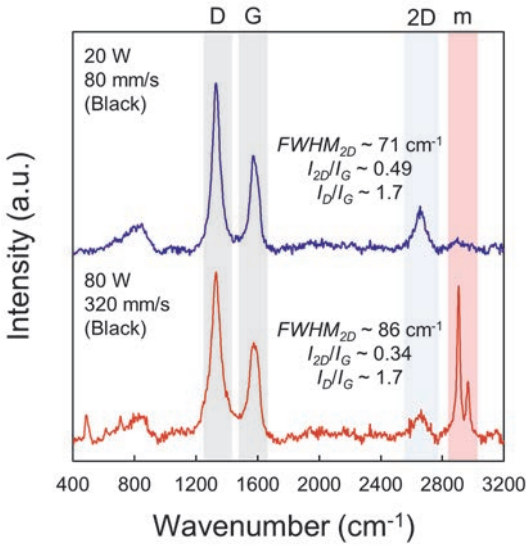

Figure 3.7 Raman spectra obtained from the observed black-colored regions of 80 W, 320 mm/s (red) and 20 W, 80 mm/s (blue). The spectrum is obtained from the region which indicated the highest I_G within the black-colored regions.

Thus far, it has been discussed that the continuous tracks are a result of the merging of smaller defects. In other words, even with parameter combinations that result in discontinuous structures, continuous tracks should be obtainable by increasing the defect density via multiple laser scans. By forming defects with the first scan, such defects can function as initiation sites for the second scan, and the formation process can start at Phase 2 of the proposed model (Figure 3.4). Figure 3.8 (a–c) shows OM images of structures formed with multiple scans for a constant parameter combination of 80 W, 800 mm/s. With 1 scan (Figure 3.8 (a)), the formation of scattered defects can be observed. As the number of scans increase (Figure 3.8 (b,c)), a gradual growth of structure into a continuous track can be observed. The multi-parameter orthogonal experiment was

repeated with multiple scans, and the type of structure formed for each parameter combination is summarized in Figure 3.8 (d). As the number of scans increase, the parameter combinations which yield continuous formation increases, particularly for higher laser powers and faster scanning speeds. Moreover, in the case of multiple scans, it can be observed that the parameter combinations which yield continuous formation can be determined from laser fluence. The results thus far clearly indicates that the processing speed limit for the formation of continuous tracks is restrained due to the time required for the nucleation and growth of laser-induced defects.

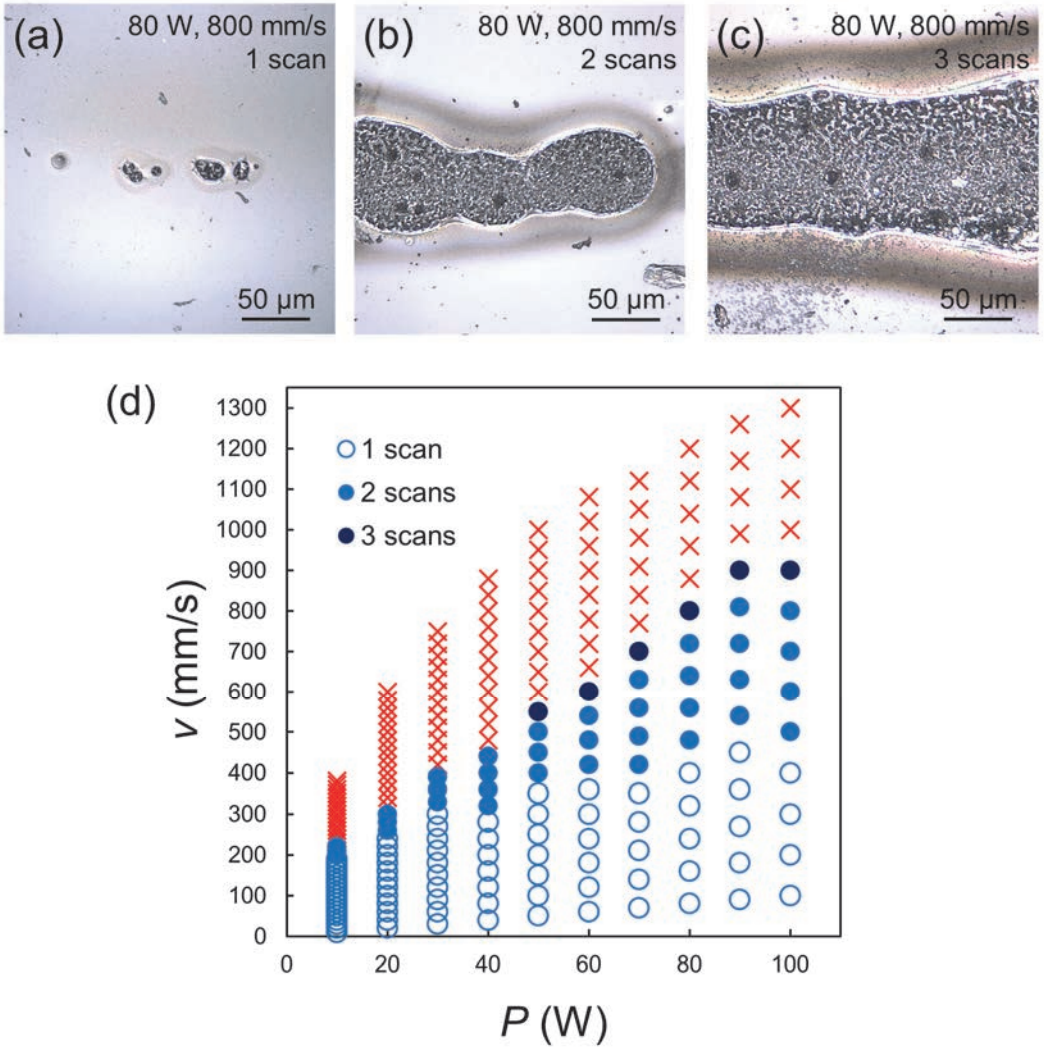

Figure 3.8 OM images of structures formed with (a) 1, (b) 2, and (c) 3 laser scans, for a constant parameter combination of 80 W, 800 mm/s. (d) Structural formation for different laser power and scanning speed combinations, with different number of laser scans. Structural formation for different laser power and scanning speed combinations. Discontinuous and continuous combinations are indicated by red crosses and blue circle markers, respectively.

3.3. Using a femtosecond and continuous wave laser

3.3.1. Materials and methods

3.3.1.1. Material preparation

A 10:1 mixture of polymer to curing agent of thermally-cured SYLGARD 184 PDMS (Dow Corning, USA) was prepared. The mixture was drop casted onto a glass slab and degassed in vacuum to remove any air bubbles trapped during the mixing procedure. Furthermore, the mixture was cured in an oven at 80℃ for 60 min to prepare PDMS sheets. The PDMS sheets prepared in this study were approximately 1 mm in thickness. Before irradiation experiments, the surfaces of PDMS were washed with ethanol to remove any debris.

3.3.1.2. Laser irradiation

Fs-LDW laser irradiation experiments were conducted using a Solstice Ace fs laser (Spectra Physics, USA) which generated 100-fs laser pulses with a central wavelength of 800 nm at a RR of 1 kHz. Laser pulses were focused onto the top surface of the PDMS sheet using a 10× objective lens, with a numerical aperture (NA) of 0.25. The defocusing method was not used for the patterning of all structures in this section, and the energy per laser pulse, or pulse energy (PE), was 20 μJ. A three-axis (*xyz*) translation stage was utilized to scan laser pulses in three dimensions.

CW-LDW laser irradiation experiments were conducted using a YLR-100 CW laser (IPG Photonics, USA) which generated a CW laser beam with a central wavelength of 1060 nm. The CW laser beam was tightly focused and scanned across the top surface of the PDMS sheet using a Focus Shifter digital galvo laser scanner (Raylase GmbH, Germany).

All irradiation experiments were conducted in ambient conditions.

3.3.1.3. Characterization

OM images were obtained using an LEXT confocal laser scanning microscope (Olympus, Japan). Raman spectra were obtained using a LabRAM Aramis laser-excited Raman spectrometer (Horiba, Japan). The excitation wavelength and laser power for

Raman analyses were set to 532 nm and approximately 36 mW, respectively. SEM images were obtained using an Inspect F50 scanning electron microscope (FEI, USA). Prior to SEM observations, iridium coatings with a thickness of approximately 10 nm were applied by ion sputtering.

3.3.2. Results and discussions

3.3.2.1. Implications of using a fs laser for defect nucleation

In order to further validate the importance of defects on the formation of continuous tracks, defects were intentionally introduced to the PDMS surface by irradiating fs laser pulses (Figure 3.9 (a)), prior to the scanning of a CW laser beam (Figure 3.9 (b)).

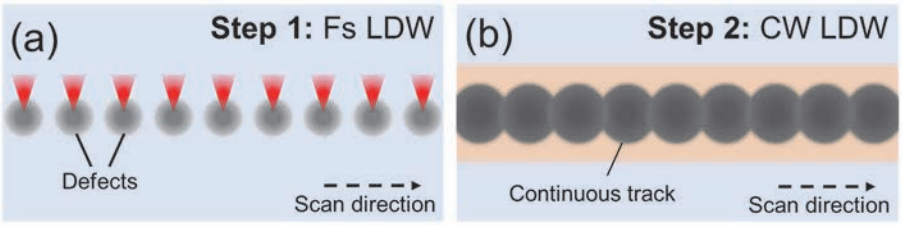

Figure 3.9 Two-laser LDW technique in which (a) first, fs laser pulses are scanned to mark defects, (b) then, a CW laser beam is traced to form a continuous track.

Figure 3.10 (a) shows a SEM image of an array of defects marked with a spacing of *s* on the surface of a PDMS sheet via fs LDW. Each defect was formed by the irradiation of a single fs laser pulse. From the Raman spectra obtained from various locations of the defect, the formation of graphitic carbon was not confirmed by the irradiation of a single fs laser pulse (Figure 3.10 (b,c)). Moreover, the visible surface of the defect formed by the irradiation of fs laser pulses (Figure 3.10 (b)) were significantly smoother than those formed by the irradiation of a CW laser beam (Figure 3.10 (d)). This may suggest that the formation mechanism of the defects is different depending on the laser used. In the case of a CW laser, it is expected that the defects formed as a result of the explosion of the below-surface macrobubble (Section 2.6.3.). On the other hand, in the case of a fs laser, it can be expected that the defects were formed by non-thermal laser ablation (i.e., coulomb explosion), without significant thermalization (discussions in Section 2.5.4.). Consistent with this assumption, a polymeric flap, as those observed for the defect formed by irradiation of a CW laser beam (Figure 3.10 (d)), is not observed for a defect formed by the irradiation of a fs laser pulse (Figure 3.10 (b)).

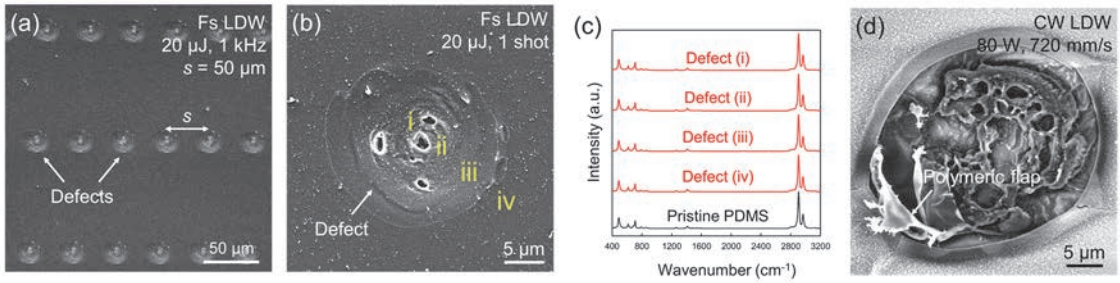

Figure 3.10 SEM images of (a) an array of defects and (b) a single defect formed by fs LDW. (c) Raman spectra obtained from the fs-LDW defect. (d) SEM image of a defect formed by CW LDW.

Although a continuous track could not be formed with a parameter combination of 80 W, 800 mm/s in the case of an un-marked PDMS surface (Figure 3.1 (g)), a continuous track was successfully formed along the defects in the case of the marked PDMS surface (Figure 3.11 (a)). Moreover, the Raman spectra obtained from the track indicates the formation of graphitic carbon; suggesting the successful thermal conversion of the defect into a carbonaceous structure by the subsequent scanning of a CW laser beam (Figure 3.11 (b)). Therefore, it is demonstrated that the formation threshold for continuous carbonaceous tracks was lowered due to the initial introduction of laser-induced defects on the PDMS surface. It is suggested that a continuous carbonaceous track was successfully patterned even with a parameter combination of 80 W, 800 mm/s in the case of a marked PDMS surface due to slight alterations in the PDMS surface due to pulse irradiation, such as the absorption properties. However, the surface morphology of the track patterned using two lasers (Figure 3.11 (b)) is significantly less flaky compared to the track patterned using only a CW laser (Figure 3.1 (a)). This difference in the surface morphology will be discussed later (Section 3.4.2.1.).

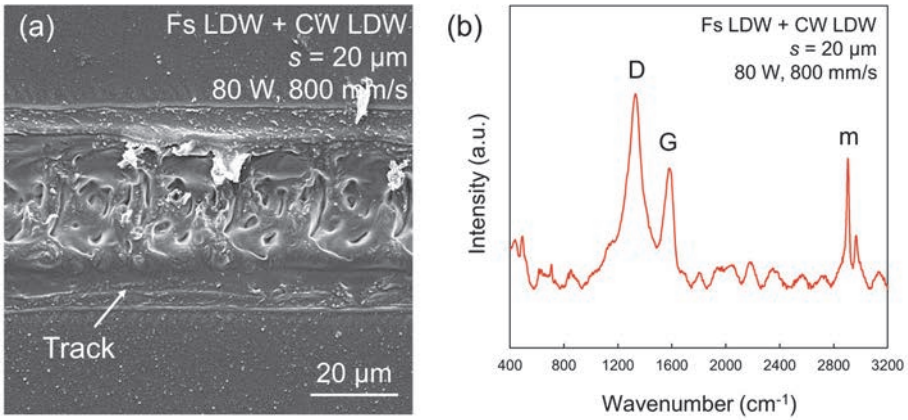

Figure 3.11 (a) SEM image of a continuous track formed by the scanning of a CW laser beam over fs-LDW defects. (b) Raman spectra obtained from the continuous track indicating evident graphitization.

The relationship between the defect spacing for fs LDW, and the laser power and scanning speed of CW LDW determined if the resulting structure was continuous or not (Figure 3.12 (a–c)). For example, for a constant laser power, the defect spacing required for continuous track formation decreased with an increase scanning speed of the CW laser beam (Figure 3.9 (a–f)). This is expected as the increase in scanning speed will decrease the laser fluence for CW LDW, resulting in smaller growths of the defects to become continuous. Nonetheless, this demonstration of the two-laser LDW technique evidently shows that the temporal aspect of LICG, and furthermore, indicates that the processing scanning speed is limited by the nucleation of defects, in addition to the growth kinetics of structures.

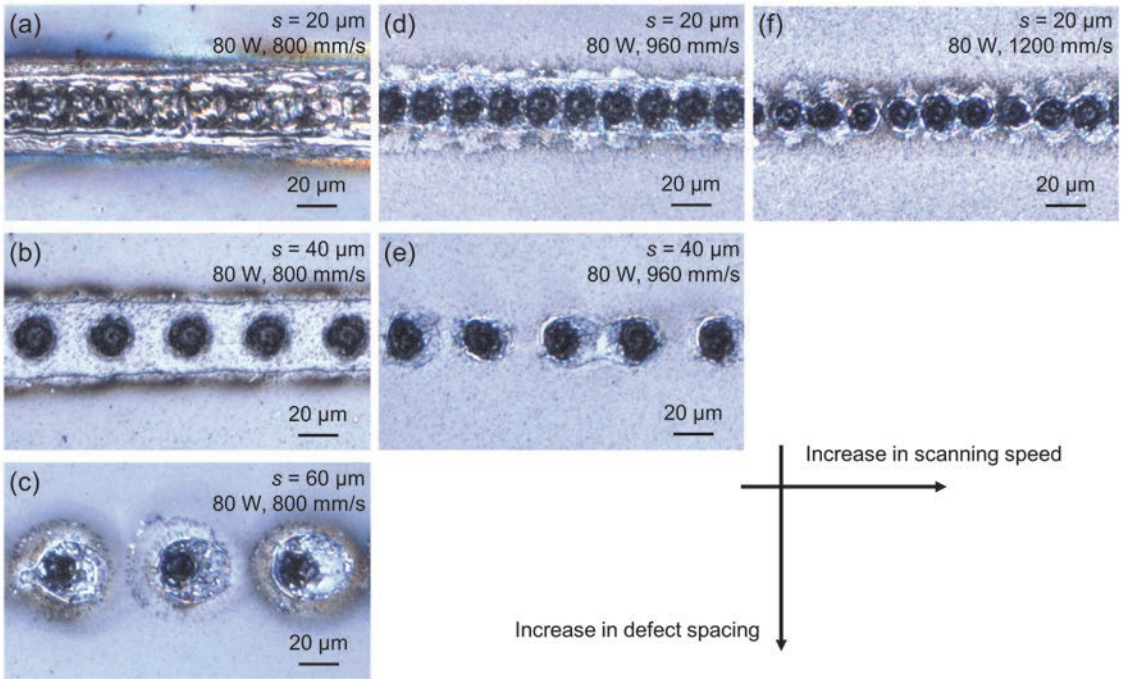

Figure 3.12 OM images of structures formed by CW LDW with defect spacings *s* and scanning speeds of (a) 20 µm, 800 mm/s, (b) 40 µm, 800 mm/s, (c) 60 µm, 800 mm/s, (d) 20 µm, 960 mm/s, (e) 20 µm, 960 mm/s, and (f) 20 µm, 1200 mm/s, for a constant laser power of 80 W.

3.3.2.2. Discussions on the processing limits

The current results shows that the temporal limitations for the formation of continuous carbonaceous tracks can be significantly improved by the intentional introduction of laser-induced defects via fs LDW. Therefore, for example, by designing an optical setup which incorporates a fs laser system for defect formation and a CW laser system for thermal conversion into the same beam path the current processing limits may be

overcome. According to Figure 3.13, the necessary condition for the formation of continuous tracks for such a technique can be expressed by Eq. 3.5 as,

$$2x + \Delta x \geq s \qquad \text{Eq. 3.5}$$

where x is the radius of the defect and Δx is the radial growth in size from the edge of the defect.

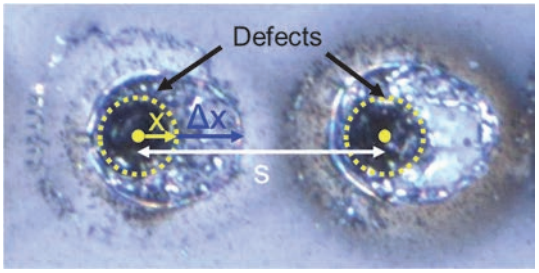

Figure 3.13 OM images of structures indicating the necessary condition for the formation of continuous tracks.

The initial size and spacing of the defects, will be determined by fs LDW, and can be approximated by Eq. 3.6 and Eq. 3.7 as,

$$x = \frac{R_{fs}}{\sqrt{2}}\sqrt{\ln\left(\frac{F_{fs}}{F_{th}}\right)} \qquad \text{Eq. 3.6}$$

$$s = \frac{v_{fs}}{f} \qquad \text{Eq. 3.7}$$

where R_{fs} is the focal beam radius, F_{fs} is the laser fluence, v_{fs} is the scanning speed, and f is the RR of the fs laser system. F_{th} is the laser fluence threshold for ablation, and will be dependent on the target material.

The radial growth in size will be determined by CW LDW, and more specifically the temperature gradient induced by laser irradiation. The temperature gradient induced due to heating of the defect as a function of distance $T(r)$ can be expressed Eq. 3.8 by as,

$$T(r) = T_{\mathrm{CW}} e^{-\left(\frac{r}{\sqrt{4\alpha t}}\right)^2} \qquad \text{Eq. 3.8}$$

where T_{CW} is the peak temperature induced at the defect and t is the resident time of the CW laser beam. Note that the temperature induced within the defect is approximated to be constant for this case.

To determine the position of the growth front r_{growth}, the r when the temperature reaches the threshold for modification T_{th} needs to be solved. Eq. 3.8 can be rewritten as,

$$r_{growth} = \sqrt{4\alpha t \ln\frac{T_{CW}}{T_{th}}} \quad \text{Eq. 3.9}$$

Moreover, r_{growth} will be greatest for a maximum resident time *t'*. *t'* will be determined by the focal beam radius R_{CW} and the scanning speed v_{CW} of the CW laser system as expressed by Eq. 3.10 as,

$$t' = \frac{2R_{CW}}{v_{CW}} \quad \text{Eq. 3.10}$$

By substituting Eq. 3.10 to Eq. 3.9, the maximum growth distance Δx can be determined as,

$$\Delta x = \sqrt{4\alpha \frac{2R_{CW}}{v_{CW}} \ln\frac{T_{CW}}{T_{th}}} \quad \text{Eq. 3.11}$$

Substituting *x* and *s* expressed as Eq. 3.6 and Eq. 3.7, respectively, as well as Δx expressed as Eq. 3.11 into the initial condition for the formation of continuous tracks expressed as Eq. 3.5 gives,

$$\frac{2\mathrm{R}_{fs}}{\sqrt{2}}\sqrt{\ln(\frac{F_{fs}}{F_{th}})} + \sqrt{4\alpha \frac{2R_{CW}}{v_{CW}} \ln\frac{T_{CW}}{T_{th}}} \geq \frac{v_{fs}}{f} \quad \text{Eq. 3.12}$$

which can be further rearranged to be rewritten as a relationship between the conditions of the two laser systems as,

$$\sqrt{4\alpha \frac{2R_{CW}}{v_{CW}} \ln\frac{T_{CW}}{T_{th}}} \geq \frac{v_{fs}}{f} - \frac{2\mathrm{R}_{fs}}{\sqrt{2}}\sqrt{\ln(\frac{F_{fs}}{F_{th}})} \quad \text{Eq. 3.13}$$

To offer a more accurate way to estimate the parameter combinations which allow for continuous formation of tracks using the two-laser LDW technique, T_{CW} can also be expressed in terms on laser parameters. However, this requires more consideration of the processing conditions. For example, for a complete surface source (absorption length does not exist), the temperature increase with respect to laser parameters of the CW laser system can be expressed by Eq. 3.14 as,

$$T(t) = \frac{P_{CW}\sqrt{4\alpha t}}{k\pi {R_{CW}}^2} \quad \text{Eq. 3.14}$$

where k is the thermal conductivity of the target material.

Moreover, to calculate T_{cw}, *t'* expressed in Eq. 3.10 can be substituted for *t* in Eq. 3.14 to be rewritten as,

$$T_{CW} = \frac{P_{CW}\sqrt{4\alpha\frac{2R_{CW}}{v_{CW}}}}{k\pi {R_{CW}}^2} \quad \text{Eq. 3.15}$$

However, if a penetrating source (absorption length exists) is considered, Eq. 3.14 will not hold true and the expression will change. Note that this discussion is aimed to provide a starting point or framework towards future manufacturing. Parameter combinations can be predicted with more accuracy by further considering other complex factors, such as a moving heat source or dynamic changes in beam and material properties, and is a target of future studies.

3.4. Using a high repetition rate femtosecond laser

3.4.1. Materials and methods

3.4.1.1. Material preparation

A 1:1 mixture of polymer to curing agent of optically-cured KER-4690 PDMS (Shin-Etsu Chemical Co., Ltd., Japan) was prepared. The mixture was poured into a rectangular mold and degassed in vacuum to remove any air bubbles trapped during the mixing procedure. Furthermore, the mixture was cured under a 365-nm ultraviolet lamp for 30 min to prepared PDMS sheets. The PDMS sheets prepared in this study were approximately 2 mm in thickness. Before irradiation experiments, the surfaces of PDMS were washed with ethanol to remove any debris.

3.4.1.2. Laser irradiation

Laser irradiation experiments were conducted using a High Q-2 fs laser (Spectra-Physics, USA) which generated 192-fs laser pulses with a central wavelength of 522 nm (second harmonic wave of a 1045-nm fs laser) at a RR of 63 MHz. PDMS sheets were placed onto a cover glass with a 140-μm spacing (Figure 3.14). Then, laser pulses were focused onto the bottom surface of the PDMS sheet using a 20× objective lens, with a NA of 0.4. The laser power and scanning speed when the defocusing method was not used was 150 mW and 2.00 mm/s, and when the defocusing method was used was 100 mW and 2.00 mm/s, respectively. A three-axis (*xyz*) translation stage was utilized to scan laser pulses in three dimensions. All irradiation experiments were conducted in ambient conditions.

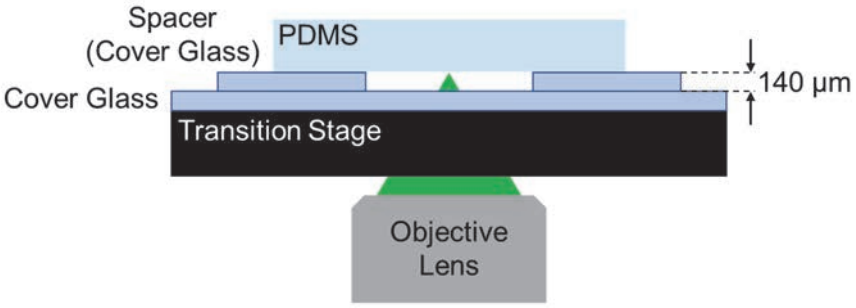

Figure 3.14 Schematic illustration of the laser irradiation setup.

3.4.1.3. Characterization

OM images were obtained using a MS-100 optical microscope (Asahikogaku, Japan). SEM images were obtained using a Inspect F50 scanning electron microscope (FEI, USA). Energy-dispersive X-ray (EDX) mappings were obtained during SEM observations using an Octane Elect energy-dispersive X-ray spectrometer (EDAX, USA). Prior to SEM observations, osmium coatings with a thickness of approximately 12 nm were applied by ion sputtering. TEM images were obtained using a Tecnai G2 transmission electron microscope (FEI, USA). Raman spectra were obtained using a InVia laser-excited Raman spectrometer (Renishaw, UK). The excitation wavelength and laser power for Raman analyses were set to 532 nm and approximately 0.075 mW, respectively.

3.4.2. Results and discussions

3.4.2.1. Patterning using a high repetition rate fs laser

As the implications of establishing a two-laser setup that combines defect formation and thermal conversion was indicated in Section 3.2.2.4., a high RR (63 MHz) fs laser was used for the LICG of PDMS. The high laser intensity of the individual fs laser pulses will facilitate defect nucleation, while the high RR will allow for heat accumulation and the subsequent formation of carbonaceous structures with a single irradiation step (HR-fs LDW). Fs laser pulses were focused tightly onto the surface of a PDMS sheet and scanned once to pattern a track. Figure 3.15 shows an OM image of the track patterned on the surface of PDMS by HR-fs LDW. The width of the track was significantly larger than the focal beam diameter (approximately 2 μm), which is attributable to heat accumulation owing to the high RR (63 MHz). Moreover, consistent with the case of CW LDW (Figure 3.1 (e)), the modification of the transparent PDMS sheet into a black-

colored material is confirmed, suggesting carbonization. It should be noted that a continuous track could be patterned with a significantly lower laser power using a fs laser compared to when a CW laser was used, which is attributable to the difference in laser wavelengths. PDMS is visibly transparent and has a relatively low linear absorbance of 522-nm-wavelength (fs laser) and 1060-nm-wavelength (CW laser) light. Using a fs laser, by tightly focusing the laser pulses onto the surface of PDMS, carbonization can be induced via nonlinear absorption owing to the high laser intensity. On the other hand, using a CW laser, as it is difficult to induce nonlinear absorption, a significantly higher laser power is required to induce sufficient thermalization by linear absorption for carbonization. However, a unidirectional groove can be observed at the center of the resulting track. The formation of such groove is attributable to laser ablation, due to the high peak laser intensity at the center.

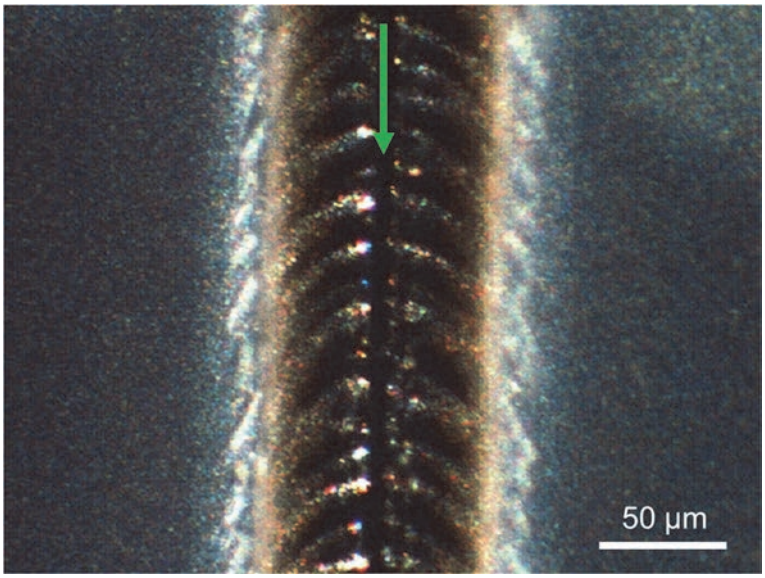

Figure 3.15 OM image of the track patterned on PDMS by HR-fs LDW. Green arrow indicates the location of laser scanning and not the direction.

It can be observed that the surface of the track patterned by HR-fs LDW (Figure 3.15) is visibly different from the surface of the track patterned by CW LDW (Figure 3.1 (a)). Consistent with the case when two lasers were used, for tracks patterned using a fs laser, the surface is relatively flat and continuous; whereas for tracks patterned using a CW laser, the surface possessed a flake-like morphology. The difference between the structural morphologies can be explained by considering the formation mechanism discussed in Section 3.2.2.3. based on laser-induced defects. In the case of fs LDW, the laser-induced defects will form along the irradiated path with relatively high uniformity and stability owing to the high laser intensity (Figure 3.4). If the defects form non-thermally, the

entirety of the defect surface will be smooth, as observed in Figure 3.10 (a). On the other hand, if the defects form thermally, they will protrude from the surface and the peripherals may possess a flake-like morphology owing to the formation of polymeric flaps during explosive formation (Section 2.6.), as observed in Figure 3.10 (d). Currently it is unclear whether defect nucleation in the case of HR-fs LDW is non-thermal and/or thermal. It is expected that the laser intensity of each laser pulse will determine if the defect form non-thermally and/or thermally, but the specifics of this is out of the scope of the current study and should be a topic for future studies. Nonetheless, as heat accumulation ensues, the defects will grow and merge with neighboring defects to eventually form a continuous carbonaceous track (as discussed in Section 3.2.2.3.). It is expected that defect formation occurs prominently within the irradiated area, and considering that multiphoton absorption takes place when tightly focused fs laser pulses are irradiated, defect formation is most likely confined within a small portion of the irradiated area in the case of fs LDW (assumed focal beam diameter is 2 μm). Therefore, as the track width is approximately 130 μm in the case of HR-fs LDW (Figure 3.15), it can be speculated that structural formation is dominated by thermal diffusion out of the irradiated area.

For CW LDW, the laser-induced defects will form along the irradiated path with significantly lower uniformity and stability due to the low laser intensity. Moreover, most, if not all, defects will form thermally by below-surface bubbling. Considering the wavelength of the CW laser (i.e., infrared), and that only single-photon absorption takes place, the induced hotspot will be deeper within the material compared to when fs laser pulses were irradiated (i.e., visible). The deeper hotspot induced by the irradiation of a CW laser beam will result in the formation of a larger macrobubble surrounded by a thicker layer of polymeric material. As the macrobubble explodes, a larger polymeric flap will form (as discussed in Section 2.6. and Section 3.2.), and with sufficient thermalization, the polymeric flap can be converted into a carbonaceous flake. Additionally, as the macrobubbles explodes, it can rupture neighboring carbonaceous structures, resulting in the increase in carbonaceous flakes. Therefore, it can be understood that of the track patterned by CW LDW possess a flaky morphology due to the explosive formation of defects. For the tracks patterned by CW LDW after defects were formed on the surface non-thermally (Figure 3.11 (a)), the surface did not possess a flaky morphology. This is attributable to the change in depth of the induced hotspots (i.e., shallower) due to the initial fs LDW step. Since the fs-LDW defects will serve as initiation sites for structure formation, the subsequent CW laser beam will not penetrate as deep within the surface, resulting in a smaller macrobubble, and consequently, significantly smaller flaps. Note that the above discussions have not been thoroughly investigated yet,

for example, structural evolutions of the flakes in Figure 3.1 (a,b), and future studies are required to reveal the reason for the differences in structural morphologies depending on the used laser type.

Figure 3.16 (a) and (b) are SEM images of the surface and cross-section of the track patterned by HR-fs LDW, respectively. In the case of the surface adjacent to the unidirectional groove at the center (area A in Figure 3.16 (a)), non-distinctive masses are observed, for area B in Figure 3.16 (a), distinctive spherical particles are observed, and for area C in Figure 3.16 (a), particles smaller than those observed for area B are observed. It is assumed that such spherical particles formed by the precipitation of materials removed by laser ablation rather than below-surface bubbling, as such particles were observed for areas beyond C where black-colored material was not observed (i.e., non-carbonized areas). After the ablated material is deposited, thermalization due to laser irradiation may lead to the merging of neighboring small particles, such as the particles observed at area C. Since thermalization will be the greatest at the center and exponentially decrease as the distance from the center increases, this difference in temperature between area A and B may have resulted in a different number of particles merging, leading to the formation of non-distinctive masses and the larger particles, respectively. From the cross-sectional SEM image shown in Figure 3.16 (b), the clean edge resulting from laser ablation is observed. Moreover, the visible density of the structure appears different depending on the distance from the center. For example, for area A in Figure 3.16 (b), the modified region appears significantly denser than area B in Figure 3.16 (b). Considering a thermalization gradient similar to the case of the surface, the temperature will be higher for area A compared to area B. As discussed in Section 2.6.3., macro-pores can form during structural formation due to the release of condensable gases. Since the heating rate would be higher for area A as it is closer to the center, this may result in the rapid release of gases without gas condensation. Moreover, as mentioned in Section 2.5.3., the instantaneous thermalization can result in high localized pressures due to laser-induced shockwaves. The rapid release of gases, in conjunction with the laser-induced shockwaves, may have suppressed the formation of large macro-pores, resulting in a highly dense region. On the other hand, for area B, the heating rate will be significantly lower, allowing for sufficient time for the condensation of gases and lower localized pressures. This in turn will lead to the formation of larger macro-pores, resulting in a less dense region. For area C in Figure 3.16 (b), a visibly smooth material can be observed. Since area C is the boundary between the modified region and the PDMS sheet, the observed material may be amorphous polymeric intermediate products due to insufficient thermalization.

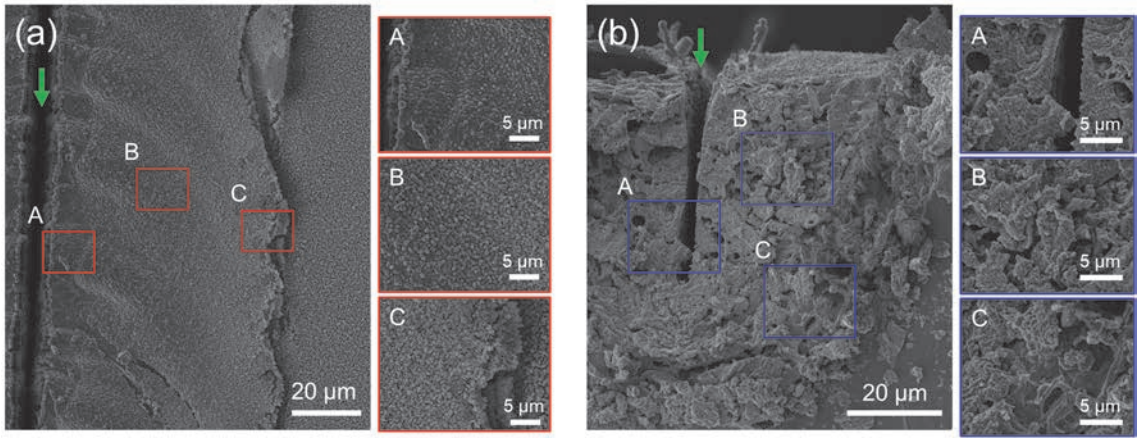

Figure 3.16 SEM images of the (a) surface, and (b) cross-section of the structure patterned by HR-fs LDW. A, B, and C are enlarged images of the respective areas. Green arrow indicates the location of laser scanning and not the direction.

3.4.2.2. Material composition of the carbonaceous structure

To reveal the material compositions of the tracks formed by HR-fs LDW, TEM observations were performed. Figure 3.17 (a) shows a typical TEM image of the materials obtained from the patterned track. From the TEM image, nanoparticles, with an average grain size of approximately 50 nm, can be observed throughout the observed area. From the selected area electron diffraction (SAED) pattern of the field-of-view shown in Figure 3.17 (a), clear spot diffractions are confirmed, indicating that the observed nanoparticles are crystalline (i.e., NC). Figure 3.17 (b) is a higher magnification TEM image of the area A in Figure 3.17 (a). A single NC is outlined by the dashed red line in Figure 3.17 (b), and two distinctively different lattice spacings can be observed at areas B and C, besides and on the NC, respectively. Furthermore, the material observed in the area C seems to be sprouting from the edge of the NC. Figure 3.17 (c) and (d) are enlarged images of areas B and C, respectively. In Figure 3.17 (c), lattice spacings of approximately 0.34 nm were measured, which corresponds to the (002) plane of graphitic carbon. In Figure 3.17 (d), lattice spacings of approximately 0.25 nm are measured. This spacing corresponds to the (111) plane of 3C-SiC, and confirms the formation of SiC-NCs. Additionally, since the direction of the fringes is uniform throughout the entirely of the observed NC, the observed NC is presumed to be a single crystal of SiC. These TEM observations are consistent with the previously Raman results indicating the formation of graphitic carbon and SiC-NCs by the LICG of PDMS (Figure 3.3), and confirms that the carbonaceous structure formed by the irradiation of a train of high RR fs pulses are also composed of

these two carbonaceous materials. In Section 2.3.5., it was discussed that SiC-NCs form as a result of the reduction of silica domains by carbon species. However, this is in the case of carbonization using a conventional furnace and may not apply completely for the carbonization of PDMS using a laser. In the future, by revealing if the formation mechanism of SiC-NCs in the case of LICG of PDMS, further control of the resulting materials may be realized.

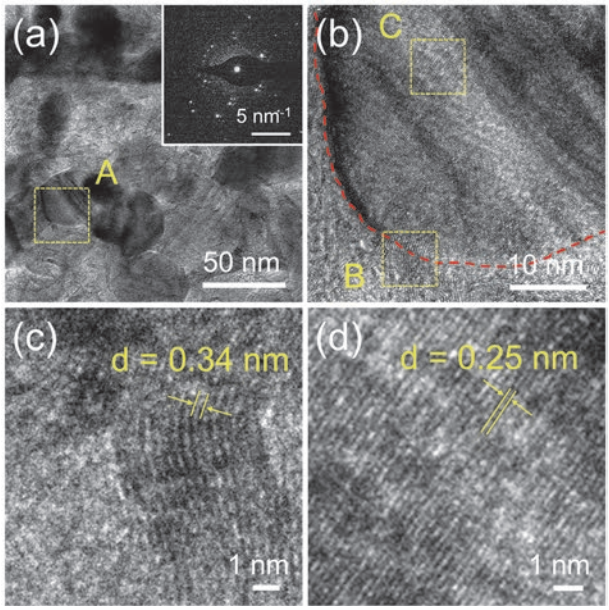

Figure 3.17 (a) Typical TEM image of the formed carbonaceous materials. Inset is a corresponding SAED pattern of the field-of-view. (b) Enlarged image of the area marked A in (a). (d,e) Enlarged images of the areas marked B and C in (b), respectively.

3.4.2.3. Defocusing and ablation suppression

Although the successful patterning of a carbonaceous composite structure composed of graphitic carbon and SiC-NCs was demonstrated by HR-fs LDW, the center of the patterned structure was severely damaged due to laser irradiation. To overcome this issue, a defocusing method was applied to suppress laser ablation during structural formation (Figure 3.18 (a)). First, fs laser pulses were tightly focused onto the bottom surface of the PDMS sheet for 2 sec to pattern a black dot on the surface (Figure 3.18 (b)). Then, the PDMS sheet was shifted along the *z*-axis (incident laser pulse axis) without laser irradiation, to defocus the fs laser pulses at the surface. The distance of the *z*-axis shift is hereon referred to as the defocus distance (DD). Finally, the PDMS sheet was irradiated by the defocused laser pulses and scanned in the *xy*-plane to pattern tracks (Figure 3.18 (c)).

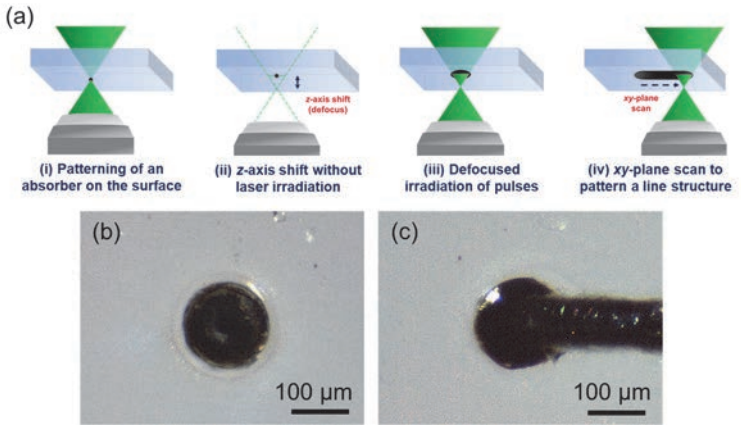

Figure 3.18 (a) Schematic of the defocusing method for ablation suppression (not drawn to scale). OM images of (b) the black dot which acts as an absorber, and (c) the track patterned by scanning a train of defocused fs laser pulses. Scale bars indicate 100 μm.

As pristine PDMS is transparent and has a relatively low linear absorbance in the visible wavelength range, [171] when defocused fs laser pulses are irradiated onto a pristine PDMS sheet there is no visible carbonization due to the substantial decrease in laser intensity. By initially irradiating tightly focused laser pulses, a black dot structure which acts as an absorber of the 522 nm wavelength light can be patterned, to subsequently carbonization the PDMS sheet presumably via linear absorption. It can be hypothesized that there are two vastly different laser intensity thresholds for the initial carbonization of the transparent PDMS sheet I_{Th1}, and the subsequent continuous growth of the carbonaceous structure I_{Th2}, where $I_{Th1} >> I_{Th2}$. This difference in laser intensity threshold can be explained by the significant change in absorption after carbonization (as discussed in Section 2.6.3. and Section 3.2.2.). Therefore, if fs laser pulses are continuously irradiated with I_{Th1} after the initial formation of the carbonaceous structure, the high laser intensity will result in the excessive thermalization and subsequent ablation. The defocusing step after the initial formation of the black dot will alleviate the large difference between I_{Th1} and I_{Th2}, preventing ablation.

SEM images of the tracks patterned with various DDs are shown in Figure 3.19. For a DD of 0 μm, consistent with Figure 3.15, a unidirectional groove attributable to the laser ablation is observed at the center of the track (Figure 3.19 (a)). For a DD of 50 μm, a similar but thinner groove can be observed at the center of the track (Figure 3.19 (b)). On the other hand, for the tracks patterned with a DD of 100 or 150 μm, no grooves are observed (Figure 3.19 (c,d)). Especially for the track patterned with a DD of 150 μm, the center of the track is continuous, and gaps or holes, such as those observed for a DD of 100 μm (Figure 3.19 (c)), are not observed throughout the entirety of the structure surface

(Figure 3.19 (d)). No surface modification was observed for a defocus distance of 200 μm, indicating that the laser intensity became less than I_{Th2}.

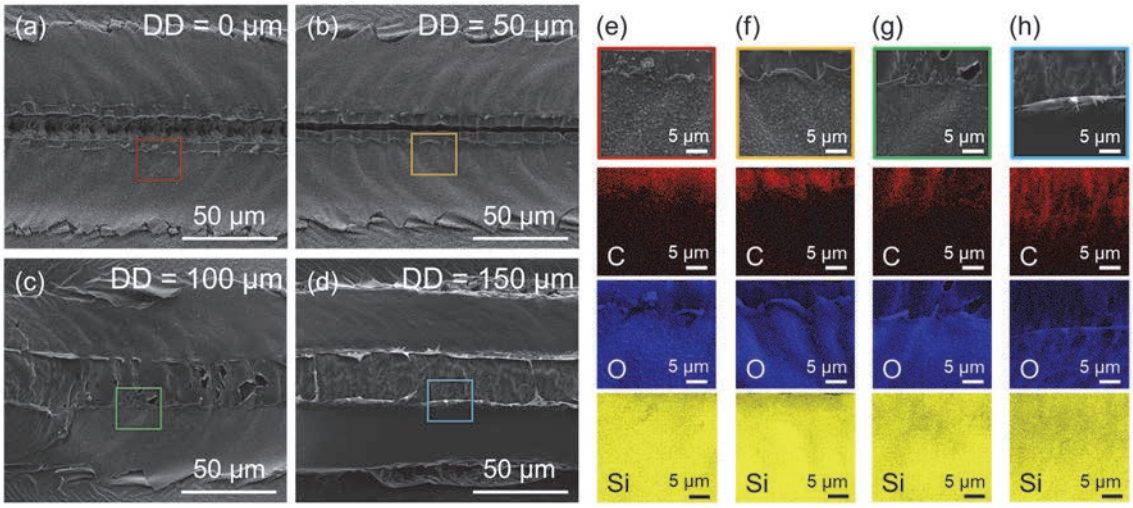

Figure 3.19 SEM surface images of the tracks patterned with a DD of (a) 0 μm, (b) 50 μm, (c) 100 μm, and (d) 150 μm. Enlarged SEM images of the mapping area and the obtained EDX mapping of C, O, and Si for tracks patterned with a DD of (e) 0 μm, (f) 50 μm, (g) 100 μm, and (h) 150 μm. The mapping areas shown in (e–h) are enlarged images of the areas indicated by the respective colored rectangle in (a–d).

From the enlarged images of the areas indicated by the respective colored rectangles (Figure 3.19 (e–h)), two distinctive regions are confirmed for all the tracks. For the tracks patterned with DDs of 0–100 μm (Figure 3.19 (e–g)), a smooth region is observed proximal to the groove, followed by a rougher region with particles. EDX mappings of the observed areas indicate a strong C signal mainly for the smooth regions, and a strong O signal for the entire field-of-view (Figure 3.19 (e–g)). Since the peak temperatures are higher at the center, the strong C signals may be attributable to the progression of LICG and the formation of graphitic carbon. Furthermore, considering the low C signal, high O signal, and high Si signal for the rough regions, the particles observed on the surface are considered to be silica particles. On the other hand, for the track patterned with a DD of 150 μm (Figure 3.19 (h)), a smooth region is observed at the center, followed by a uniform region without particles. EDX mapping of the observed area indicates a strong C signal for the smooth region, similar to the case for the tracks patterned with DDs of 0–100 μm. However, the strong C signal is confirmed for a larger area, suggesting the existence of graphitic carbon in a larger area. Moreover, a relatively weaker O, as well as Si, signal is indicated for both the smooth regions and the adjacent uniform area (Figure 3.19 (h)), compared to the case for the tracks patterned with DDs of 0–100 μm. The low O and Si

signals is attributable to the lack of silica particles on the surface of the track patterned with DDs of 150 μm. The fact that the particles were only observed for the tracks in which grooves or gaps were observed supports the previous assumption that the particles formed due to the precipitation of ablated material rather than carbonization and/or graphitization (discussed in Section 3.4.2.1.).

SEM images of the tracks patterned at various scanning speeds with a constant DD of 150 μm are shown in Figure 3.20 (a–p). For relatively fast scanning speeds (ie., 4.00 and 3.50 mm/s, Figure 3.20 (a,b)), a groove is observed at the center, followed by flakes similar to those observed for tracks patterned by CW LDW (Figure 3.1 (a,b)) at the edges of the groove. As the scanning speed is decreased (i.e., 3.00–2.00 mm/s, Figure 3.20 (c–e)), both the groove as well as the flakes become less prominent, and relatively continuous structure is observed. However, as the scanning speed is further decreased (i.e., 1.50–0.50 mm/s, Figure 3.20 (f–h)), a groove visibly different from that observed for fast scanning speeds is observed, indicating the reoccurrence of ablation. Considering that the laser intensity is constant and the number of irradiated pulses is different for the patterning of all structures shown in Figure 3.20, it can be speculated that the unidirectional groove at the center is a result of thermalization, rather than non-thermal ablation. However, as the visible morphologies of the grooves in Figure 3.20 are different from those observed for Figure 3.19 (a), further investigation on the formation mechanism of the grooves may be required.

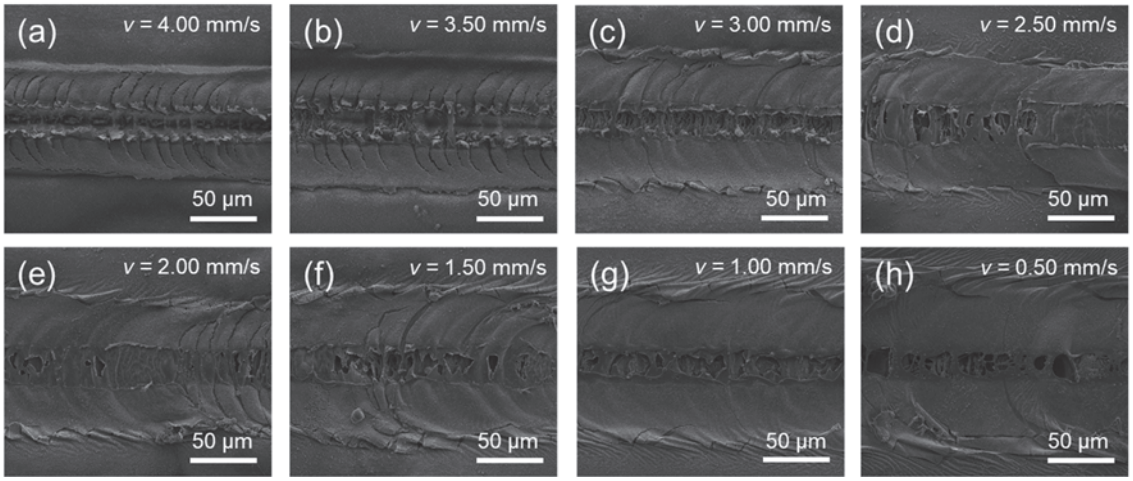

Figure 3.20 SEM images of the surfaces of tracks patterned with a scanning speed of (a) 4.00 mm/s, (b) 3.50 mm/s, (c) 3.00 mm/s, (d) 2.50 mm/s, (e) 2.00 mm/s, (f) 1.50 mm/s, (g) 1.00 mm/s, and (h) 0.50 mm/s, with a constant DD of 150 μm.

With the decrease in scanning speed, thermalization should increase as a result of the increase in laser fluence. Therefore, it is expected that laser ablation should gradually

increase as the scanning speed is increased. However, it can be clearly seen that the structural morphologies transition from “yes groove” to “no groove” to “yes groove”, rather than a simple transition from “no groove” to “yes groove”. One explanation for the initial transition from “yes groove” to “no groove” as the scanning speed is decreased is the sufficient formation of thermally stable intermediates (as discussed in Section 2.7.). As the resident times were too short in the case of fast scanning speeds, the formation of thermally stable intermediates, such as amorphous carbon, may have been insufficient. As the scanning speed is decreased, such intermediate products will increase in volume, suppressing laser ablation although the laser fluence is increased. Another explanation for the transition between the initial “yes groove” to “no groove” as the scanning speed is decreased, is the merging of the flakes due to the increase in laser fluence. Considering that the flakes are a result of the explosive formation (as discussed in Section 3.3.2.2. and 3.4.2.1.), the flakes may be mostly composed of partially carbonized polymeric materials. Thermalization induced by the subsequent irradiation of laser pulses, may lead to the flattening, stacking, and/or merging of the flakes to form a continuous carbonaceous structure. Agreeably, the formation of a layered structure can be observed as the scanning speed is decreased, for example from 4.00 mm/s (Figure 3.20 (a)) to 3.00 mm/s (Figure 3.20 (c)). However, regardless of the reason for the initial transition between “yes groove” to “no groove”, the reappearance of the groove at slower scanning speeds is attributable to the excessive thermalization due to the excessive laser fluence. Appropriately, surface ripples disappear and the structure becomes visible smoother, possibly due to melting.

3.5. Summary

In Chapter 3, the experimental results regarding the structural formation of carbonaceous structures by the LICG of PDMS was described. Orthogonal multi-parameter experiments conducted by scanning a CW laser beam across a PDMS surface indicated that structure formation is not solely dependent on the laser fluence but rather on the resident time of the CW laser beam. According to this, a formation mechanism based on the nucleation and growth of laser-induced defects was proposed, and further validated by intentionally introducing laser-induced defects in a controlled manner using a fs laser. As the implications of establishing a two-laser system which incorporates defect formation and thermal conversion was indicated, a high RR fs laser was used for the LICG of PDMS. The formation of a carbonaceous structure composed of graphitic carbon and SiC-NCs was demonstrated using a high RR fs laser; however, the center of the structure was severely damaged by laser ablation due to the high peak laser intensity. By using the

defocusing method, laser ablation was significantly suppressed, realizing the successful patterning of continuous carbonaceous structures using a high RR fs laser.

The contents of this chapter were reused and built upon the following references with permission from the Royal Society of Chemistry ©2020 and John Wiley & Sons ©2021, respectively.

- Hayashi, S., Morosawa, F. & Terakawa, M. Synthesis of silicon carbide nanocrystals and multilayer graphitic carbon by femtosecond laser irradiation of polydimethylsiloxane. *Nanoscale Adv* **2**, 1886–1893 (2020).
- Hayashi, S., Morosawa, F. & Terakawa, M. Laser Direct Writing of Highly Crystalline Graphene on Polydimethylsiloxane for Fingertip-Sized Piezoelectric Sensors. *Adv Eng Mater* **23**, 2100457 (2021).

4. Electrical property of carbonaceous structures

4.1. Introduction

As the carbonaceous structures formed by LICG are generally composed of graphitic carbon, specifically turbostratic graphite, the structures can conduct electricity. Moreover, as discussed in Section 2.4.1., the electrical conductivity of graphitic carbon is highly dependent on the structural order, or crystallinity, of the graphitic carbon. However, as the carbonaceous structures formed by the LICG of PDMS is also composed of SiC-NCs, the electrical property can transition from a conducting to semiconducting regime depending on the features of SiC-NCs. The aim of Chapter 4 is to reveal the relationship between the carbonaceous material and the electrical property for the carbonaceous structure formed by the LICG of PDMS. In Section 4.2., the patterning of electrically conductive structures is demonstrated and the effect of graphitic carbon on the electrical property will be indicated. Then, in Section 4.3., the transition from the electrically conducting regime to the semiconducting regime is demonstrated, and the effect of SiC-NCs on the electrical property is indicated. According to this, it is concluded that the key to achieving semiconducting structures is to suppress graphitization while enhancing SiC-NCs formation, and the laser parameters capable of achieving this will be discussed.

4.2. Graphitic carbon and the conducting regime

4.2.1. Materials and methods

4.2.1.1. Material preparation

A 1:1 mixture of polymer to curing agent of optically-cured KER-4690 PDMS (Shin-Etsu Chemical Co., Ltd., Japan) was prepared. The mixture was poured into a rectangular mold and degassed in vacuum to remove any air bubbles trapped during the mixing procedure. Furthermore, the mixture was cured under a 365-nm ultraviolet lamp for 30 min to prepared PDMS sheets. The PDMS sheets prepared in this study were approximately 2 mm in thickness. Before irradiation experiments, the surfaces of PDMS were washed with ethanol to remove any debris.

4.2.1.2. Laser irradiation

Laser irradiation experiments were conducted using a High Q-2 fs laser (Spectra-Physics, USA) which generated 192-fs laser pulses with a central wavelength of 522 nm (second harmonic wave of a 1045-nm fs laser) at a RR of 63 MHz. PDMS sheets were placed onto a cover glass with a 140-μm spacing (Figure 3.14). Then, laser pulses were focused onto the bottom surface of the PDMS sheet using a 20× objective lens, with a NA of 0.4. A three-axis (*xyz*) translation stage was utilized to scan laser pulses in three dimensions. The defocusing method was used for the patterning of conductive tracks (DD = 150 μm), and the laser power and scanning speed was 100 mW and 2.00 mm/s, respectively. The defocusing method was not used for the patterning of conductive 2D structures (DD = 0 μm), and the laser power and scanning speed was 150 mW and 2.00 mm/s, respectively. All irradiation experiments were conducted in ambient conditions.

4.2.1.3. Characterization

Electrical conductivity measurements of the structures were obtained using a 2401 digital source meter (Keithley, USA). Before electrical conductivity measurements, a gold electrode with a thickness of approximate 50 nm was deposited on both ends of the structures (total of 2 electrodes). A probe was contacted onto each of the gold electrodes deposited on the ends, and the electrical resistance was measured by the two-probe method. OM images were obtained using a MS-100 optical microscope (Asahikogaku, Japan). SEM images were obtained using a Inspect F50 scanning electron microscope (FEI, USA). Prior to SEM observations, osmium coatings with a thickness of approximately 12 nm were applied by ion sputtering.

4.2.2. Results and discussions

4.2.2.1. Electrically conductivity of carbonaceous structures

The electrical conductivity of tracks patterned by HR-fs LDW with different DDs was assessed via the two-probe method for a 2-mm length (Figure 4.1). Although the formation of electrically conductive graphitic carbon was confirmed (Figure 3.17) evident electrical conductivity was not confirmed for the track patterned with a DD of 0 μm (conductance ≈ 0 μS). This is attributable to the severe damaging of the patterned track due to laser ablation (Figure 3.15). Due to laser ablation, for example, the formed

graphitic carbon could be partially removed preventing the formation of the conductive network (discussion on percolation in Section 2.4.1.), or portions of the ablated material could adhere during the formation of graphitic carbon making the material highly defective (discussion on defects in Section 2.4.1.). On the other hand, in the case of tracks patterned using the defocusing method (i.e., DD > 0 μm), notable electrical conductivity was confirmed. Moreover, with the increase in DD, the electrical conductance of the structures increased exponentially to a maximum of approximately 117 μS for a DD of 150 μm (Figure 4.1). These results clearly indicate that the suppression of ablation by implementing the defocusing method is crucial for the patterning of electrically conductive tracks in the case of HR-fs LDW. Considering the cross-sectional area of the structure, the electrical conductivity of the structure was calculated to be approximately 51.6 S/m (resistivity: approximately 0.0194 ohm·cm). Compared to pristine graphite (approximately 10^6 S/m), the calculated electrical conductivity was significantly lower. As the carbonaceous structure is a composite structure, the existence of low conducting intermediates, such as amorphous carbon and silica, and semiconducting SiC-NCs can decrease the overall electrical conductivity of the structure.

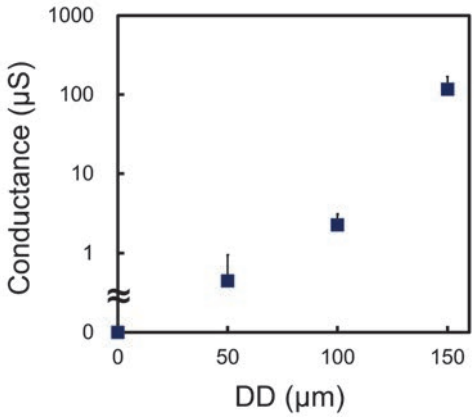

Figure 4.1 Electrical conductance of tracks patterned with various DDs. The error bars indicate the standard deviation for n = 5 samples.

Representative Raman spectra obtained from the tracks are shown in Figure 4.2. Note that the spectra were all obtained from the smooth regions which exhibited relatively stronger C signals near the center of tracks observed in Figure 3.19 (a–d). For the Raman spectra obtained from the tracks patterned with a DD of 100 μm and smaller, the D and G bands are observed, indicating the formation of graphitic carbon. However, consistent with the EDX results (Figure 3.19 (e–h)), it is suggested that the formed graphitic carbon is highly defective, and only exist as small crystals.[172,173] As a groove, gap, and/or hole was observed for all of these tracks, it is suggested that laser ablation hindered the growth

of graphitic carbon into larger crystals. In contrast, for the Raman spectrum obtained from the track patterned with a DD of 150 μm, in addition to the D and G band peaks, a sharp 2D band can be observed. The confirmation of both a low I_D/I_G ratio (approximately 0.34) and a sharp 2D band for the track patterned with a DD of 150 μm suggests the existence of graphitic carbon crystals with lateral and vertical dimensions significantly greater than those for the tracks patterned with a DD of 100 μm and smaller. Considering that electrical conductivity was confirmed for all of the tracks patterned using the defocusing method, it can be concluded that the concentration of graphitic carbon is higher than the percolation threshold. However, the larger crystal dimensions for a DD of 150 μm may have resulted in higher electron mobilities and/or number of conductive paths within the conductive network, leading to the significantly higher electrical conductance. However, even for a DD of 150 μm, a prominent D band peak is observed suggesting the existence of a notable amount of crystal defects, which may also be partially responsible for the lower electrical conductivity compared to ideal graphite. Note that the evolution in Raman spectra can only suggest that the increase in crystal size of the graphitic carbon is related to the increase in electrical conductance with an increase in DD, and cannot conclude whether there was any increase in concentration of graphitic carbon.

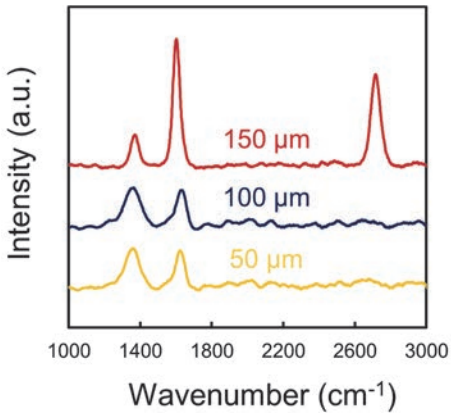

Figure 4.2 Raman spectra obtained from the center of the tracks patterned with various DDs.

To evaluate the uniformity of graphitic carbon for the track patterned with a DD of 150 μm, 1D Raman mapping was performed. The Raman spectra obtained point-by-point from the center (0 μm) to the edge of the track (52 μm) are shown in Figure 4.3 (a). The Raman spectrum for a DD of 150 μm in Figure 4.2 corresponds to the Raman spectrum for 0 μm in Figure 4.3 (a). As the distance from the center increased, the Raman spectrum distinctively evolved. At 14 μm, the D, G, and 2D bands, as observed at 0 μm, were also observed; however, the relative intensity of the D band was significantly stronger at 14 μm than at 0 μm. Furthermore, at 24 μm, only the D and G bands were observed. At 40

μm, two peaks were observed at 1100 cm^{-1} and 1200 cm^{-1}, in addition to the D band. These peaks originated from the stretching vibration of the aliphatic group and are sometimes referred to as the trans-polyacetylene (TPA) bands, suggesting the formation of amorphous carbons with partially aromatic domains.[174,175] At 52 μm, the m band is observed, suggesting the existence of methyl bonds, possibly derived from the partially modified or pristine PDMS. For distances in which graphitic carbon was formed (< 30 μm), the degree of graphitization was evaluated using I_D/I_G and I_{2D} with respect to the distance from the center. As the distance from the center increased, the I_D/I_G decreased accordingly, indicating that the graphitic carbon crystals are larger, the closer to the center of the track (Figure 4.3 (b)). The observation of graphitic carbon at distances < 30 μm from the center (with fewer defects near the center), partially aromatic amorphous carbon at distances of 30–50 μm from the center, and polymeric materials with no significant modification at distances > 50 μm from the center, agrees well with the general process of carbonization and graphitization of polymers. Owing to the Gaussian nature of the laser pulses, the laser intensity will be the highest at the center, and correspondingly, LICG will progress closer to the center. This results in a carbonaceous structure with relatively low uniformity. Therefore, as in the case of laser-induced powder bed fusion[176], it can be expected that by irradiating laser pulses with a gentler spatial distribution in laser intensity, the spatial gradient of thermalization may become gentler, leading to an enhancement in uniformity. By improving the uniformity of the graphitized regions, the overall electrical conductivity of the patterned track may be significantly improved.

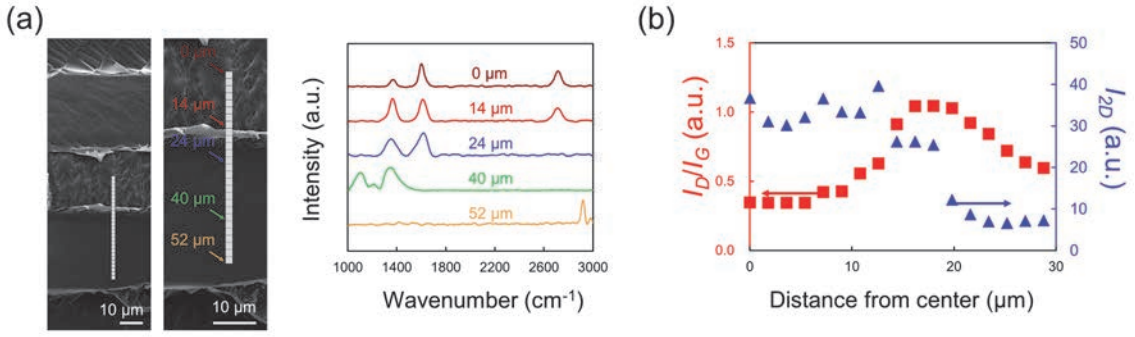

Figure 4.3 (a) SEM images indicating the analyzed locations of the track patterned with a DD of 150 μm, and the Raman spectra obtained from the respective locations. (b) I_D/I_G (red) and I_{2D} (blue) at various distances from the center. Scale bars indicate 10 μm.

4.2.2.2. Raster scanning and growth in conductive network

2D carbonaceous structures were patterned on the surface of a PDMS sheet by HR-fs

LDW without using the defocusing method (i.e., DD = 0 μm). Figure 4.4 (a) shows the electrical conductance of the structures patterned with a different number of raster scans. The hatch spacing was set to be 50 μm. Assuming that the width of a single track patterned with the current laser power and scanning speed parameter combinations (i.e., 150 mW, 2.00 mm/s) was approximately 130 μm (Figure 3.15), each subsequent structure should overlap approximately 40% with the adjacent structure. Evident electrical conductivity was not confirmed for the structure patterned with 1 scan (conductance ≈ 0 μS), which is consistent with the previous results regarding the electrical conductivity of tracks patterned with a DD of 0 μm (Figure 4.1 (a)). Evident electrical conductivity was not confirmed for the structure patterned with 2 scans either (conductance ≈ 0 μS). On the contrary, structures patterned with 3 or more raster scans indicated electrical conductivity. Moreover, the electrical conductance of the carbonaceous structures increased exponentially with an increase in the number of raster scans (Figure 4.4 (a)). The change in electrical conductance with the increase in the number of scanned lanes could be explained by various factors, such as the increase in cross-sectional area and/or further modification of the initially patterned carbonaceous structures due to the subsequent scanning.

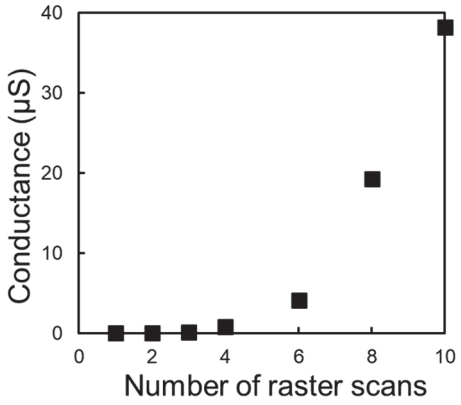

Figure 4.4 Change in electrical conductance with respect to number of raster scans. Electrical conductivity was confirmed for structures patterned with 3 or more scans.

The carbonaceous structures mentioned in Figure 4.4 were cut perpendicular to the laser scanning direction to analyze the cross-sections. Figure 4.5 (a–c) shows the OM images of the cross-sections of the 2D structures patterned with 1 scan (Figure 4.5 (b)), 2 scans (Figure 4.5 (c)), and 3 scans (Figure 4.5 (d)). Laser pulses were raster scanned in to and out of the page from the right side to the left side of the image. It can be clearly observed that the structures formed by the consecutive scans (Figure 4.5 (b,c)) are visibly different from than the structure formed by the initial laser scan (Figure 4.5 (a)).

Specifically, the structure formed by the second laser scan is clearly smaller than the structure formed by the initial laser scan, and less expansion of the structure, both horizontally and vertically, is confirmed for the second laser scan (Figure 4.5 (b)). Since the location of the second laser scan overlaps the carbonaceous structure formed by the initial laser scan, the laser pulses of the second laser scan will be absorbed by the carbonaceous structure rather than the PDMS sheet. Considering that graphitic carbon has a significantly higher thermal conductivity than pristine PDMS, the thermalization due to the second laser scan may rapidly dissipate through the pre-existing carbonaceous structure instead of radially through the PDMS sheet, resulting in the formation of a significantly smaller structure. On the other hand, the location of the third laser scan will not overlap the carbonaceous structure formed by the second laser scan since the structure for the second laser scan is not as wide as the initial laser scan (Figure 4.5 (c)). However, contrary to the case of the initial laser scan, a carbonaceous structure exists to the right side of the scan, therefore the formed structure will not expand as much as the initial laser scan, although more than the second laser scan. Considering that the cross-sectional area did not increase exponentially (Figure 4.5 (a–c)), whereas the electrical conductivity did (Figure 4.4), the change in electrical conductance with the increase in the number of raster scans cannot be explained with the change in cross-sectional area alone.

Figure 4.5 (d) shows the Raman spectra obtained from the cross-sections of the 2D structures patterned with a different number of raster scans. Analysis for each structure was conducted for the location slightly left of the first unidirectional groove formed due to the first laser scan, indicated by the respective blue arrows in Figure 4.5 (a–c). With an increase in the number of raster scans, the I_D/I_G changed from approximately 1.4 to 1.2 to 1.0, indicating a respective growth in the graphitic carbon crystals in the *ab* direction with consecutive laser scans. Furthermore, for the spectrum obtained from the structure patterned with 3 scans, the appearance of the 2D band is observed, indicating the stacking of ordered layers and the growth of the graphitic carbon crystals in the *c* direction. With successive raster scanning, the subsequent laser scans can thermalize the pre-existing structure, and in-turn progress carbonization and graphitization. Considering the cross-sectional area of the structures, the electrical conductivity of the carbonaceous structures patterned with 1, 2, 3, and 4 scans were calculated to be approximately 2.56×10^{-12} S/m, 2.08×10^{-12} S/m, 1.60×10^{-3} S/m, and 1.20×10^{-2} S/m, respectively. As the electrical conductivity increased nonlinearly, this clearly indicates the formation of percolation networks within the structure with an increase in the number of raster scans. By continuing the raster scanning process, it can be expected that the size of the graphitic carbon crystals can be further increased, until the location of laser scanning is too far from

the pre-existing structure to thermalize. Moreover, with the increase in laser scans, the concentration of large graphitic carbon crystals may also increase as graphitization can progress. Therefore, although laser ablation prevents the formation of a conductive network when tightly focused fs laser pulses are scanned once (DD = 0 μm), by raster scanning, the percolation threshold can also be overcome through the increase in size and/or concentration of graphitic carbon.

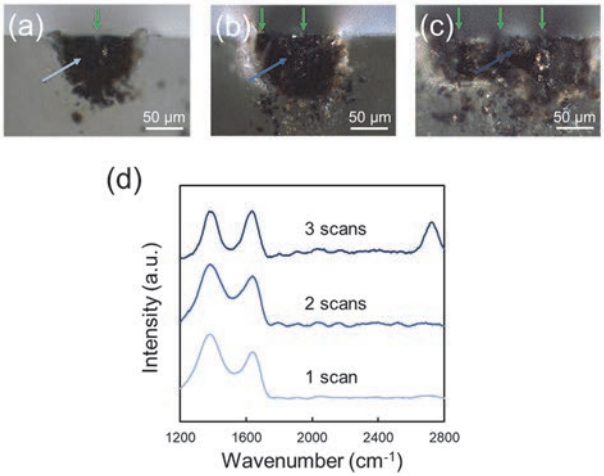

Figure 4.5 Cross-sectional OM images of carbonaceous structures patterned with (a) 1 scan, (b) 2 scans, and (c) 3 scans. Green arrow indicates the location of laser scanning. (d) Raman spectra obtained from different locations of the cross-section. Arrows indicate the location of analysis, and the color of the arrow corresponds to the color of the obtained Raman spectrum.

4.3. Silicon carbide and the semiconducting regime

4.3.1. Materials and methods

4.3.1.1. Material preparation

A 1:1 mixture of polymer to curing agent of optically-cured KER-4690 PDMS (Shin-Etsu Chemical Co., Ltd., Japan) was prepared. The mixture was poured into a rectangular mold and degassed in vacuum to remove any air bubbles trapped during the mixing procedure. Furthermore, the mixture was cured under a 365-nm ultraviolet lamp for 30 min to prepared PDMS sheets. The PDMS sheets prepared in this study were approximately 2 mm in thickness. Before irradiation experiments, the surfaces of PDMS were washed with ethanol to remove any debris.

4.3.1.2. Laser irradiation

Laser irradiation experiments were conducted using a High Q-2 fs laser (Spectra-Physics, USA) which generated 192-fs laser pulses with a central wavelength of 522 nm (second harmonic wave of a 1045-nm fs laser) at a RR of 63 MHz. PDMS sheets were placed onto a cover glass with a 140-μm spacing (Figure 3.14). Then, laser pulses were focused onto the bottom surface of PDMS using a 50× objective lens, with a NA of 0.75. The defocusing method was not used for the patterning of all tracks in this Section (DD = 0 μm). The PE and RR for patterning was altered using a NDHN-100 round continuous variable neutral density filter (OptoSigma, Japan) and a 3250-220 acousto-optic modulator (Gooch & Housego, UK), respectively.

Depending on the RR, the time between consecutive pulses of the pulse train will be different, and thus the time required to irradiate the same number of pulses will be different (Figure 4.6 (a)). To keep the number of irradiated pulses per unit spot (pps) the same between RRs, the scanning speed was adjusted accordingly. For example, for slower RRs the scanning speed was set slower compared to higher RRs to keep the distance between pulses, and resultantly the pps, the same with the case of higher RRs (Figure 4.6 (b)). All structures mentioned in Section 4.3. were patterned with a pps of 2500, and the scanning speed was 8.40 mm/s, 3.60 mm/s, 2.29 mm/s, and 1.68 mm/s for a RR of 21 MHz, 9.0 MHz, 5.7 MHz, and 4.2 MHz, respectively. For the patterning of carbonaceous structures, a two-stepped method was implemented. First, fs laser pulses were focused and scanned onto the bottom surface of PDMS to pattern a black structure on the surface, which acted as an absorber (Step 1). The PE, RR, and scanning speed for the patterning of the absorber were set to 1.27 nJ, 63 MHz, 3.00 mm/s, respectively. Then, structures were patterned with various laser parameters from the absorber (Step 2).

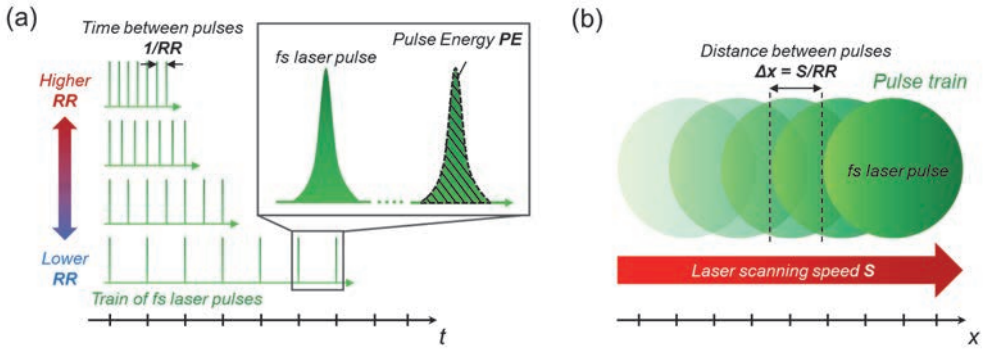

Figure 4.6 Schematics illustrating (a) pulse trains with different RRs consisting of the same number of pulses (i.e., 7 pulses), and (b) scanning of a pulse train.

4.3.1.3. Characterization

Structures patterned in Step 2 were subject to characterizations. SEM images were obtained using an Inspect F50 scanning electron microscope (FEI, USA). Prior to SEM observations, osmium coatings with a thickness of approximately 12 nm were applied to the patterned structures by ion sputtering. Raman spectra were obtained using a InVia laser-excited Raman spectrometer (Renishaw, UK). The excitation wavelength and laser power for Raman analyses were set to 532 nm and 0.075 mW, respectively. Current-voltage (I-V) curves were obtained using a 2401 digital source meter (Keithley, USA), for the range of -5 V to 5 V in 0.1 V steps. Prior to electrical conductivity measurements, gold electrodes with a thickness of approximately 50 nm were deposited on both ends of the structures by ion sputtering. Distance between electrodes was approximately 2 mm. TEM images were obtained using Tecnai G2 F20 and Tecnai Osiris transmission electron microscopes (both FEI, USA). Prior to TEM observations, the patterned structures were removed from the PDMS surface and dispersed in an ethanol solution. The prepared sample-containing solution was dropped onto a TEM grid and air dried before observations. XRD spectra were obtained using a D8 Discover X-ray diffractometer (Bruker, USA).

4.3.2. Results and discussions

4.3.2.1. Transition into the semiconducting regime

Fs laser pulses with varying PEs were irradiated at different RRs and scanned across the surface of a PDMS sheet to pattern tracks by HR-fs LDW. Figure 4.7 (a–d) and Figure 4.7 (e–h) shows the SEM images of the tracks patterned with various PEs at a constant RR of 21 MHz, and tracks patterned at different RRs with a constant PE of 3.96 nJ, respectively. Although the defocusing method was not used, evident ablation of the surface is not confirmed for any of the tracks. It is assumed that the lower laser powers in this section (approximately 10% of that in Section 4.2.), suppressed the laser ablation. Note that tracks cannot be patterned with such laser powers without the initial patterning of an absorber (as indicated in the Materials and methods for this section). The measured widths of the tracks patterned with a PE in the range of 0.40 nJ to 3.96 nJ, at a RR in the range of 4.2 MHz to 21 MHz, are summarized in Figure 4.7 (i). Note that the PE could not be set greater than 3.96 nJ, since this was the maximum output of the current laser setup. The track width was greater when the PE and/or RR was relatively higher, as it is

expected that thermalization increases. It is worth mentioning that for tracks with similar widths, the visible surface morphology was also analogous (Figure 4.7 (b) and Figure 4.7 (e)). Visible modification of the PDMS sheet could not be confirmed for the corresponding parameter combinations where data is not plotted. For such parameter combinations, it is assumed that thermalization was too low to induce the LICG of PDMS.

Figure 4.7 (j) and Figure 4.7 (k) shows the Raman spectra obtained from the tracks patterned with various PEs at a constant RR of 21 MHz, and the tracks patterned at different RRs with a constant PE of 3.96 nJ, respectively. For all of the Raman spectra obtained, distinctive peaks corresponding to the D, G, and 2D bands were observed, indicating the formation of graphitic carbon. However, the I_D/I_G differed depending on the parameter combination. As the general trend, the I_D/I_G ratios were lower for tracks patterned with higher PEs and/or RRs, and suggests the formation of larger graphitic carbon crystals for such parameter combinations.[164]

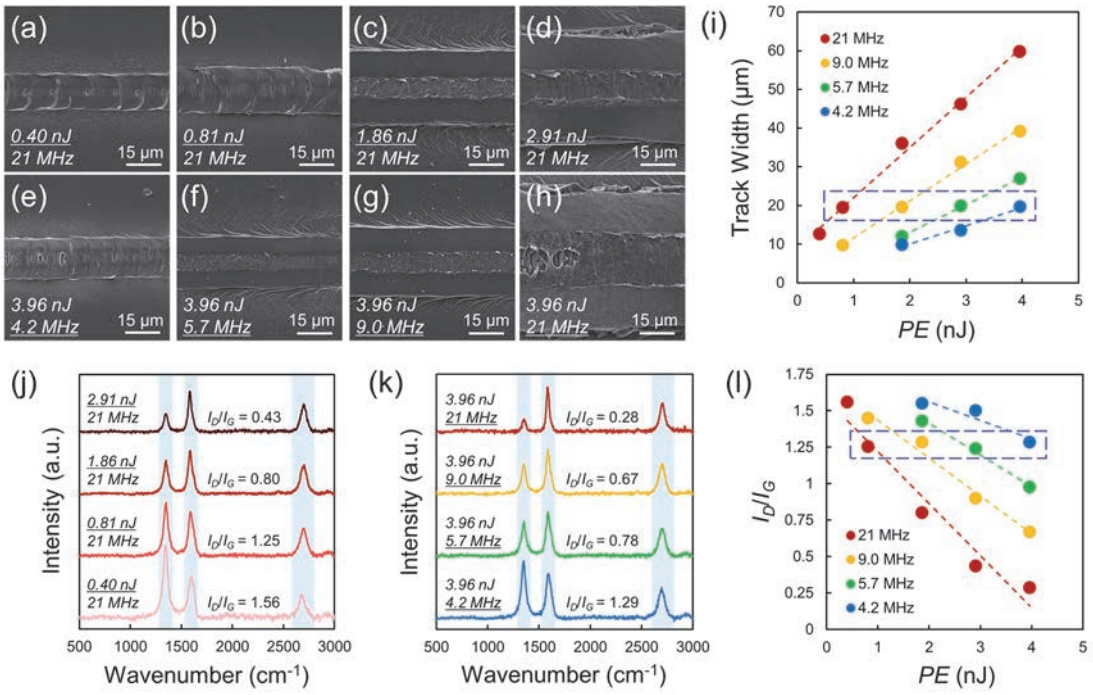

Figure 4.7 SEM images of the tracks patterned with a PE of (a) 0.40 nJ, (b) 0.81 nJ, (c) 1.86 nJ, or (d) 2.91 nJ at a constant RR of 21 MHz. SEM images of the tracks patterned at a RR of (e) 4.2 MHz, (f) 5.7 MHz, (g) 9.0 MHz, and (h) 21 MHz, with a constant PE of 3.96 nJ. (i) Measured widths of the tracks patterned with various parameter combinations. (j) Raman spectra obtained from the tracks patterned with various PEs at a constant RR of 21 MHz. (k) Raman spectra obtained from the tracks patterned at different RRs with a constant PE of 3.96 nJ. (l) I_D/I_G ratios for the tracks patterned with various parameter combinations.

When a material is irradiated by a train of fs laser pulses, localized heat accumulation occurs when the time between consecutive pulses is shorter than the time required for the effects of the former pulse to completely relax (as discussed in Section 2.5.3.). If the total number of irradiated pulses is kept constant, by increasing the PE and/or RR, heat accumulation will increase correspondingly. Agreeably, the track width was wider for such parameter combinations, as the attained peak temperatures will be higher. Comparing the results of Figure 4.7 (i) with Figure 4.7 (l), the track width and I_D/I_G was inversely correlated. As discussed in Sections 2.2. and 2.3., carbonization is a complex process consisting of three phases, in which the peak temperature determines which phase the process can progress to. Consistent with the assumption that the attained peak temperatures were higher for wider tracks, the formation of larger graphitic carbon crystals was confirmed. For tracks where the structural widths were relatively similar even if the parameter combinations for patterning were vastly different, the degree of graphitization was comparable, and the attained peak temperatures were deduced to be analogous.

Figure 4.8 (a) shows the I-V curves for the tracks which possessed similar widths and I_D/I_G (indicated with blue squares in Figure 4.7 (i) and Figure 4.7 (l)). The parameter combinations for the patterning of these tracks were, 0.81 nJ at 21 MHz, 1.86 nJ at 9.0 MHz, 2.91 nJ at 5.7 MHz, and 3.96 nJ at 4.2 MHz. Although the tracks possessed similar widths and I_D/I_G, these structures exhibited strikingly different electrical properties. For the track patterned with a PE of 0.81 nJ, the electrical current increased linearly with applied voltage, indicate a metal-like electrical property. As the PE for patterning increased and the RR for patterning decreased, the I-V curves became progressively nonlinear, indicating a transition from the conducting to semiconducting regime. Figure 4.8 (b) shows the relative electrical resistances with regards to the electrical resistance at -5 V for an applied voltage range of -5 V to 5 V. For the track patterned with a PE of 0.81 nJ, the electrical resistance was for the most part constant with applied voltage. The voltage-dependency of the electrical resistance becomes significantly greater as the PE increases, and for the track patterned with a PE of 3.96 nJ, the electrical resistance varied greatly depending on the applied voltage, exhibiting evident semiconducting behavior.

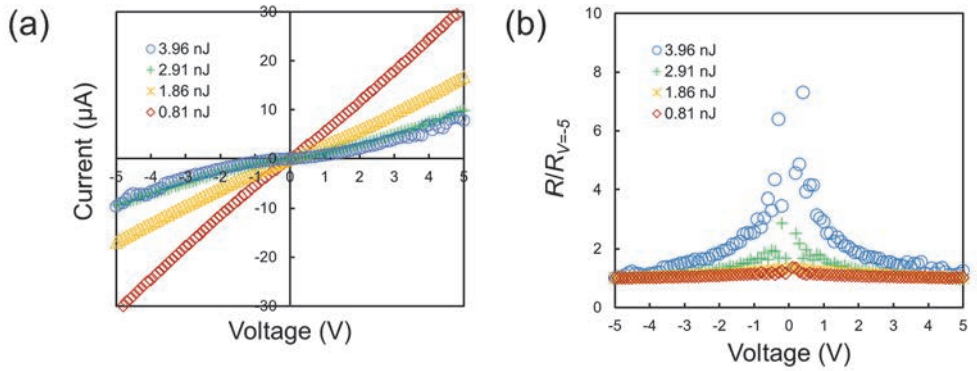

Figure 4.8 (a) I-V curves of tracks patterned with 0.81 nJ at 21 MHz, 1.86 nJ at 9.0 MHz, 2.91 nJ at 5.7 MHz, and 3.96 nJ at 4.2 MHz. (b) Change in relative resistances with respect to applied voltage.

4.3.2.2. Change in material composition with laser parameters

Analyses performed hereafter were conducted on the tracks mentioned in Figure 4.8 which exhibited different electrical properties. TEM images of the material formed with different parameter combinations are shown in Figure 4.9 (a–h). For the TEM image of the material formed with 0.81 nJ at 21 MHz (Figure 4.9 (a)), NCs (indicated with red arrows) can be observed. For the NCs, lattice spacings that correspond to the (111) planes of 3C-SiC are identified (Figure 4.9 (b)), indicating that the observed NCs are 3C-SiC-NCs. The formation of NCs is also confirmed for the tracks patterned with 1.86 nJ at 9.0 MHz (Figure 4.9 (c)), 2.91 nJ at 5.7 MHz (Figure 4.9 (e)), and 3.96 nJ at 4.2 MHz (Figure 4.9 (g)). As the lattice spacings are all comparable (Figure 4.9 (d,f,h)), it is inferred that the observed crystals are all 3C-SiC. Particularly for the TEM image of the material formed with 3.96 nJ at 4.2 MHz (Figure 4.9 (a)), it can be observed the formed SiC-NCs are surrounded by sheets which resemble wrinkled graphitic sheets (indicated with blue arrows).[177] Moreover, it is interesting to note that lattice spacings that correspond to the (002) planes of graphitic carbon are also identified at the outer edges of the SiC-NCs, suggesting surface exfoliation.[178] Peaks corresponding to the vibrational modes of 3C-SiC were not confirmed from the Raman analyses (Figure 4.7 (j,k)) probably due to the hinderance of excitation of SiC-NCs by the surrounding graphitic carbon as observed in Figure 4.9 (g).[179]

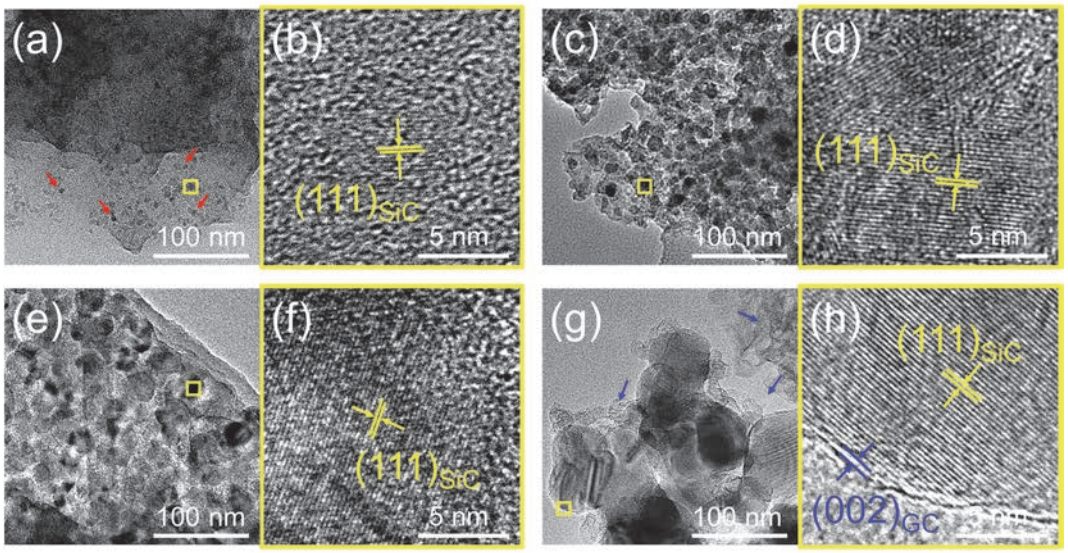

Figure 4.9 TEM images of the material formed with parameter combinations of (a) 0.81 nJ at 21 MHz, (c) 1.86 nJ at 9.0 MHz, (e) 2.91 nJ at 5.7 MHz, and (g) 3.96 nJ at 4.2 MHz. (b), (d), (f), and (h) are enlarged images of the areas indicated by the yellow square in (a), (c), (e), and (g), respectively.

However, the crystal size varied greatly depending on the parameter combination (Figure 4.10 (a)). For the track patterned with 0.81 nJ at 21 MHz, only SiC-NCs smaller than 20 nm were observed. With an increase in PE and decrease in RR, the distribution of crystal size becomes narrower, and for the track patterned with 3.96 nJ at 4.2 MHz, the crystal size of the observed SiC-NCs ranged from smaller than 10 nm to larger than 100 nm. The average crystal size was measured to be approximately 7.7 nm, 16.9 nm, 40.3 nm, and 49.2 nm, for the tracks patterned with 0.81 nJ at 21 MHz, 1.86 nJ at 9.0 MHz, 2.91 nJ at 5.7 MHz, and 3.96 nJ at 4.2 MHz, respectively. For the XRD spectra obtained from the structures, diffraction peaks corresponding to the (111), (220), and (311) planes of 3C-SiC were observed for all spectra at approximately 36, 60, and 72 degrees, respectively (Figure 4.9 (j)). As the PE increased and RR decreased, the relative diffraction intensity of the (111) peak of SiC increased, suggesting the existence of a greater quantity of SiC-NCs for the track patterned with 3.96 nJ at 4.2 MHz compared to the other tracks. Therefore, the difference in electrical property measured in Figure 4.8 is attributable to the difference in SiC-NCs, as the difference in graphitic carbon was not confirmed from the Raman spectra (Figure 4.7 (j,k)).

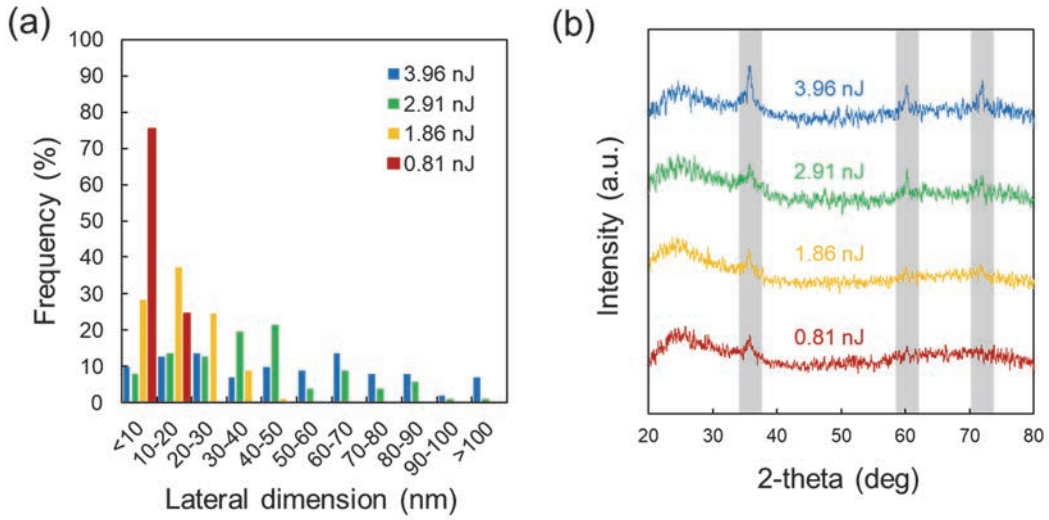

Figure 4.10 (a) Frequency of the measured crystal size of 100 observed SiC-NCs. (b) XRD spectra obtained from the tracks patterned with different parameter combinations.

Thus far, it was indicated that a low PE but high RR parameter combination (0.81 nJ at 21 MHz) results in a track with low SiC-NC content which exhibits a conducting property; whereas, a high PE but low RR parameter combination (3.96 nJ at 4.2 MHz) results in a track with high SiC-NC content which exhibits a semiconducting property. To further investigate the effect of parameter combinations on the electrical property, a track was patterned with a high PE and high RR parameter combination (3.96 nJ at 21 MHz). From the XRD spectrum obtained from the track patterned with 3.96 nJ at 21 MHz, diffraction peaks corresponding to the (111), (220), and (311) planes of 3C-SiC were also observed. Note that the diffraction intensity was substantially greater compared to that observed for the track patterned with a PE of 3.96 nJ at a RR of 4.2 MHz, suggesting the existence of a significantly greater quantity of SiC-NCs (Figure 4.11 (a)). Moreover, the small diffraction peak at 42 degrees corresponds to the (100) plane of graphitic carbon, and suggests that the quantity of graphitic carbon is also significantly greater. Despite the high content of SiC-NCs suggested by the XRD spectrum, evident semiconducting behavior was not confirmed for this track (Figure 4.11 (b,c)).

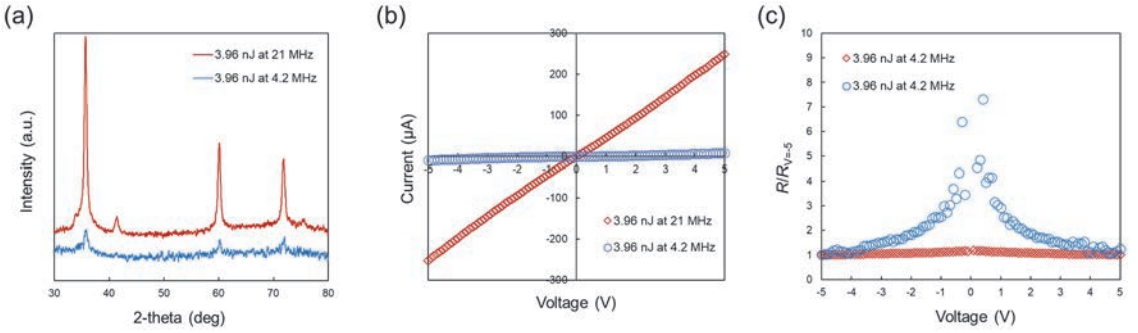

Figure 4.11 (a) XRD spectra, (b) I-V curves, and (c) change in relative electrical resistances with respect to applied voltage, for tracks patterned with a PE of 3.96 nJ at a RR of 21 MHz or 4.2 MHz.

4.3.2.3. Discussions on the transition in conducting regimes

As indicated by the material analyses thus far, the carbonaceous structure resulting from the LICG of PDMS is a composite structure consisting of two notable carbonaceous materials: graphitic carbon and SiC-NCs (Figure 4.12). As discussed in Section 2.4.1., the transition in the electrical conduction regime of the composite structure can be discussed in terms of the percolation threshold. The theoretical combinations of material concentrations can be simplified into the following four types: low graphitic carbon and low SiC-NC (i.e., both concentrations are below the percolation threshold), high graphitic carbon but low SiC-NC (i.e., only graphitic carbon concentration is above the percolation threshold), low graphitic carbon but high SiC-NC (i.e., only SiC-NC concentration is above the percolation threshold), and high graphitic carbon and high SiC-NC (i.e., both concentrations are above the percolation threshold). When both concentrations are below the percolation threshold, the resulting structure will be electrically insulating as neither conductive nor semiconductive networks are existent. On the other hand, when only the graphitic carbon concentration is above the percolation threshold, the resulting structure will exhibit a metal-like electrical property, distinctive of graphitic carbon. Moreover, when only the SiC-NC concentration is above the percolation threshold, the resulting structure will exhibit a semiconductor-like electrical property, distinctive of SiC. As the electron mobility of SiC-NC is significantly lower than that of turbostratic graphite, the overall electrical conductivity will be lower for such a composite structure. When both concentrations are above the percolation threshold, the resulting structure will once again exhibit a metal-like electrical property, as the electrons will preferentially conduct through the metal-like graphitic carbon.

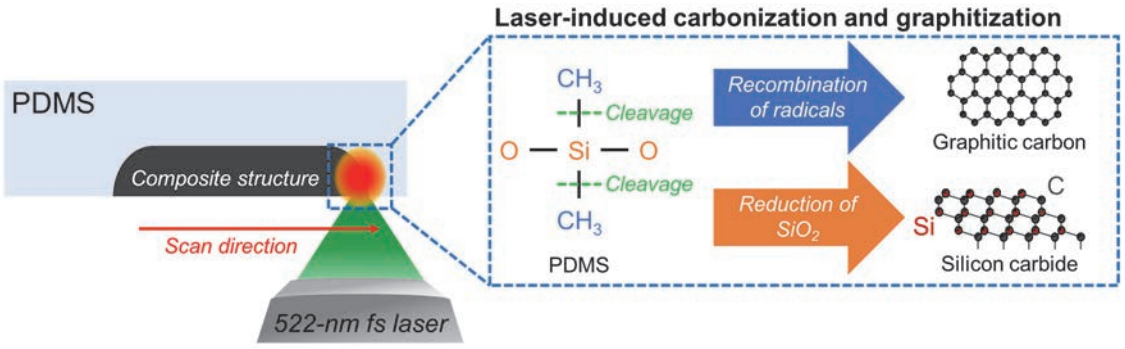

Figure 4.12 Schematic illustrating the LICG of PDMS into composite carbonaceous structures composed of graphitic carbon and SiC-NCs.

The parameter combinations in this study can be simplified into the following four types: low PE and low RR, low PE but high RR, high PE but low RR, and high PE and high RR. Summarizing the material analyses thus far, the relative concentrations of graphitic carbon and SiC-NCs and the overall electrical property of the resulting composite structure with the four types of parameter combinations can be organized by Table 4.1.

Table 4.1 Effect of parameter combinations on the resulting material composition.

PE	RR	Example	Graphitic carbon	SiC-NCs	Property
Low	Low	0.81 nJ at 4.2 MHz	No modification	No modification	N/A
Low	High	0.81 nJ at 21 MHz	Moderate	Low	Metal-like
High	Low	3.96 nJ at 4.2 MHz	Moderate	High	Semiconductor-like
High	High	3.96 nJ at 21 MHz	Very high	Very high	Metal-like

Considering that the tracks patterned with a low PE but a high RR exhibited a metal-like electrical property, it is indicated that the concentration of graphitic carbon was above the percolation threshold for a parameter combination of 0.81 nJ at 21 MHz (Figure 4.8 (a)). Therefore, as the Raman spectra for the track patterned with a low PE but a high RR (0.81 nJ at 21 MHz) was comparable with that for the track patterned a high PE but a low RR (3.96 nJ at 4.2 MHz), it can be assumed that the that the concentration of graphitic carbon was also above the percolation threshold for a parameter combination of 3.96 nJ at 4.2 MHz (Figure 4.7 (l)). However, for the track patterned with a high PE but a low RR a semiconductor-like electrical property was confirmed. This suggests that the percolation threshold for graphitic carbon was increased due to the formation of large SiC-NCs in greater quantities in the case of high PE but low RR parameter combinations (Figure 4.9 and Figure 4.10). Due to this, for example, a greater concentration and/or longer ribbons

of graphitic carbon are required to form a conductive network, increasing the percolation threshold (as discussed in Section 2.4.1.). Nonetheless, when the concentration of the graphitic carbon was significantly high, the resulting track exhibited a metal-like electrical property regardless of the high concentration of SiC-NCs (3.96 nJ at 21 MHz, Figure 4.11). Therefore, it can be concluded that the key to achieving semiconducting composite structures is to suppress graphitization while enhancing SiC-NCs formation. Considering that the electrical conductivity values of the patterned carbonaceous structures were well below that of pure graphite, as discussed in Section 4.2.2., it can be expected that perfect ohmic contact is not achieved even for structures which linear I-V curves were measured. In other words, it can be expected that in the case of all structures the percolation network is composed of both graphitic carbon and SiC-NCs. Therefore, it can be deduced that the differences in measured I-V curves are a result of the differences in the ratios of the material compositions of the conductive network, rather than the presence or absence of a conductive network.

Analyzing the parameter combinations which yielded high SiC-NC concentrations, the PE may have an important role in SiC formation in the case of LICG. As also discussed in Section 2.5.3., it has been widely accepted that by utilizing ultrashort-pulsed lasers the efficient crystallization of various materials can be driven by laser-induced shockwaves.[180,181] For the thermalization of materials due to ultrashort-pulse irradiation, the generated shockwaves can induce instantaneous pressures in the MPa and GPa regime, particularly for shorter pulse durations and higher PEs. Since high-temperature and high-pressure conditions are generally favorable for the nucleation and growth of SiC, it is presumed that SiC-NCs formed more easily by irradiating fs laser pulses with higher PEs. In the case of graphitic carbons, there are several reports suggesting that unidirectional pressure may assist in the rearrangement of carbon atoms during graphitization; however, the facilitation of graphitization by radial pressure as those induced via laser irradiation has been inconclusive (as discussed in Section 2.5.3.). Moreover, the low RR may also play a role in the enhanced formation of SiC-NCs, as the heating rate can be slowed down to allow for more nucleation. However, if this was the main reason for the facilitation of SiC-NC formation, it should also aid in the formation of graphitic carbon equally. In this study, the range of PEs and RRs, as well as the number of tunable laser parameters, was limited by the current laser setup. In the future, by designing a new laser setup, which incorporates a laser with higher output powers or optical elements that allows, for example, pulse duration or beam shape modulation, the influence of a wider range of laser parameters on the LICG of PDMS can be further explored to uncover more details regarding the formation mechanism of carbonaceous materials.

4.4. Summary

In Chapter 4, the electrical property of the carbonaceous structure formed by the LICG of PDMS by HR-fs LDW was investigated. Furthermore, the relationship between the carbonaceous material and the overall electrical property of the carbonaceous structure was discussed. Although the carbonaceous structure patterned by scanning tightly focused fs laser pulses was composed of graphitic carbon, electrical conductivity was not confirmed. However, it was demonstrated that conductive carbonaceous structures could be successfully patterned by suppressing laser ablation using the defocusing method. By suppression in laser ablation, progresses carbonization and graphitization, leading to the formation of large crystals of graphitic carbon. Moreover, even without using the defocusing method, conductive carbonaceous structures were patterned by raster scanning. It was discussed that the subsequent laser scans increased the crystal size and/or concentration of graphitic carbon leading to the successful formation of a conductive network. Depending on the parameter combinations for patterning (i.e., PE and RR), the electrical property of the carbonaceous structures patterned by the LICG of PDMS transitioned from the conducting regime to the semiconducting regime. Semiconductive carbonaceous structures were patterned by suppressing graphitization while progressing SiC formation through the combination of laser parameters. It was discussed that the PE may have an important role in SiC formation, as higher PEs can assist the crystallization of materials by laser-induced shockwaves.

The contents of this chapter were reused and built upon the following references with permission from John Wiley & Sons ©2021, the Royal Society of Chemistry ©2020, and the American Chemical Society ©2023, respectively.

- Hayashi, S., Morosawa, F. & Terakawa, M. Laser Direct Writing of Highly Crystalline Graphene on Polydimethylsiloxane for Fingertip-Sized Piezoelectric Sensors. *Adv Eng Mater* **23**, 2100457 (2021).
- Hayashi, S., Morosawa, F. & Terakawa, M. Synthesis of silicon carbide nanocrystals and multilayer graphitic carbon by femtosecond laser irradiation of polydimethylsiloxane. *Nanoscale Adv* **2**, 1886–1893 (2020).
- Hayashi, S. & Terakawa, M. Direct Writing of Fluorescent Semiconducting Nanoparticles on Polydimethylsiloxane by Ultrashort-Pulsed Laser Processing: Implications for Electronic and Photonic Device Fabrication. *ACS Appl Nano Mater* **6**, 2125–2132 (2023).

5. Electrical application of carbonaceous structures

5.1. Introduction

The spatially selective and high-resolution patterning of electrically conductive carbonaceous structures directly on an elastomer offers the rapid fabrication of flexible electronics. The aim of Chapter 5 is to reveal the applicability of the carbonaceous structures formed by the LICG of PDMS using a high RR fs laser towards electrical applications. When considering the applicability of the electrically conductive carbonaceous structures for flexible electronics, the assessment of the effects of mechanical deformations on the electrical conductance is crucial. For example, if the electrical conductance changes according to mechanical deformations, in other words the carbonaceous structures exhibit piezoresistive property, such structures can be utilized for mechanical sensing. In Section 5.2., the piezoresistive property of the carbonaceous structures patterned by LICG will be indicated, and the carbonaceous structures will be applied towards pressure sensing. Furthermore, the patterning capabilities of LICG will be explored in Section 5.3., and the directional sensing of strain using the carbonaceous structures will be demonstrated.

5.2. Fabrication of a sensitive micro-pressure sensor

5.2.1. Materials and methods

5.2.1.1. Material preparation

A 1:1 mixture of polymer to curing agent of optically-cured KER-4690 PDMS (Shin-Etsu Chemical Co., Ltd., Japan) was prepared. The mixture was poured into a rectangular mold and degassed in vacuum to remove any air bubbles trapped during the mixing procedure. Furthermore, the mixture was cured under a 365-nm ultraviolet lamp for 30 min to prepared PDMS sheets. The PDMS sheets prepared in this study were approximately 2 mm in thickness. Before irradiation experiments, the surfaces of PDMS were washed with ethanol to remove any debris.

5.2.1.2. Laser irradiation

Laser irradiation experiments were conducted using a High Q-2 fs laser (Spectra-Physics, USA) which generated 192-fs laser pulses with a central wavelength of 522 nm (second harmonic wave of a 1045-nm fs laser) at a RR of 63 MHz. PDMS sheets were placed onto a cover glass with a 140-μm spacing (Figure 3.14). Then, laser pulses were focused onto the bottom surface of the PDMS sheet using a 20× objective lens, with a NA of 0.4. A three-axis (*xyz*) translation stage was utilized to scan laser pulses in three dimensions. The defocusing method was used for the patterning of all structures in this section (DD = 150 μm), and the laser power and scanning speed was 100 mW and 2.00 mm/s, respectively. All irradiation experiments were conducted in ambient conditions.

5.2.1.3. Characterization

OM images were obtained using a MS-100 optical microscope (Asahikogaku, Japan) and an HRX-01 optical microscope (HIROX, Japan). Electrical conductivity measurements of the structures were obtained using a 2401 digital source meter (Keithley, USA). Before electrical conductivity measurements, a gold electrode with a thickness of approximate 50 nm was deposited on both ends of the structures (total of 2 electrodes). A probe was contacted onto each of the gold electrodes deposited on the ends, and the electrical resistance was measured by the two-probe method. For pressure sensing experiments, objects with varying masses and surface areas were placed on the structure, and the change in electrical resistance was recorded after sufficient time has passed for the electrical resistance to become stable (>> 3 sec). A constant voltage of 5 V was applied to the structures. The pressure *p* induced by gravitational force *G* for a placed object with a surface area of *S* was approximated by Eq. 5.1 as,

$$p = \frac{G}{S} = \frac{mg}{lw} \qquad \text{Eq. 5.1}$$

where *m* is the mass of the object, *g* is the gravitational acceleration constant, *l* is the length of the object, and *w* is the width of the object. Mass of the object was measured using an AUX 120 digital analytical balance (Shimadzu, Japan). For heart rate (HR) sensing experiments, the structure was placed on various locations of a voluntary human subject (structure-side facing the human subject), and the change in electrical resistance was recorded. To prevent electrical shocks, a piece of dielectric tape was placed between the structure and the voluntary human subject. All physiological data were obtained from the same voluntary human subject, with consent. Necessary procedures to perform human

experiments were followed, and approval from an institutional ethics committee was obtained.

5.2.2. Results and discussions

5.2.2.1. Piezoresistive properties of the carbonaceous structures

Conductive carbonaceous tracks were patterned on the surface of a PDMS sheet by HR-fs LDW using the defocusing method (Figure 5.1 (a)). When a downward pressure was applied to and released from the track, a change in relative electrical resistance with respect to the initial electrical resistance R/R_0 was confirmed only when the pressure was applied, indicating evident piezoresistive property (Figure 5.1 (b)). There are two distinctively different mechanisms that contribute to the piezoresistive property of carbonaceous structures: change in the distance between nanodomains or macrodomains. In the case of nanodomains, the applied pressure can alter the distance between the graphitic carbon nanodomains of the composite structure leading to the brief formation of a conducting network during compression. Moreover, even if the graphitic carbon nanodomains do not come into contact, if the distance is sufficiently close, electrons can conduct via tunneling effects. Therefore, piezoresistive properties dominated by the changes in the nanodomains typically exhibits in a decrease in electrical resistance with respect to applied pressure. On the other hand, in the case of macrodomains, the applied pressure can alter the porous structure, forming or severing conductive pathways.[182,183] As the end number of conductive pathways depend heavily on various properties of compressed structure (i.e., porosity, electrical conductivity, and flexibility), macrodomains can exhibit both an increase and decrease in electrical resistance with respect to applied pressure. Nonetheless, as the electrical resistance did not decrease with respect to applied pressure in this study, it can be concluded that the piezoresistive property for the carbonaceous structures are dominated by the changes in the macrodomains.

The PDMS sheet with a track patterned on the surface will be hereby referred to as sensor. The sensor was able to detect a pressure as low as approximately 0.1 Pa (Figure 5.1 (b)), and exhibited a linear response to pressure in the investigated range (0 Pa–1 kPa) (Figure 5.1 (c)). Moreover, the sensor exhibited a sensitivity of approximately 2.2 kPa^{-1}, a response time of < 50 ms, and a recovery time of < 50 ms. The mechanical durability of the sensor was assessed by conducting 1000 compression cycles at a loading pressure of approximately 250 Pa (Figure 5.1 (d)). The R/R_0 at the end of the compression cycles

were comparable to those at the beginning, indicating high stability and repeatability of the sensor (Figure 5.1 (e)). Furthermore, the electrical resistance at the un-strained state was minimal even after 1000 compression cycles (< 0.1%), indicating high mechanical durability.

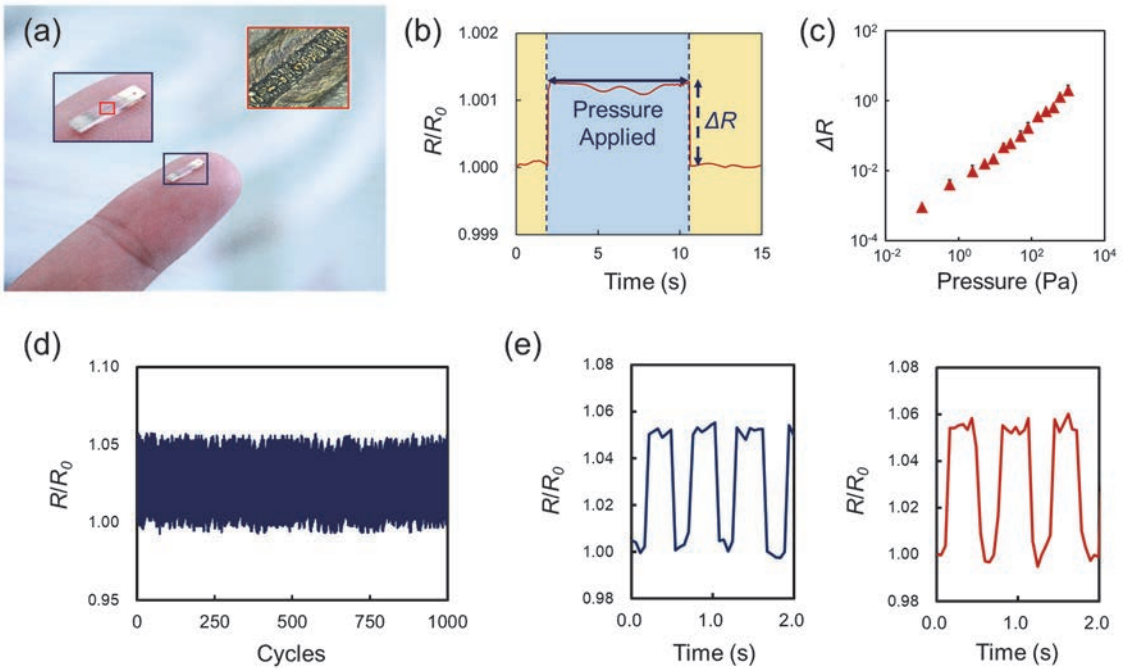

Figure 5.1 (a) Photograph of fabricated fingertip-sized pressure sensor. Blue inset is a higher-magnification photograph of the sensor. Red inset is an OM image of the track. (b) Relative changes in electrical resistance R/R_0 to applied pressure (applied pressure: approximately 0.1 Pa). (c) Sensor responses for various applied pressures. The error bars indicate the standard deviation for n = 5 samples. (d) Compression cycles conducted on the sensor at a loading pressure of approximately 250 Pa, and (e) enlarged plots of the first three (left) and last three cycles (right).

The high performance indicated by the pressure sensor fabricated by the LICG of PDMS, regardless of the small size, is attributable to the high elasticity of PDMS. An elastic substrate facilitates greater deformation of the substrate for the same force, resulting in improved sensitivity. This concept has been presented in previous reports, in which electrically conductive carbonaceous structures patterned on PI by LICG were subsequently transferred onto a PDMS sheet to improve the sensitivity of the resulting strain sensor.[184,185] In this study, the patterning of conductive carbonaceous structures directly on a PDMS sheet was achieved without pre- and post-procedures, such as transferring. Furthermore, complex architectures, such as 2D or multilayered architectures reported previously, were not required in this study to achieve a highly-

sensitive pressure sensor owing to the inherent elasticity of PDMS.[83,182,186] The current response and recovery times in this study were limited by the sampling rate of the utilized multimeter (approximately 50 ms). However, the use of a higher-resolution multimeter and proper assessment of the sensor performance can be expected in the future (i.e., faster response and recovery times).

For practical applications, a simple demonstration of the pressure mapping was performed by placing five independent sensors in an array orientation. Various objects (i.e., screw (approximately 1.0 g), oral tablet (approximately 0.3 g), magnetic stirring bar (approximately 0.5 g), and cotton ball (< 0.001 g)) were placed on the 5-sensor array, and the R/R_0 at each sensor (i.e., position) was measured (Figure 5.2 (a–d)). The positions where the changes in electrical resistance was measured agreed well with the positions where the contact between the object and the sensor was visibly confirmed. In addition to the contact positions, the relative weight distribution of the objects was clearly identified, where a larger R/R_0 indicated a greater weight and vice versa. For example, in the case of the screw, because the head of the screw is considerably heavier than its tip, a significantly larger R/R_0 was measured at contact position two compared to position four (Figure 5.2 (a)). However, in the case of the oral tablet, because the weight distribution is balanced between the left and right sides of the object, a similar R/R_0 was measured at contact positions two and three (Figure 5.2 (b)). The demonstrated five-sensor array is capable of subtle detection, in addition to the weight distribution of small and extremely lightweight objects (Figure 5.2 (c,d)), indicating its potential for electronic skin applications. In this study, the width of each sensor was approximately 2.0 mm and the distance between each sensor was approximately 1.0 mm. The width of the carbonaceous track that were used for sensing was approximately 100 μm; hence, by preparing PDMS sheets with sub-millimeter widths, the width of each sensor could be significantly reduced without significantly altering the sensing capabilities. Furthermore, by simply placing each sensor closer, a higher resolution mapping of pressure can be realized for tactile sensor applications.

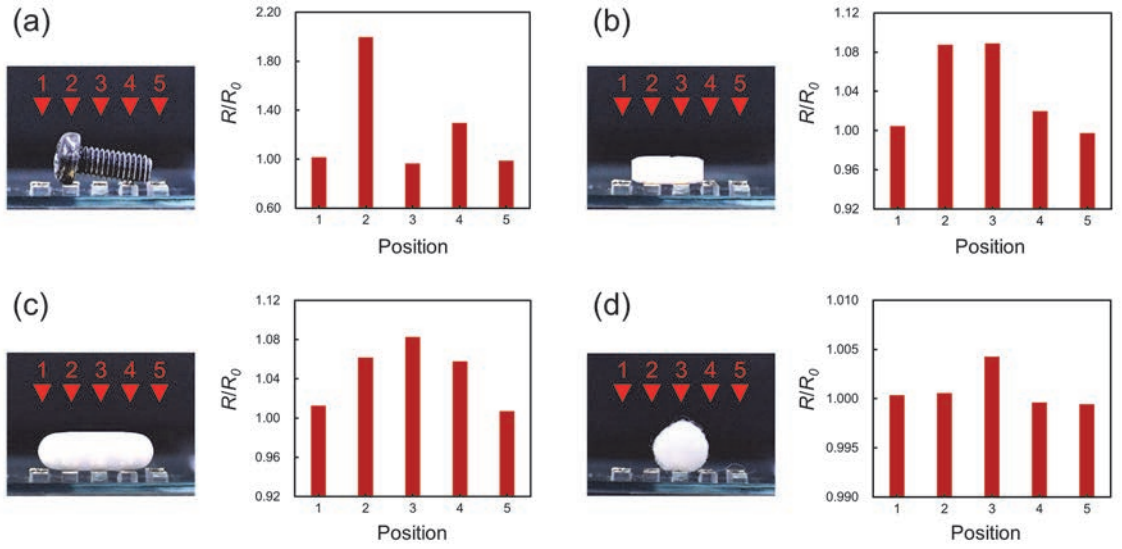

Figure 5.2 Photographs of five-sensor arrays with various objects placed on top, such as (a) screw, (b) oral tablet, (c) magnetic stirring bar, and (d) cotton ball, and the respective R/R_0 at each position for each object.

5.2.2.2. Elastic PDMS-based health monitor

To demonstrate the potential for health-monitoring applications, the sensor was used for human pulse-wave monitoring. A sensor was placed on the wrist and at the backside of the palm of a human subject, indicated as A and B in Figure 5.3 (a), respectively, and the R/R_0 was measured. Evident pulses were detected by the sensor placed on the wrist as the radial artery was located at A (Figure 5.3 (b), blue). In contrast, no pulses were detected by the sensor placed on the backside of the palm, as there were no major arteries located at B (Figure 5.3 (b), red). The obtained pulse waveform is similar to the typical two-peaked pulse waveforms previously reported for radial arteries.[187,188] Moreover, a HR of approximately 72 beats/min (bpm) can be estimated using the obtained waveform, which is within the range of an average male HR in the rest state.

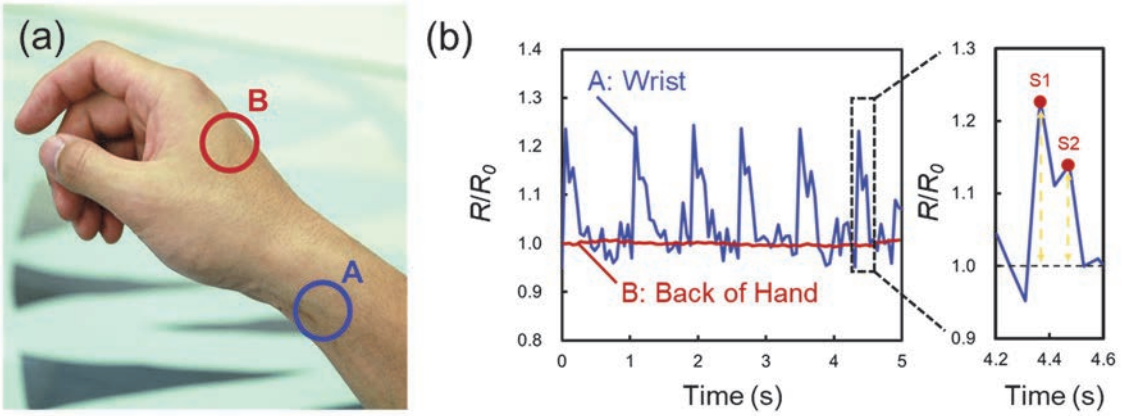

Figure 5.3 (a) Photograph indicating the locations where the sensor was placed. Note that the sensor surface with the patterned structures faced the human subject's skin. (b) Pulse waveforms obtained when the sensor was placed on the wrist and at the backside of the palm (left). Enlarged plot of a single pulse, indicating two peaks that originate from the first *S1* and second *S2* systolic pressure (right).

The two peaks of the radial artery pulse originate from the increase in pressure due to the ejection of blood from the heart to the fingertips, called the first systolic pressure *S1*, and the reflection of blood back from the fingertips to the heart, called the second systolic pressure *S2*.[188] It has been previously recognized that, the ratio between the *S1* and *S2* peak intensities, referred to as the augmentation index *AI* expressed by Eq. 5.2 as,

$$AI = \frac{S2}{S1} \qquad \text{Eq. 5.2}$$

is an important clinical information and an effective method to assess the stiffness of the radial artery.[189] The radial *AI* calculated from the obtained pulse waveform was approximately 56%, which corresponds to the reference values of a male in his twenties, and is consistent with the age and gender of the human subject.[189]

To further demonstrate the sensitivity and advantages of the fabricated sensor, a ring-shaped HR monitor composed entirely of PDMS was developed (Figure 5.4 (a)). The radialis indicis artery is a branch of the radial artery that supplies blood to the index finger. Similar to the mechanism of detecting pulses at the wrist, by placing the sensor at the location of radialis indicis artery, although extremely minimal, the changes in electrical resistance corresponding to the swelling of the artery (i.e., pulse) could be measured at the index finger. The obtained pulse waveform from the index finger of the human subject at rest is shown in Figure 5.4 (b). Two-peaked pulse waveforms, comparable to those obtained at the wrist, were also obtained from the index finger using the sensor. As expected, the R/R_0 measured for the index finger were significantly small compared to the wrist, as the artery is thinner at the finger and the pressure is substantially less. A

different HR of approximately 85 bpm can be estimated for the same human subject, which is also within the range of a healthy male in his twenties. Considering that the pressure measurements at the wrist and finger were conducted on different dates, the discrepancies in the rested-state HR can be attributed to various environmental factors, such as the time-of-day (i.e., before or after noon), intake of caffeine, etc. Nonetheless, for the pulse waveform obtained from the same subject following hard-intensity exercise (i.e., running up and down six flights of stairs), an increase in arterial pressure, larger between the wrist and, and notably faster HR (approximately 136 bpm) was observed, indicating the potential of the sensor in health monitoring applications (Figure 5.4 (c)).

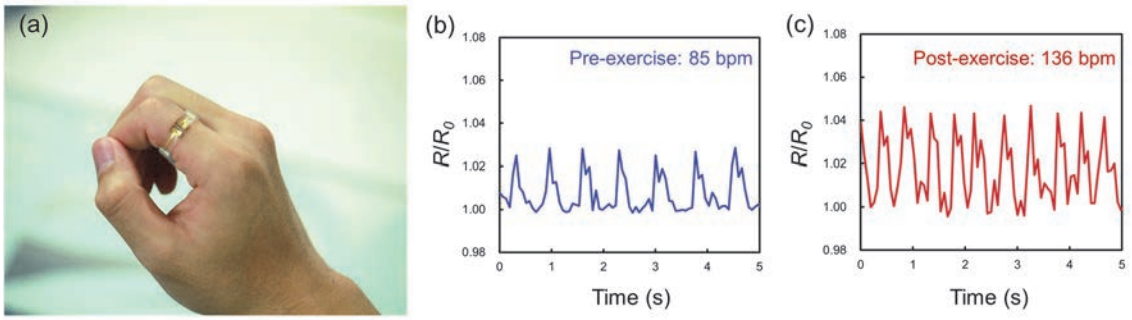

Figure 5.4 (a) Photograph of PDMS-based ring-shaped HR monitor. Pulse waveform obtained from the index finger, (b) before and (c) after exercise using the ring-shaped HR monitor.

5.3. Fabrication of an anisotropic strain sensor

5.3.1. Materials and methods

5.3.1.1. Material preparation

To prepare thinner PDMS sheets, a 5:5:1 mixture of polymer to curing agent of optically-cured KER-4690 PDMS (Shin-Etsu Chemical Co., Ltd., Japan) to hexane was prepared. 3.0 mL of the mixture was poured into a rectangular mold with base dimensions of 3.5 cm × 6.5 cm and degassed in vacuum to remove any air bubbles trapped during the mixing procedure. Furthermore, the mixture was cured under a 365-nm ultraviolet lamp for 30 min to prepared PDMS sheets. The PDMS sheets prepared in this study were approximately 680 μm in thickness. Before irradiation experiments, the surfaces of PDMS were washed with ethanol to remove any debris.

5.3.1.2. Laser irradiation

Laser irradiation experiments were conducted using a High Q-2 fs laser (Spectra-Physics, USA) which generated 192-fs laser pulses with a central wavelength of 522 nm (second harmonic wave of a 1045-nm fs laser) at a RR of 63 MHz. PDMS sheets were placed onto a cover glass with a 140-μm spacing (Figure 3.14). Then, laser pulses were focused onto the bottom surface of the PDMS sheet using a 20× objective lens, with a NA of 0.4. A three-axis (*xyz*) translation stage was utilized to scan laser pulses in three dimensions. The defocusing method was not used for the patterning of all structures in this section (DD = 0 μm), and the laser power and scanning speed was 150 mW and 2.00 mm/s, respectively. All irradiation experiments were conducted in ambient conditions.

5.3.1.3. Characterization

OM images were obtained using a MS-100 optical microscope (Asahikogaku, Japan). SEM images were obtained using a Inspect F50 scanning electron microscope (FEI, USA). Electrical conductivity measurements of the structures were obtained using a 2401 digital source meter (Keithley, USA). Before electrical conductivity measurements, a gold electrode with a thickness of approximate 72 nm was deposited on both ends of the structures (total of 2 electrodes). A probe was contacted onto each of the gold electrodes deposited on the ends, and the electrical resistance was measured by the two-probe method. Surface morphology observations and electrical conductivity measurements for the bent state were conducted by placing the PDMS sheets onto curved polyvinyl chloride platforms with different radii.

5.3.2. Results and discussions

5.3.2.1. Piezoresistive properties of the 2D structures

As raster scanning allows for the patterning of electrically conductive 2D carbonaceous structures without defocusing, two types of 8 mm × 3 mm structures, S1 and S2, were patterned on the PDMS surface with different laser scanning directions. For S1, laser pulses were raster scanned in the longitudinal direction (8 mm direction), as shown in Figure 5.5 (a). On the other hand, for S2, laser pulses were raster scanned in the transversal direction (3 mm direction), as shown in Figure 5.5 (b). The hatch spacing was 25 μm for the patterning of both S1 and S2. Figure 5.5 (c) shows a SEM image of the

surface morphology of the patterned structure. Unidirectional grooves with directions and periods corresponding to the scanning direction and hatch spacing were observed on the surface. As the DD was 0 μm for the patterning of this structure, such grooves are attributable to laser ablation, consistent with Figure 3.15. Moreover, bridges that connect adjacent grooves were observed on the surface. The formation of a bridge is attributable to the melting and subsequent solidification of materials. However, it should be noted that PDMS, graphitic carbon, nor SiC, have a melting point, and therefore, the bridging is assumed to be due to the melting and solidification of intermediate products. For example, the formation of silica particles was observed on the surface when tightly focused fs laser pulses were scanned over the PDMS surface (Figure 3.16 and Figure 3.19). The thermalization of such silica particles due to subsequent laser scanning may result in the melting and merging of neighboring particles to form a large molten pool of silicon-based products. If the molten pool is large enough, it can crossover adjacent grooves and eventually solidify to form bridges that cross the grooves. During thermalization of the particles, other carbon-based products can be trapped within the molten pool to form a bridge that is composed of various materials.

Bending tests were performed on the patterned 2D structures by measuring the electrical resistance when bent to various radii. Note that both S1 and S2 were bent in the longitudinal direction. Figure 5.5 (d) shows the R/R_0 when the structures were bent to various bending radii. For both S1 and S2, an increase in R/R_0 with respect to the decrease in bending radii was measured. S1 initially exhibited a gradual increase in R/R_0 for bending radii greater than 38 mm. However, when the bending radii was < 38 mm, the R/R_0 increased drastically to more than 2000%. Contrarily, S2 exhibited a significantly smaller increase in R/R_0 throughout the entire range of bending radii investigated in this study, even for bending radii < 38 mm. In other words, the R/R_0 was significant when the 2D structures were bent parallel to the laser scanning direction; whereas, was almost negligible when the 2D structures were bent perpendicularly to the laser scanning direction. This indicates that the 2D structures patterned by raster scanning exhibits directional sensitivity to strain, according to the relationship between laser scanning direction for patterning and the direction of applied strain.

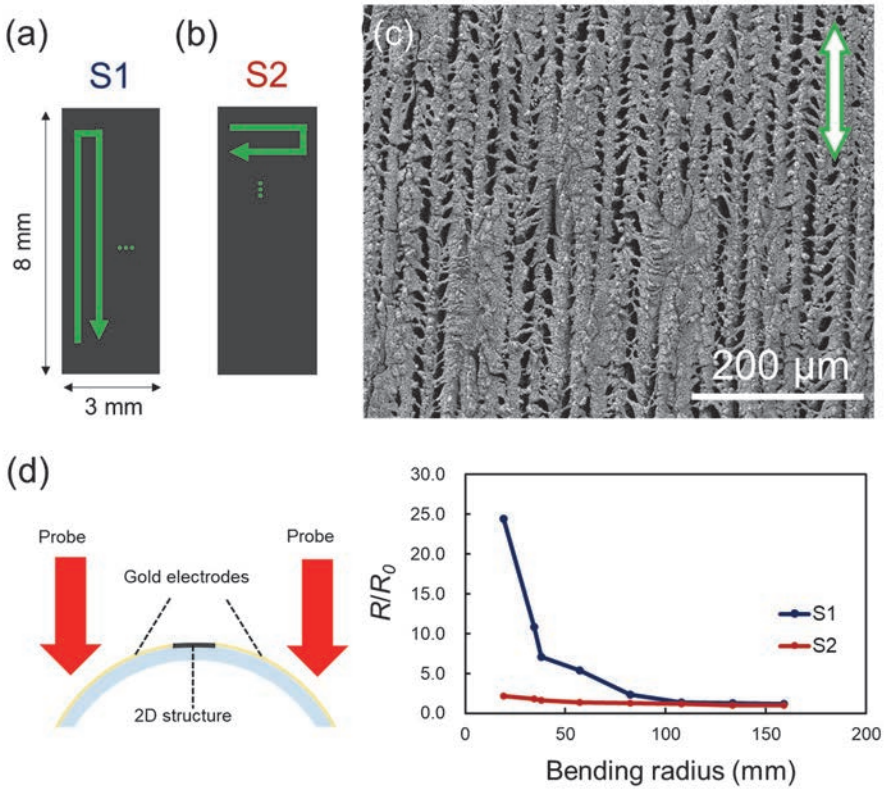

Figure 5.5 (a,b) Schematics of the two types of 2D structures patterned with different laser scanning directions: (a) S1 was patterned by scanning in the longitudinal direction (8 mm) and (b) S2 was patterned by scanning in the transversal direction (3 mm). (c) SEM image of the surface of the patterned 2D structure. The green double-headed arrow indicates the laser scanning direction. (c) R/R_0 of the 2D structures when bent to different radii.

5.3.2.2. Discussion of the reason for anisotropy

To discuss the reason for the directional sensitivity to strain, the surfaces of the 2D structures during bending were observed by SEM. SEM images of the surfaces, for both S1 and S2, are shown in Figure 5.6. Note that the same location of the same sample at different bending radii was observed. For bending radii of 134 mm and 83 mm, no obvious differences in the surface morphology were observed for both S1 (Figure 5.6 (a,b)) and S2 (Figure 5.6 (f,g)), compared to the un-strained state (Figure 5.5 (c)). For bending radii of 38 mm and 19 mm, the generation of large cracks perpendicular to the laser scanning direction were observed on the surface of S1, Figure 5.6 (c,d). When the 2D structure was returned to the un-strained state, such cracks could not be identified (Figure 5.6 (e)). On the contrary, the generation of such cracks were not observed on the surface of S2 (Figure 5.6 (h,i)). Therefore, the substantial increase in R/R_0 at small

bending radii measured for S1 ((Figure 5.5 (d)) is attributable to the generation of the large cracks perpendicular to the laser scanning direction. As such cracks did not generate even at small bending radii in the case of S2, the measured increase in R/R_0 was minimal.

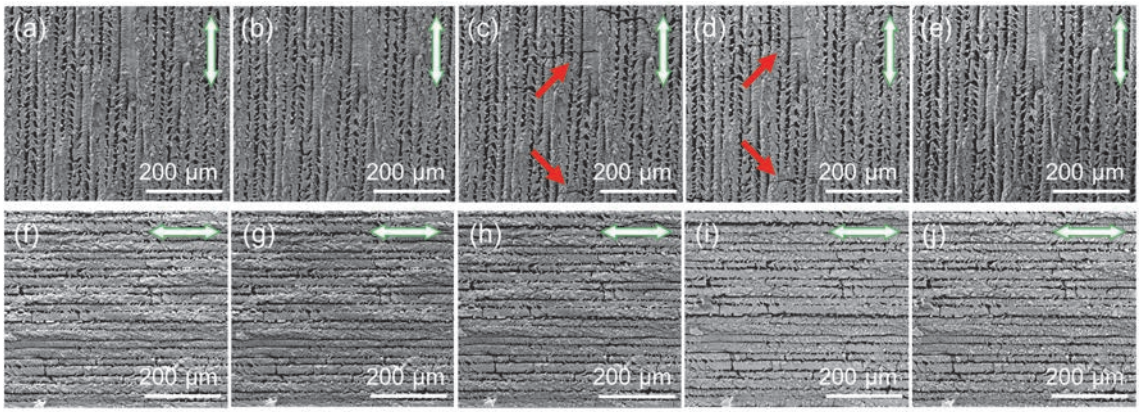

Figure 5.6 SEM images of the surface of the 2D structures when bent to different radii. S1: (a) 134 mm, (b) 83 mm, (c) 38 mm, and (d) 19 mm. S2: (f) 134 mm, (g) 83 mm, (h) 38 mm, and (i) 19 mm. (e) and (j) are SEM images of the surface when returned to the un-strained state for S1 and S2, respectively. Large cracks can be observed on the surface in (d) and (d), indicated by the red arrows. The green double-headed arrow indicates the direction of laser scanning.

It has been previously reported that the texturing of a surface with grooves enhances the mechanical flexibility and the prevention of fracturing of structures.[190,191] As the grooves are only formed along one direction of the 2D structures, the stiffness of the structure will be significantly decreased only in one direction. Accordingly, the existence of periodic grooves perpendicular to the bending direction for S2 will lower the stiffness of the structure, and in-turn, enhance the mechanical flexibility and prevent the generation of large cracks. Therefore, the anisotropy of the 2D structures is attributable to the periodic unidirectional grooves on the surface. In the future, it can be expected that by tuning the depth as well as the period of the formed grooves via laser parameters, such as the laser power and hatch spacing, the optimization of surface-textures may be achieved to further tune the directional sensitivity of the structures to strain. Moreover, by tuning the thickness of the PDMS sheet, which is currently approximately 700 μm, as well as the 2D structure, which is currently approximately 60 μm, the sensitivity of the fabricated structures to strain may be also tuned.

The effect of repeated bending on the 2D structures was evaluated by subjecting both S1 and S2 to 10 bending cycles. The 2D structure was bent to a specific bending radius (either, 134 mm, 83 mm, or 35 mm), and then the 2D structure was returned to the un-strained state to measure the change in electrical resistance at the un-strained state R_0'/R_0

(Figure 5.7). In the case of bending cycles conducted with a bending radius of 134 mm, no apparent change in electrical resistance was measured after 10 cycles (R_0'/R_0<2%), for both S1 and S2. In the case of bending cycles conducted with bending radii of 83 mm and 35 mm, R_0'/R_0 increased by 20% to 30% after 10 bending cycles for S1; while, R_0'/R_0 was relatively constant even after 10 bending cycles for S2.

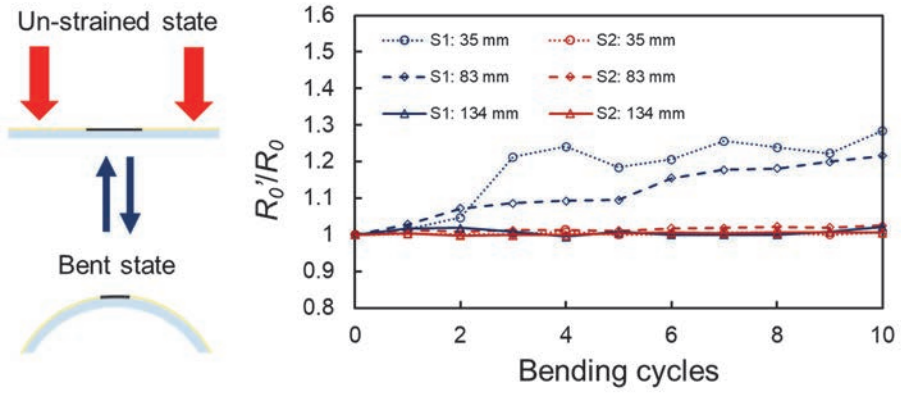

Figure 5.7 Change in R_0'/R_0 with repeated bending (10 cycles) for different bending radii (35 mm, 83 mm, 134 mm).

As indicated in Figure 5.6, the significant changes in electrical resistance in the case of small bending radii is due to the generation of large cracks. Therefore, for S1, with repeated bending to such small bending radii (83 and 35 mm) it is assumed that the structural destruction due to additional generation and propagation of cracks lead to the increase in electrical resistance. In the case of larger bending radii (134 mm), since large cracks did not generate, the electrical resistance did not increase with more cycles. Moreover, for S2, it is expected that since large cracks did not generate for any of the tested bending radii, there was no significant change in electrical resistance with repeated bending. Nonetheless, considering that S1 was progressively destroyed due to repeated bending to small bending radii, the increase in electrical resistance at the flat state after 10 bending cycles was relatively small (i.e., approximately 30% increase for a bending radius of 35 mm). This could be explained by the fact that, although the cracks are still existent, when the structures are returned to the flat-state, the opposite walls of the cracks can re-contact without significant distortion (Figure 5.6 (f,k)), restoring conductivity. Nonetheless, such generation of cracks may be detrimental for the repeated used, and the overall durability of the sensor when considering commercial applications. However, as a fs laser is used for the fabrication of the strain sensors mentioned in this study, by fabricating such sensors inside PDMS the durability may be significantly improved allowing for commercial applications in the future.

5.4. Summary

In Chapter 5, it was revealed that the carbonaceous structures patterned by the LICG of PDMS exhibit piezoresistive property, and the applicability of the structures for mechanical sensing was indicated. Using the defocusing method, a highly sensitive micro-pressure sensor was fabricated by patterning a track with a single laser scan. The fabricated sensor was capable of not only detecting the relative weight distribution of small objects, but also monitoring subtle vital signs of a human subject (i.e., HR). Moreover, without using the defocusing method, an anisotropic strain sensor was fabricated by patterning a 2D structure with multiple laser scans. Depending on if the 2D structure was bent parallel or perpendicular to the laser scanning direction, the structure exhibited a contrastive piezoresistive response. The periodic unidirectional grooves formed on the surface as a result of scanning tightly focused fs laser pulses was considered to contribute to the directional sensitivity. Depending on the patterning scheme (i.e., defocusing or focusing, single scan or raster scan), strain sensors with different functionalities (i.e., miniature size, high sensitivity, or directional sensing) can be easily fabricated, indicating the versatility of the LICG of PDMS for the fabrication of mechanical sensors. Moreover, as the PDMS substrate can be prepared in any shape and/or thickness, the fabrication of highly customized PDMS-based healthcare devices may be realized in the future owing to the LICG of PDMS.

The contents of this chapter were reused and built upon the following references with permission from John Wiley & Sons ©2021 and the Optica Publishing Group ©2019, respectively.

- Hayashi, S., Morosawa, F. & Terakawa, M. Laser Direct Writing of Highly Crystalline Graphene on Polydimethylsiloxane for Fingertip-Sized Piezoelectric Sensors. *Adv Eng Mater* **23**, 2100457 (2021).
- Hayashi, S., Nakajima, Y. & Terakawa, M. Strain sensing using electrically conductive structures fabricated by femtosecond-laser-based modification of PDMS. *Opt Mater Express* **9**, 2672 (2019).

6. Towards optical applications

6.1. Introduction

LICG offers the simultaneous synthesis and patterning of graphitic carbon; however, to date, most, if not all, studies regarding LICG has been concentrated on electrical applications and aimed to pattern large crystals of graphitic carbon. Over the past decade, carbon-based QDs, particularly GQDs, have emerged as a promising new class of cadmium-free QDs to be used towards a variety of optical applications. However, two major issues have been hindering the development of GQDs: (1) complex synthesis procedures (i.e., initial preparation of precursors, time-consuming post-treatment processes) and (2) restrictions of conventional patterning techniques (i.e., not suitable for organic materials, limited to 2D planar patterning). As the formation of large crystals of graphitic carbon can be easily achieved by LICG, the aim of Chapter 6 is to explore the possibility of using LICG for the patterning of small fluorescent crystals of graphitic carbon, or GQDs. In Section 6.2., the patterning of fluorescent carbonaceous structures composed of GQDs by the LICG of PDMS will be demonstrated. Furthermore, in Section 6.3., the applicability of the fluorescent carbonaceous structures for optical applications will be indicated.

6.2. Formation of fluorescent carbonaceous structures

6.2.1. Materials and methods

6.2.1.1. Material preparation

A 1:1 mixture of polymer to curing agent of optically-cured KER-4690 PDMS (Shin-Etsu Chemical Co., Ltd., Japan) was prepared. The mixture was poured into a rectangular mold and degassed in vacuum to remove any air bubbles trapped during the mixing procedure. Furthermore, the mixture was cured under a 365-nm ultraviolet lamp for 30 min to prepared PDMS sheets. The PDMS sheets prepared in this study were approximately 2 mm in thickness. Before irradiation experiments, the surfaces of PDMS were washed with ethanol to remove any debris.

6.2.1.2. Laser irradiation

Laser irradiation experiments were conducted using a High Q-2 fs laser (Spectra-Physics, USA) which generated 192-fs laser pulses with a central wavelength of 522 nm (second harmonic wave of a 1045-nm fs laser) at a RR of 63 MHz. The defocusing method was not used for the patterning of all structures in this section. PDMS sheets were placed onto a cover glass with a 140-μm spacing (Figure 3.14). Then, laser pulses were focused onto the bottom surface of the PDMS sheet using a 20× objective lens, with a NA of 0.4. The defocusing method was not used for the patterning of all structures in this section (DD = 0 μm), and the laser power was 150 mW. All irradiation experiments were conducted in ambient conditions.

6.2.1.3. Characterization

2D fluorescence images were obtained using an Eclipse Ti-E (Nikon, Japan) and a BZ-X800 (Keyence, Japan) fluorescence microscope. X-ray photoelectron spectroscopy (XPS) spectra were obtained using an JPS-9010 X-ray photoelectron spectrometer (JEOL, Japan). FTIR spectra were obtained using an Alpha Fourier transform infrared spectrometer (Bruker, USA). Fluorescence and absorbance spectra were obtained using a Duetta spectrophotometer (Horiba, Japan). TEM images were obtained using a Tecnai G2 F20 (Thermo Fisher Scientific, USA) and Tecnai Osiris (Thermo Fisher Scientific, USA) transmission electron microscope. Raman spectra were obtained using a InVia laser-excited Raman spectrometer (Renishaw, UK), using an objective lens with a NA of 0.75, an excitation wavelength of 532 nm, and a laser power of 0.075 mW. Prior to Raman analyses, the sample was cut perpendicular to the laser scanning direction, and the exposed cross-section was analyzed. XRD spectra were obtained using a D8 Discover X-ray diffractometer (Bruker, USA).

6.2.2. Results and discussions

6.2.2.1. Patterning of fluorescent carbonaceous structures

By scanning tightly focused fs laser pulses onto the surface of pristine PDMS (DD = 0 μm), a carbonaceous structure exhibiting bright blue fluorescence was directly patterned on the surface by HR-fs LDW. Blue fluorescence is typical of GQDs prepared by the hydrothermal cleavage of graphene sheets, as reported previously.[192,193] Using a

computer-controlled translation stage, such fluorescent structures can be readily patterned into arbitrary designs, such as intersecting fountain pens (Figure 6.1 (a–c)). Moreover, the fluorescence intensity of the structure depended highly on the scanning speed for patterning. Generally, a slower scanning speed led to higher fluorescence intensity (Figure 6.1 (a)); however, no significant increase in fluorescence was observed for scanning speeds slower than 0.25 mm/s.

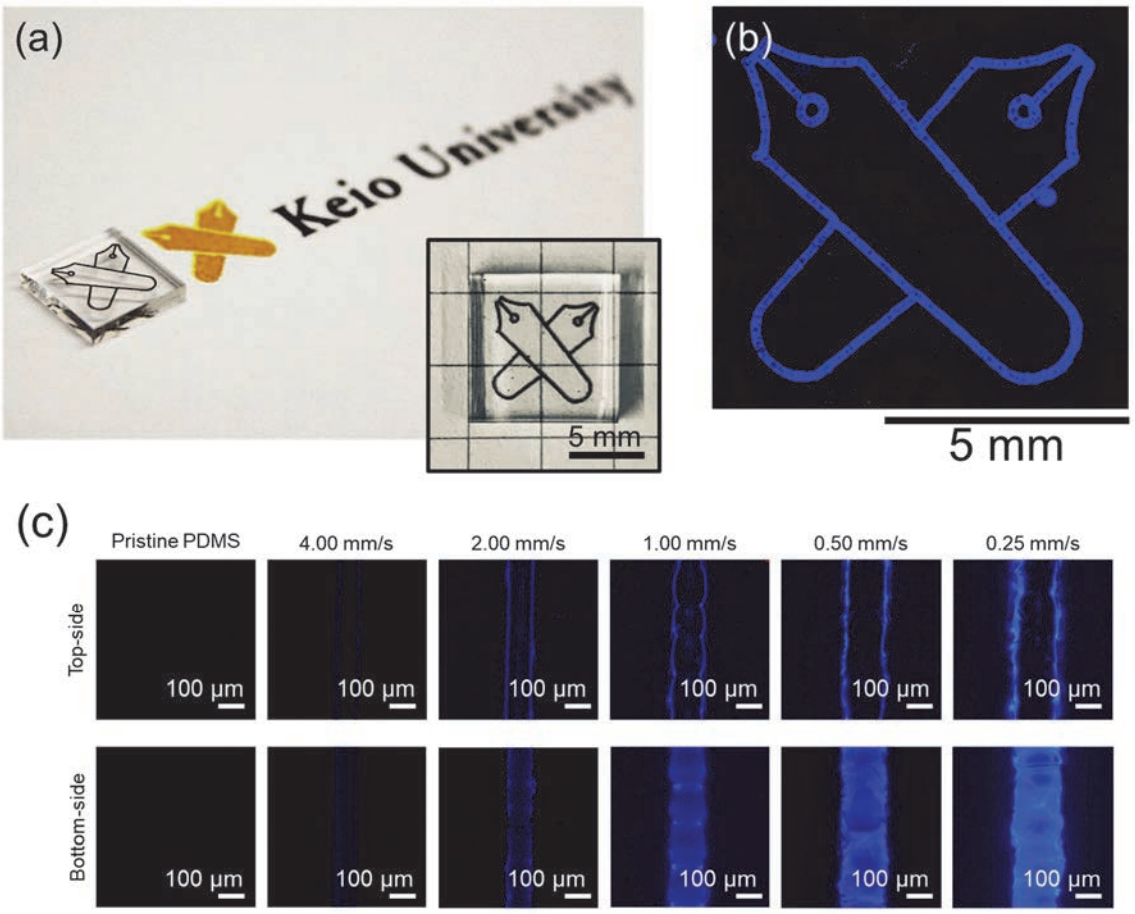

Figure 6.1 (a) Photograph and (b) fluorescence images of intersecting fountain pens patterned on the surface of PDMS (excitation wavelength (ex.): 360 nm). (c) Fluorescence images of the top-side and bottom-side of pristine PDMS and tracks patterned with different scanning speeds (ex. 360 nm).

6.2.2.2. Characterization of fluorescent carbonaceous structures

Changes to the material induced by laser irradiation were assessed by comparing pristine PDMS with the fluorescent structures patterned via HR-fs LDW. As carbonaceous structures that exhibit exceptionally strong fluorescence were obtained with a scanning speed of 0.25 mm/s, the following characterizations were performed on these

structures. The analyzed carbonaceous structures are denoted as "irradiated PDMS". XPS spectra showed a decrease in the intensities of O_{s1}, C_{s1}, Si_{2s}, and Si_{2p} peaks, particularly those of Si, after laser irradiation (Figure 6.2 (a)). This observation suggests bond cleavage and the release of atoms as gaseous products.[120] Additionally, all of the XPS peak locations were shifted toward higher binding energies after laser irradiation, implying oxidation (Figure 6.2 (b)).[194] For the FTIR spectra (Figure 6.2 (c)), the elimination of FTIR peaks corresponding to pristine PDMS bonds and the appearance of FTIR peaks corresponding to C-H, C=C, and C-C bonds signify the graphitization of PDMS. Moreover, peaks corresponding to the O-H, C=O, C-O, and C-O-C bonds of oxygen-containing functional groups were detected after laser irradiation, consistent with the XPS analyses.

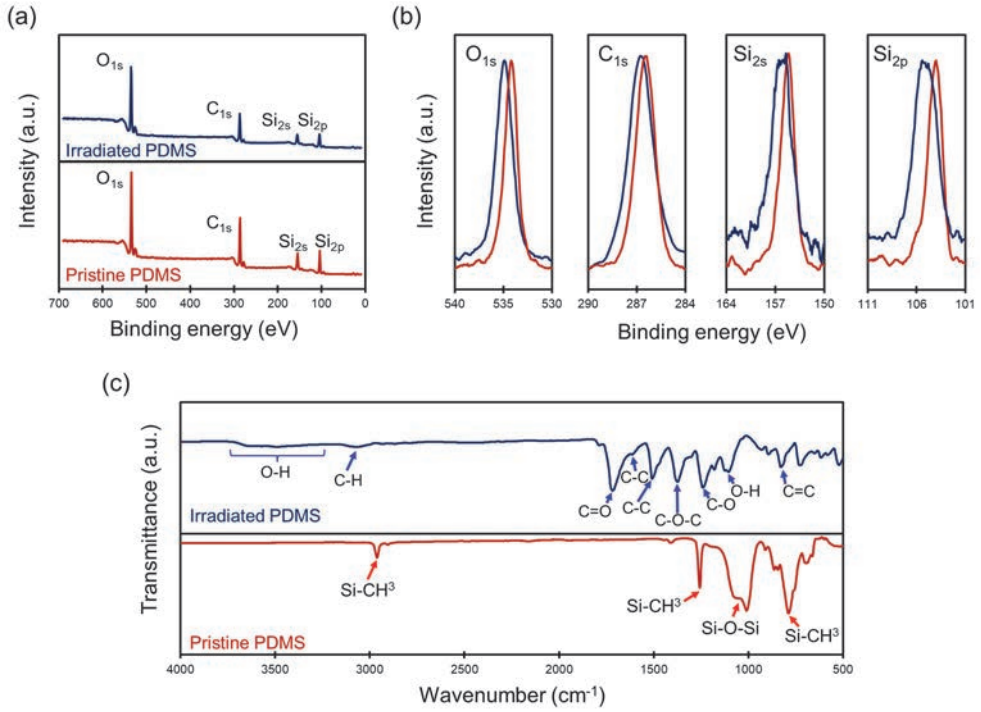

Figure 6.2 (a) Wide-area XPS, (b) narrow-area XPS, and (c) FTIR spectra obtained from pristine PDMS and irradiated PDMS.

The chemical changes induced by laser irradiation will also result in the changes in optical properties of the material. From the absorption spectra shown in Figure 6.3 (a), a broad elevation in the visible wavelengths is observed for the irradiated PDMS, which agrees well with the visible change in the material from transparent to black-colored. Moreover, absorption peaks at approximately 225 nm and approximately 320 nm in the ultraviolet-wavelength range are observed, which corresponds to the π-π* transitions of graphitic sp^2 domains and n-π* transitions of C=O bonds, respectively. Such peaks are

typically observed for functionalized GQDs.[195,196] From the fluorescence spectra (Figure 6.3 (b)), a strong emission in the high-energy visible wavelength (i.e., 400–500 nm) range is observed for the irradiated PDMS, which agrees well with the observed blue fluorescence. Moreover, a sharp emission peak is observed at approximately 405 nm, followed by a less-pronounced emission peak at approximately 420 nm. Such emission peaks have been associated with the C(=O)OH and C-O-C surface functional groups of GQDs, respectively.[197] Therefore, it is suggested that the observed fluorescence originates from GQDs decorated with oxygen-containing surface functional groups.

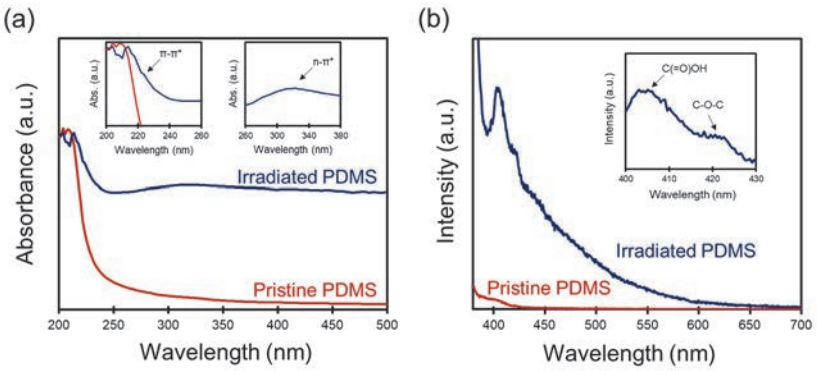

Figure 6.3 (a) Optical absorption, and (b) fluorescence spectra obtained from pristine PDMS and irradiated PDMS. Insets in (a) are magnified views of the peaks assigned to π-π* and n-π* transitions. Inset in (b) is a magnified view of emission peaks associated with C(=O)OH and C-O-C surface functional groups.

Figure 6.4 (a) shows a typical cluster complex formed for the structure which exhibited strong fluorescence (scanning speed: 0.25 mm/s). The enlarged images show that the cluster complex is an aggregation of circular NCs (Figure 6.4 (b,c)). The observed NCs have an average lateral dimension of 11.59 ± 2.24 nm, which is consistent with the dimensions previously reported for GQDs that exhibit blue fluorescence.[193,196,198] Lattice spacings of approximately 0.213 and approximately 0.237 nm (Figure 6.4 (d)) and fast Fourier transform (FFT) patterns (Figure 6.4 (e)) clearly show the presence of the (1100) and (1120) planes of graphitic carbon crystals, confirming the formation of GQDs. As mentioned in Section 2.4.2, the fluorescent properties of GQDs are closely related to the degree of confinement and surface states. It can be observed from Figure 6.4 (a) that the GQDs are slightly overlapped with one another, each with different degrees of overlapping. The addition of graphitic layers, for example by overlapping, can quench confinement and alter the fluorescent properties.[135] Such overlapping, in addition to different surface states (i.e, edge groups as confirmed from Figure 6.2 (c)) may have led to the broad fluorescence spectrum observed in Figure 6.3 (b). Note that the lattice

spacings distinctive of those for SiC-NCs were not observed.

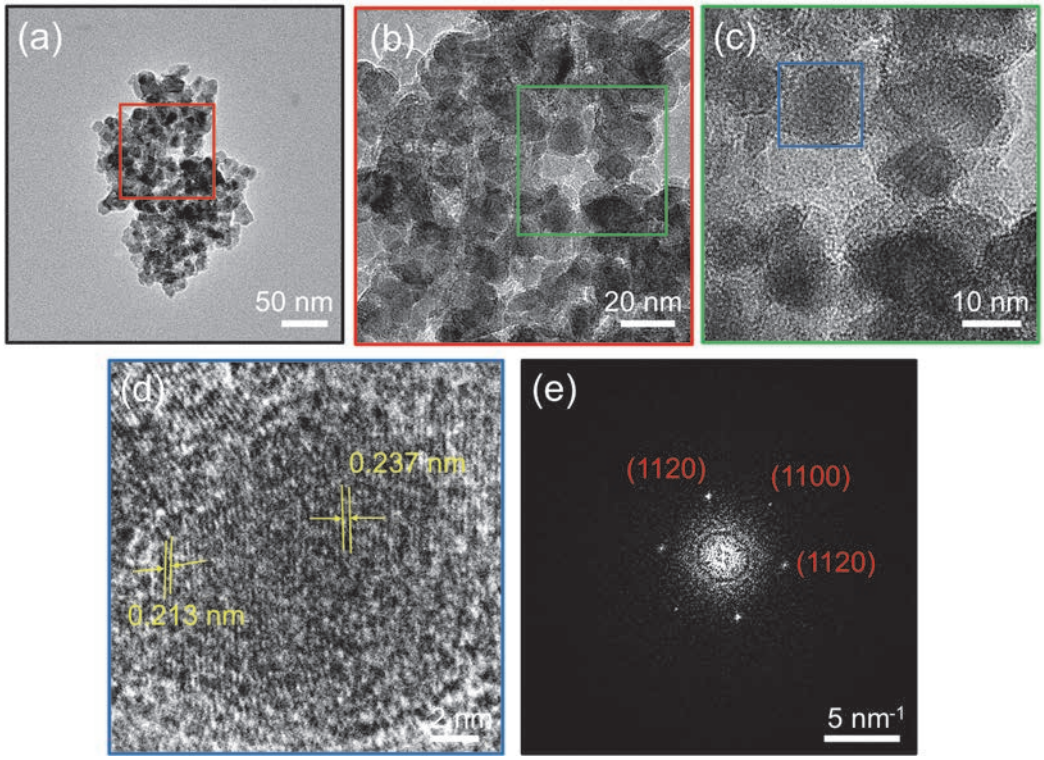

Figure 6.4 (a) TEM image of a typical cluster complex of GQDs. (b) Enlarged image of the area indicated by the red square in (a). (c) Enlarged image of the area indicated by the green square in (b). (d) Enlarged image of the area indicated by the blue square in (c). (e) FFT pattern obtained from the field-of-view shown in (d).

Figure 6.5 (a,b) shows another cluster complex composed of characteristically different NCs. These particular NCs have an average lateral dimension of 62.07 ± 14.97 nm, and a lattice spacing of approximately 0.204 and approximately 0.225 nm, which correspond to the (111) and (100) planes of ND and graphitic carbon, respectively (Figure 6.5 (c)). Contrary to those obtained from Figure 6.4 (d), distinctive spots located at distances that correspond to the (111) and (200) of NDs, in addition to those that correspond to the (100) plane of graphitic carbon, are observed from the FFT, revealing the formation of NDs containing partially graphitic domains (Figure 6.5 (d)). Moreover, these particular NDs possesses a multilayered shell with an interlayer spacing of approximately 0.335 nm which corresponds to the (002) plane of graphitic carbon (Figure 6.5 (e)). Such NDs with a multilayered shell are analogous to graphitized NDs prepared by the thermal annealing of NDs.[199,200] However, considering that such cluster complexes of NDs were observed rarely, in addition to the fact that FTIR peaks corresponding to typical ND-related bonds were not confirmed, it can be implied that the formation volume of graphitized NDs was

insignificant.

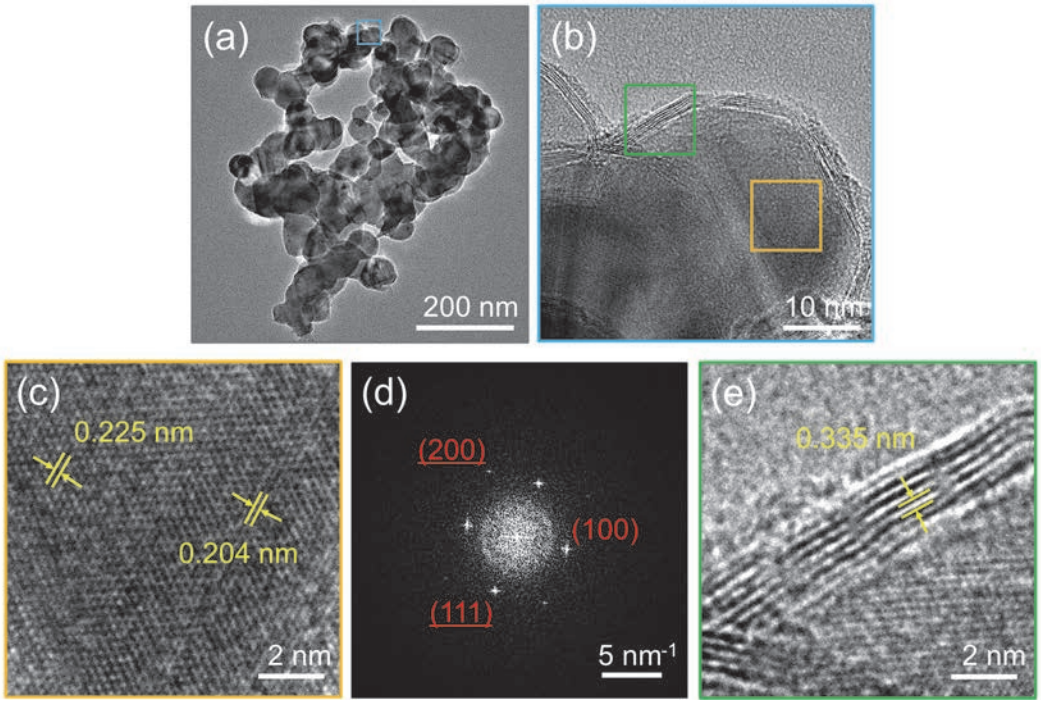

Figure 6.5 (a) TEM image of a cluster complex of NDs. (b) Enlarged image of the area indicated by the light blue square in (a). (c) Enlarged image of the area indicated by the orange square in (b). (d) FFT pattern obtained from the entire field-of-view shown in (c). Lattice planes without underlining correspond to planes of graphitic carbon, and with underlining correspond to planes of ND. (e) Enlarged image of the area indicated by the green square in (e).

6.2.2.3. Discussions on the formation mechanism

Figure 6.6 (a) shows the representative Raman spectra obtained from carbonaceous structures patterned with different scanning speeds. The Raman peaks distinctive of graphitic carbon are confirmed for all spectra, and the formation of graphitic carbon is indicated. However, the disappearance in the 2D band is observed as the scanning speed is decreased, suggesting the decoupling between graphitic layers in the *c* direction, and a decrease in overall crystal order (Figure 6.6 (a)). Such decoupling is attributable to the damaging of the 3D crystal structure of the graphitic carbon due to significant oxidation and/or exfoliation of the graphitic layers.[201] Moreover, notable shifts in the D and G band peak wavenumbers from commonly assigned wavenumbers (for D approximately 1350 cm^{-1} and for G approximately 1580 cm^{-1}) are also observed at slower scanning speeds (Figure 6.6 (b)). The red-shifts in the D band can be attributed to an increase in functional group edge defects, particularly those of C(=O)OH, as well as to sp^2-to-sp^3

transitions.[202,203] On the other hand, the blue-shifts in the G band are attributable to a decrease in the lateral dimensions of the graphitic sp^2 domains.[204] The evolution in the Raman spectra can be explained by the cleavage of larger structures (i.e., multilayered graphitic carbon) into smaller fragments (i.e., GQDs). The intensity ratio of the D and G bands for the highly fluorescent structure (at 0.25 mm/s) was 1.21, which is comparable to previously reported results for GQDs prepared by thermal cleavage of oxidized graphitic carbon (i.e., 1.26).[193]

From the XRD spectra shown in Figure 6.6 (c), the formation of SiC-NCs is confirmed by the diffraction peaks. However, it can be observed that the intensity of the diffraction peaks distinctive of SiC decreases as the scanning speed is decreased, suggesting the existence of a lower concentration of SiC-NCs for slower scanning speeds (Figure 6.6 (d)). This decrease in concentration with respect to the scanning speed is attributable to the thermal modification of SiC-NCs into GQDs due to the sublimation of Si atoms.[205] Appropriately, a specific decrease in the Si atom content was observed upon laser irradiation in the XPS spectra (Figure 6.2 (a))

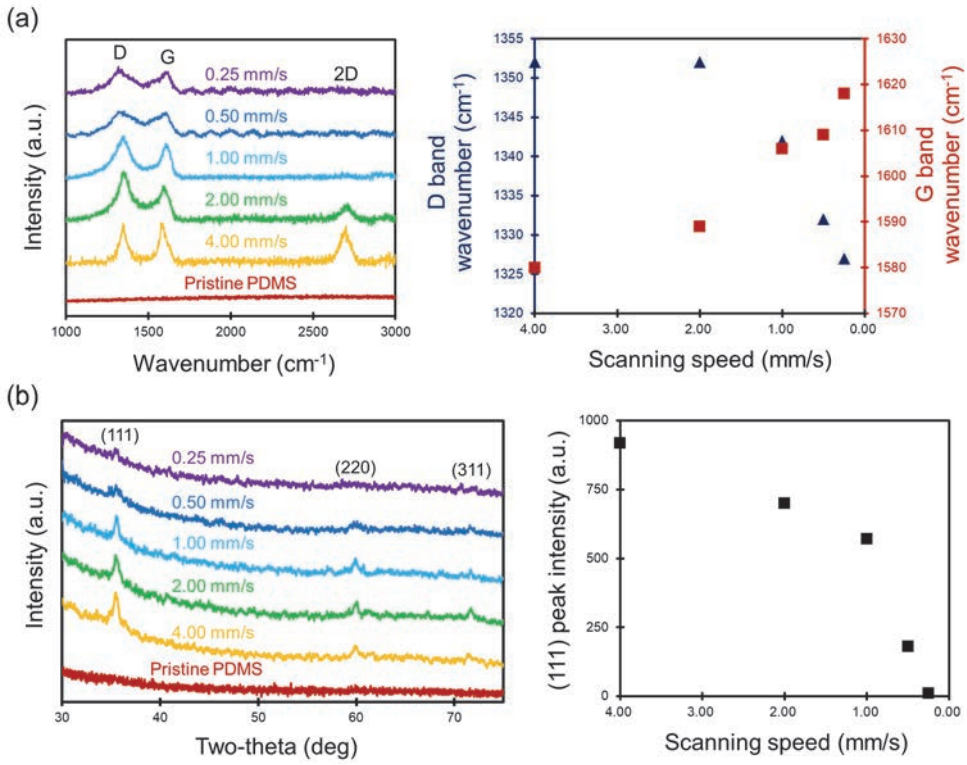

Figure 6.6 (a) Raman spectra obtained from the fluorescent structures patterned with different scanning speeds. (b) Measured D and G band peak wavenumbers for each structure. (c) XRD spectra obtained from the fluorescent structures patterned at different scanning speeds. (d) Measured peak intensity of the SiC (111) diffraction plane for each structure.

The results suggest that the formation mechanism of the GQDs in this study is a top-down method based on the laser-induced pyrolysis of the formed graphitic carbon and SiC-NCs. From the Raman and XRD spectra (Figure 6.6), both graphitic carbon and SiC-NCs formed even at a scanning speed of 4.00 mm/s. The graphitic carbon formed by the initial pulses are continuously irradiated by consecutive pulses, and thus, the attained peak temperatures due to heat accumulation will be different for each scanning speed. This is because the number of irradiated pulses and the irradiation time per spot are different. Owing to the reactive nature of the LICG process in air, the graphitic carbon subsequently contains defects, as indicated by the D band peak in the Raman spectra. With heat accumulation, the in-plane functional groups attached at the defect sites are desorbed, cleaving the graphitic carbon into smaller nano-sized graphitic particle fragments. Similar to previously reported synthesis methods based on the thermal cleavage of oxidized graphene derivatives,[193,197] the in-plane linear defects, particularly epoxy functional groups, make the graphitic lattice fragile and reactive, resulting in cleavage under thermal treatment. Moreover, when SiC crystals are thermally treated at high temperatures, Si atoms are desorbed first, leaving excess C atoms, which can then rearrange to form carbon-rich crystals, specifically GQDs.[206] However, it is currently unclear whether these two formation mechanisms are related or independent. In the future, the controlled surface functionalization and diameter control of the GQDs, realized by the elucidation of the formation mechanism, may allow for the fine-tuning of the emission wavelength and will be a target for future studies.

6.3. Application of fluorescent carbonaceous structures

6.3.1. Materials and methods

6.3.1.1. Material preparation

A 1:1 mixture of polymer to curing agent of optically-cured KER-4690 PDMS (Shin-Etsu Chemical Co., Ltd., Japan) was prepared. The mixture was poured into a rectangular mold and degassed in vacuum to remove any air bubbles trapped during the mixing procedure. Furthermore, the mixture was cured under a 365-nm ultraviolet lamp for 30 min to prepared PDMS sheets. The PDMS sheets prepared in this study were approximately 2 mm in thickness. Before irradiation experiments, the surfaces of PDMS were washed with ethanol to remove any debris.

6.3.1.2. Laser irradiation

Laser irradiation experiments were conducted using a High Q-2 fs laser (Spectra-Physics, USA) which generated 192-fs laser pulses with a central wavelength of 522 nm (second harmonic wave of a 1045-nm fs laser) at a RR of 63 MHz. For the patterning of structures on the surface, PDMS sheets were placed onto a cover glass with a 140-μm spacing (Figure 3.14), and laser pulses were focused onto the bottom surface of the PDMS sheet using a 20× objective lens, with a NA of 0.4. For the patterning of structures inside, PDMS sheets were placed onto a cover glass without air-spacing, and laser pulses were focused inside the PDMS sheet using a water-immersion 60× objective lens, with a NA of 1.0. The defocusing method was not used for the patterning of all structures in this section, and the laser power for the patterning of structures on the surface and inside was 150 mW and 50 mW, respectively. All irradiation experiments were conducted in ambient conditions.

6.3.1.3. Characterization

2D fluorescence images were obtained using an Eclipse Ti-E (Nikon, Japan) and a BZ-X800 (Keyence, Japan) fluorescence microscope. 3D fluorescence images were obtained using an FVMPE-RS multiphoton laser scanning microscope (Olympus, Japan). Coherent light with a wavelength of 720 nm was irradiated to excite the structures via two-photon absorption for 3D fluorescence images.

6.3.2. Results and discussions

6.3.2.1. Fabrication of a 2D anticounterfeiting security tag

Although the fluorescence intensity differed greatly depending on the scanning speed for patterning, no distinctive differences between the visible color of the carbonaceous structures could be distinguished under normal lighting (Figure 6.7 (a)). Since indistinguishable, black-colored structures with differing fluorescence intensities could be patterned by altering the scanning speeds, a security tag with a hidden QR code was patterned. In this study an inverted QR code was realized by patterning the dark-colored regions with a fast-scanning speed and by patterning the bright-colored regions with a slow scanning speed. The QR code is imperceptible under normal light, and only a black-colored square is observed on the surface (Figure 6.7 (b)). By contrast, under 360-nm

wavelength light the QR code is revealed (Figure 6.7 (c)), demonstrating the practicality of the HR-fs LDW technique in fabricating security tags with concealed information visible only under light with ultraviolet wavelengths.

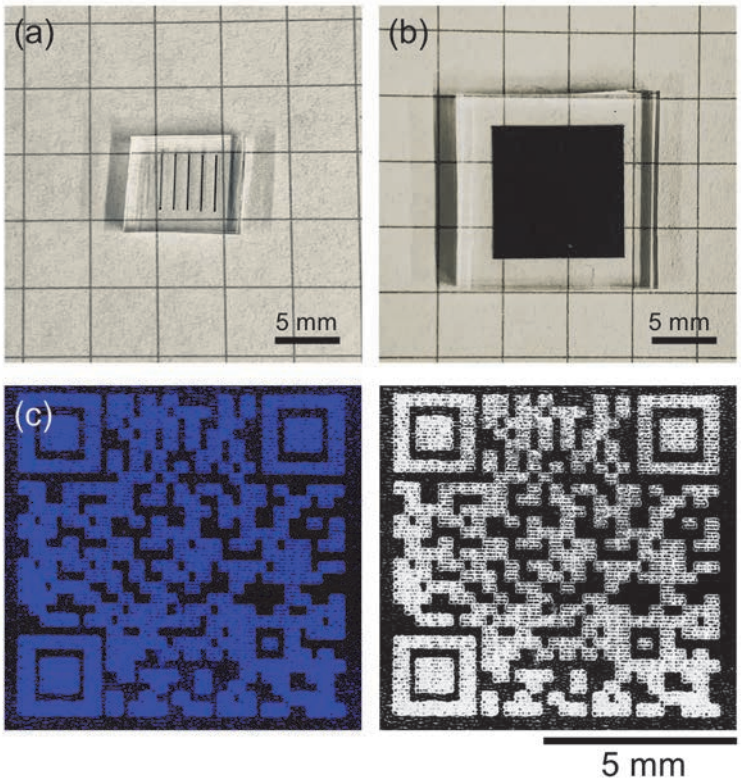

Figure 6.7 (a) Photograph of tracks patterned on the surface of PDMS using different scanning speeds. From left to right, the scanning speed for patterning was 4.00 mm/s, 2.00 mm/s, 1.00 mm/s, 0.50 mm/s, and 0.25 mm/s. (b) Photograph of the security tag patterned on the PDMS surface. (c) Normal (left) and greyscale (right) fluorescence images of the security tag under 360-nm wavelength light.

6.3.2.2. Implications as an elastic 3D data storage device

As the transparent PDMS sheet has low linear absorption of 522-nm wavelength light, and that nonlinear absorption initiates the formation of fluorescent structures, a 4 × 4 array of fluorescent dots was generated by tightly focusing fs laser pulses inside the PDMS sheet. The two left columns of the array were generated 300 μm from the bottom surface, where the two right columns were generated 500 μm from the bottom surface (Figure 6.8 (a)). The dots generated inside the PDMS sheet exhibited bright blue fluorescence, comparable to when fs laser pulses were focused onto the PDMS surface. When the dot array on the left side was focused on (z = 300 μm), fluorescence was observed exclusively from the two left columns, and vice versa (Figure 6.8 (b)). Figure

6.8 (c–e) show fluorescence images obtained by multiphoton microscopy, demonstrating that the fluorescent structures composed of GQDs can be precisely generated in three dimensions directly inside a transparent elastomer by LICG using a high RR fs laser. The fluorescent structures patterned internally are oval-shaped and elongated along the pulse propagation direction, possibly due to the elliptical focal spot and/or slight growth of the resulting carbonaceous structure due to subsequent absorption of defocused pulses.

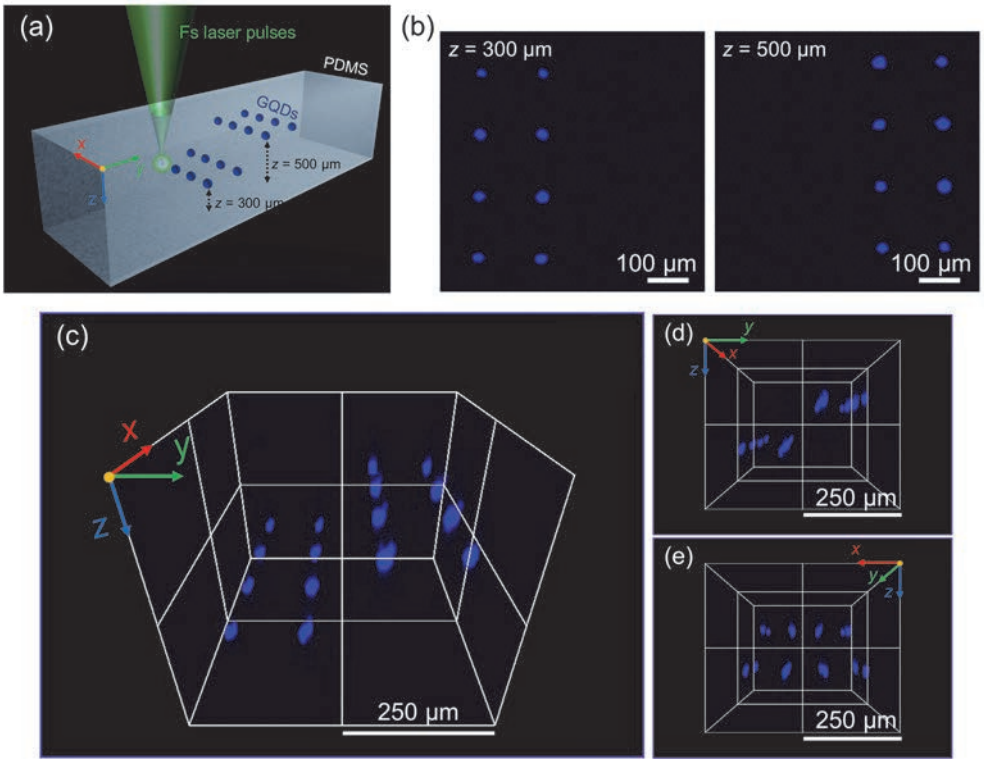

Figure 6.8 (a) Schematic of the dot array. (b) 2D fluorescence images obtained at different *z*-axis focuses. Scale bars in (a,b) indicate 100 μm. (c) 3D reconstruction fluorescence image. (d) and (e) are side and front views, respectively. Scale bars in (c–e) indicate 250 μm.

In the context of dynamic applications, such as chemical sensing, the reactivity of the surface functional groups of the GQDs is beneficial, as the fluorescence intensity changes according to the surrounding environment.[207] However, for static applications, such as security tags, the deterioration in fluorescence intensity over time is undesirable. It should be emphasized that the dots generated inside of the PDMS sheet in this study are naturally encased by the chemically stable PDMS matrix, and therefore is significantly less affected by the surrounding environment. For example, no significant decay in fluorescence intensity was observed for the generated dots, regardless of the stored medium (i.e., air, water, acid, base) even after 75 days (Figure 6.9 (a)). Moreover, even when the PDMS sheet containing the fluorescent dots were compressed (i.e., mechanical stress), although

the spacings between the dots changed, no evident deterioration of the fluorescence intensity was observed (Figure 6.9 (b)).

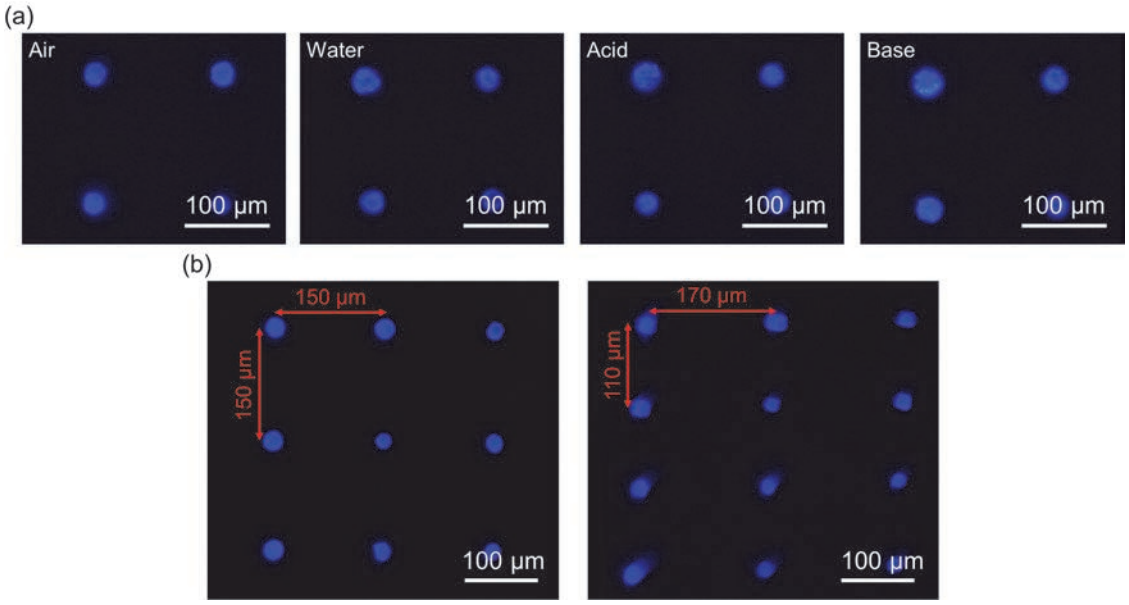

Figure 6.9 (a) Fluorescence images showing the stable fluorescence of the dot array after being stored in different environments for 75 days. The samples were stored in a 1.0 mol acetic acid solution and 1.0 mol sodium hydroxide solution for the acid and base environments, respectively. (b) Fluorescence images showing the stable fluorescence of the dot array before (left) and after compression (right) of the PDMS substrate. Pressure was applied to the PDMS substrate along the *y*-axis (up/down).

As fluorescent dots can be generated directly inside an optically transparent, chemically stable, and elastic material, the LICG of PDMS may become an effective technique to rapidly fabricate elastic 3D data storage devices.[208] It should be emphasized that 3D fluorescent structures were successfully achieved in this current study as pristine PDMS exhibited high optical transparency towards the wavelengths of both the laser light and the excitation light. For example, if a CW laser outputting light with a wavelength in which PDMS efficiently absorbs linearly was used, the spatially selective patterning of GQDs inside the bulk material cannot be achieved. Moreover, if the polymer substrate was PI instead of PDMS in this study, as PI exhibits high absorption towards 360-nm-wavelength light, sufficient excitation of the GQDs patterned internally cannot be achieved. Nonetheless, the currently achieved average voxel dimensions of the dots are approximately 26.23 μm × 35.75 μm, and limits the storage capacity. Moreover, since the fluorescent structures are black-colored if multiple layers of the arrays are generated inside bulk PDMS, the inner layers may exhibit weaker fluorescence intensities due to the hindrance of excitation by the surrounding layers. The significant improvement in the

resolution of the graphitized regions down to a few microns or less may lessen the hindrance of the upper layers. In practice, the resolution of the fluorescent tracks is able to be controlled by, for example, the laser power and the confinement of the light-material interaction area by utilizing a higher NA objective lens (Figure 6.10); however, sufficiently small resolutions have not been achieved at this point, and is subject to future studies.

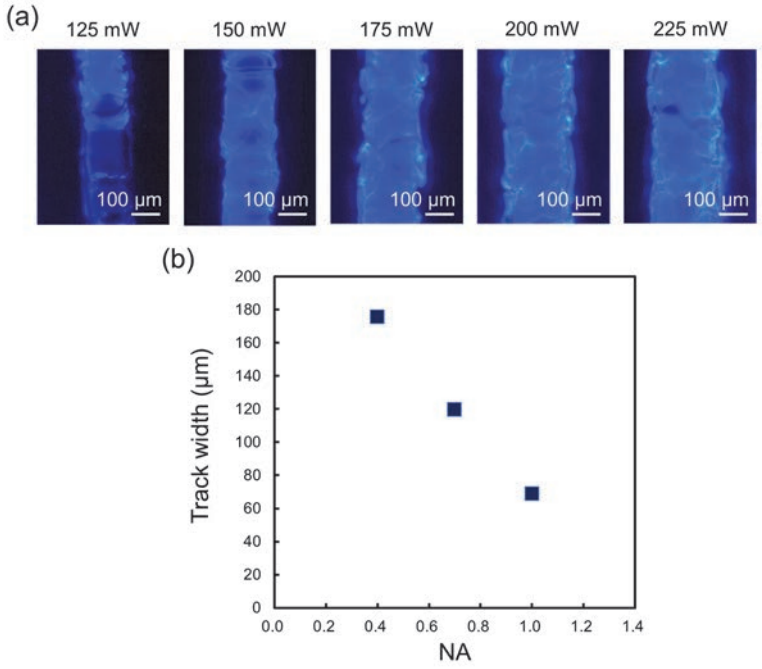

Figure 6.10 (a) Fluorescence images of the fluorescent carbonaceous structures patterned with different laser powers (ex. 360 nm). Scanning speed was set to 0.25 mm/s. (b) Relationship between the track width and the NA when the laser intensity was kept constant (approximately 6.2×10^{11} W/cm^2).

6.4. Summary

In Chapter 6, the formation of carbonaceous structures exhibiting blue fluorescence by the LICG of PDMS was demonstrated. TEM observations confirmed that the fluorescent carbonaceous structures were composed of NCs of graphitic carbon, or GQDs. Material analyses on the structures patterned with different scanning speeds suggests that the formation mechanism of the GQDs in this study is a top-down method based on the thermal degradation of graphitic carbon and SiC-NCs into smaller crystals of graphitic carbon. By adjusting the laser parameters and selectively controlling the GQD content, a black security tag with a concealed QR code, which is imperceptible under normal light

but is revealed under excitation, is realized. Furthermore, the 3D generation of fluorescent dos inside a transparent polymer is demonstrated by utilizing multiphoton interactions. This study indicates the applicability of LICG towards the patterning of GQDs directly on and inside polymer substrates, and open novel routes for the direct fabrication of 2D and 3D elastic optical devices.

The contents of this chapter were reused and built upon the following reference with permission from the American Chemical Society ©2022.

- Hayashi, S., Tsunemitsu, K. & Terakawa, M. Laser Direct Writing of Graphene Quantum Dots inside a Transparent Polymer. *Nano Lett* **22**, 775–782 (2022).

7. Conclusions and future studies

7.1. Conclusions

7.1.1. Chapter conclusions

Various techniques to synthesize and/or pattern a variety of carbonaceous materials and/or structures towards a multitude of applications have been developed over time. Out of the many techniques, LICG offers the seamless integration of carbonaceous structures with flexible and/or elastic polymers, and accordingly, has been regarded as a facile technique to rapidly fabricate polymer-based devices. In this thesis, the chemical and physical processes that ensue when a transparent elastomer, PDMS, is irradiated by a laser light were discussed to reveal the fundamental mechanisms in which carbonaceous structures form by LICG. Moreover, by analyzing the carbonaceous structures formed by LICG, the relationship between the material and the electrical property of the structure was revealed. Lastly, the electrical and optical properties of the carbonaceous structures were applied towards different applications to indicate the possibilities of the LICG of PDMS for the fabrication of various devices. Below, the key points of this thesis are recapped.

Chapter 2 established a theoretical framework of LICG, outlining the various chemical and physical process which can be involved. Considering the fundamental principles of carbonization and graphitization and light-material interactions, it was established in this thesis that the principles of LICG consists of three parts: light absorption, bond fragmentation, and structural formation. By changing the laser parameters, the details regarding these three parts can be vastly altered making LICG a highly versatile, but complicated, technique.

Chapter 3 proposed and further validated a mechanism for the formation of carbonaceous structures by LICG. Although the formation mechanism was thought to be a simple photothermal conversion reaction, this thesis successfully revealed that the formation mechanism of the carbonaceous structures is based on the nucleation and growth of laser-induced defects. As the implications of establishing a laser setup which enables both efficient nucleation of defects and thermal conversion was indicated, a high RR fs laser was used for the LICG of PDMS. However, due to the high laser intensity, the scanning of tightly focused fs laser pulses resulted in the severe damaging of the resulting

carbonaceous structure by laser ablation. In order to suppress laser ablation, a defocusing method was devised, and the successful patterning of continuous carbonaceous structures using a high RR fs laser was demonstrated.

Chapter 4 revealed the effects of the graphitic carbon and SiC-NCs consisting the carbonaceous structures on the electrical property of the resulting carbonaceous structure. As displayed in this thesis, in order to realize electrically conductive structures by LICG, it is required that the crystal dimension and/or formation content of graphitic carbon is sufficiently large/high to form a conductive network. On the other hand, in order to realize electrically semiconductive structures by LICG, it is required that the crystal dimension and/or formation content of SiC-NCs is sufficiently large/high while those of graphitic carbon are small/low. Moreover, it was discussed that the PE may have an important role in achieving such semiconducting carbonaceous structures, as can affect the localized pressures resulting from laser-induced shockwaves.

Chapter 5 indicated the applicability of the carbonaceous structures patterned by LICG towards electrical mechanical sensors. The electrical resistance of the patterned carbonaceous structure changed with respect to structural deformation, exhibiting evident piezoresistive property. By applying the small size of the carbonaceous structure patterned by a single scan with the defocusing method, a sensitive micro-pressure sensor was realized. Whereas, by applying the unidirectional grooves of the carbonaceous structure patterned by multiple scans without the defocusing method, an anisotropic strain sensor was realized. Not only did this thesis indicate the possibility of LICG for the fabrication of electrical mechanical sensors, it showed that depending on the patterning scheme, strain sensors with different functionalities can be easily fabricated.

Chapter 6 unveiled the hidden possibilities of LICG for the fabrication of optical devices. The patterning of carbonaceous structures composed of fluorescent GQDs was demonstrated. It was discussed the formation mechanism of the GQDs in this study is based on the thermal decomposition of larger crystals or graphitic carbon and SiC-NCs into smaller carbon-rich particles. By simply adjusting the laser parameters and selectively controlling the GQD content, a black security tag with a concealed QR code, which is imperceptible under normal light but is revealed under excitation, was realized. Furthermore, by utilizing multiphoton interactions, the patterning of 3D fluorescent structures inside PDMS was achieved. This thesis indicated the applicability of LICG towards the fabrication of, not only electrical applications, but also optical devices.

7.1.2. General conclusions

The aim of this thesis was to discuss the processes that ensue when PDMS is irradiated by laser light (1) to reveal the mechanisms in which carbonaceous structures form by LICG, (2) to clarify the effect of the materials on the electrical properties, and (3) to indicate the applicability of the carbonaceous structures for application. The first point was engaged through theoretical and experimental approaches. Previous theories regarded LICG considered the laser light as a simple heat source, and thus largely ignored the general aspects of light-material interactions. Therefore, the previous theories were insufficient in understanding the experimental results. In Chapter 2, a new theoretical set of processes involved in LICG which considered light-material interactions was outlined. As the new theory considers light-material interactions, the nonlinearity in LICG can be discussed in more depth and insight. Although this is currently only a theory, the ideas mentioned in this thesis may provide a foundation in developing a computational model of LICG to, for example, predict the morphologies and characteristics of the resulting structures with high accuracy simply from the laser parameters. In Chapter 3, it was experimentally revealed that the formation of carbonaceous structures by LICG is based on the nucleation and growth of laser-induced defects. and the consideration of “time”, such as in the form of heating rates, is crucial for the patterning of continuous carbonaceous structures. It was further indicated that the use of a fs laser is advantageous for LICG as the efficient nucleation of laser-induced defects can be realized, and may allow for faster processing speeds compared to CW lasers. However, when using a fs laser careful consideration of the laser intensity is required since the inherently high laser intensity leads to undesirable damaging of the resulting structure by laser ablation. Therefore, in the case of LICG using a fs laser the laser intensity should be decreased, for example, by implementing a defocusing method for the patterning of continuous carbonaceous structures. The second point was worked on by assessing the electrical properties and material compositions of the resulting carbonaceous structures. It was demonstrated in Chapter 4 that carbonaceous structures that exhibit conducting or semiconducting behavior can be selectively patterned on PDMS by tuning the laser parameters. This transition in conducting regimes was attributed to the relative changes in size and concentration of the graphitic carbon and SiC-NCs consisting the structure, and the effect of the carbonaceous materials on the electrical property of the overall structure was clarified. Lastly, the third point was tackled by applying the carbonaceous structures towards various electrical and optical applications. It was demonstrated that the electrically conductive carbonaceous structures possess piezoresistive property, and

therefore could be successfully applied towards mechanical sensing. Thus far, LICG has been mostly used for the fabrication of electrical devices, and the application of LICG for non-electrical applications was extremely minimal. However, it was demonstrated in this thesis for the first time that fluorescent carbonaceous structures can also be patterned by LICG. Since the patterning of fluorescent carbonaceous structures on elastomers offers the development of attractive polymer-based optical devices, such as soft security tags, it is expected that the application of LICG for optical applications will become a hot topic in the future owing to this study. Nonetheless, in this thesis it was shown that the carbonaceous structures patterned by LICG can be applied towards various practical consumer applications. The exquisite control and prediction of the morphologies and properties of the resulting carbonaceous structures realized by the development of a computational model may allow for the LICG technique to transition towards a viable manufacturing process capable of the rapid roll-to-roll fabrication of highly-customized polymer-based devices in the future.

7.2. Future studies

However, the insights shown in this thesis also raises new questions and points which are worth exploring in the future. Below possible future studies will be discussed.

7.2.1. Fundamental aspects

Previous results regarding the LICG of polymers should be re-examined and re-discussed according to the principles of LICG established in Chapter 2. For example, although the effect of the laser wavelength has been investigated, it has only been discussed mostly in terms of “efficiency”. In this thesis, the initial absorption process of LICG was discussed to result in a hotspot slightly below the surface leading to the formation of a microbubble below the surface. Therefore, the effect of the laser wavelength may need to be discussed in terms of “penetration depth” in addition to efficiency. This difference in the penetration depth will affect the formation of microbubbles and consequently, the surface morphology of the carbonaceous structure. Although this was suggested by the difference in morphology of the tracks patterned by CW LDW and HR-fs LDW (Figure 3.1 (a) and Figure 3.15 (b), respectively), the results shown in this thesis are not definitive, as various laser parameters are different, such as laser intensity, scanning speed, and pulse duration. In the future, by irradiating CW laser beams with different wavelengths, while keeping the absorbed laser energy constant, the

effects of penetration depth may be revealed. By concurrently analyzing the flakes formed by LICG, the formation mechanism of the flakes may be identified.

Moreover, the re-examination of previous results with the newly established principles may also provide new insight into the evolution of nano-scaled details of the structures. For example, although many of the studies on LICG discussed the effect of laser parameters on the micropores of the resulting carbonaceous structure (as Figure 2.16), the effect of laser parameters on the nanopores of the individual graphitic layers have not been heavily investigated. As discussed in Chapter 2, the rapid release of gases during graphitization leads to the formation of nanopores. Theoretically, the formation of such nanopores will appear as an increase in I_D/I_G of the obtained Raman spectrum. However, most of the previous studies would have concluded this increase in I_D/I_G simply as a deterioration in crystallinity of the formed graphitic carbon, implying a negative result. However, the same increase in I_D/I_G may also indicate an increase in overall porosity of the graphitic carbon owing to the nanopores, which would be a positive result with regards to high surface-area applications (i.e., supercapacitors). Of course, if the formation of nanopores is excessive (i.e., high I_D/I_G), this will result in low electron mobilities and a low electrical conductivity; and therefore, there should be an optimum concentration of nanopores for the desired application. Nonetheless, this discussion may encourage to re-examine the idea that a low I_D/I_G is always optimum for all electronic applications.

The effects of peak temperature on the fragmentation of the chemical bonds have been well established. However, the effects of the non-thermal fragmentation of bonds, which may be induced in the case of the irradiation of high intensity laser light, on LICG have not been revealed yet. As discussed in this thesis, the non-thermal fragmentation of bonds may assist in the carbonization and graphitization processes owing to the slight alterations in the absorption coefficient and/or acceleration of bond fragmentation. For the former effect, as the use of a fs laser can facilitate LICG through the formation of laser-induced defects (Section 3.3.), this has been primitively suggested by this thesis. But in addition to this, the LICG threshold for polymers that have been photodegraded to different degrees, by for example the irradiation of light with ultraviolet wavelengths, can be investigated to further validate this theory. For the latter effect, the peak temperatures required for the formation of similar graphitic products by LICG depending on the laser intensity can be investigated. As a simple approach to this, thermographic analyses can be conducted for the tracks composed of similar graphitic products patterned by either CW-LDW or HR-fs LDW.

7.2.2. Material aspects

The selective patterning of conducting or semiconducting structures may offer the fabrication of complex electric devices by simply irradiating a transparent elastomer. However, in order to achieve complex electric devices, such as transistors, various challenges need to be overcome. For instance, currently, the semiconducting behavior of the patterned structures in this study are too weak for practical applications and need to be enhanced. By further revealing the formation mechanism of the carbonaceous materials through, for example, the development of a new laser setup, the further increase in SiC-NC formation may be achieved. Moreover, the inclusion of additives before the LICG of PDMS may enhance the semiconducting behavior of the resulting structure by progressing SiC-NC formation. However, as discussed in Section 4.3., it is imperative that the additive preferably aids in the formation of SiC-NC and not graphitic carbon. Moreover, the careful consideration between the laser wavelength and the added material is required, as the addition of additives may negatively alter the absorption and/or scattering behavior of the irradiated material. It is also expected that depending on the chemical composition of the additive, the formation of n or p-doped SiC-NCs may be achieved by LICG.

7.2.3. Application aspects

A variety of practical devices was fabricated by the LICG of PDMS, and the applicability of the carbonaceous structures towards electrical and optical applications was indicated by this thesis. However, as the current study mainly aimed to develop proof-of-concept devices using the carbonaceous structures, the optimization in device performance and the investigation of device limits was not comprehensive. For example, although it was indicated in Section 5.3. that anisotropic strain sensors can be fabricated by patterning 2D structures by raster scanning, the effect of laser parameters, such as laser power, scanning speed, and hatch spacing, on the performance, such as anisotropy, sensitivity, and bending limits, of the strain sensor was not revealed. By investigating the relationships between the parameter combinations, structure morphology, and structure properties, the fabrication of mechanical sensors with different or improved performances, for example higher sensitivities, may be realized in the future.

For optical applications, it was indicated that fluorescent structures can be patterned in three dimensions inside of a transparent elastomer, which is extremely difficult to achieve

with conventional patterning techniques. Although it has not been demonstrated, as discussed in Section 6.3., the 3D fluorescent carbonaceous structures patterned inside PDMS by LICG has implications to be applied towards elastic 3D data storage devices in the future. In the current study, the carbonaceous structures patterned inside PDMS were assumed to be similar to the carbonaceous structures patterned on the PDMS surface; however, it is expected that the environmental conditions are significantly different between the surface and inside and the carbonaceous structures patterned inside PDMS should be characterized in more detail. Comparing the structures formed on the surface and inside may provide a deeper understanding of the formation mechanism, realizing the fine tuning of the size and fluorescent properties of the patterned carbonaceous structures.

If the patterning of highly semiconducting structures, as well as the selective doping of the resulting structures, are achieved (as discussed in 7.2.2.), the development of semiconductor devices and high-performance electronic devices can be expected. By simply irradiating an elastomer with laser light, these complex devices can be rapidly fabricated with minimal procedures. Furthermore, if the selective doping of semiconducting structures can be realized, various optoelectrical devices, such as photovoltaics, light emitting diodes, and solar cells, may be realized by utilizing the high optical transparency of PDMS. It should be noted that these resulting devices can be potentially flexible and stretchable as the substrate, PDMS, is also highly elastic. Moreover, by utilizing a high repetition rate femtosecond laser, such structures can be spatially patterned inside the substrate, realizing the fabrication of more complex electronic devices which are inherently incased in an insulating material.

It is evident the future potential of the LICG of PDMS is limitless, but there are still many challenges that need to be overcome.

References

1. Gupta, T. *Carbon–The Black, the Gray and the Transparent*. (Springer International Publishing, 2018).

2. Horiuchi, S. *et al.* Above-room-temperature ferroelectricity in a single-component molecular crystal. *Nature* **463**, 789–792 (2010).

3. Hazen, R. M., Jones, A. P. & Baross, J. A. *Carbon in Earth*. (De Gruyter, 2013).

4. Tuček, J. *et al.* Emerging chemical strategies for imprinting magnetism in graphene and related 2D materials for spintronic and biomedical applications. *Chem Soc Rev* **47**, 3899–3990 (2018).

5. Sabu, T., Sarathchandran, C., Ilangovan, S. A. & Moreno-Pirajan, J. C. *Handbook of Carbon-Based Nanomaterials*. (Elsevier, 2021).

6. Pierson, H. O. *Handbook of Carbon, Graphite, Diamonds and Fullerenes*. (Noyes Publications, 1994).

7. Jäger, H. & Frohs, W. *Industrial Carbon and Graphite Materials.* vol 1. (Wiley, 2021).

8. Sangiao, E. T., Holban, A. M. & Gestal, M. C. Applications of nanodiamonds in the detection and therapy of infectious diseases. *Materials* **12**, 1639 (2019).

9. Willander, M., Friesel, M., Wahab, Q.-U. & Straumal, B. Silicon carbide and diamond for high temperature device applications. *J Mater Sci: Mater Electron* **17**, 1–25 (2006).

10. Fan, J. *et al.* 3C-SiC nanocrystals as fluorescent biological labels. *Small* **4**, 1058–1062 (2008).

11. Jiříčková, A., Jankovský, O., Sofer, Z. & Sedmidubský, D. Synthesis and Applications of Graphene Oxide. *Materials* **15**, 920 (2022).

12. Watson, A. Y. & Valberg, P. A. Carbon black and soot: Two different substances. *Am Ind Hyg Assoc J* **62**, 218–228 (2001).

13. Abbas, Q. *et al.* Graphene Synthesis Techniques and Environmental Applications. *Materials* **15**, 7804 (2022).

14. Garcia-Nunez, J. A. *et al.* Historical Developments of Pyrolysis Reactors: A Review. *Energy Fuels* **31**, 5751–5775 (2017).

15. Devi, M. & Rawat, S. A comprehensive review of the pyrolysis process: From

carbon nanomaterial synthesis to waste treatment. *Open Mater Sci* **1**, itab014 (2021).

16. Nizamuddin, S. *et al.* An overview of effect of process parameters on hydrothermal carbonization of biomass. *Renewable Sustainable Energy Rev* **73**, 1289–1299 (2017).

17. Akiya, N. & Savage, P. E. Roles of water for chemical reactions in high-temperature water. *Chem Rev* **102**, 2725–2750 (2002).

18. Muñoz, R. & Gómez-Aleixandre, C. Review of CVD synthesis of graphene. *Chem Vap Depos* **19**, 297–322 (2013).

19. Pedersen, H. *et al.* Chloride-based CVD growth of silicon carbide for electronic applications. *Chem Rev* **112**, 2434–2453 (2012).

20. Dushik, V. V., Rozhanskii, N. V., Lifshits, V. O., Rybkina, T. V. & Kuzmin, V. P. The formation of tungsten and tungsten carbides by CVD synthesis and the proposed mechanism of chemical transformations and crystallization processes. *Mater Lett* **228**, 164–167 (2018).

21. Mattevi, C., Kim, H. & Chhowalla, M. A review of chemical vapour deposition of graphene on copper. *J Mater Chem* **21**, 3324–3334 (2011).

22. Matsumoto, K. *Frontiers of Graphene and Carbon Nanotubes*. (Springer Japan, 2015).

23. Liu, Y., Ge, Z., Li, Z. & Chen, Y. High-power instant-synthesis technology of carbon nanomaterials and nanocomposites. *Nano Energy* **80**, 105500 (2021).

24. Liu, Q., Duan, Y., Ma, H., Long, X. & Han, Y. Review on the exploration of condensed carbon formation mechanism in detonation products. *AIP Adv* **10**, 050701 (2020).

25. Danilenko, V. V. On the History of the Discovery of Nanodiamond Synthesis. *Phys Solid State* **46**, 595–599 (2004).

26. Yin, H. *et al.* Detonation synthesis of carbon-encapsulated magnetic nanoparticles. *Fuller Nanotub Carbon Nanostructures* **23**, 605–611 (2015).

27. Langenderfer, M. J. *et al.* Detonation synthesis of silicon carbide nanoparticles. *Ceram Int* **46**, 6951–6954 (2020).

28. Du, L., Xu, C., Liu, J., Lan, Y. & Chen, P. One-step detonation-assisted synthesis of Fe_3O_4-Fe@BCNT composite towards high performance lithium-ion batteries. *Nanoscale* **9**, 14376–14384 (2017).

29. Arora, N. & Sharma, N. N. Arc discharge synthesis of carbon nanotubes: Comprehensive review. *Diam Relat Mater* **50**, 135–150 (2014).

30. Wyss, K. M., Luong, D. X. & Tour, J. M. Large-Scale Syntheses of 2D Materials: Flash Joule Heating and Other Methods. *Adv Mater* **34**, 2106970 (2022).

31. Iijima, S. & Ichihashi, T. Single-shell carbon nanotubes of 1-nm diameter. *Nature* **363**, 603–605 (1993).

32. Pak, A., Ivashutenko, A., Zakharova, A. & Vassilyeva, Y. Cubic SiC nanowire synthesis by DC arc discharge under ambient air conditions. *Surf Coat Technol* **387**, 125554 (2020).

33. Luong, D. X. *et al.* Gram-scale bottom-up flash graphene synthesis. *Nature* **577**, 647–651 (2020).

34. Deng, B. *et al.* Phase controlled synthesis of transition metal carbide nanocrystals by ultrafast flash Joule heating. *Nat Commun* **13**, 262 (2022).

35. Deng, B. *et al.* Urban mining by flash Joule heating. *Nat Commun* **12**, 5794 (2021).

36. Chen, W. *et al.* Flash Recycling of Graphite Anodes. *Adv Mater* **35**, 2207303 (2023).

37. Liang, C. *et al.* Green synthesis of graphite from CO_2 without graphitization process of amorphous carbon. *Nat Commun* **12**, 119 (2021).

38. Dąbrowska, A. *et al.* Ultra-fast efficient synthesis of one-dimensional nanostructures. *Phys Status Solidi B Basic Res* **248**, 2704–2707 (2011).

39. Chen, L., Yu, H., Zhou, W. & Tam, K. C. One-Step Acid-Induced Confined Conversion of Highly Oriented and Well-Defined Graphitized Cellulose Nanocrystals: Potential Advanced Energy Materials. *ACS Sustain Chem Eng* **10**, 16760–16769 (2022).

40. Chakrabarti, A. *et al.* Conversion of carbon dioxide to few-layer graphene. *J Mater Chem* **21**, 9491–9493 (2011).

41. Lu, G., Yu, K., Wen, Z. & Chen, J. Semiconducting graphene: Converting graphene from semimetal to semiconductor. *Nanoscale* **5**, 1353–1368 (2013).

42. Kim, K., Choi, J. Y., Kim, T., Cho, S. H. & Chung, H. J. A role for graphene in silicon-based semiconductor devices. *Nature* **479**, 338–344 (2011).

43. Htwe, Y. Z. N. & Mariatti, M. Printed graphene and hybrid conductive inks for flexible, stretchable, and wearable electronics: Progress, opportunities, and challenges. *J Sci: Adv Mater and Dev* **7**, 100435 (2022).

44. Jang, H. *et al.* Graphene e-tattoos for unobstructive ambulatory electrodermal activity sensing on the palm enabled by heterogeneous serpentine ribbons. *Nat Commun* **13**, 6604 (2022).

45. Wei, T., Bao, L., Hauke, F. & Hirsch, A. Recent advances in graphene patterning. *ChemPlusChem* **85**, 1655–1668 (2020).

46. Han, M. Y., Özyilmaz, B., Zhang, Y. & Kim, P. Energy band-gap engineering of graphene nanoribbons. *Phys Rev Lett* **98**, 206805 (2007).

47. Fasoli, A., Colli, A., Lombardo, A. & Ferrari, A. C. Fabrication of graphene nanoribbons via nanowire lithography. *Phys Status Solidi B Basic Res* **246**, 2514–2517 (2009).

48. Zhang, M. *et al.* Patterning of graphene using wet etching with hypochlorite and UV light. *Sci Rep* **12**, 4541 (2022).

49. Lemme, M. C. *et al.* Etching of graphene devices with a helium ion beam. *ACS Nano* **3**, 2674–2676 (2009).

50. Sahin, R., Simsek, E. & Akturk, S. Nanoscale patterning of graphene through femtosecond laser ablation. *Appl Phys Lett* **104**, 053118 (2014).

51. Park, J. B., Yoo, J. H. & Grigoropoulos, C. P. Multi-scale graphene patterns on arbitrary substrates via laser-assisted transfer-printing process. *Appl Phys Lett* **101**, 043110 (2012).

52. Cho, E. H. *et al.* A graphene mesh as a hybrid electrode for foldable devices. *Nanoscale* **10**, 628–638 (2018).

53. Hines, D. R., Ballarotto, V. W., Williams, E. D., Shao, Y. & Solin, S. A. Transfer printing methods for the fabrication of flexible organic electronics. *J Appl Phys* **101**, 024503 (2007).

54. Carlson, A., Bowen, A. M., Huang, Y., Nuzzo, R. G. & Rogers, J. A. Transfer printing techniques for materials assembly and micro/nanodevice fabrication. *Adv Mater* **24**, 5284–5318 (2012).

55. Fuchsberger, K. *et al.* Multiwalled carbon-nanotube-functionalized microelectrode arrays fabricated by microcontact printing: Platform for studying chemical and electrical neuronal signaling. *Small* **7**, 524–530 (2011).

56. Kim, H. *et al.* Soft lithography of graphene sheets via surface energy modification. *J Mater Chem C Mater* **1**, 1076–1079 (2013).

57. Singh, M., Haverinen, H. M., Dhagat, P. & Jabbour, G. E. Inkjet printing-process and its applications. *Adv Mater* **22**, 673–685 (2010).

58. Soum, V. *et al.* Inkjet-Printed Carbon Nanotubes for Fabricating a Spoof Fingerprint on Paper. *ACS Omega* **4**, 8626–8631 (2019).

59. Parvez, K., Worsley, R., Alieva, A., Felten, A. & Casiraghi, C. Water-based and inkjet printable inks made by electrochemically exfoliated graphene. *Carbon* **149**, 213–221 (2019).

60. Delaporte, P. & Alloncle, A. P. Laser-induced forward transfer: A high resolution additive manufacturing technology. *Opt Laser Technol* **78**, 33–41 (2016).

61. Serra, P. & Piqué, A. Laser-Induced Forward Transfer: Fundamentals and Applications. *Adv Mater Technol* **4**, 1800099 (2019).

62. Wei, T., Hauke, F. & Hirsch, A. Evolution of Graphene Patterning: From Dimension Regulation to Molecular Engineering. *Adv Mater* **33**, 2104060 (2021).

63. Park, S. J., Zhao, H., Kim, S., De Volder, M. & John Hart, A. Predictive Synthesis of Freeform Carbon Nanotube Microarchitectures by Strain-Engineered Chemical Vapor Deposition. *Small* **12**, 4393–4403 (2016).

64. Arul, R. *et al.* The mechanism of direct laser writing of graphene features into graphene oxide films involves photoreduction and thermally assisted structural rearrangement. *Carbon* **99**, 423–431 (2016).

65. Zhang, Y. *et al.* Direct imprinting of microcircuits on graphene oxides film by femtosecond laser reduction. *Nano Today* **5**, 15–20 (2010).

66. Choi, S. J., Kim, S. J. & Kim, I. D. Ultrafast optical reduction of graphene oxide sheets on colorless polyimide film for wearable chemical sensors. *NPG Asia Mater* **8**, e315 (2016).

67. Sharif, A., Farid, N., Collins, A., Jilani, A. & O'Connor, G. M. Extensive reduction of graphene oxide on thin polymer substrates by ultrafast laser for robust flexible sensor applications. *Appl Surf Sci* **613**, 156067 (2023).

68. Kymakis, E., Savva, K., Stylianakis, M. M., Fotakis, C. & Stratakis, E. Flexible organic photovoltaic cells with in situ nonthermal photoreduction of spin-coated graphene oxide electrodes. *Adv Funct Mater* **23**, 2742–2749 (2013).

69. Lin, J. *et al.* Laser-induced porous graphene films from commercial polymers. *Nat Commun* **5**, 5714 (2014).

70. Le, T. S. D. *et al.* Recent Advances in Laser-Induced Graphene: Mechanism, Fabrication, Properties, and Applications in Flexible Electronics. *Adv Funct Mater* **32**, 2205158 (2022).

71. Raffel, J. I., Freidin, J. F. & Chapman, G. H. Laser-formed connections using polyimide. *Appl Phys Lett* **42**, 705–706 (1983).

72. Rice, G. W. Laser Synthesis of Si/C/N Powders from 1,1,1,3,3,3-Hexamethyldisilazane. *J Am Ceram* **69**, C-183-C-185 (1986).

73. Li, L. *et al.* High-Performance Pseudocapacitive Microsupercapacitors from Laser-Induced Graphene. *Adv Mater* **28**, 838–845 (2016).

74. Ye, R. *et al.* Laser-Induced Graphene Formation on Wood. *Adv Mater* **29**, 1702211 (2017).

75. Nakajima, Y., Hayashi, S., Katayama, A., Nedyalkov, N. & Terakawa, M. Femtosecond laser-based modification of PDMS to electrically conductive silicon carbide. *Nanomaterials* **8**, 558 (2018).

76. Gao, Y. *et al.* Laser Direct Writing of Ultrahigh Sensitive SiC-Based Strain Sensor Arrays on Elastomer toward Electronic Skins. *Adv Funct Mater* **29**, 1806786 (2019).

77. Nair, V. *et al.* Laser writing of nitrogen-doped silicon carbide for biological modulation. *Sci Adv* **6**, eaaz2743 (2020).

78. Dreimol, C. H. *et al.* Sustainable wood electronics by iron-catalyzed laser-induced graphitization for large-scale applications. *Nat Commun* **13**, 3680 (2022).

79. Funayama, R., Hayashi, S. & Terakawa, M. Laser-Induced Graphitization of Lignin/PLLA Composite Sheets for Biodegradable Triboelectric Nanogenerators. *ACS Sustain Chem Eng* **11**, 3114–3122 (2023).

80. Miyakoshi, R., Hayashi, S. & Terakawa, M. Direct Patterning of Conductive Structures on Hydrogels by Laser-Based Graphitization for Supercapacitor Fabrication. *Adv Electron Mater* **9**, 2201277 (2023).

81. Tao, L. Q. *et al.* An intelligent artificial throat with sound-sensing ability based on laser induced graphene. *Nat Commun* **8**, 14579 (2017).

82. Chyan, Y. *et al.* Laser-Induced Graphene by Multiple Lasing: Toward Electronics on Cloth, Paper, and Food. *ACS Nano* **12**, 2176–2183 (2018).

83. Zhu, Y., Cai, H., Ding, H., Pan, N. & Wang, X. Fabrication of Low-Cost and Highly Sensitive Graphene-Based Pressure Sensors by Direct Laser Scribing Polydimethylsiloxane. *ACS Appl Mater Interfaces* **11**, 6195–6200 (2019).

84. Dupas-Bruzek, C., Robbe, O., Addad, A., Turrell, S. & Derozier, D. Transformation of medical grade silicone rubber under Nd:YAG and excimer laser irradiation: First step towards a new miniaturized nerve electrode fabrication process. *Appl Surf Sci* **255**, 8715–8721 (2009).

85. Hautefeuille, M. *et al.* New perspectives for direct PDMS microfabrication using a

CD-DVD laser. *Lab Chip* **13**, 4848–4854 (2013).

86. Alshehri, A. M., Deepak, K. L. N., Marquez, D. T., Desgreniers, S. & Bhardwaj, V. R. Localized nanoclusters formation in PDMS upon irradiation with femtosecond laser. *Opt Mater Express* **5**, 858 (2015).

87. Stankova, N. E. *et al.* Optical properties of polydimethylsiloxane (PDMS) during nanosecond laser processing. *Appl Surf Sci* **374**, 96–103 (2016).

88. Atanasov, P. A. *et al.* Fs-laser processing of medical grade polydimethylsiloxane (PDMS). *Appl Surf Sci* **374**, 229–234 (2016).

89. Wang, W. *et al.* Direct Laser Writing of Superhydrophobic PDMS Elastomers for Controllable Manipulation via Marangoni Effect. *Adv Funct Mater* **27**, 1702946 (2017).

90. Hayashi, S., Nakajima, Y. & Terakawa, M. Strain sensing using electrically conductive structures fabricated by femtosecond-laser-based modification of PDMS. *Opt Mater Express* **9**, 2672 (2019).

91. Parmeggiani, M. et al. PDMS/Polyimide Composite as an Elastomeric Substrate for Multifunctional Laser-Induced Graphene Electrodes. *ACS Appl Mater Interfaces* **11**, 33221–33230 (2019).

92. Torrisi, L. *et al.* IR ns pulsed laser irradiation of Polydimethylsiloxane in vacuum. *Vacuum* **177**, 109361 (2020).

93. Boisvert, J.-S. *et al.* Photosensitised PDMS for femtosecond laser writing. *OSA Contin* **3**, 1334 (2020).

94. Hayashi, S., Morosawa, F. & Terakawa, M. Synthesis of silicon carbide nanocrystals and multilayer graphitic carbon by femtosecond laser irradiation of polydimethylsiloxane. *Nanoscale Adv* **2**, 1886–1893 (2020).

95. Sinha, K., Meng, L., Xu, Q. & Wang, X. Laser induction of graphene onto lignin-upgraded flexible polymer matrix. *Mater Lett* **286**, 129268 (2021).

96. Jeong, S. Y. *et al.* Highly skin-conformal laser-induced graphene-based human motion monitoring sensor. *Nanomaterials* **11**, 951 (2021).

97. Hayashi, S., Morosawa, F. & Terakawa, M. Laser Direct Writing of Highly Crystalline Graphene on Polydimethylsiloxane for Fingertip-Sized Piezoelectric Sensors. *Adv Eng Mater* **23**, 2100457 (2021).

98. Shin, J. *et al.* Monolithic digital patterning of polydimethylsiloxane with successive laser pyrolysis. *Nat Mater* **20**, 100–107 (2021).

99. Zaccagnini, P. *et al.* Laser-Induced Graphenization of PDMS as Flexible Electrode

for Microsupercapacitors. *Adv Mater Interfaces* **8**, 2101046 (2021).

100. Hayashi, S., Tsunemitsu, K. & Terakawa, M. Laser Direct Writing of Graphene Quantum Dots inside a Transparent Polymer. *Nano Lett* **22**, 775–782 (2022).

101. Lee, C. W. *et al.* Fabrication of laser-induced graphene-based multifunctional sensing platform for sweat ion and human motion monitoring. *Sens Actuators A Phys* **334**, 113320 (2022).

102. Ji, Y. *et al.* Flexible Metal Electrodes by Femtosecond Laser-Activated Deposition for Human-Machine Interfaces. *ACS Appl Mater Interfaces* **14**, 11971–11980 (2022).

103. Du, Y., Wu, T., Xie, H. & Qu, J. P. One-step laser etching of a bionic hierarchical structure on a silicone rubber surface with thermal and acid/alkali resistance and tunable wettability. *Soft Matter* **18**, 3412–3421 (2022).

104. Wang, H., Zhao, Z., Liu, P. & Guo, X. A soft and stretchable electronics using laser-induced graphene on polyimide/PDMS composite substrate. *npj Flexible Electronics* **6**, 26 (2022).

105. Lu, L., Zhang, D., Xie, Y., He, H. & Wang, W. Laser Induced Graphene/Silicon Carbide: Core–Shell Structure, Multifield Coupling Effects, and Pressure Sensor Applications. *Adv Mater Technol* **7**, 2200441 (2022).

106. Wang, W., Lu, L., Zhang, D., Yao, Y. & Xie, Y. Experimental and modeling study of laser induced silicon carbide/graphene on cotton cloth for superhydrophobic applications. *Opt Laser Technol* **158**, 108782 (2023).

107. Hayashi, S. & Terakawa, M. Direct Writing of Fluorescent Semiconducting Nanoparticles on Polydimethylsiloxane by Ultrashort-Pulsed Laser Processing: Implications for Electronic and Photonic Device Fabrication. *ACS Appl Nano Mater* **6**, 2125–2132 (2023).

108. Morosawa, F., Hayashi, S. & Terakawa, M. Femtosecond Laser-Induced Graphitization of Transparent Cellulose Nanofiber Films. *ACS Sustain Chem Eng* **9**, 2955–2961 (2021).

109. Le, T. S. D., Park, S., An, J., Lee, P. S. & Kim, Y. J. Ultrafast Laser Pulses Enable One-Step Graphene Patterning on Woods and Leaves for Green Electronics. *Adv Funct Mater* **29**, 1902771 (2019).

110. Peng, Y., Zhao, W., Ni, F., Yu, W. & Liu, X. Forest-like Laser-Induced Graphene Film with Ultrahigh Solar Energy Utilization Efficiency. *ACS Nano* **15**, 19490–19502 (2021).

111. Stanford, M. G. *et al.* High-Resolution Laser-Induced Graphene. Flexible Electronics beyond the Visible Limit. *ACS Appl Mater Interfaces* **12**, 10902–10907 (2020).

112. Gandla, S., Moon, C., Baek, S., Park, H. & Kim, S. Laser-Induced Carbonization for Anticounterfeiting Tags. *Adv Funct Mater* **33**, 2211762 (2023).

113. Delhaes, P. *Graphite and Precursors*. (CRC Press, 2000).

114. Oberlin, A. Carbonization and Graphitization. *Carbon* **22**, 541 (1984).

115. Nagornov, Y. S. Thermodynamics of silicon carbide nucleation during the carbonization of nanoporous silicon. *Technical Physics* **60**, 700–709 (2015).

116. Wang, Y. M. & Zhang, C. H. Study on Structural Evolution of Synthetic Graphite Derived from Lignite Prepared by High Temperature–High Pressure Method. *Crystals* **12**, 464 (2022).

117. Manohar, D. M. & Raju, V. Effect of pressure and temperature on properties of carbon-carbon composites prepared from renewable material. in *ICCCCM 2016 - 2nd IEEE International Conference on Control Computing Communication and Materials* (2017).

118. Funke, A. & Ziegler, F. Hydrothermal carbonization of biomass: A summary and discussion of chemical mechanisms for process engineering. *Biofuels Bioprod Biorefin* **4**, 160–177 (2010).

119. Camino, G., Lomakin, S. M. & Lazzari, M. Polydimethylsiloxane thermal degradation Part 1. Kinetic aspects. *Polymer* **42**, 2395–2402 (2001).

120. Camino, G., Lomakin, S. M. & Lageard, M. Thermal polydimethylsiloxane degradation. Part 2. The degradation mechanisms. *Polymer* **43**, 2011–2015 (2002).

121. Scarmi, A., Sorarù, G. D. & Raj, R. The role of carbon in unexpected visco(an)elastic behavior of amorphous silicon oxycarbide above 1273 K. *J Non Cryst Solids* **351**, 2238–2243 (2005).

122. Saha, A., Raj, R. & Williamson, D. L. A model for the nanodomains in polymer-derived SiCO. *J Am Ceram* **89**, 2188–2195 (2006).

123. Wen, Q., Yu, Z. & Riedel, R. The fate and role of in situ formed carbon in polymer-derived ceramics. *Prog Mater Sci* **109**, 100623 (2020).

124. Zumdahl, S. S. & Zumdahl, S. A. *Chemistry, 6th Edition*. (McDougal Littell/Houghton Mifflin, 2003).

125. Liu, L., Qing, M., Wang, Y. & Chen, S. Defects in Graphene: Generation, Healing,

and Their Effects on the Properties of Graphene: A Review. *J Mater Sci Technol* **31**, 599–606 (2015).

126. Thiyagarajan, K., Ananth, A., Saravanakumar, B., Mok, Y. S. & Kim, S. J. Defect-induced metallic-to-semiconducting transition in multilayer graphene. *RSC Adv* **5**, 16821–16827 (2015).

127. McLachlan, D. S. An equation for the conductivity of binary mixtures with anisotropic grain structures. *J Phys C: Solid State Phys* **20**, 865 (1987).

128. Cordelair, J. & Greil, P. Electrical conductivity measurements as a microprobe for structure transitions in polysiloxane derived Si-O-C ceramics. *J Eur Ceram Soc* **20**, 1947–1957 (2000).

129. Wang, Y. *et al.* Effect of thermal initiator concentration on the electrical behavior of polymer-derived amorphous silicon carbonitrides. *J Am Ceram* **91**, 3971–3975 (2008).

130. Trassl, S., Puchinger, M., Rösslerrössler, E. & Ziegler, G. G. Electrical properties of amorphous $SiC_xN_yH_z$-ceramics derived from polyvinylsilazane. *J Eur Ceram Soc* **23**, 781–789 (2003).

131. Rhys-Williams, A. T. *An Introduction to Fluorescence Spectroscopy*. (Perkin-Elmer, 1981).

132. Divsar, F. *Quantum Dots - Fundamental and Applications*. (IntechOpen, 2020).

133. Xu, Q. *et al.* Two-dimensional quantum dots: Fundamentals, photoluminescence mechanism and their energy and environmental applications. *Mater Today Energy* **10**, 222–240 (2018).

134. Zhu, S. *et al.* Photoluminescence mechanism in graphene quantum dots: Quantum confinement effect and surface/edge state. *Nano Today* **13**, 10–14 (2017).

135. Rakovich, A. & Rakovich, T. Semiconductor versus graphene quantum dots as fluorescent probes for cancer diagnosis and therapy applications. *J Mater Chem B* **6**, 2690–2712 (2018).

136. Fujiwara, H. *Spectroscopic Ellipsometry: Principles and Applications*. (Wiley, 2007).

137. Sundaram, S. K. & Mazur, E. Inducing and probing non-thermal transitions in semiconductors using femtosecond laser pulses. *Nat Mater* **1**, 217–224 (2002).

138. Siegal, Y., Glezer, E. N., Huang, L. & Mazur, E. Laser-Induced Phase Transitions in Semiconductors. *Annu Rev Mater Sci* **25**, 223–247 (1995).

139. Kittle, C. *Introduction to Solid State Physics, 8th Edition*. vol. 8 (John Wiley &

Sons, Inc., 2005).

140. Cohen, M. L. & Chelikowsky, J. R. *Electronic Structure and Optical Properties of Semiconductors*. (Springer Berlin, Heidelberg, 1988).

141. Van Driel, H. M. Kinetics of high-density plasmas generated in Si by 1.06-and 0.53-pm picosecond laser pulses. *Phys Rev B* **35**, 8166–8176 (1987).

142. von Allmen, M. *Laser-Beam Interactions with Materials*. vol. 2 (Springer Berlin Heidelberg, 1987).

143. Köstli, K. P., Frenz M., Bebie H. & Weber, H. P. Temporal backward projection of optoacoustic pressure transients using Fourier transform methods. *Phys Med Biol* **46**, 1863 (2001).

144. Cox, B. T. & Beard, P. C. Fast calculation of pulsed photoacoustic fields in fluids using k-space methods. *J Acoust Soc Am* **117**, 3616–3627 (2005).

145. Ito, Y., Shinomoto, R., Otsu, A., Nagato, K. & Sugita, N. Dynamics of pressure waves during femtosecond laser processing of glass. *Opt Express* **27**, 29158 (2019).

146. Harilal, S. S., Miloshevsky, G. V., Diwakar, P. K., Lahaye, N. L. & Hassanein, A. Experimental and computational study of complex shockwave dynamics in laser ablation plumes in argon atmosphere. *Phys Plasmas* **19**, 083504 (2012).

147. Rethfeld, B., Ivanov, D. S., Garcia, M. E. & Anisimov, S. I. Modelling ultrafast laser ablation. *J Phys D* **50**, 193001 (2017).

148. Popruzhenko, S. V. Keldysh theory of strong field ionization: History, applications, difficulties and perspectives. *J Phys B: At Mol Opt* **47**, 204001 (2014).

149. Tiliakos, A., Ceaus, C., Iordache, S. M., Vasile, E. & Stamatin, I. Morphic transitions of nanocarbons via laser pyrolysis of polyimide films. *J Anal Appl Pyrolysis* **121**, 275–286 (2016).

150. Murray, R., Burke, M., Iacopino, D. & Quinn, A. J. Design of Experiments and Optimization of Laser-Induced Graphene. *ACS Omega* **6**, 16736–16743 (2021).

151. Behrent, A., Griesche, C., Sippel, P. & Baeumner, A. J. Process-property correlations in laser-induced graphene electrodes for electrochemical sensing. *Microchimica Acta* **188**, 159 (2021).

152. Misra, U., Dixit, N. & Singh, S. P. Effect of Laser Parameters on Laser-Induced Graphene Filter Fabrication and Its Performance for Desalination and Water Purification. *ACS Appl Mater Interfaces* **15**, 7899–7910 (2023).

153. Duy, L. X. *et al.* Laser-induced graphene fibers. *Carbon* **126**, 472–479 (2018).

154. Lee, J., Kim, H. C., Choi, J. W. & Lee, I. H. A review on 3D printed smart devices for 4D printing. *Int J Precis Eng Manuf - Green Technol* **4**, 373–383 (2017).

155. Rybaltovskii, A., Minaev, N., Tsypina, S., Minaeva, S. & Yusupov, V. Laser-induced microstructuring of polymers in gaseous, liquid and supercritical media. *Polymers* **13**, 3525 (2021).

156. Lazare, S., Elaboudi, I., Castillejo, M. & Sionkowska, A. Model properties relevant to laser ablation of moderately absorbing polymers. *Appl Phys A* **101**, 215–224 (2010).

157. Rabek, J. F. *Polymer Photodegradation* (Springer Netherlands, 1995).

158. Abdulhafez, M., Tomaraei, G. N. & Bedewy, M. Fluence-Dependent Morphological Transitions in Laser-Induced Graphene Electrodes on Polyimide Substrates for Flexible Devices. *ACS Appl Nano Mater* **4**, 2973–2986 (2021).

159. Chung, J. Y., Nolte, A. J. & Stafford, C. M. Diffusion-controlled, self-organized growth of symmetric wrinkling patterns. *Adv Mater* **21**, 1358–1362 (2009).

160. Ruan, X., Wang, R., Luo, J., Yao, Y. & Liu, T. Experimental and modeling study of CO_2 laser writing induced polyimide carbonization process. *Mater Des* **160**, 1168–1177 (2018).

161. Smausz, T. *et al.* Determination of UV–visible–NIR absorption coefficient of graphite bulk using direct and indirect methods. *Appl Phys A* **123**, (2017).

162. Ferrari, A. C. Raman spectroscopy of graphene and graphite: Disorder, electron-phonon coupling, doping and nonadiabatic effects. *Solid State Commun* **143**, 47–57 (2007).

163. Wieligor, M., Wang, Y. & Zerda, T. W. Raman spectra of silicon carbide small particles and nanowires. *J Phys Condens Matter* **17**, 2387–2395 (2005).

164. Ferrari, A. C. & Basko, D. M. Raman spectroscopy as a versatile tool for studying the properties of graphene. *Nature Nanotech* **8**, 235-246 (2013).

165. Malard, L. M., Pimenta, M. A., Dresselhaus, G. & Dresselhaus, M. S. Raman spectroscopy in graphene. *Phys Rep* **473**, 51–87 (2009).

166. Pimenta, M. A. *et al.* Studying disorder in graphite-based systems by Raman spectroscopy. *Phys Chem Chem Phys* **9**, 1276–1291 (2007).

167. Colombo, P., Mera, G., Riedel, R. & Sorarù, G. D. Polymer-derived ceramics: 40 Years of research and innovation in advanced ceramics. *J Am Ceram* **93**, 1805–1837 (2010).

168. Dinh, T. N., Tu, J. P., Dinh, A. T. & Theofanous, T. G. Nucleation phenomena in

boiling on nanoscopically smooth surfaces. in *41st Aerospace Sciences Meeting and Exhibit* (2003).

169. Lenski, D. R. & Fuhrer, M. S. Raman and optical characterization of multilayer turbostratic graphene grown via chemical vapor deposition. *J Appl Phys* **110**, 013720 (2011).

170. Lee, D. S. *et al.* Raman spectra of epitaxial graphene on SiC and of epitaxial graphene transferred to SiO_2. *Nano Lett* **8**, 4320–4325 (2008).

171. Cotton, D. P. J., Popel, A., Graz, I. M. & Lacour, S. P. Photopatterning the mechanical properties of polydimethylsiloxane films. *J Appl Phys* **109**, (2011).

172. Claramunt, S. *et al.* The importance of interbands on the interpretation of the raman spectrum of graphene oxide. *J Phys Chem C* **119**, 10123–10129 (2015).

173. Yang, D. *et al.* Chemical analysis of graphene oxide films after heat and chemical treatments by X-ray photoelectron and Micro-Raman spectroscopy. *Carbon* **47**, 145–152 (2009).

174. Prawer, S. & Nemanich, R. J. Raman spectroscopy of diamond and doped diamond. *Philos Trans Royal Soc A* **362**, 2537–2565 (2004).

175. Merlen, A., Buijnsters, J. G. & Pardanaud, C. A guide to and review of the use of multiwavelength Raman spectroscopy for characterizing defective aromatic carbon solids: From graphene to amorphous carbons. *Coatings* **7**, 153 (2017).

176. Shi, R. *et al.* Microstructural control in metal laser powder bed fusion additive manufacturing using laser beam shaping strategy. *Acta Mater* **184**, 284–305 (2020).

177. Lin, A. Y. W., Yu, X. Xiang, Dato, A., Krauss, G. & Marks, L. D. In situ observations of graphitic staples in crumpled graphene. *Carbon* **132**, 760–765 (2018).

178. Mishra, N., Boeckl, J., Motta, N. & Iacopi, F. Graphene growth on silicon carbide: A review. *Phys Status Solidi A* **213**, 2277–2289 (2016).

179. Cao, T., Cheng, Y., Zhang, H., Yan, B. & Cheng, Y. High rate fabrication of room temperature red photoluminescent SiC nanocrystals. *J Mater Chem C Mater* **3**, 4876–4882 (2015).

180. Yonesaki, Y., Miura, K., Araki, R., Fujita, K. & Hirao, K. Space-selective precipitation of non-linear optical crystals inside silicate glasses using near-infrared femtosecond laser. *J Non Cryst Solids* **351**, 885–892 (2005).

181. Tsujino, M. *et al.* Synthesis of submicron metastable phase of silicon using femtosecond laser-driven shock wave. *J Appl Phys* **110**, 126103 (2011).

182. Carvalho, A. F. *et al.* Laser-Induced Graphene Strain Sensors Produced by Ultraviolet Irradiation of Polyimide. *Adv Funct Mater* **28**, 1805271 (2018).

183. Wan, S. *et al.* A Highly Skin-Conformal and Biodegradable Graphene-Based Strain Sensor. *Small Methods* **2**, 1700374 (2018).

184. Luong, D. X. *et al.* Laminated Object Manufacturing of 3D-Printed Laser-Induced Graphene Foams. *Adv Mater* **30**, 1707416 (2018).

185. Rahimi, R., Ochoa, M., Yu, W. & Ziaie, B. Highly stretchable and sensitive unidirectional strain sensor via laser carbonization. *ACS Appl Mater Interfaces* **7**, 4463–4470 (2015).

186. Li, H. *et al.* Ultrahigh-Sensitivity Piezoresistive Pressure Sensors for Detection of Tiny Pressure. *ACS Appl Mater Interfaces* **10**, 20826–20834 (2018).

187. Yoo, J. Y. *et al.* Industrial Grade, Bending-Insensitive, Transparent Nanoforce Touch Sensor via Enhanced Percolation Effect in a Hierarchical Nanocomposite Film. *Adv Funct Mater* **28**, 1804721 (2018).

188. Polat, E. O. et al. Flexible graphene photodetectors for wearable fitness monitoring. *Sci Adv* **5**, eaaw7846 (2019).

189. Kohara, K. *et al.* Radial augmentation index: A useful and easily obtainable parameter for vascular aging. *Am J Hypertens* **18**, 11–14 (2005).

190. Kashyap, K. *et al.* Elimination of strength degrading effects caused by surface microdefect: A prevention achieved by silicon nanotexturing to avoid catastrophic brittle fracture. *Sci Rep* **5**, 10869 (2015).

191. Kang, M. G., Kim, C., Lee, Y. J., Kim, S. Y. & Lee, H. Picosecond UV laser induced scribing of polyethylene terephthalate (PET) films for the enhancement of their flexibility. *Opt Laser Technol* **82**, 183–190 (2016).

192. Liu, F. *et al.* Facile synthetic method for pristine graphene quantum dots and graphene oxide quantum dots: Origin of blue and green luminescence. *Adv Mater* **25**, 3657–3662 (2013).

193. Pan, D., Zhang, J., Li, Z. & Wu, M. Hydrothermal route for cutting graphene sheets into blue-luminescent graphene quantum dots. *Adv Mater* **22**, 734–738 (2010).

194. Parent, P. *et al.* Nanoscale characterization of aircraft soot: A high-resolution transmission electron microscopy, Raman spectroscopy, X-ray photoelectron and near-edge X-ray absorption spectroscopy study. *Carbon* **101**, 86–100 (2016).

195. Abbas, A., Tabish, T. A., Bull, S. J., Lim, T. M. & Phan, A. N. High yield synthesis

of graphene quantum dots from biomass waste as a highly selective probe for Fe^{3+} sensing. *Sci Rep* **10**, 21262 (2020).

196. Zhang, M. *et al.* Facile synthesis of water-soluble, highly fluorescent graphene quantum dots as a robust biological label for stem cells. *J Mater Chem* **22**, 7461–7467 (2012).

197. Chen, X. *et al.* Blue and green double band luminescent carbon quantum dots: Synthesis, origin of photoluminescence, and application in white light-emitting devices. *Appl Phys Lett* **118**, 153102 (2021).

198. Dong, Y. *et al.* Blue luminescent graphene quantum dots and graphene oxide prepared by tuning the carbonization degree of citric acid. *Carbon* **50**, 4738–4743 (2012).

199. Jang, D. M. *et al.* Laser-induced graphitization of colloidal nanodiamonds for excellent oxygen reduction reaction. *Phys Chem Chem Phys* **16**, 2411–2416 (2014).

200. Ozawa, M. *et al.* Preparation and behavior of brownish, clear nanodiamond colloids. *Adv Mater* **19**, 1201–1206 (2007).

201. Krishnamoorthy, K., Veerapandian, M., Yun, K. & Kim, S. J. The chemical and structural analysis of graphene oxide with different degrees of oxidation. *Carbon* **53**, 38–49 (2013).

202. Rajender, G. & Giri, P. K. Formation mechanism of graphene quantum dots and their edge state conversion probed by photoluminescence and Raman spectroscopy. *J Mater Chem C Mater* **4**, 10852–10865 (2016).

203. Piazza, F. *et al.* Low temperature, pressureless sp^2 to sp^3 transformation of ultrathin, crystalline carbon films. *Carbon* **145**, 10–22 (2019).

204. Kim, S. *et al.* Size-dependence of Raman scattering from graphene quantum dots: Interplay between shape and thickness. *Appl Phys Lett* **102**, 053108 (2013).

205. Daviau, K. & Lee, K. K. M. Decomposition of silicon carbide at high pressures and temperatures. *Phys Rev B* **96**, 174102 (2017).

206. Lee, N. E., Lee, S. Y., Lim, H. S., Yoo, S. H. & Cho, S. O. A novel route to high-quality graphene quantum dots by hydrogen-assisted pyrolysis of silicon carbide. *Nanomaterials* **10**, 277 (2020).

207. Li, M., Chen, T., Gooding, J. J. & Liu, J. Review of carbon and graphene quantum dots for sensing. *ACS Sens* **4**, 1732–1748 (2019).

208. Albrecht, M., Hu, G., Moser, A., Hellwig, O. & Terris, B. D. Magnetic dot arrays with multiple storage layers. *J Appl Phys* **97**, 103910 (2005).

List of publications

Publications related to this thesis

1. Shuichiro Hayashi, Mitsuhiro Terakawa, “Direct writing of fluorescent semiconducting nanoparticles on polydimethylsiloxane by ultrashort-pulsed laser processing: Implications for electronic and photonic device fabrication,” ACS Applied Nano Materials, Vol. 6, Issue 3, pp. 2125–2132, (2023).

2. Shuichiro Hayashi, Kaneto Tsunemitsu, Mitsuhiro Terakawa, “Laser direct writing of graphene quantum dots inside a transparent polymer,” Nano Letters, Vol. 22, Issue 2, pp. 775–782, (2022).

3. Shuichiro Hayashi, Fumiya Morosawa, Mitsuhiro Terakawa, “Laser direct writing of highly crystalline graphene on PDMS for fingertip-sized piezoelectric sensors,” Advanced Engineering Materials, Vol. 23, Issue 10, 2100457, (2021).

4. Shuichiro Hayashi, Fumiya Morosawa, Mitsuhiro Terakawa, “Synthesis of silicon carbide nanocrystals and multilayer graphitic carbon by femtosecond laser irradiation of polydimethylsiloxane,” Nanoscale Advances, Vol. 2, Issue 5, pp. 1886–1893, (2020).

5. Shuichiro Hayashi, Yasutaka Nakajima, Mitsuhiro Terakawa, “Strain sensing using electrically conductive structures fabricated by femtosecond-laser-based modification of PDMS,” Optical Materials Express, Vol. 9, Issue 6, pp. 2672–2680, (2019).

Other publications

1. Rikuto Miyakoshi, Shuichiro Hayashi, Mitsuhiro Terakawa, “Direct patterning of conductive structures on hydrogels by laser-based graphitization for supercapacitor fabrication,” Advanced Electronic Materials, Vol. 9, Issue 5, 2201277, (2023).

2. Rei Funayama, Shuichiro Hayashi, Mitsuhiro Terakawa, “Laser-induced graphitization of lignin/PLLA composite sheet for biodegradable triboelectric nanogenerator,” ACS Sustainable Chemistry & Engineering, Vol. 11, Issue 7, pp. 3114–3122, (2023).

3. Marco Rupp, Shuichiro Hayashi, Claire Dashe, Shashank Gupta, Reza Moini, Craig B. Arnold, “Continuous wave laser grooving of cementitious materials,” Applied Physics A, Vol. 129, Issue 160, pp. 1–6, (2023).

4. Rikuto Miyakoshi, Shuichiro Hayashi, Mitsuhiro Terakawa, “Simultaneous laser-

based graphitization and microstructuring of bamboo for supercapacitors derived from renewable resources," RSC Advances, Vol. 12, Issue 46, pp. 775–782, (2022).

5. Nikolay Nedyalkov, Anna Dlkovska, Rumen Nikov, Genoveva Atanasova, Shuichiro Hayashi, Mitsuhiro Terakawa, "Laser-induced periodic structure formation in AlN ceramic," Optics & Laser Technology, Vol. 144, pp. 1886–1893, (2021).

6. Fumiya Morosawa, Shuichiro Hayashi, Mitsuhiro Terakawa, "Femtosecond-laser-induced graphitization of transparent cellulose nanofiber films," ACS Sustainable Chemistry & Engineering, Vol. 9, Issue 7, pp. 2955–2961, (2021).

7. Yasutaka Nakajima, Shuichiro Hayashi, Akito Katayama, Nikolay Nedyalkov, Mitsuhiro Terakawa, "Femtosecond laser-based modification of PDMS to electrically conductive silicon carbide," Nanomaterials, Vol. 8, Issue 7, 558, (2018).

International conferences

1. Shuichiro Hayashi, Xiaohan Du, Marco Rupp, Kai A. Filsinger, Mitsuhiro Terakawa, Craig B. Arnold, "Consideration of heating rates on structure formation for laser-induced graphitization of polymers," The 24th International Symposium on Laser Precision Microfabrication (LPM 2023), Hirosaki, Japan.

2. Marco Rupp, Shuichiro Hayashi, Xiaohan Du, Claire Dashe, Craig B. Arnold, "Control of chemical composition for metals in laser-based powder bed fusion," The 24th International Symposium on Laser Precision Microfabrication (LPM 2023), Hirosaki, Japan.

3. Yannick Eatmon, Shuichiro Hayashi, Craig B. Arnold, "High Power Laser Sintering of LISICON electrolytes," The 24th International Symposium on Laser Precision Microfabrication (LPM 2023), Hirosaki, Japan.

4. Shuichiro Hayashi, Mitsuhiro Terakawa, "Direct writing of conductive and semiconductive structures via the femtosecond laser-induced carbonization of a silicone elastomer," SPIE Photonics West 2023, San Francisco, USA.

5. Rei Funayama, Shuichiro Hayashi, Mitsuhiro Terakawa, "Fabrication of biodegradable triboelectric nanogenerator by laser-induced graphitization of lignin/PLLA composite sheets," SPIE Photonics West 2023, San Francisco, USA.

6. Shuichiro Hayashi, Mitsuhiro Terakawa, "Direct writing of graphene and silicon carbide quantum dots on an elastomer by laser-induced carbonization," Material Research Society (MRS) Fall Meeting and Exhibit 2022, Boston, USA.

7. Rikuto Miyakoshi, Shuichiro Hayashi, Mitsuhiro Terakawa, “Hydrogel supercapacitor fabricated by lignin-mediated laser-induced graphitization,” Material Research Society (MRS) Fall Meeting and Exhibit 2022, Boston, USA.

8. Shuichiro Hayashi, Kaneto Tsunemitsu, Mitsuhiro Terakawa, “Laser direct writing of graphene quantum dots using a femtosecond laser,” 16th International Conference on Laser Ablation (COLA2021/2022), Matsue, Japan.

9. Rei Funayama, Shuichiro Hayashi, Mitsuhiro Terakawa, “Laser direct writing of electrically conductive structure on biodegradable polymer composite,” 16th International Conference on Laser Ablation (COLA2021/2022), Matsue, Japan.

10. Shuichiro Hayashi, Kaneto Tsunemitsu, Mitsuhiro Terakawa, “Laser-based direct synthesis and patterning of graphene quantum dots,” SPIE Photonics West 2022, Virtual Conference.

11. Rikuto Miyakoshi, Fumiya Morosawa, Shuichiro Hayashi, Mitsuhiro Terakawa, “Fabrication of supercapacitor using electrically-conductive-porous carbon patterned by laser carbonization of bamboo,” SPIE Photonics West 2022, Virtual Conference.

12. Fumiya Morosawa, Shuichiro Hayashi, Mitsuhiro Terakawa, “Fabrication of supercapacitor by femtosecond laser-induced graphitization of cellulose nanofiber film,” SPIE Photonics West 2022, San Francisco, USA.

13. Shuichiro Hayashi, Fumiya Morosawa, Mitsuhiro Terakawa, “Direct Writing of Highly Crystalline Laser-Induced Graphene on Polydimethylsiloxane for Wearable Devices,” Material Research Society (MRS) Fall Meeting and Exhibit 2021, Virtual Conference.

14. Rikuto Miyakoshi, Fumiya Morosawa, Shuichiro Hayashi, Mitsuhiro Terakawa, “Electrically conductive porous carbon structures fabricated by laser direct carbonization of bamboo,” Conference on Lasers and Electro-Optics (CLEO)/Europe-EQEC, Virtual Conference.

15. Shuichiro Hayashi, Fumiya Morosawa, Mitsuhiro Terakawa, “Laser-direct writing of a small and sensitive pressure sensor by laser-induced graphitization of PDMS,” The 22nd International Symposium on Laser Precision Microfabrication (LPM 2021), Virtual Conference.

16. Fumiya Morosawa, Shuichiro Hayashi, Mitsuhiro Terakawa, “Laser direct writing of electrically conductive graphitic carbon on cellulose nanofiber using 522-nm femtosecond laser,” The 22nd International Symposium on Laser Precision Microfabrication (LPM 2021), Virtual Conference.

17. Shuichiro Hayashi, Fumiya Morosawa, Mitsuhiro Terakawa, “Femtosecond-laser direct writing of electrically conductive structures on PDMS for flexible device applications,” SPIE Photonics West 2021, Virtual Conference.

18. Fumiya Morosawa, Shuichiro Hayashi, Mitsuhiro Terakawa, “Femtosecond-Laser-Induced Graphitic Carbon from Transparent Cellulose Nanofiber Films,” 14th Pacific Rim Conference on Lasers and Electro-Optics, Virtual Conference.

19. Shuichiro Hayashi, Yasutaka Nakajima, Mitsuhiro Terakawa, “Laser direct writing of electrically conductive structures with anisotropic sensitivity to strain on an elastic polymer,” Material Research Society (MRS) Fall Meeting and Exhibit 2019, Boston, USA.

20. Shuichiro Hayashi, Yasutaka Nakajima, Mitsuhiro Terakawa, “Surface morphology analysis of electrically conductive β-SiC fabricated by femtosecond laser irradiation,” The 8th International Congress on Laser Advanced Materials Processing (LAMP2019), Hiroshima, Japan.

21. Shuichiro Hayashi, Yasutaka Nakajima, Mitsuhiro Terakawa, “Strain sensing using electrically conductive structures composed of β-SiC fabricated by femtosecond laser direct modification of PDMS,” International Symposium on SSS Laser Processing (3S-LP), Yokohama, Japan.

22. Yasutaka Nakajima, Shuichiro Hayashi, Akito Katayama, Nikolay Nedyalkov, Mitsuhiro Terakawa, “Femtosecond laser-based formation of electrically conductive silicon carbide on PDMS,” SPIE Photonics West 2019, San Francisco, USA.

Domestic conferences

1. 舩山怜, 林秀一郎, 寺川光洋, “レーザー直接描画による生分解性摩擦帯電型ナノ発電機の作製,” 第 83 回応用物理学会秋季学術講演会, 仙台, 2022 年 9 月 22 日.

2. 宮越陸人, 林秀一郎, 寺川光洋, “リグニン含有ハイドロゲルのレーザー炭化による電気二重層キャパシタの作製,” 第 83 回応用物理学会秋季学術講演会, 仙台, 2022 年 9 月 22 日.

3. 林秀一郎, 寺川光洋, “フレキシブル材料のフェムト秒レーザ炭化と黒鉛化,” 第 166 回光・量子デバイス技術委員会, オンライン, 2022 年 6 月 24 日. 【令和 3 年電気学会各賞受賞記念講演】

4. 甲斐将人, 林秀一郎, 寺川光洋, “PDMS のフェムト秒レーザー炭化によるカーボンナノオニオンの生成,” 第 69 回応用物理学会春季学術講演会, オンライン,

2022 年 3 月 24 日.

5. 舩山怜, 林秀一郎, 寺川光洋, “リグニン/ポリ-L-乳酸複合シートへのフェムト秒レーザーパルス照射による導電性炭素構造の作製,” レーザー学会学術講演会第 42 回年次大会, オンライン, 2022 年 1 月 12 日.

6. 林秀一郎, 寺川光洋, “フレキシブル材料のフェムト秒レーザ炭化と黒鉛化,” 電気学会　電子・情報・システム部門 光・量子デバイス研究会, オンライン, 2021 年 3 月 29 日.

7. 林秀一郎, 茂呂澤郁也, 寺川光洋, “フレキシブルデバイス応用に向けた PDMS のフェムト秒レーザー改質による導電性構造作製,” 第 68 回応用物理学会春季学術講演会, オンライン, 2021 年 3 月 18 日. 【講演奨励賞受賞記念講演】

8. 茂呂澤郁也, 林秀一郎, 寺川光洋, “セルロースナノファイバーへのフェムト秒レーザーパルス照射による炭化構造の作製,” レーザー学会学術講演会第 41 回年次大会, オンライン, 2021 年 1 月 18 日.

9. 宮越陸人, 茂呂澤郁也, 林秀一郎, 寺川光洋, “竹材へのフェムト秒レーザーパルス照射による多孔質炭素の作製,” レーザー学会学術講演会第 41 回年次大会, オンライン, 2021 年 1 月 18 日.

10. 林秀一郎, 茂呂澤郁也, 寺川光洋, “フェムト秒レーザー直接描画による PDMS への導電性構造作製,” 第 81 回応用物理学会秋季学術講演会, オンライン, 2020 年 9 月 9 日.

11. 茂呂澤郁也, 林秀一郎, 寺川光洋, “セルロースナノファイバーのフェムト秒レーザー炭化による導電性構造作製,” 第 67 回応用物理学会春季学術講演会, 東京, 2020 年 3 月 12 日.